LARGE SCALE 2D HYDRAULIC MODELLING: IMPROVING THE ANALYSIS OF FLOOD DYNAMICS WITH REMOTE SENSING AND VOLUNTARY GEOGRAPHIC INFORMATION

Dissertation

submitted to and approved by the

Department of Architecture, Civil Engineering and Environmental Sciences
University of Braunschweig – Institute of Technology

and the

Department of Civil and Environm/ental Engineering
University of Florence

in candidacy for the degree of a
Doktor-Ingenieur (Dr.-Ing.) /
Dottore di Ricerca in Civil and Environmental Engineering[*)]

by

Antonio Annis
born 29/08/1986
from Oristano, Italy

Submitted on	20 February, 2018
Oral examination on	07/05/2018
Professorial advisors	Prof. Wolfgang Niemeier Prof. Fabio Castelli

2019

To Mariagrazia, Francesco and Francesca

To Nadia

Summary

Population growth driving the human pressure in riverine areas, mostly in developing countries, together with the sea level rise due to climate change is causing an intensification of flood-related damages and fatalities. As a result, territorial planning for managing flood risk and flood-prone areas and non-structural measures (e.g. early warning systems) for flood forecasting are usually developed, principally adopting hydrologic and hydraulic modelling. Numerical models require a large amount of data for model calibration, validation towards flood dynamics understanding and inundation map updating. Data Assimilation (DA) methods are useful tools for improving flood forecasting models and reducing their uncertainties.

This work investigates the integration of hydro-geomorphic models, traditional data (static stage gages) and novel data sources, such as remotely sensed images and Crowdsourced data (Volunteering Geographic Information or VGI), for observation-driven improvements of hydro-modelling tools. The Tiber river basin, the second largest basin in Italy, was selected as case study with a focus domain on the approximately 120 km channel upstream of Rome for its strategic importance in the protection of the historical city centre and the coastal urbanized zone.

Hydro-geomorphic models are used both as forcing inputs and for delineating the computational domain of a quasi-2D hydraulic model that represents the core of the water level forecasting model within the Data Assimilation framework. Specifically, a parsimonious hydrological modelling algorithm was implemented, calibrated and validated for calculating the flow hydrographs of the ungauged small basins contributing to the study area. Furthermore, to delineate the boundaries computational domain of the hydraulic model for the Data Assimilation application, a DEM-based hydro-geomorphic floodplain delineation algorithm adapted from literature was tested with different DEMs and considering also its parametrization varying the stream orders. Results obtained by the geomorphic algorithm also provided reasonable ranges of the scaling law parameters, originally calibrated from in situ surveys, and here adapted for a DEM-based approach, paving the way for larger scale expeditious flood prone area mapping, that can be consider as a secondary aim of the proposed research. The delineation of the computational domain with this methodology is aimed to avoid the inclusion of hillslope areas, improving the computational efficiency of the Data Assimilation method.

The adopted DA methodology is the Ensemble Kalman Filter (EnKF) that requires multiple simulations for representing the uncertainties related to the model and the observations errors.

New approaches were proposed for integrating, as observations in the DA method, traditional static sensors, and simultaneously remotely sensed images and VGI data. Despite the static sensor have already been adopted in literature as observations in a DA framework, some new technical measures were necessary for integrating them in Quasi-2D hydraulic model. As auxiliary analysis for the application of the DA methodology, water extension mapping from multispectral images was investigated for selected flood events and a methodology taking into account the ensemble of the hydraulic simulations for deriving the water surface elevation from the satellite image was developed. The assimilation of satellite images resulted to be effective, since the whole computational domain is interested by the water levels correction, although the improvement of the model performance persisted for only some hours of simulation. Despite the scarce availability of VGI data for real flood events in the study area, their usefulness have been investigated considering the uncertainties related to their reliability mostly in terms of accuracy and time allocation. Results show the potential of new data for improving the performance of the flood model, partially overcoming the limitations and the potential scarce availability of the traditional sensors. Finally, the simultaneous integration of all the three types of observations gave promising results, improving the performance of the model compared to the ones obtained assimilating only Satellite images or VGI observations.

Future work is needed to test satellite images but mostly the VGI data component because of the limited availability of these data and the not well known error related to their reliability. Furthermore, computational time for an ensemble of 2D hydraulic model simulations is still quite onerous. However, these limitations can be overcome soon by the increasing availability of Satellite remote sensed and VGI data and the considerable growth of the computational power of processors.

Table of contents

List of figures

List of tables

List of acronyms

1D	One Dimensional
2D	Two Dimensional
3D	Three Dimensional
API	Application Programming Interfaces
ASTER	Advanced Spaceborne Thermal Emission and Reflection Radiometer
AWEISH	Automated Water Extraction Index shadow
AWEINSH	Automated Water Extraction Index non shadow
CDE	Correlation Distance Error
CS	Crowdsourced
DA	Data Assimilation
DEM	Digital Elevation Model
DTM	Digital Terrain Model
DyS	Dynamic Sensor
FH	Flow Height
FL	Flow Length
FT	Flow Time
EWS	Early Warning Systems
HSG	Hydrologic Soil Group
IDW	Inverse Distance Weighting
IUH	Instantaneous Unit Hydrograph
LiDAR	Light Detection And Ranging
MDWI	Modified Normalized Difference Water Index
NDWI	Normalized Difference Moisture Index
NRR	Normalized RMSE Ratio
NSE	Nash-Sutcliffe Efficiency
PAI	Piano di Assetto Idrogeologico
pdf	probability density function
POI	Point Of Interest
RMSE	Root Mean Square Error
SAR	Synthetic Aperture Radar
SI	Satellite Imagery
SLC	Scan Line Corrector

SRTM	Shuttle Radar Topography Mission
StS	Static Sensor
SWOT	Surface Water Ocean Topography
TCW	Tasselled Cap Wetness
UAV	Unmanned Aerial Vehicles
UGC	User Generated Contents
VGI	Volunteered Geographic Information
WF	Width Function
WI	Water Index
WRI	Water Ratio Index
WSE	Water Surface Elevation

1.Introduction

The human activity in the last two centuries heavily influenced the natural processes on Earth so that the scientific community recognized a new geological Era, named Anthropocene (Crutzen, 2002). During this Anthropogenic era, hydrological processes are undergoing noticeable changes. The intensification of the water cycle due to a warming climate is projected to change the magnitude, frequency, and timing of river floods (Min et al, 2011; Pachauri et al., 2014), even if existing studies have been unable to identify a consistent climate change signal in flood magnitudes (Blöschl & Montanari, 2010; Blöschl et al., 2017). Demographic expansion enhanced the human pressure in riverine areas (Tockner & Stanford. 2002) and this phenomenon is still exacerbating mostly in developing countries, since societies tend to settle near deltas and floodplain areas (Di Baldassarre et al., 2015).

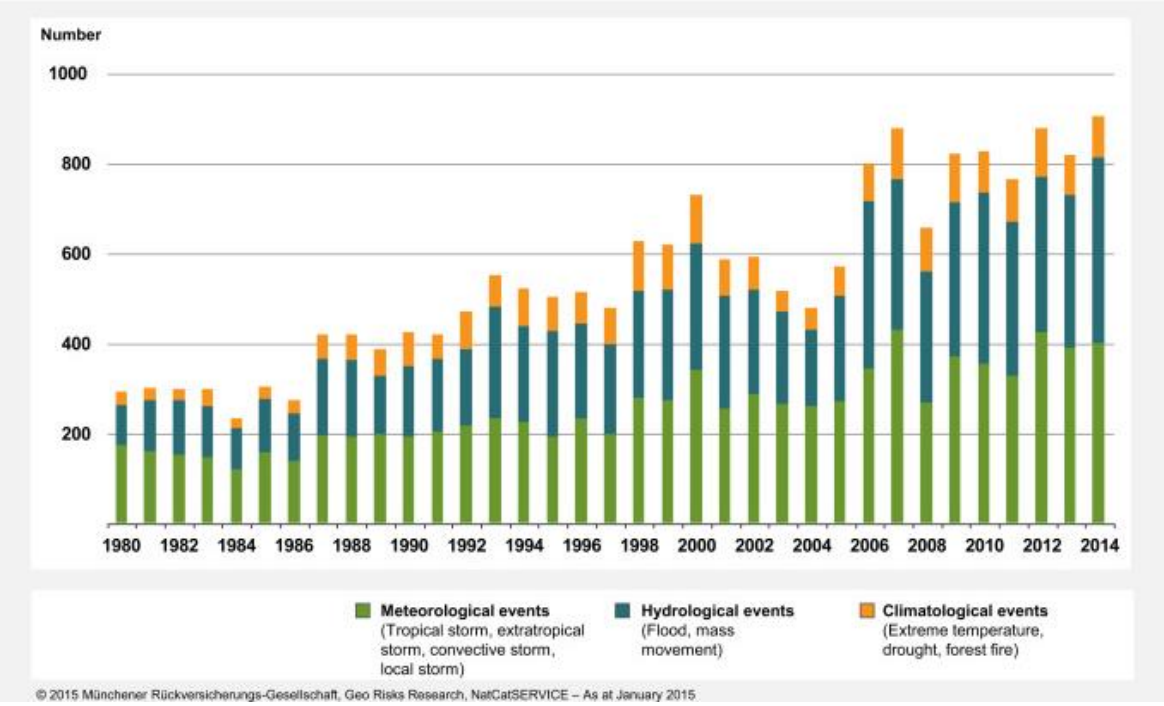

Figure 1. Annual numbers of global loss relevant natural events in the time 1980–2014. Adapted from Hoeppe (2016)

These factors caused a dramatic increasing of flood-related damages and fatalities (Emergency Events Database, 2013, Aerts et al., 2014, Dankers et al., 2014), with an estimated global annual average loss of US $104 billion (UNISDR, 2015) and this trend, together also with the sea level rise, seems to worsen year by year (Hinkel at al., 2014; Jongman et al., 2014), as illustrated in Figure 1.

Different approaches have been adopted for both avoiding the worsening of the flood risk in the future and mitigating the current flood risk: regional plans, structural and non-structural measures, e.g. Early Warning Systems (EWS).

Regional plans for flood risk mitigation aim to constrain flood prone areas and optimize the spatial distribution of human activities minimizing the flood related risk. The structural measures for flood risk mitigation, like levees, dams and weirs are designed to modify the flood extension and the flow regimes, sometimes causing imbalances in the floodplain ecology (Tockner & Stanford, 2002) and in the sediment transport that influence the river and the shorelines morphology (Poff et al., 1997). These structural measures sometimes are not enough to prevent flooding in many countries (Wilby et al., 2008). This caused an increasing need of EWS (Krzhizhanovskaya et al., 2011) in order to predict the flood levels and to allow decision makers to take the most effective decision to reduce the fatalities and economic losses in urbanized areas.

Flood modelling and mapping typically involve the use of hydrologic and hydraulic models with various degrees of complexity. Such models require large amounts of data for being calibrated, validated or, in case of EWS, updated in real time (Data Assimilation). This large amount of data is due to the complex physical phenomena that have to be simulated from the temporal and spatial rain distribution and intensity to infiltration, flow routing and flood propagation, that are influenced by several factors related to meteorology, geomorphology, soil characteristics, and topography.

However, traditional in situ measurements used for gather these data are often scarce and inadequate. For example, the classical static sensors, like the stage gages, require installation and maintenance costs so that sometimes they are completely missing in developing countries or, even in richer countries, their positioning never cover the whole stream network but only the most important rivers. For this reason, the scientific community in hydrological and hydraulic science set the goal of employing new observational technologies in improved predictive methods (Sivapalan et al., 2003).

On the other hand, new data sources are becoming more and more freely and largely available and their use paved, and it is still paving, the way for re-thinking new methods of calibrating, validating and updating the physical models (Bates, 2012). Satellite remote sensed data and, more recently, citizen data (Bonney et al., 2014) are proving to be of great support for flood mitigation.

In the following sections, an introduction of the state of the art of main topics related to this work is illustrated.

Specifically, Section 1.1 gives an overview on hydrologic and hydraulic modelling in terms of represented physical phenomena and related uncertainties.

Section 1.2 describes how remote sensing influenced not only the way of validating and updating hydraulic models but also their evolution considering the new information related to topography, vegetation, observed water levels and water extension.

Section 1.3 concerns how citizen science , mostly in the last five years, started to be considered in the field of flood mapping for reconstructing the flood extent of past events, for validating hydraulic models and even for updating simplified hydrologic and hydraulic models.

Section 1.4 briefly mentions the principal Data Assimilation techniques adopted in hydrologic and hydraulic models also referring to the different type of observations used for updating these models.

After the introductions on the state of the art of these topics, the main motivations and objectives of this work are illustrated in Section 1.5.

1.1. Hydrological and hydraulic models

Hydrological models schematize the hydrologic cycle with the aim of predicting water dynamics in quantitative terms, and sometimes the water quality, in space and time. Considering their structure, these models can be divided in three classes (Wheater at al., 1993; Devia et al., 2015): *physically-based* models (or mechanistic), *conceptual* models (or parametric) and *empirical* models (or black box models, data-drive models). These models can be also classified according to the spatial discretization as distributed, semi-distributed and lumped (Xu, 2002).

In the *physically-based* models, the physic phenomena involved in the water cycle (i.e. infiltration, evapotranspiration, surface flow, groundwater flow) are mathematically idealized. Usually they requires a large amount of input data, because of the complexity of the described physic phenomena. For their nature, these models are usually distributed because they need to take in to account the spatial distribution of the input and output variables (e.g. rain, soil moisture, soil properties heterogeneity, morphology variability, etc.). However, the lack of measurements in the whole domain and the spatial scale effects introduce uncertainties in the parameter values so that the output predictions can compromise their reliability (Beven, 2001). For this reason, these kind of models are quite difficult to be applied in data scarce regions where some of the many input parameters are missing. Examples of the physically-based models are MIKE SHE (Abbott et al., 1986), SWAT (Neitsch et al., 2011) and the Representative Elementary Watershed framework (REW, Reggiani et al., 1998).

Conceptual models describe the components of the hydrological processes using the continuity equation. The physical elements in a catchment are represented as reservoirs charged by rainfall, runoff, infiltration, percolation and emptied by evaporation, runoff and drainage. Usually, semi-empirical equation are used in these models and parameters can be estimated from field data and from calibration if enough measurements are available. There are many conceptual models in literature, among which there are the Stanford Watershed Model IV (SWM, Crawford & Linsley, 1966), Probability Distributed model (Moore, 1985), NAM-MIKE11 (Havnø et al., 1995), Sacramento model (Burnash, 1995), Hydrologiska Byras Vattenbalansavdelning (HBV, Lindström et al., 1997), GR4J model (Perrin et al., 2003), HEC-HMS (USACE-HEC, 2006), PCR-GLOBWB model (Van Beek et al., 2011).

Empirical models are so called “observation oriented” because they take only the information from the existing data without considering the features and processes of hydrological system and hence these models are also called data driven models or black box models. The

Instantaneous Unit Hydrograph (IUH) is an example of this kind of models and it has been, and still is, widely used. This methodology has the strong assumption of the linear theory for hydrologic system (Dooge, 1973). Among the empirical models, there are also statistically based methods that use regression and correlation models to find functional relationships between inputs and outputs starting from past observations of physical variables. Artificial neural networks (ANN, Tokar & Johnson, 1999; Dawson and Wilby, 2001; Dibike and Solomatine, 2001; Govindaraju and Rao, 2013), fuzzy regression (Bardossy et al., 1990; Kim et al., 1996; Özelkan & Duckstein, 2000) and Genetic Programming (GP, Savic et al., 1999; Whigham & Crapper, 2001; Babovic & Keijze, 2002; Rabuñal et al., 2007) are some empirical models used in hydrology supported by informatics.

There are also models based on the linear IUH function that is derived from the geomorphology of the basin, thus including a physically based concept on the empirical model. These models are widely used thanks to their easy integration with Digital Elevation Models and land use data available at global scale, such as GIUH (Rodriguez-Iturbe & Valdes, 1979; Gupta et al., 1980; Rodriguez-Iturbe et al., 1982) and WFIUH (Mesa and Mifflin 1986; Rinaldo et al. 1991; Naden, 1992; Rodríguez-Iturbe and Rinaldo 1997; Giannoni et al. 2005; Noto and La Loggia 2007; Grimaldi et al., 2012).

Hydraulic models simulate the flow propagation applying the Saint Venant continuity and momentum equations or the Lattice-Boltzman approach, providing the flow depths (FD), flow velocities and the flood extent. Most of the models in literature apply numerical solutions to the Saint Venant equations, such as the finite difference, finite elements or finite volume methods. Hydraulic models can be classified, considering the dimensional aspect, in one dimensional (1D), two dimensional (2D) and three dimensional (3D) models. Most common 1D models are HEC-RAS 1-4. (Brunner, 1995), MIKE11, ISIS, ONDA, FLUCOMP. The availability of DEMs, together with the increasing computational speed of the computers, allowed to develop and distribute 2D hydraulic models, such MIKE 21 (Warren & Bach, 1992), RMA-2 (Feldhaus et al., 1992), TELEMAC-2D (Bates et al., 1992), TUFLOW (Syme, 1992), RiverFlow-2D (Garcia et al., 2006), TRENT (Villanueva & Wright, 2006) and Quasi-2D models such as FLO-2D (O'brien et al., 1993), LISFLOOD-FP (Bates & De Roo, 2000), InfoWorks2D (Woolhouse, 2008).

For detailed case studies in smalls scale simulations, also 3D models are available, like CFX, FLUENT and PHEONIX.

1D models are still often used in domains where the 2D effects can be considered negligible (Bates et al., 1995), but in some cases they cannot simulate in a proper way the flow propagation along the floodplain (Hunter et al., 2005b; Pappenberger et al., 2006), especially in cases of low water levels in the floodplain area. Usually the dynamics inside the channel domain can be simulated with a 1D simulation, so the already mentioned Quasi-2D models, to optimize the computational time of the simulation, have a hybrid behaviour, adopting the 1D simulation in the channel and the 2D simulation in the floodplain (Figure 2).

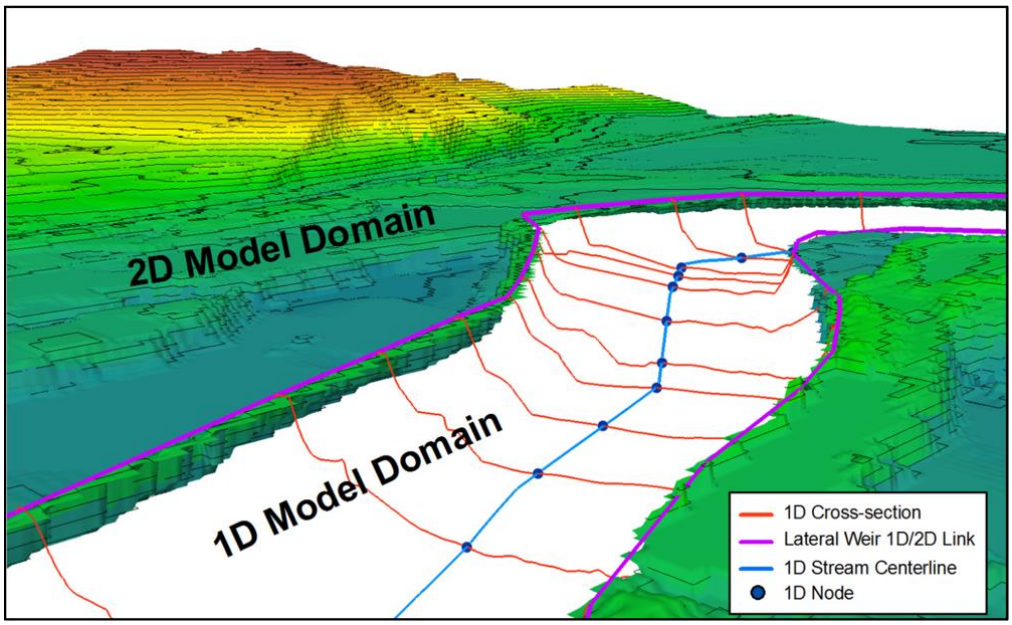

Figure 2. Depiction of a general 1D model of the river channel coupled with a 2D model of the floodplain. Source: Gilles et al. (2012)

Hydrologic and hydraulic models are affected by uncertainties that need to be taken into account for better managing the risk-based decision making processes for disaster risk reduction (Pappenberger and Beven, 2006), because it's important to assign the proper reliability to their results (Krzysztofowicz, 2001). The uncertainty of the hydrologic and hydraulic models is caused partially by the so called "aleatory uncertainty" of the hydrological and hydraulic processes because of their inherent stochastic behaviour (Koutsoyiannis, 2010; Beven, K., 2016) and partially by the so called "epistemic uncertainty", namely the limited knowledge of the studied physic systems of the scientific community and the approximated modelling of these systems (Merz & Thieken, 2005). Inside these two macro-categories, we can classify four different sources of uncertainties related to hydrologic and hydraulic models (Liu & Gupta, 2007) listed below:

- *Structural uncertainty* given by the simplification of the modelled physical processes, based on assumption and approximation made to reduce the computational resources in terms of cost and time.
- *Input uncertainty* related to the observed variables, like rainfall, temperature, river discharge, soil moisture, water stage, or other variables obtained by forcing models (i.e. hydrologic input in hydraulic models).
- *Output uncertainty* related to transforming the outputs to other linked variables of interest, e.g. the rating curve errors for deriving the runoff estimation from the simulated water level in a hydraulic model.
- *Parametric uncertainty* due to the inaccuracy of the model calibration, that need calibration data affected by the other abovementioned uncertainties; additionally some model parameters that have a spatial variability are uniformly assigned because of the lack of distributed measurements.

In order to quantify the uncertainties related to the hydrologic and hydraulic models, different approaches have been proposed in literature. One of the most used technique is the Monte Carlo approach, consisting in the random sampling of the model's inputs and/or outputs, starting from the probability distribution of the errors associated to each perturbed variable. This technique has the advantage of being simple to be applied, but usually requires considerable computational efforts because of the large number of elements in the sample that it requires to reach the appropriate statistical accuracy. Generalized Likelihood Uncertainty Estimation (GLUE, Beven & Binley, 1992) is one example of the Monte Carlo application for determining the uncertainty in hydrologic (Beven & Freer, 2001) and hydraulic (Aronica et al., 2002, Pappenberger et al., 2006) modelling. However, some critical issues emerged from this methodology (Mantovan & Todini, 2006). As alternatives of applying the Monte Carlo approach, several Bayesian approaches have been proposed in literature: the standard Bayesian approach (e.g. Krzysztofowicz, 1999 for hydrology, Romanowicz et al., 1996 for flood inundation), Bayesian Recursive Estimation (Thiemann et al., 2001 for hydrology; Kapelan et al., 2007 for hydraulics), Bayesian hierarchical models (Kuczera et al, 2006 for hydrology), Bayesian model averaging (Duan et al., 2007).

1.2. Remote sensing for flood mapping

Until the late 1990s, hydraulic models were built, validated and calibrated using ground measuring, from the topographic survey, to the flow/stage gauging stations, with high costs and poor spatially distribution of validation measurements. Even with the infrequent air photos gathered from the past floods, a testing of the model performance could not be done in a proper way because of the lack of sufficiently detailed and spatially distributed terrain data. The limited information about the flood extensions on a spatially distribute way also compromised the possibility to discriminate between different parametrizations and physics of the models, because different models could equally fit the scarce available punctual measurements but predicted differently the following flood events. The equifinality related to this issue, didn't allow the development, testing, thus the springing up, of the 2D hydraulic models; in fact the topography of the domain were typically provided as a series of cross sections perpendicular to the channel and to the main floodplain direction, so the 1D models were more easy to be implemented. Furthermore, the ability of a model to route a 1D wave along the river network was the only aspect to be tested and the 2D models could add only additional complexity without giving any tangible benefit (Bates, 2012).

At the beginning of the new millennium, the first remote sensing techniques for mapping the topography of wide areas using the airborne altimetry (i.e. Light Detection And Ranging - LiDAR) allowed to test the hydraulic models in a new way (Pereira & Wicherson, 1999; Marks & Bates, 2000; Bates and De Roo, 2000; French, 2003), providing continuous distributed data with a spatial resolution of 2-5 meters with a vertical accuracy around 10-15 cm. Moreover, LiDAR data provided also information on vegetation height that started to be used as information for parametrizing the floodplain friction, being very influenced by the vegetation drag (Cobby et al., 2003; Mason et al., 2003; Straatsma & Baptist, 2008). On the other hand, also Synthetic Aperture Radar (SAR) images started to be used for validating hydraulic models (Horrit, 2000), being able to capture both terrain topography and water extension (Horrit et al., 2001) at any light or weather condition. In fact, flood extent mapping using SAR images is a common issue, because very low backscatters are typical of water surfaces compared to other objects (Smith, 1997). Simultaneously, the Shuttle Radar Topography Mission (SRTM) was launched in 2000 and, after the processing of the raw data, it provided freely available topography for 80% of the Earth surface at 3 arc resolution (≈ 90 m) and, more recently (in 2017 globally), also at 1 arc resolution (≈ 30 m), with an absolute height error in all continents between 5.6 and 9.0 meters, and a relative height error between 4.7 and 9.8 meters at 90% confidence interval (Rodríguez et al., 2006; Yan et al., 2015a). These errors tend to be lower

(around 3.2 m in Falorni et al., 2005; around 2.3 m in Patro et al., 2009) in lowland like floodplains, rivers and deltas because of the absence of reliefs. SRTM DEM includes also vegetation canopy heights, which could lead to underestimate inundations if not pre-processed for being used as base topography for hydraulic modelling (Yan et al., 2015a). Despite their considerable vertical errors and their inability to penetrate the vegetation canopy, in some cases they have been proven to be used successfully in flood models (LeFavour & Alsdorf, 2005; Sanders, 2007; Schumann et al., 2008; Patro et al., 2009; Wang et al., 2012; Alfieri et al., 2014; Yan et al 2013, 2015b). There are also other globally available DEMs, such the Advanced Spaceborne Thermal Emission and Reflection Radiometer (ASTER) Global Digital Elevation Model (GDEM), with a 30 m resolution and a vertical accuracy of 17 m (Tachikawa et al, 2011), the Altimeter Corrected Elevations 2 (ACE2 GDEM) with 1 km resolution and vertical accuracy > 10 m, the Global 30 arc-second Elevation (GTOPO30) with 1 km resolution and vertical accuracy varying from 9 to 30 m, TanDEM-X from TerraSAR-X mission, with a resolution < 12 m and a vertical accuracy < 2 m.

This new availability of having spatially distributed remote sensed data allowed to test also the 2D hydraulic models using distributed field data. The availability of remote sensed data takes on even more importance if we consider that most of the basins in the world are still ungauged or poorly gauged (Stokstad, 1999).

The results on 2D models using topography data with different spatial resolutions leaded to an important outcome that has irreversibly influenced the research on the 2D codes development: the improvement of terrain data resolution and quality is much more important than the improvement in the representation of physical processes (Bates and De Roo, 2000); the pressure gradient, friction and local acceleration are the most important physical process that need to be included. This “reductionist paradigm” (Bates, 2012) lead to develop simpler and faster models, e.g. based on diffusion waves (Hunter et al., 2005a), or on mass spreading without conserving momentum (Lhomme et al., 2009), simplified version of shallow water equations (Bates at al., 2010), allowing to run simulations in larger areas at finer grid resolution, to better represent the terrain.

The increasing of the resolution and the spatial scale in the physical models has been assisted also by new computing techniques such parallelization (Neal et al., 2010) and Graphics Processing Unit (GPU) hardware (Lamb et al., 2009; Kalyanapu et al., 2011; Lacasta et al., 2014). Simultaneously the computer power, according to the Moore’s law has rapidly increased,

thus also the frequency of typical airborne LiDAR systems, bringing to spatial resolution lower than 10 cm and the vertical precision to ~ 5 cm RMSE (Fewtrell et al, 2011).

The importance of the spatial resolution of the model has been proven to be crucial mostly in floodplain wetting and drying phenomena along preferential flow pathways in both rural and urban settings (Nicholas & Mitchell, 2003; Neal et al., 2011). On the other hand, larger floods tend to be valley filling and the maximum extent can be easily predicted even by models with coarse resolution (Bates, 2012). Another limitation in data availability is the bathymetry of the rivers, because DEMs return the water surface elevation at the time of the acquisition, and additionally, in coarse resolution DEMs, the elevation at the river can be influenced by its surrounding regions. Many researches proposed different approaches to overcome this issue, for example: correcting the bed elevation DEM with the average difference between ground surveys data and DEM data (Patro et al., 2009); using a power law relationship between channel width and depth (Neal et al., 2012) according to Leopold and Maddock (1953); assuming that the river bed elevation given by the DEM corresponds to average runoff conditions and reducing the inflow hydrographs by subtracting the mean discharge (Alfieri et al., 2014); calibrating the DEM based hydraulic model using the bed elevation as additional parameter to calibrate (Yan et al., 2015b). Moreover, the global river bank-full width and depth databases were developed and are freely available at Andreadis et al., 2013 and Yamazaki et al., 2014. These databases have been used to build the first large-scale flood inundation forecasting models (Schumann et al., 2013; Alfieri et al., 2014; Sampson et al., 2015; Dottori et al., 2016; Wing et al., 2017). However, the channel geometry approximation is the source of major inaccuracy in water level simulation, particularly at low flow conditions, and more reliable approaches to estimate the channel geometry in absence of ground surveys is one of the future research frontiers (Yan et al., 2015a).

Boat-mounted side-scan sonar systems can provide the channel bathymetry that can be integrated in the terrain models for high-resolution hydraulic simulations (Horrit et al., 2006), but there are still no bathymetry data available at large scale.

Remote sensed data have also been used not only for calibrating and validating the hydraulic models at different spatial scale (Horrit & Bates, 2001; Lane, 2005) but also for evaluating the model uncertainties (Aronica et al., 1998; Pappenberger et al., 2006, 2007) and even reducing them (Bates et al., 2004; Hunter et al., 2005b; Di Baldassarre et al., 2009a; Mason et al., 2009; Stephens et al., 2012). The evaluation of the model uncertainties is, in fact, a crucial aspect

since deterministic predictions of flood extent for territorial planning could provide a misleading impression of accuracy (Di Baldassarre et al., 2010). For this reason, techniques for uncertainty visualizations (Leedal at al., 2010) and protocols for flood risk decision-making under uncertainty (Hall & Solomatine, 2008) have been developed. Where detailed topography is not available, topographic data are considered one of the most significant source of uncertainty in hydraulic modelling (Jung & Merwade, 2012).

Together with topographic data, the measurement error in gauging station seems to be another important limiting uncertainty in hydraulic modelling, so that errors in discharge measurements, during peak flows can reach $\pm 40\%$ (Di Baldassarre & Montanari, 2009; Di Baldassarre et al., 2012). However, also unknown parameters such as roughness and bathymetry are still issues that can be resolved through calibration, validation or data assimilation (Bates, 2012).

Airborne aerial photography and thermal (optical) imagery can give probably the best information in terms of accuracy for the flood extent (Yu & Lane, 2006) but their high costs and their limitations on cloud conditions make their use not very appealing. SAR-derived flood images have also been used to extract the water extension and also the water elevation along the shoreline intersecting them with DEMs (Mason at al., 2009) even at coarse resolution, such the ones from the Shuttle Radar Topography Mission SRTM (Schumann et al., 2010). The main issues related to these data are image resolution and the satellite revisit time (Yan et al., 2015a). Different satellite missions provide imagery with various resolution (from 1 to 1000 meters) and repeat cycles ranging from 11 to 46 days. A comprehensive view of the available satellite imagery products is given by Schumann et al. (2009), Di Baldassarre et al. (2011) and Yan et al. (2015a). The ability of the new satellite missions of leaning on more satellite constellations allowed to reduce the global revisit time (6 days for Sentinel-1, 2 hours for COSMO-SkyMed). Several techniques have been proposed to retrieve the water extent from satellite imagery. The most common are the visual interpretation (MacIntosh & Profeti, 1995), automatic classification algorithms (Hess et al., 1995), statistical active contour models (Horrit, 1999), image histogram thresholding (Brivio et al., 2002), image texture algorithms (Schumann et al., 2005), automatic thresholding procedures on high resolution SAR data (Martinis et al., 2009; Schumann et al., 2010; Matgen et al., 2011; Mason et al.,2012b; Pulvirenti et al., 2011), tailored specifically for urban areas (Giustarini et al., 2013; Mason et al., 2014). Some of these techniques have been inserted in web-based fully automated processing chain for near real time flood detection using high-resolution SAR data (e.g. Martinis et al., 2014). These images have been used for calibrating and validating hydraulic models using different spatial performance

measurements and varying mainly channel and floodplain roughness (Horrit, 2000; Horrit et al., 2007; Di Baldassarre et al., 2009b; Mason et al., 2009; Tarpanelli et al., 2013) and for producing probabilistic flood maps, considering the uncertainties related to the model and the observation data (Hunter et al., 2005b; Di Baldassarre et al., 2010). Multispectral images, such as the ones provided by the Landsat 5, 7 and 8 missions, have not been widely integrated with hydraulic models for calibration or data assimilation purposes, because of their limitation in detecting the water extension in cloud conditions (typically occurring during floods) and during night time. However, multispectral images have been used for monitoring water extension, taking advantage of the different sensitivity of the water surface to some bands compared to the ones of the bare soil, the vegetation and the built-up surfaces. Many water extracting indexes have been proposed and tested in literature, such as Normalized Difference Water Index (NDWI, McFeeters, 1996), the Modified Normalized Difference Water Index (MNDWI, Xu, 2006), the Water Ratio Index (WRI, Shen & Li, 2010), the Automated Water Extraction Index shadow (AWEISH) and non-shadow (AWEINSH) indexes (Feyisa et al., 2014), the water index (WI, Fisher et al., 2016). These indexes have been tested mainly in steady conditions of the water bodies and, for flood detection purposes, should be tested considering the usual increase of turbidity of the rivers during extreme events.

Large scale hydraulic models have been also calibrated and validated using interferometric water elevation changes (*dh/dt)* derived from Interferometric Synthetic Aperture Radar (IfSAR) (Alsdorf et al., 2007a; Jung et al., 2012), satellite gravimetry (GRACE, Alsdorf et al., 2010) and satellite radar altimeters (Wilson et al., 2007). The accuracy of the vertical elevation ranges around 50 and 10 cm, reaching also 3-4 cm for large areas (Frappart et al., 2006) but can be also lower, until 2 meters (Birkinshaw et al., 2010). Some studies have been done also to use the radar altimetry as input for hydraulic models (Biancamaria et al., 2009; Hall et al., 2011; Domeneghetti et al., 2014; Yan et al., 2015b).

In the last years, the Unmanned Aerial Vehicles (UAV) started to be used as remote sensing systems for not only generating very high resolution DTM with high vertical accuracy, but also for flood monitoring (Abdelkader et al., 2013) and mapping (Feng et al., 2015). UAVs have low dependences on launching and landing conditions, making them safer than piloted aircrafts in urban flood monitoring; they also fly at low altitude, making them immune to the cloud covering and at the same time providing in real-time many details of ground objects in heterogeneous urban landscapes (Feng et al., 2015). However, they still have strong limitations related to the small areas they can monitor, due to their relatively limited autonomy (few hours).

Water levels directly gathered from space have also been used as observations to be assimilated by hydraulic models and have been proven to improve the forecast reliability and also to estimate the discharge from space (Andreadis et al., 2007; Matgen et al., 2007; Neal et al., 2009; Matgen et al., 2010; Giustarini et al., 2011; Mason et al., 2012). Andreadis & Schumann (2014) demonstrated that the assimilation of satellite observation, with a local ensemble transform Kalman Filter, can have a positive effect on flood forecasting even for long leading time (up to 11 days in their work, that is similar to the satellite revisit time). A more effective way of updating would thus consist in adjusting both model states and inputs (Matgen et al., 2010). García-Pintado et al. (2013) investigated the forecasting performance assimilating water levels from satellite, and the influence of the satellite revisit parameter. For this aspect, future satellite missions will be crucial in improving the current DA frameworks integrated in hydraulic models.

Bates et al. (2014) reviewed the surface water data sets available to hydrologists on a global scale. A breakthrough in this aspect at larger scale will be the NASA/CNES Surface Water Ocean Topography (SWOT) satellite mission (Alsdorf et al., 2007b), scheduled for launch in 2019. This mission will provide both 100 m resolution images h (with 50 cm of accuracy), dh/dx and dh/dt globally approximately every 10 days and also global floodplain DEM with decametric vertical accuracy. This mission is also expected to penetrate vegetation through canopy. This information will be useful not only for the data assimilation framework at global scale, but also for estimates of bathymetry, friction and discharge in ungauged basins (Bates, 2012).

This tremendous development of the new data sources shifted flood modelling from a data-poor to a data-rich environment (Schumann et al., 2009). The integration of remote sensed data, ground-based observations and models as well as estimating associated uncertainties related to hydraulic modelling still remains an important scientific challenge (Yan et al., 2015)

1.3. Crowdsourced data and floods

Both traditional physical static sensors and remote sensed data sometimes can be considered not sufficient as input of flood models or for validating them, mostly in the secondary river network, where often static gages are missing and the flood dynamics, occurring in few hours, are too fast to be captured by satellite remote sensors, whose revisit times still require days. This led to consider new sources of information looking at the crowdsourced observations, giving more attention to a relatively new scientific branch, called Citizen Science (Irwin, 1995). Crowdsourced observation can be adopted for deriving hydrological or hydraulic variables and using them in decision-making (Bonney et al., 2014). The exploring of these new kinds of data is having support from the incredible increasing of smartphone users worldwide (Figure 3) and, at the same time, of social media accounts, that allow people to share geotagged messages, photos and videos in real time. For example, Figure 3 shows how the number of twitter accounts grown in the last 8 years (Statista, 2017b).

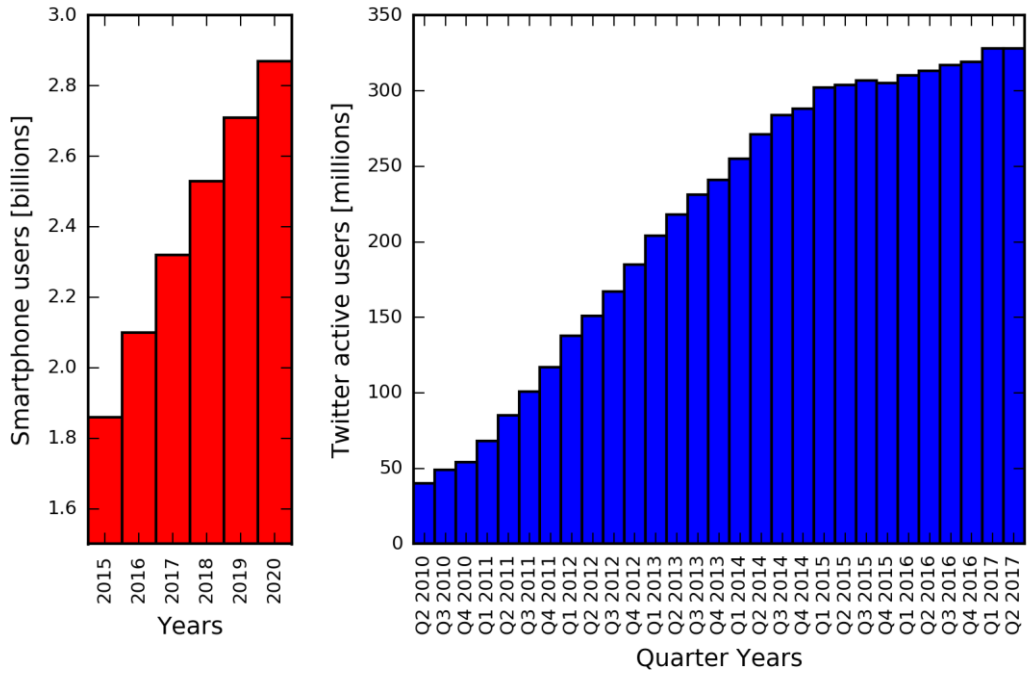

Figure 3. Number of smartphone users worldwide from 2014 to 2020 (left) and Number of monthly active Twitter users (in millions) worldwide from 1st quarter 2010 to 2nd quarter 2017 (right). (Adapted from Statista 2017a, 2017b)

Field information gathered from citizen trough social media (*Facebook*, *Instagram*, *Twitter*, *Flickr*, *Foursquare*, *Youtube*) and news media are principally defined in three different ways: *Crowdsourced* data (CS), *User Generated Contents* (UGC) and *Volunteering Geographic Information (VGI)*. Goodchild (2007) defines VGI as spatial information collected voluntarily

by private citizen. CS and UGC terms are used more generally referring to information created involuntarily or voluntarily for a specific purpose, i.e. for monitoring natural disasters. In this work, the VGI acronym has been used for generally referring to every crowdsourced information. Until a couple of years ago, crowdsourced data were not universally accepted as a valid source of scientific investigation (Bonney et al., 2014), because of their low reliability having sources of information given by not trained and not expert people. Buytaert et al. (2014) stated that motivations of citizen engagement vary according to geographical location; in fact, wealthy countries are more aware of the importance of scientific progress, while in poor countries, the main concerns are related to poverty alleviation (Gura, 2013). However, citizen engagement can be also involuntary, because people tend to use social media just for sharing their experiences and could catch information of phenomena whose utility could not be get immediately from them. Buytaert et al. (2014) give some examples of citizen engagement in hydrology and water science.

In hydrology, there are several project aimed to test the usefulness of VGI observation using low cost sensors given by citizens. *CoCoRaHS* (Cifelli et al., 2005) is a community-based network of volunteers trained for collecting precipitation, hail and snow measurements. *CrowdHydrology* (Lowry & Fienen, 2013) is a project for monitoring water stages using crowdsourced text messages from untrained people. *iSPUW Project* (Seo et al., 2015) integrates data from weather radar systems, wireless sensors and crowdsourced data via mobile applications to improve the prediction of flood events in a urban area. *ABC* is a crowdmap platform for collecting and sharing information about the flood in Australia in 2011 (http://www.abc.net.au/technology/articles/2011/01/13/3112261.htm). *QLD FLOOD CRISIS MAP* launched by the Australian Broadcasting Corporation allowed people to end information on flood via email, text message, twitter or website (McDougall, 2011). *PetaJakarta.org* is a research project led by the SMART Infrastructure Facility, in collaboration with the Jakarta Emergency Management Agency (BPBD DKI Jakarta) and Twitter Inc. that enabled Jakarta's citizens to report the locations of flood events using the social media network Twitter. This project has been proven to be useful for mitigating flood-related disasters like the monsoon effect in Indonesia in 2016. *WeSenseIt* (Ciravegna et al., 2013), funded by the Seventh Framework Programme for Research and Technological Development (FP7) of the European Union, proposed to develop a citizen observatory of water through environmental non-structured data collection from citizens, to develop descriptive and predictive models and decision making tools starting from social and traditional data, to develop communication

strategies for exchanging environmental knowledge/experience between citizens and authorities. Collaborative international projects, like some ongoing European Commission funded projects, are also being developed investigating Citizen Observatories for water management (Ground Truth 2.0, SCENT, LANDSENSE, GROW observatory, WeObserve).

Several platforms can be considered as VGI tools. *Wikimapia* allows anyone to select an area of the Earth's surface, and provide it with a description (http://wikimapia.org/). *OpenStreetMap* is an "editable map of the whole world, which is being built largely from scratch, and released with an open content license" (https://www.openstreetmap.org/). *Ushahidi* is a non-profit technology company that specialises in developing free and open source software for information collection, visualisation and interactive mapping (https://www.ushahidi.com/). *Crowdmap* is an on online interactive mapping service, based on the Ushahidi platform (https://crowdmap.com). It offers the ability to collect information from cell phones, email and the web, aggregate that information into a single platform, and visualise it on a map and timeline.

It is worth to mention also other web platforms allowing to map geotagged information gathered from the social media. The *ArcGIS social media web app* allows to map the geotagged information from Instagram, Flickr, Twitter and Youtube in near real time. There are also new platforms providing similar services like *Echosec (https://www.echosec.net), BirdIQ (https://birdiq.net/).* These information can be very useful if integrated with other spatial data as the potential or real extension of a flood (Figure 4).

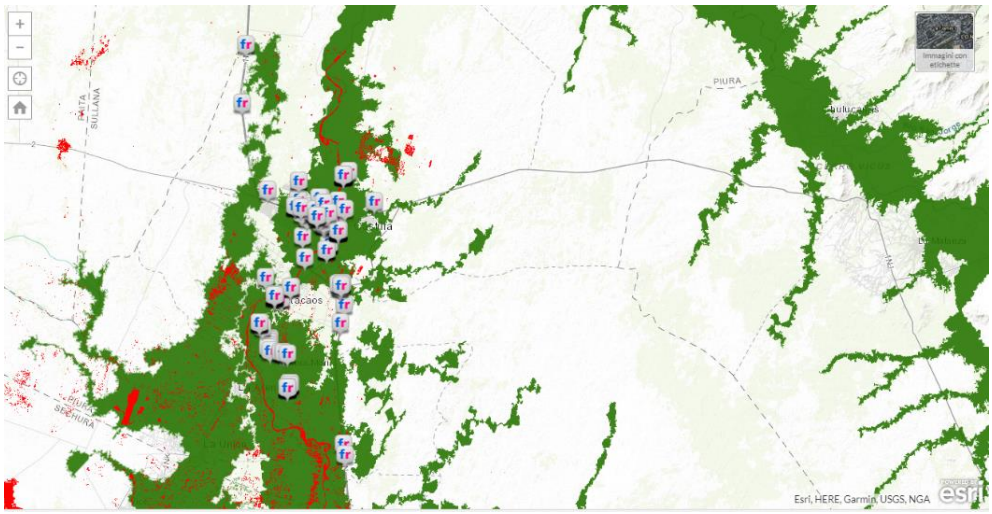

Figure 4. Example of integrating the geotagged social media information with the potential (green) and flooded (red) areas using the ArcGIS social media web app. Piura, flood 2017.

Some platforms are born specifically for gathering information regarding floods. *FloodTags* (https://www.floodtags.com/) analyses online media (news articles, blogs, forums) and UGC (Twitter, Facebook) for water management and food security. The analysis is performed using a mix of artificial intelligence, natural language processing and combinations with external data sources, including satellite imagery.

Currently Flickr and Twitter are the most used social media for getting crowdsourced information related to disasters, allowing all public data to be found and extracted using their Application Programming Interfaces (API). In this context, the interpretation of the contents (e.g. hashtags, images, text, tags, geolocations) is one of the most important research frontier in social media analytics (Tkachenko et al., 2017).

In the field of flood mapping, social media data have been already used as auxiliary data for improving and testing the performance of hydrologic and hydraulic models or remote sensed data. Sun et al. (2015) evaluated the accuracy of flood maps derived by remote sensing using Flickr data. Smith et al. (2015) used Twitter information to select the most realistic result of a series of hydraulic model ensemble. Mazzoleni (2017) demonstrated the benefits of assimilating both traditional and VGI observations with simplified hydrological and hydraulic modelling for improving the flood prediction. Tkachenko et al, 2017 used polysemous tags of images posted during several flood events and demonstrate how volunteered geographic data can be used as hazard predictor choosing proper words as filters for getting information.

VGI data have been also used for directly creating flood maps. Schnebele & Waters (2014) used crowdsourced photos and volunteered geographic data to create an estimation of flood damage in New York City following Hurricane Sandy using a geostatistical interpolation. Holderness and Turpin (2015) used the tweet spatial density to detect the most affected flooded areas in Jakarta, Indonesia (see PetaJakarta.org project). Other examples of using social media for mapping flood extents are provided by Poser & Dransch (2010), McDougall (2011), Triglav-Čekada & Radovan (2013), Cervone et al. (2016), Rosser et al. (2017). Water levels manually (Fohringer et al. 2015) or automatically (Eilander et al. 2016) derived from photographs on Flickr and/or Twitter have been used to create flood maps. Brouwer at al. (2017) create deterministic and probabilistic flood maps from Twitter messages performing uncertainty analysis on location and water depth derivation errors.

The principal drawback of the crowdsourced information is their relatively low reliability compared to the traditional measurements, therefore the uncertainty related to these data have

to be assigned in a proper way, considering the expertise level of the users, their credibility (e.g. volunteer group) and the accuracy, completeness and precision level (Tulloch & Szabo, 2012; Bordogna et al., 2014). To handle this reliability assessment some ad hoc statistical tools have been developed to determine the random error and bias to be assigned to these observations (Bird et al., 2014). Data reliability can be assigned considering not only the expertise of the source, but also the time and the position in which that information is received. To address this issue, semantic rules governing what can occur at given location can be used as filter for observations (Vandecasteele & Devillers, 2013), or taking the mean and the standard deviation of compared measurements at predefined time windows (Mazzoleni, 2017). Further steps in the definition of VGI data errors need to be done, especially if the location and timing uncertainties need to be integrated in data assimilation frameworks. Additionally, the use of VGI within DA and flood forecasting is still not well deepened, since few case studies have been developed with simplified hydrologic and hydraulic models using synthetic crowdsourced data (Mazzoleni, 2017).

1.4. Data assimilation in hydrologic and hydraulic modelling

The Data Assimilation approach (DA), allows to update states, inputs, parameters of a physical model with real time observations for reducing the predictive uncertainty. These models have been widely used in water modelling starting from the beginning of the 90's (World Meteorological Organization, 1992). Figure 5 shows how the DA framework works for a generic state variable X, that is filtered and corrected considering the uncertainties of the model and of the observations each time step.

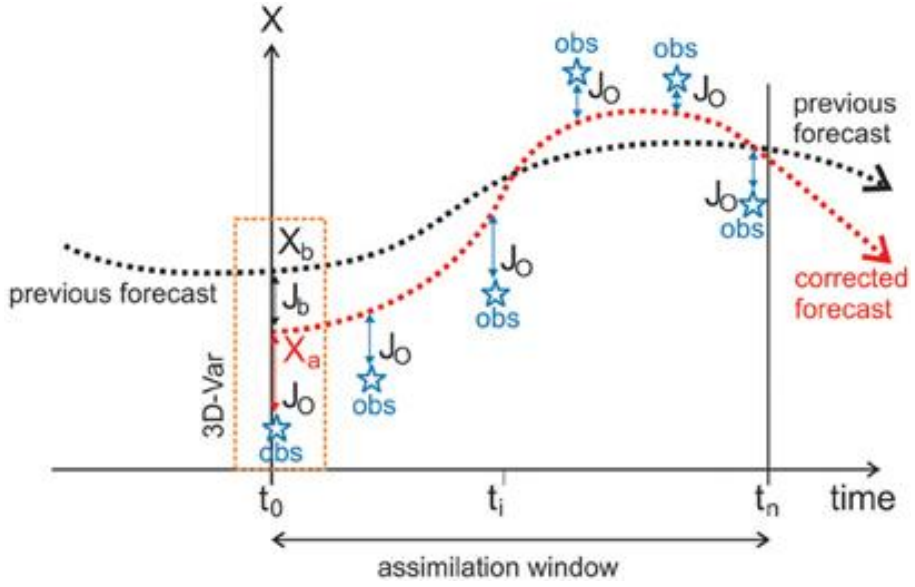

Figure 5. Example of a Data Assimilation application in a forecast model for a generic variable X. Source: Lahoz & Schneider, 2014

There are several techniques of DA adopted in literature in water modelling. One of the most popular is the Kalman Filter (Kalman, 1960) and its variants. The simple Kalman filter method has the strong limitation of being valid only for linear systems; for this reason, many variants of this method have been developed and proposed for non-linear processes, such the Extented Kalman Filter (EKF, Ljung, 1979), unscented Kalman filter (UKF, Wan &Van Der Merwe, 2000), ensemble Kalman Filter (EnKF, Evensen, 2003), the recursive ensemble Kalman filter (REnKF, McMillan et al., 2013). Among these, the EnKF is maybe the most used in water modelling despite being time consuming, because of its flexibility even in strong non-linear dynamics (Madsen & Cañizares, 1999).

Another DA method adopted in Water modelling is the Particle Filter (PF, Arulampalam et al., 2002) in which the posterior density function is represented by a set of random samples with associated weights according to the full prior density and resampling approach used. This methodology is usually more computational onerous than the family of the Kalman filters.

Besides the aforementioned DA methods, variational assimilation methods (Le Dimet & Talagrand, 1986) have been widely used in weather forecasting, coastal hydrodynamics but also in hydrologic modelling (Seo et al., 2003; Lee et al., 2011; Liu et al., 2012; Ercolani & Castelli, 2017). In these methods, the cost function that measures the difference between the error in the initial conditions and the error between model predictions and observations over time is minimised to identify the best estimate of the initial state condition

Specifically in hydrological modelling, the DA approach have been adopted using as updating observations traditional physical sensors (McLaughlin, 2002; Moradkhani et al., 2005a; Walker & Houser, 2005; Liu and Gupta, 2007).

More recently, the significant amount of real time data requested by the data assimilation methodology (e.g. water levels, streamflow, soil moisture, snow cover) applied to complex physical models even in poorly gauged areas, pushed the scientific community to find new types of observation to be assimilated. For this reason, from 2007 many applications of the DA framework starting from satellite remote sensed water stages started to be adopted. Section 1.2 of this work already mentioned some of these studies. The real time assimilation of remote sensed data is still an issue because of the temporal availability of the remote information, but some important progresses have been done gathering SAR-derived real time water stages and water extensions (Garcìa-Pintado et al., 2013; Matgen et al., 2010).

The performance of the DA assimilation applied to hydrologic and hydraulic models have been assessed not only in terms of the quality of the observation measurements, but also in terms of the distribution of the sensors. For example, Mendoza et al., 2012 demonstrated that the hydrologic modelling of the upstream part of the basin can be the mayor source of uncertainty in a flood forecasting model. Many authors demonstrated that assimilation of observations from inner points of the basin helps to further improve the hydrograph estimation and the position of the sensors is often more important than the updating frequency (Xie & Zhang, 2010; Rakovec et al., 2012a; Chen et al., 2012; Mazzoleni et al., 2015).

Data assimilation methodologies have been developed also for updating not only the state variables, but simultaneously correcting some physical parameters (Reichle, 2008; Brocca et al., 2010) or model parameters (Moradkhani et al., 2005b; Lü et al., 2011).

Mazzoleni et al. (2015) investigated the potential integration of Crowdsourced data inside hydrologic and hydraulic models, obtaining substantially improvements on the model

performance; besides their promising results, some testing using unbiased models and real VGI observations instead of synthetic ones have to be done to avoid potential issues on the equifinality related to simplified hydrologic models (Viero, 2017).

1.5. Motivation and objectives

The main purpose of this work is to investigate the integration of traditional (i.e. stage gages measurements) and more recent data (i.e. remote sensed and crowdsourced data) for improving the flood mapping using hydro-geomorphic and Quasi-2D hydraulic models. Moreover, even the assimilation of every type of the mentioned data is still not well investigated in case of advanced 2D hydraulic modelling. For this reason, a methodology for filling the gap related to the integration of observations coming from multiple type sources in complex physical models is proposed, including Quasi-2D models instead of simplified 1D models, mostly common in literature for DA purposes because of their easy implementation and their limited computational burden. Together with the observation data, the development of hydro-geomorphic models is performed in order to test their usefulness as input forcing and boundary of the computational domain of the hydraulic model.

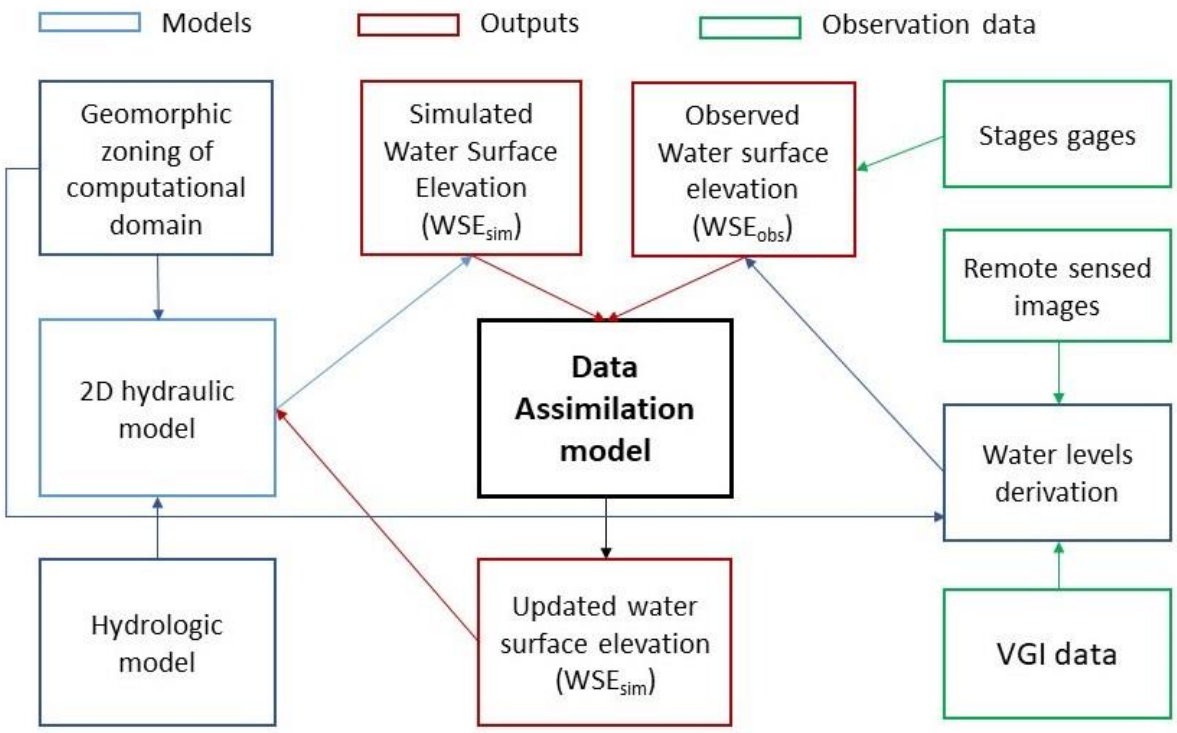

Figure 6. Scheme of the DA framework adopted for the current work

Figure 6 schematize the main objective of the work of integrating the abovementioned models and data. The main forecasting model is the 2D hydraulic model, that is forced by an hydrological model developed in GIS environment taking advantages of the geomorphologic characteristic of the basins deducible from terrain, land use and soil type analysis.

The computational domain of the hydraulic model is chosen starting from the delimited area provided by a DEM-based geomorphic model, that in this work is investigated and readapted starting from the model developed by Nardi et al. (2006). This floodplain delineation methodology is proposed not only as an expeditious tool for defining a computational hydraulic domain, but also for delineating flood prone areas at larger scale to overcome the limitation of all the portion of basins that are still ungauged and without previous advanced hydrologic and hydraulic analysis. This further purpose has to be considered as independent from the DA framework, thus as a secondary aim of the proposed research.

The physical model is integrated in a Data Assimilation framework, updating the simulated water levels every time any type of observation, among traditional static sensors, satellite images or VGI data, is available.

Moreover, a new methodology for gathering the distribution of the water levels taking information from a satellite image and an ensemble of the hydraulic profiles, generated during the Data Assimilation application, is proposed. The indirect derivation of water levels using images instead of the direct use of water levels from satellite has been considered an interesting starting point to deepen, because of the increasing free availability of Multispectral (e.g. Landsat 5, 7, 8 and also 9 soon) and SAR (e.g. Sentinel-1, Alos-1) images that can provide spatially distributed information and whose revisit time will decrease soon with the launching of new missions, as mentioned in Section 1.2. In this context, a secondary objective of the work is an investigation on the current water detection indexes from multispectral images to test their performance during flood events.

The application of proposed DA approach has the limitation of still having a scarce availability of new data (Satellite images and VGI data) for the case study that will be introduced in the next section. However, it can be considered as a first attempt of findings merits and defects related to more complex time consuming hydraulic models in a Data Assimilation framework where observations are scarce and intermittent.

2.Case study

The Tiber river basin in central Italy, the selected case study, is described in this chapter.

Specifically, Section 2.1 illustrates the whole Tiber river, giving some information on its location, land uses and river network topology and then describing the geomorphic characteristics of the sub-basins that are part of the Middle Valley, namely the part of the river basin between the inflow of the Nera river and the northern part of the city of Rome, which include the computational domain of the models described in Chapter 3.

In Section 2.2, an overview of all available data for the case study is given, focusing mainly on topographic, data, rain and flow time series, land use, satellite images and VGI data.

2.1. The Tiber River basin - General framework

The Tiber river basin is the second largest river in Italy, after the Po river basin. Its extension is approximately 17300 km^2 including mainly Umbria e Lazio regions, but also Abruzzo, Emilia-Romagna, Marche, and Toscana regions (Figure 7).

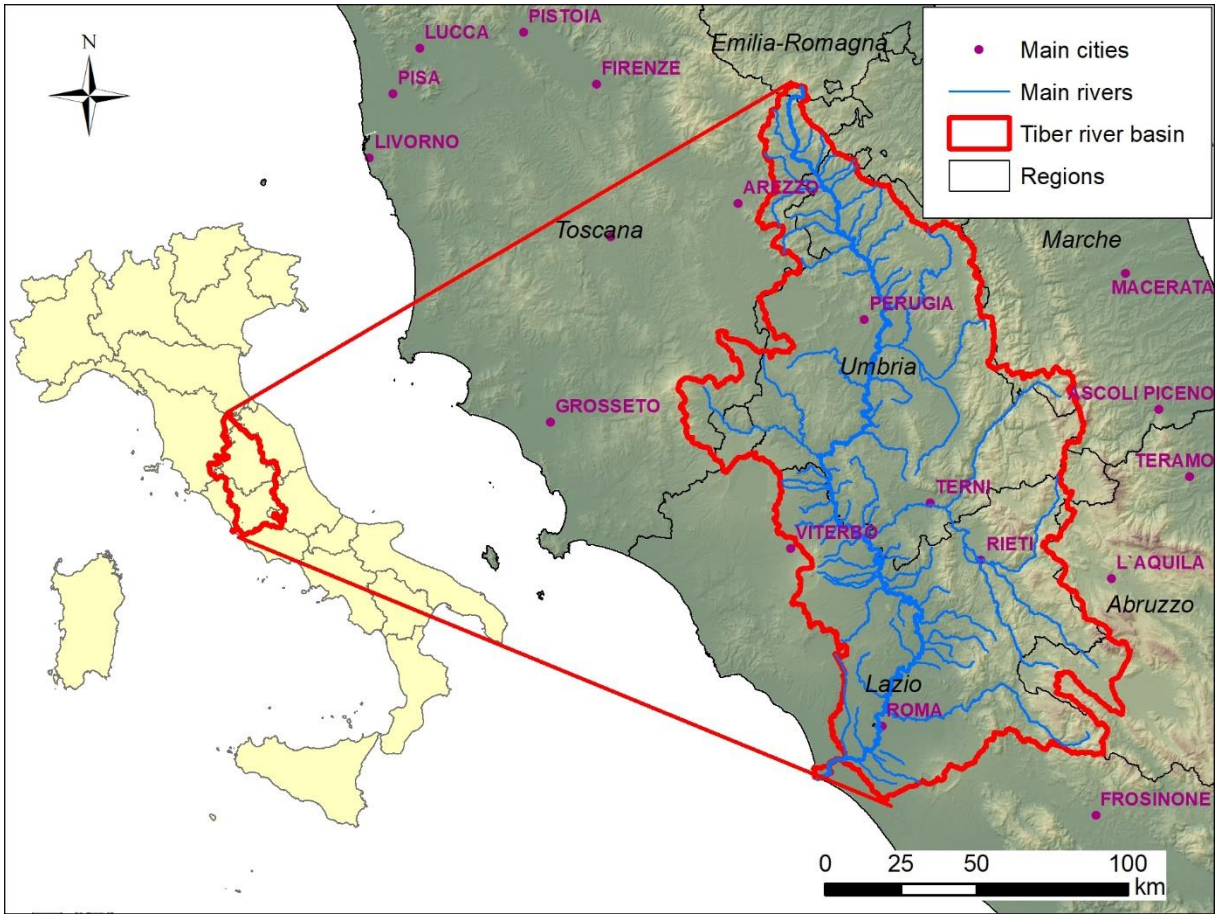

Figure 7. Tiber River basin geographic setting in central Italy as respect to the regional boundaries.

Land use is predominantly agriculture (≈55%) with the remaining area occupied by forests (≈ 40%) and urbanized areas (≈5%). The main channel of the Tiber river has an overall length of 415.8 km and flows into the Tyrrhenian Sea. The drainage network is controlled by some reservoirs, mainly developed for producing hydropower. The main ones along the Tiber channel are the Corbara and the Montedoglio dams (in the upstream part), but there are also other significant dams on the tributaries, specifically in the main left tributary (the Nera river basin) characterized by mountain ranges.

The analysed case study for the hydrologic and the hydraulic modelling is the Middle Valley, where the Tiber river is between the village of Orte Scalo and the northern part of the city of

Rome (Stage Gage: Castelgiubileo). The whole area of the Middle Valley has an extension of 5881 km^2, and the main tributary is the Nera River (Area=4180 km^2). The Nera river basin is characterized by several weirs and dams that regulate the flow so that no more than 250 m^3/s can reach the Tiber River in its confluence. The other basins of the Middle Valley (Figure 8 and Table 1) have been considered for the hydrologic modelling and their morphometry is showed in Table 1.

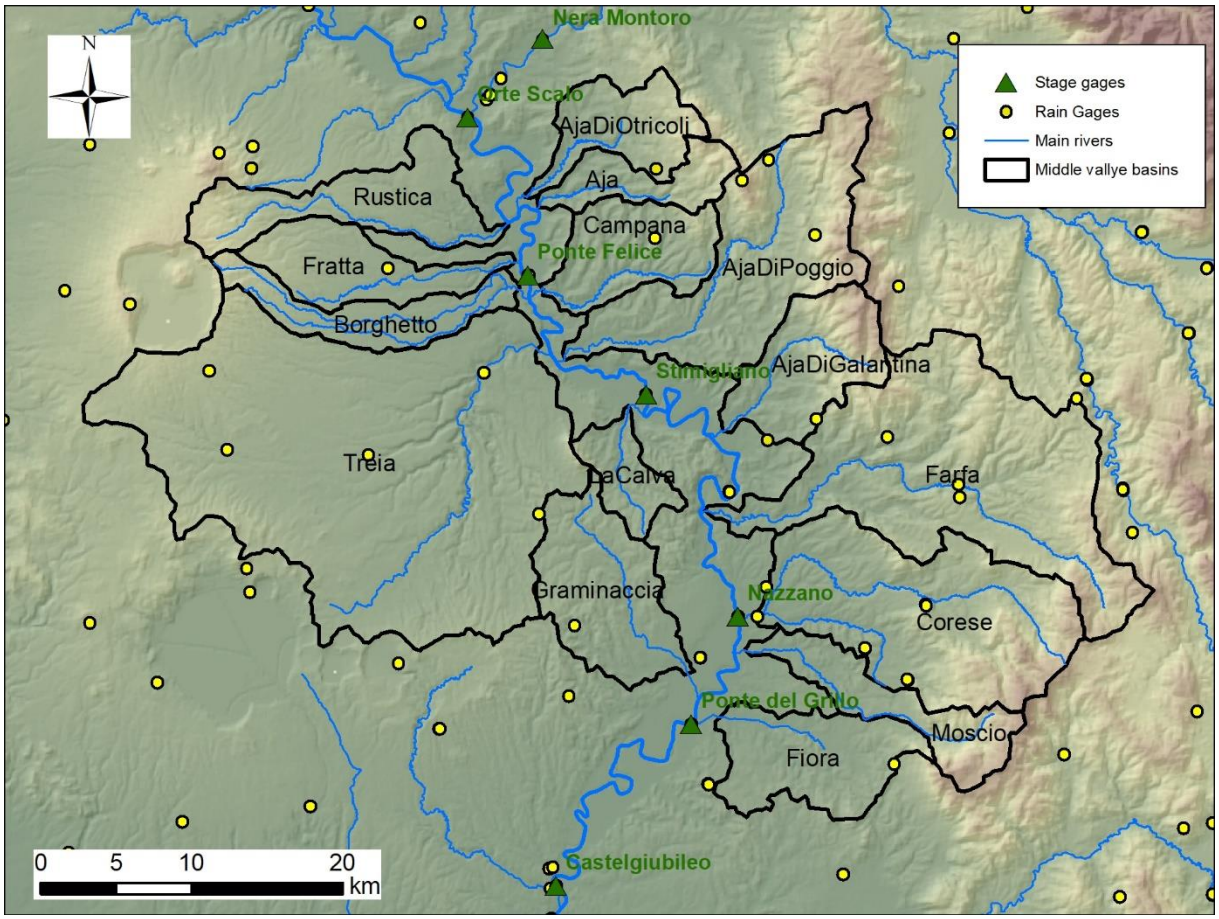

Figure 8. Map of the Tiber river Middle Valley basins

There are several urbanized areas in the floodplain of the Midde Valley (Figure 9), with four main cities: Orte Scalo, Fiano Romano, Monterotondo and the northern part of Rome. These urban centres have been affected by floods in January 2014, November 2012, November 2010, and November 2005, causing damages to buildings, roads and bridges. This area has been chosen because of its strategic importance for the flood risk mitigation of the city of Rome and its being in a partially urbanized areas makes it suitable for getting crowdsourced information for improving the flood dynamics. There are also stage gages (Figure 8) that have been adopted as hydrologic input for the hydraulic modelling and also as static sensor observations for the Data Assimilation framework.

Name	Code	Area [km^2]	Altitude [m.a.s.l.]			ΔH [m]	Basin slope [%]	Channel length [km]	Channel slope [%]
			min	max	mean				
Aja	AJA	35.3	30.0	1038.0	354.3	1008.0	19.305	15.153	4.085
Aja Di Galantina	ADG	68.5	18.0	1262.0	455.5	1244.0	23.191	17.772	5.873
Aja Di Otricoli	ADO	49.5	28.0	971.0	327.3	943.0	15.573	16.137	3.216
Aja Di Poggio	ADP	152.2	18.0	1230.0	418.9	1212.0	20.073	34.013	2.587
Borghetto	BOR	51.0	25.0	810.0	272.6	785.0	5.865	25.040	2.260
Campana	CAM	61.0	21.0	638.0	195.1	617.0	18.675	17.820	2.075
Corese	COR	180.4	13.0	1342.0	413.6	1329.0	19.443	30.287	2.622
Farfa	FAR	245.0	12.0	1205.0	484.7	1193.0	20.881	40.143	2.063
Fiora	FIO	73.9	4.0	976.0	139.2	972.0	9.993	16.253	1.692
Fratta	FRA	57.5	22.0	661.0	278.0	639.0	6.805	21.635	1.870
Graminaccia	GRA	86.0	9.0	415.0	163.2	406.0	11.104	19.213	1.093
La Calva	LAC	28.4	20.0	624.0	174.0	604.0	15.403	8.782	1.890
Moscio	MOS	55.9	8.0	1330.0	449.1	1322.0	18.125	23.665	4.306
Rustica	RUS	76.9	23.0	957.0	347.5	934.0	9.473	25.176	2.689
Treia	TRE	476.5	17.0	711.0	259.8	694.0	7.903	38.098	1.302

Table 1. Morphometry of the Middle Valley basins

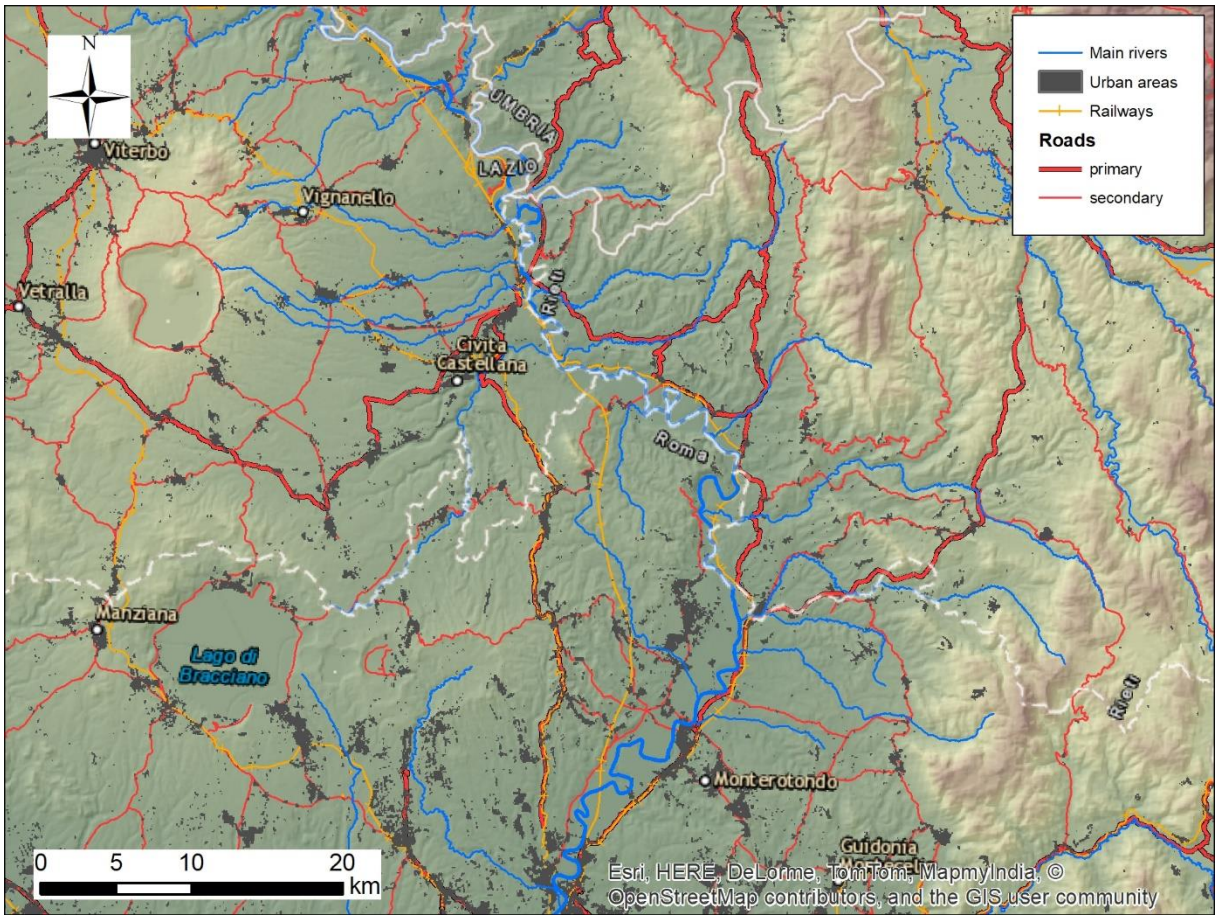

Figure 9. Urban areas, railways and roads in the Middle Valley of the Tiber River

2.2. Available data

2.2.1. Topography

The hydrologic and hydraulic modelling is performed starting from the following topographic data:

- Surveyed cross sections of the main channel of the Tiber River. These surveys have been used for the channel geometry of the river in the hydraulic modelling.
- LiDAR (1 meter resolution) covering most of the floodplain area of the Tiber River. This DTM has been used for integrating the surveyed cross sections in the domain of the hydraulic modelling.
- DEM 5 meters resolution from *Regione Lazio*, used for the hydraulic model domain where LiDAR Data were not available.
- Tinitaly DEM 10 meter resolution from *Istituto Nazionale di Geofisica e Vulcanologia* (INGV), used for hydro-geomorphological analysis described in Section 3.3.
- SRTM 1 arc (≈30 meters), 3 arc (≈90 meters) and 8.33 arc (≈250 meters) adopted for hydrologic modelling and the hydro-geomorphological analysis described in Section 3.3.

2.2.2. Rain and stage time series

Three main flood events have been considered for this work and are listed in Table 2. The *November 2012* Event is the most important one, because it affected the Middle Valley with grater severity, causing serious damages in Orte Scalo urban area (Figure 10).

Event	**Period**	**H_{max} in Orte Scalo [m]**
November 2005	11-19th November 2005	6.0
November 2010	18th November - 7th Dicember 2010	4.7
November 2012	8-19th November 2012	9.5

Table 2. List of flood events considered for the case study

For each of these events the following time series data were available:

- Rain time series from 94 rain gages with a temporal frequency ranging from 1 to 15 minutes.
- Stage time series from seven stage gages whose name and position are showed in Figure 8. Orte Scalo and Nera Montoro have been used as input for the hydraulic model using the flow rating curves provided by *Regione Umbria* e *Lazio*. The other ones are used as

measurements for the hydraulic model calibration and as observation for the Data Assimilation framework.

Figure 10. November 2012 flooding around Orte Scalo area. (Source: http://www.meteoweb.eu)

2.2.3. Other data

Beside the topographic and the time series data, the following data have also been used:

- Flow/stage rating tables related to the principal bridges and weirs in the study area, provided by the *Centro Funzionale regionale del Lazio*.
- Land use: Corine Land Cover at the 4th level for the whole national territory provided by *Istituto Superiore per la Protezione e la Ricerca Ambientale* (ISPRA) has been adopted as auxiliary layer for applying the infiltration method in the hydrologic model.
- Soil type: the lithology and permeability maps of the Tiber River basin provided by *Autorità di Bacino distrettuale dell'Appennino Centrale* have been adopted for the same purpose of the Land use map.
- Multispectral images: Some multispectral images from Lansat 5, 7 and 8 missions have been used for flood detection not only in the case study area for the DA application, but also in other countries for testing the water detection indexes gathered from literature (see Section 3.7).
- Crowdsourced images: these images have been taken from the web for investigating their usefulness in a DA application (Figure 11).

Figure 11. Some VGI images related to the November 2012 events that caused damages to some urban area. Source of images: Youtube.

3.Models and methods

In this chapter, the models and methods adopted and developed for this work are illustrated.

In Section 3.1, the main performance indexes adopted for assessing the performance of the hydrologic and hydraulic models and the spatial comparison of modelled and reference maps are introduced. Section 3.2 describes the GIS-based hydrologic model (WFIUH) that is developed and validated in order to be used as forcing input for the ungauged basins to the Quasi-2D hydraulic model. Section 3.3 illustrates the hydro-geomorphic floodplain delineation algorithm that has been developed to optimize the computational domain, excluding the hillslope areas, to improve the computational efficiency of the Data Assimilation method. Besides the main focus on the Data Assimilation framework, a deepening on the hydro-geomorphic floodplain delineation algorithm for large scale flood prone area mapping has been carried out as a secondary independent aim of the proposed research. The forecasting model of the DA methodology is the hydraulic model, described in Section 3.4. This is a Quasi-2D model (FLO-2D), namely working as 1D model inside the channel and as 2D model along the floodplain, where the 2D effects of the flood expansion become more relevant compared to the ones in the channel. The DA model is the Ensemble Kalman Filter (EnKF), described in Section 3.5, that implements a Bayesian update of the model state reproducing the uncertainties of the model and observation errors with series of Monte Carlo simulations. Finally, Section 3.7 is dedicated to the flood detection techniques, focusing the attention on the ones used for multispectral images that will be used as part of the procedure for gathering the water levels as observation for the Data Assimilation methodology. Moreover, some testing of the main water detection indexes have been done for few case studies were Landsat images and correspondent reference flood maps where available.

3.1. Performance indexes

3.1.1. Indexes for time series comparison

In order to numerically assess the hydrological and hydraulic models' performance each time step observations are available, the following measurement indexes have been taken in to account:

- The Nash-Sutcliffe Efficiency (NSE) index (Nash and Sutcliffe, 1970):

$$NSE = 1 - \frac{\sum_{t=1}^{T}(x_t^s - x_t^o)^2}{\sum_{t=1}^{T}(x_t^o - \overline{x^o})^2} \quad [1]$$

Where x_t^s and x_t^o are respectively the simulated and observed variable x at time t, $\overline{x^o}$ is the time averaged observed variable x, and T is the number of pairs of simulated and observed variables. $\mathrm{NSE} = 1$ corresponds to a perfect matching between simulated and observed variables, $\mathrm{NSE} = 0$ indicates that the simulated streamflow is as accurate as the mean of observed water depth, while $\mathrm{NSE} < 0$ occurs when the model simulation provides worse results than the observed mean because the residual variance (namely the numerator in equation [1]), is larger than the data variance (i.e. the denominator of the same equation).

- The Root Mean Square Error (RMSE):

$$RMSE = \sqrt{\frac{\sum_{t=1}^{T}(x_t^s - x_t^o)^2}{T}} \quad [2]$$

It calculates the sample standard deviation of the differences between predicted values and observed values.

- The Pearson correlation (R) coefficient (Pearson, 1895):

$$R = \frac{cov(x_t^s, x_t^o)}{\sigma(x_t^s) \cdot \sigma(x_t^o)} \quad [3]$$

Where $cov(x_t^s, x_t^o) = \sum_{t=1}^{T}(x_t^s - \overline{x^s}) \cdot (x_t^o - \overline{x^o})$ is the covariance between the simulated and observed variable, and $\sigma(x_t^s) = \sqrt{\sum_{t=1}^{T}(x_t^s - \overline{x^s})^2/(T-1)}$ and $\sigma(x_t^o) = \sqrt{\sum_{t=1}^{T}(x_t^o - \overline{x^o})^2/(T-1)}$ are the variances of the simulated and observed variable. R =1 indicates a perfect correlation between the compared variables, R =0 means no linear correlation and R =-1 indicates a perfect negative linear correlation.

- The bias index (Bias):

$$Bias = \frac{\sum_{t=1}^{T} x_t^s}{\sum_{t=1}^{T} x_t^o} \quad [4]$$

It measures the tendency of the simulated variable to averagely underestimate (Bias <1) or overestimate (Bias >1) the correspondent observed variable.

- The standard deviation of a simulation ensemble for a specific time step (STD_{ens}):

$$STD_{ens} = \sqrt{\frac{\sum_{i=1}^{n}\left(x_t^{s,i} - \overline{x_t^s}\right)^2}{n}} \quad [5]$$

It gives the measure of how much the ensemble is spread at time t.

3.1.2. Spatial measures of fit

The spatial comparison between modelled and reference maps will be numerically assessed using the following performance indexes:

- The F-index (Horrit & Bates, 2001; Aronica et al., 2002; Hunter 2005; Shumann et al. 2005; Pappenberger et al. 2007):

$$F = \frac{A_{ref} \cap A_{mod}}{A_{ref} \cup A_{mod}} \quad [6]$$

Where $A_{ref} \cap A_{mod}$is the intersection between the reference map and the model area (true positive area) and $A_{ref} \cup A_{mod}$ is the union of the abovementioned areas (true positive, false positive and false negative area). The formula can be expressed as:

$$F = \frac{A}{A + B + C} \quad [7]$$

where A, B, C represent respectively the overlapping, underpredicted or overpredicted areas. Values of F can range between 0 (poor fit between model results and reference map) and +1 (perfect fit between model results and reference map).

- The True Positive rate:

$$TP = \frac{A}{A + C} \quad [8]$$

It ranges between 0 and 1 and gives the rate of matching between the modelled map and the reference map, without considering the overprediction of the model.

- The sum of False Positive and False negative rate:

$$FPN = \frac{C}{A+C} + \frac{B}{B+D} \quad [9]$$

It considers both overprediction and underprediction (range between 0 and 2) and has to be the lowest possible for optimizing the performance of the model.

The spatial Bias:

$$Bias = \frac{A+B}{A+C} \quad [10]$$

It has to be close to one to balance the underprediction and overprediction of the models.

3.2. Hydrologic model

3.2.1. Methodology

In this work, a parsimonious hydrological modelling is developed following Grimaldi et al. (2012) and implemented in python environment. This model is based on the automated DEM-based geomorphic characterization of runoff dynamics in scarcely monitored river basins implementing the WFIUH method, namely the instantaneous unit hydrograph (IUH) concept, estimated using the width function (WF), for characterizing the travel time distribution from the river network flow velocity.

The method is characterized by the following steps:

- **DEM pre-processing**:

This procedure is performed using the following standard terrain analysis procedure (Figure 12):

- Pit filling: removal of artificial or natural depressions in order to hydrologically condition the DEM for generating a connected stream network;
- Generation of the flow direction grid that provides the direction of the overflow and runoff for each cell of the domain;
- Generation of the flow accumulation grid, namely the number of cells draining each cell of the domain
- Watershed delineation based on the flow direction grid;
- Stream network extraction, based on the definition of the threshold contributing area beyond which a cell is considered a streamline rather than hillslope. In this case, the threshold area is chosen equal to 1 km^2 iteratively comparing the streamline given by the terrain analysis with the one observable from satellite images.

- **Estimation of the IUH based on the WF (WFIUH)**

The WIUH is expressed through the following equation:

$$WFIUH(t) = FT = \frac{L_c(x)}{v_c(x)} + \frac{L_h(x)}{v_h(x)} \qquad [11]$$

where FT is the flow time, L_c and L_h are respectively, the channel and hillslope flow paths for the generic cell x, and v_c and v_h are channel and hillslope flow velocities. The flow paths (also known as flow length FL, L_c and L_h) are measured for each location of the basin along the pre-

defined topography-controlled flow direction grid. The hillslope runoff velocity component is defined as suggested by Grimaldi et al. (2010), applying NRCS (NRCS 1997) method.

The NRCS method defines the hillslope flow velocity using the formula:

$$v_h = a\sqrt{S} \quad [12]$$

Where v_h is the velocity in a single hillslope cell, *S* is the local slope cell and *a* is a coefficient related to the soil use. Literature values of the *a* coefficient for each land use are chosen according to McCuen (1989) and Haan et al (1994) and are reported in Table 3. The value of the slope *S* in Equation [12] is modified to reduce potential overestimation where S > 0.04 [-] implementing the follow formula (UDFCD 1992):

$$S' = 0.05247 + 0.06363 \cdot S - 0.182 \cdot e^{-62.38 \cdot S} \quad [13]$$

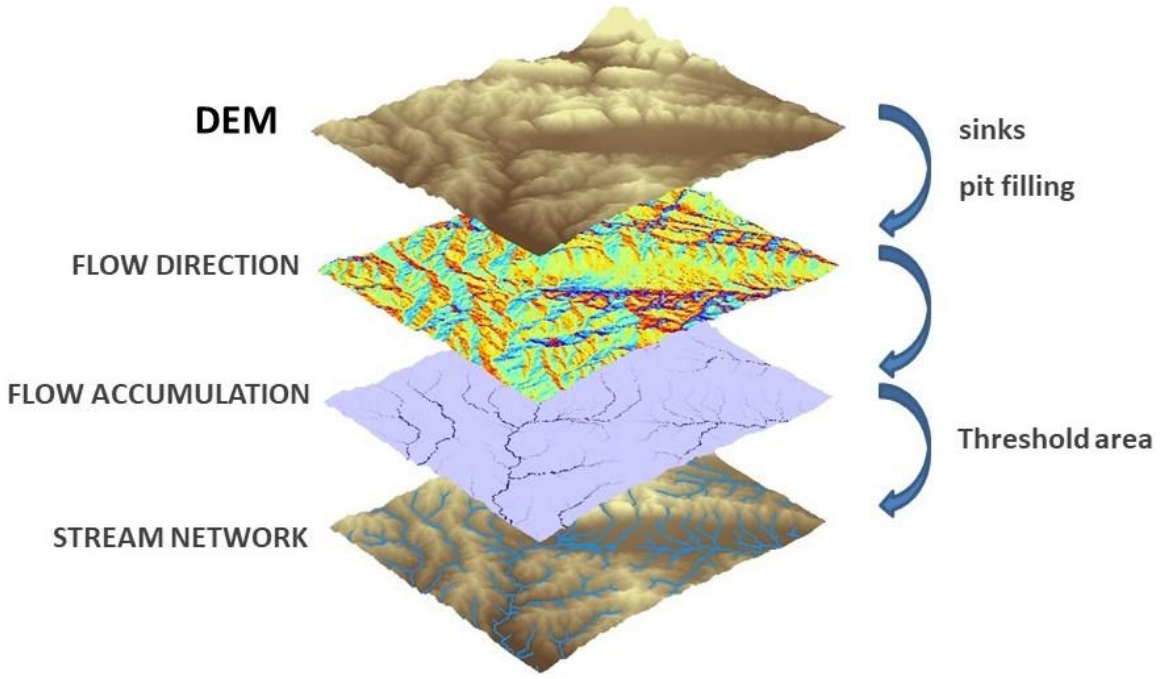

Figure 12. Scheme of the DEM pre-processing, from pit filling to flow direction, flow accumulation and stream network grids

The results of the cell-by-cell velocities have been furthermore restricted within the range 0.02–2 m/s in order to avoid unrealistic values that could be due to particular combination of slope and soil use, as suggested by Grimaldi et al. (2010).

The channel velocities are imposed constant and derived from the calibration of some small gaged basin in the Tiber River basin (see Section 3.2.3).

CLC Code	Description	a parameter (NRCS)	CLC Code	Description	a parameter (NRCS)
111	Continuous urban fabric	2.96	242	Complex cultivation patterns	2.59
112	Discontinuous urban fabric	2.96	243	Land principally occupied by agriculture, with significant areas of natural vegetation	2.59
121	Industrial or commercial units	2.96	311	Broad-leaved forest	0.73
122	Road and rail networks and associated land	2.96	312	Coniferous forest	0.73
123	Port areas	2.96	313	Mixed forest	0.73
124	Airports	2.96	321	Natural grasslands	2.59
131	Mineral extraction sites	2.96	322	Moors and heathland	2.59
133	Construction sites	2.96	323	Sclerophyllous vegetation	2.59
141	Green urban areas	2.96	324	Transitional woodland-shrub	2.59
143	Artificial, non-agricultural vegetated areas	2.06	331	Beaches, dunes, sands	2.59
211	Non-irrigated arable land	2.06	332	Bare rocks	2.96
213	Paddies	2.06	333	Sparsely vegetated areas	2.59
221	Vineyards	2.06	334	Burnt areas	2.96
222	Fruit trees and berry plantations	2.06	411	Inland marshes	2.96
223	Olive groves	2.06	511	Water courses	2.96
231	Pastures	2.59	512	Water bodies	2.96
241	Annual crops associated with permanent crops	2.59			

Table 3 Values of the "a" parameter varying with the land use (according to the Corine Land Cover calssification) for the evaluation of te hillsolpe velocities (NRCS method)

An example of the Width Function derivation for a small sub-basin of the Tiber river is illustrated in Figure 13. The flow time grid, reclassified by time intervals, defines, each time step, the portion of contributing area to the outlet section.

- **Derivation of the distribution of the cell-by-cell rainfall heights**

For this purpose, the Thiessen (Thiessen, 1911) methodology has been applied. The area of the basin is divided in many parts as the number of rain gages related to the basin. As assumption, the influence of every station reaches halfway to the next stations in every direction the analysed gage is connected to the other gages. Perpendicular bisectors of the lines that link each section define the boundaries of the Thiessen polygon. Inside the area belonging to each station, the rain value is assumed the same registered by the mentioned gage (Figure 14). To each gage, a weight is assigned considering the extension of its belonging area compared to the other ones (Chesworth et al., 1998).

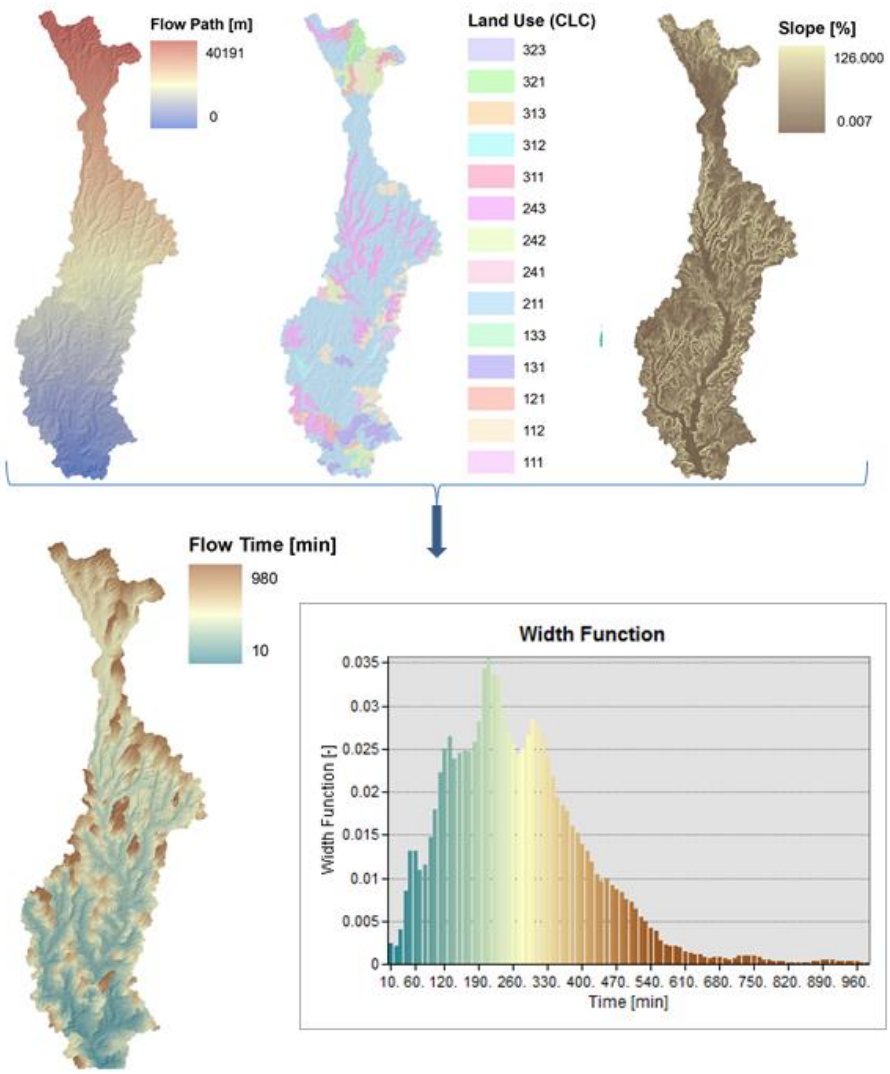

Figure 13. Scheme of the Width Function derivation for a small basin

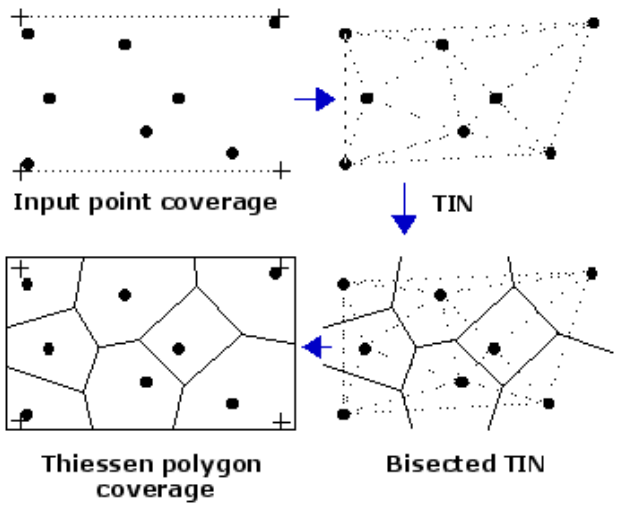

Figure 14. Example of Thiessen polygons. Source: http://resources.esri.com

This simplified method for distributing the total rain in the basin has been preferred to more sophisticated methods such as Inverse Distance Weighting (IDW) or Kriging because of its calculation speed, given the fact that the hydrologic model is supposed to be applied in real time in the Data Assimilation framework.

- **Calculation of the net rainfall**:

The SCS-CN method developed by the USDA Natural Resources Conservation Service (Cronshey, 1986) have been adopted. The infiltration rate of each cell is proportional to the runoff curve number, based on the hydrologic soil group, land use, soil type and antecedent soil moisture conditions.

Specifically, the runoff equation is given by the following expression:

$$Q = \begin{cases} 0 & for\ \ P \leq I_a \\ \dfrac{(P - I_a)^2}{P - I_a + S} & for\ \ P > I_a \end{cases} \qquad [14]$$

where Q is the net rain [mm], P is the total rain [mm]; *S* is the potential maximum soil moisture retention after runoff begins [mm]; *Ia* is the initial abstraction [mm], namely the amount of water before runoff, such as infiltration, or rainfall interception by vegetation. Its value is commonly imposed equal to 0.2·S, but for urbanized areas, it can be reduced also at 0.05·S. The S value in mm is calculated as:

$$S = 254\left(\frac{100}{CN} - 1\right) \qquad [15]$$

The curve number CN has a range from 0 to 100; lower numbers indicate low runoff potential while larger numbers are for increasing runoff potential. Its values are dependent on the land use, the soil type and the Antecedent soil Moisture Condition (AMC). The method considers three AMC (AMC I, AMC II. AMC III) conditions, from dry soil to saturated soil. Figure 15 shows the relation between the CN values and the ratio between total and net rain for *Ia=0.2·S*.

The land use distribution in the computational domain has been derived from the Corine Land Cover project (2012) and the soil type distribution, from which deriving the hydrologic soil type has been provided by the Tiber River Basin Authority (Figure 16).

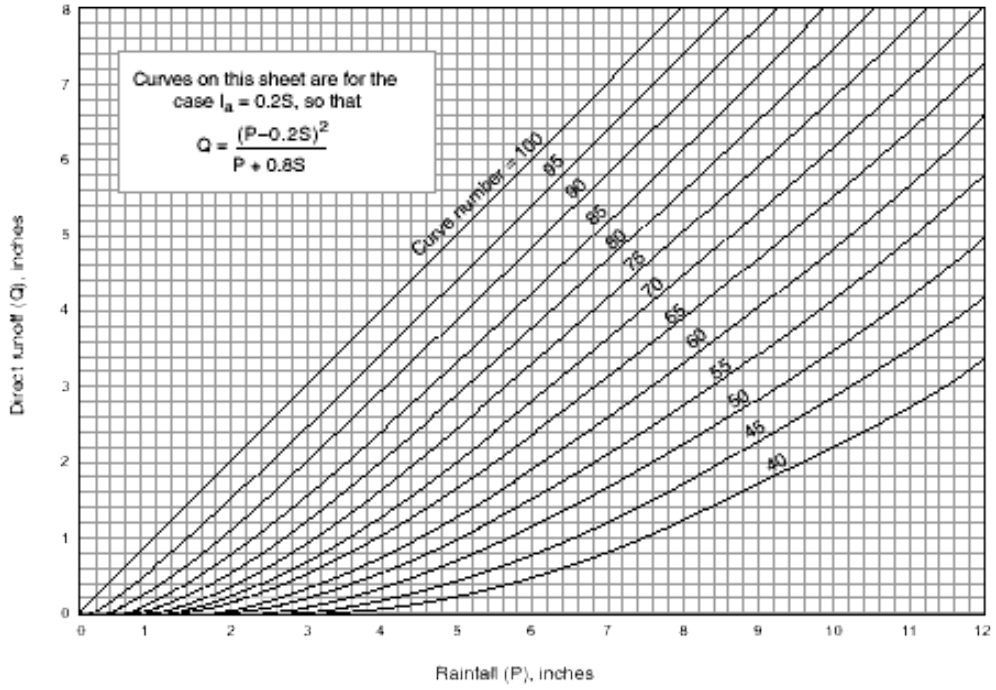

Figure 15. Example of CN curves using Ia=0.2 S. Source: Cronshey, 1986.

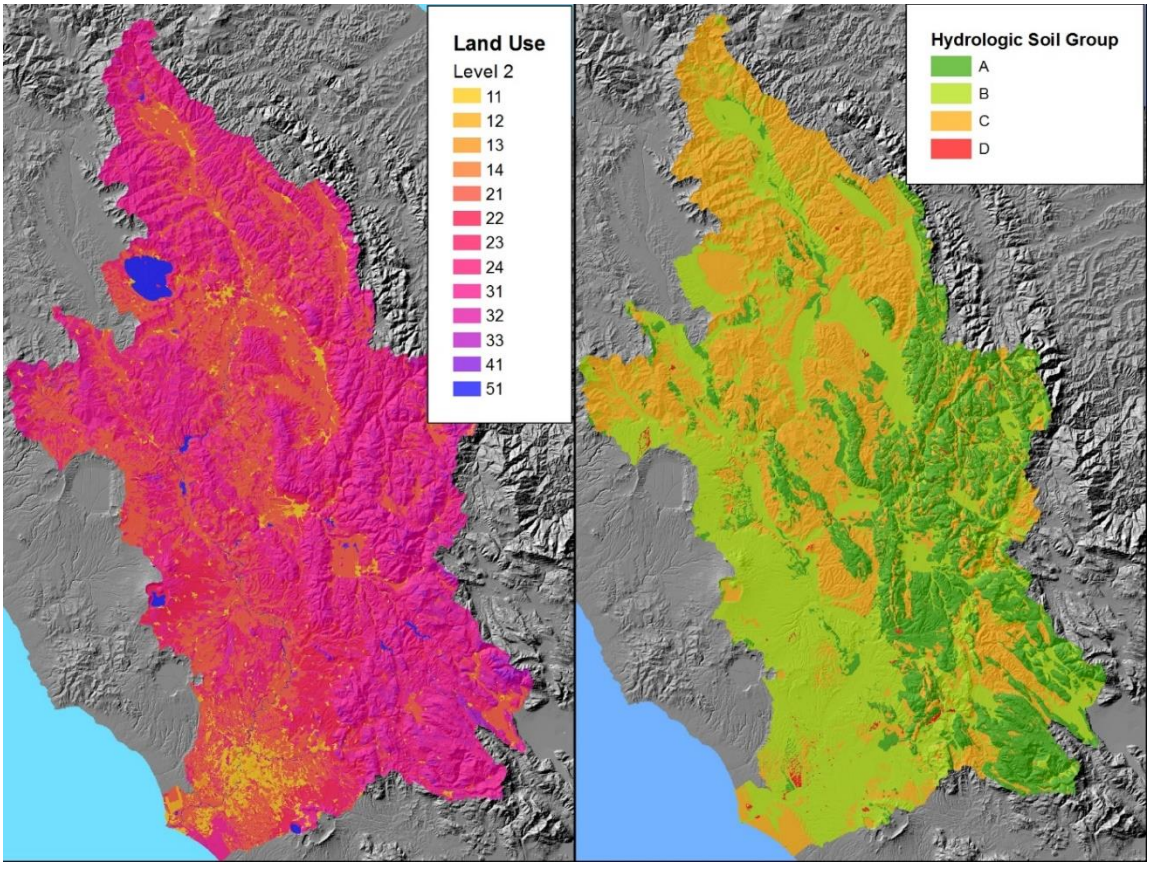

Figure 16. Map of the land uses (Codes of the Corine Land Cover 2012 at 2nd level) (left) and the Hydrologic Soil Groups (right) in the Tiber River Basin

- **Design hydrograph**:

In the hypothesis of a linear system (Chow et al., 1988), the flow hydrograph is calculated using the convolution integral, given by:

$$Q(t) = \int_0^t I(t) \cdot WFIUH(t-\tau)d\tau \qquad [16]$$

Where $Q(t)$ is the outflow function, namely the response function of the input, $I(t)$ the precipitation intensity, $WFIUH(t-\tau)$ is the unit response function, $(t-\tau)$ is the time lag since the input $I(t)$ was applied, $d\tau$ is the infinitesimal time interval.

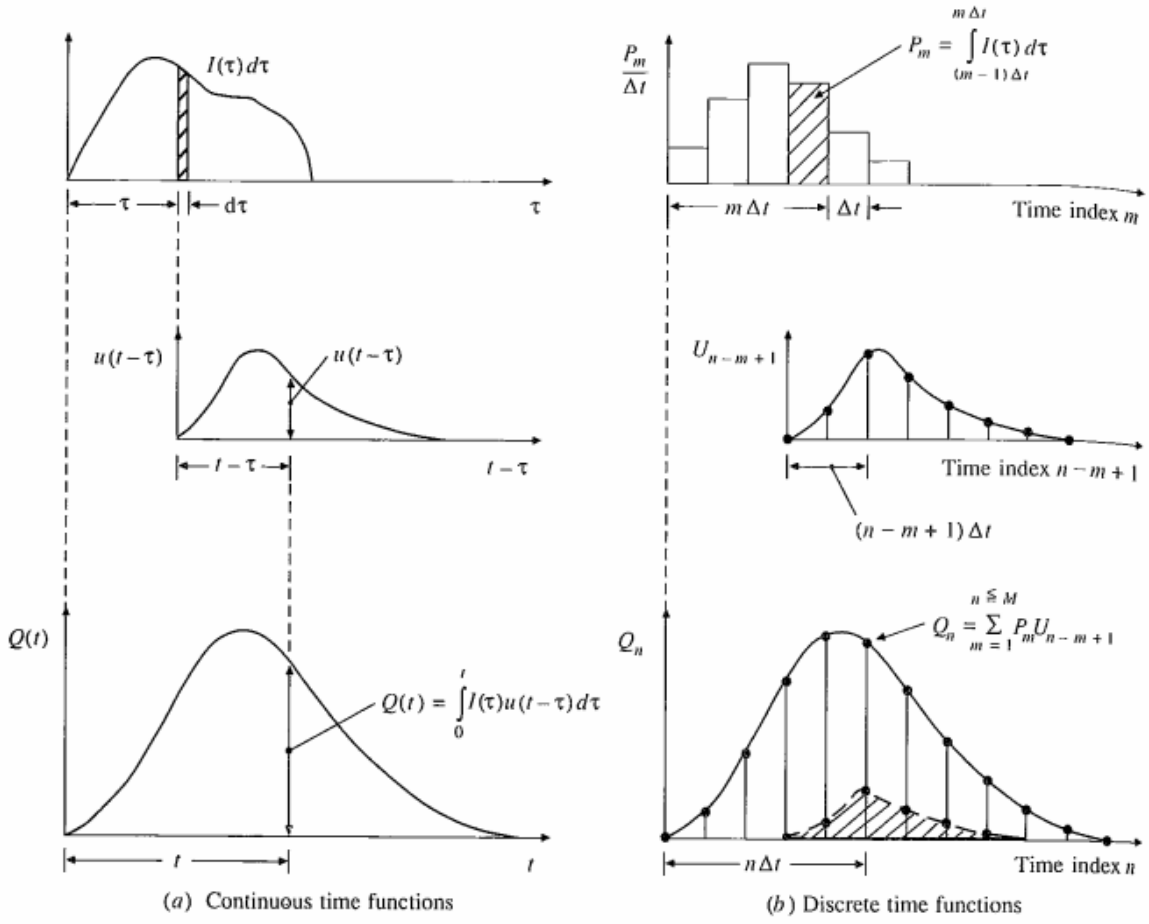

Figure 17.Scheme of the of the convolution method for a continuous (left) and discrete (right) function in case of a generic unit responseu$(t-\tau)$. Source: Chow et al., 1988

Equation [16] is the fundamental equation for solution of linear systems (Chow et al., 1988) and can be discretised for being adapted to practical applications (Figure 17) with discrete hyetographs as follows:

$$Q_n = \sum_{m=1}^{n} P_m \cdot WFIUH_{n-m+1} \qquad [17]$$

Where Q_n is flow at the *n*-time step, P_m is the input rain at the *m*-time step and $WFIUH_{n-m+1}$ is the unit response of the basin (in this case calculated with the Width Function) at the time step *m-n+1*.

3.2.2. Implementation

The hydrologic model described in the previous section has been implemented in Python environment. The model can be launched each time step together with the whole Data Assimilation Framework or separately before the DA application. For its implementation, the following measures have been taken:

- Each time step, the number of rain gages without no data are checked for each basin and, if necessary, the Thiessen polygons are re-drawn to avoid that a portion of the basin with no-data could underestimate the value of the total rain;
- The SCS-Method is implemented in GIS environment not as a result of raster calculation between different grid layers (S, Ia, P), but using the "Tabulate Area" function between the attribute table of the Thiessen polygon (that includes the column of the total rain) and the attribute table of the CN shapefile (that includes the column of *S* and *Ia* values). The "Tabulate Area" function provides the number of cells of each Thiessen polygon that belongs to a specific CN value. These numbers of cells, normalized by the total number of cells of the basin, are the weights for the application of the SCS-Method that is performed for each value of CN in the analysed basin. The weights calculated with the Tabulate Area are the same for each time step, with the exception of the cases when there are no data and Thiessen polygons have to be re-drawn. This methodology allowed to reduce the computational time of about 90% respect to the raster calculation methodology.
- The output is given for all the input basins simultaneously in order to simulate a real time scenario.

3.2.3. Calibration and validation

As anticipated in Section 3.2.1, a calibration of the hydrologic model has been performed in order to define an average value of the channel velocity, finding the minimum value of NSE between the observed and the modelled hydrograph. This approach differs from the one

proposed by Grimaldi et al. (2012), where the channel velocities were imposed considering the value of the concentration time calculated with other simplified formulas.

None of the small basins that are part of the computational domain of the case study are gauged. For this reason, four small gaged basins (Figure 18) in the northern part of the Tiber river basin have been considered for calibrating and validating the hydrologic model, considering their close geographic position and their similar morphology and land use compared to the case study area. Specifically, the Naja river, namely the closest basin to the computational domain, has been chosen for the calibration. The other three basins have been considered for the validation. A range of 0.5-2.5 m/s for the channel velocities has been considered for calibrating the hydrologic model. Figure 19 shows a comparison between the simulated flows with different channel velocities and the observed ones for the November 2012 event. Figure 20 shows that best performance parameters values are obtained with a channel velocity equal to 2 m/s. Figure 21 and Figure 22 show the results obtained from the validation. The values of NSE stay between 0.843 and 0.973, and the R values between 0.954 and 0.979.

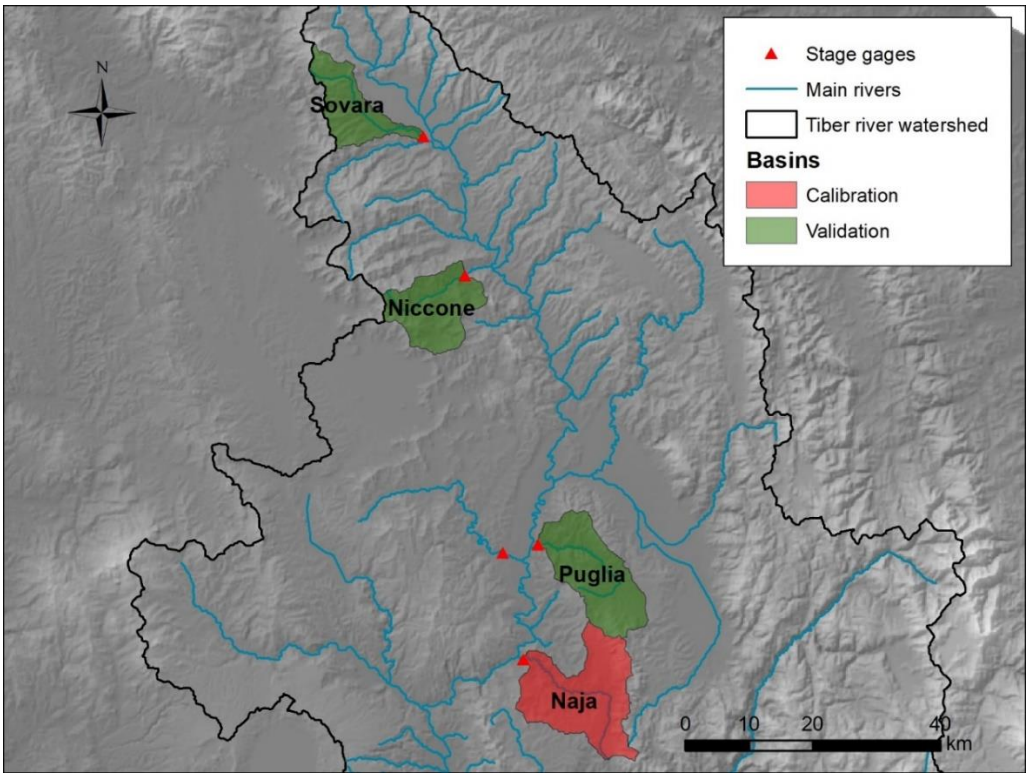

Figure 18. Map of the basins considered for calibrating and validating the hydrologic model

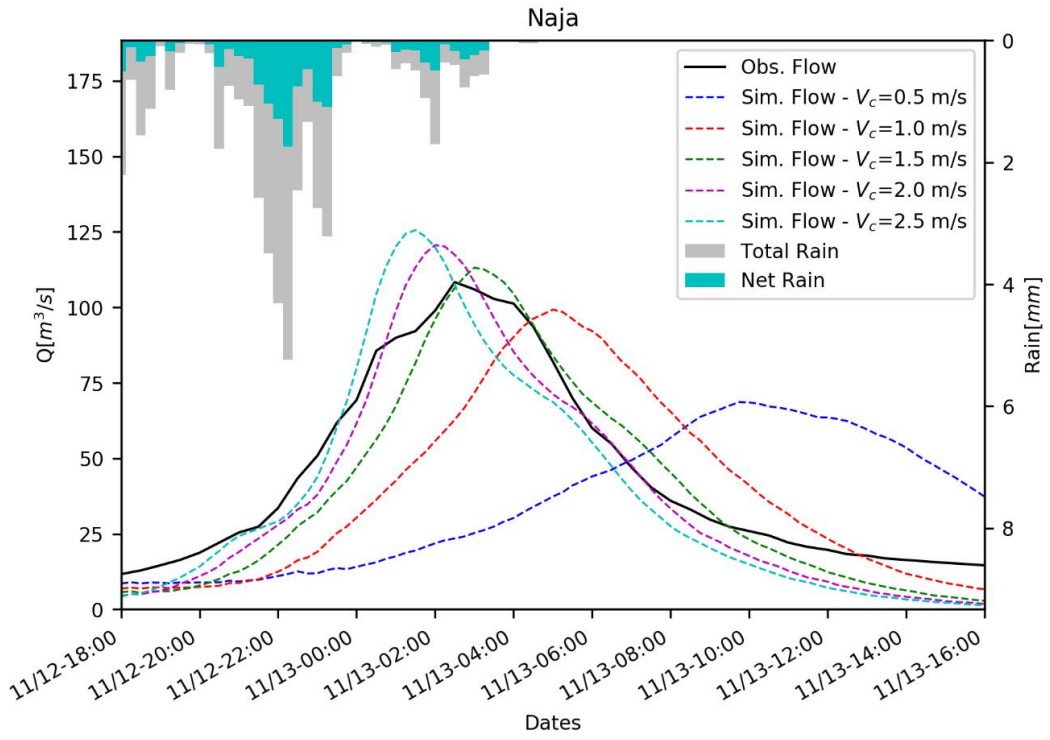

Figure 19. Comparison among the observed flow and the simulated flows for the Naja river basin (calibration). Event: November 2012

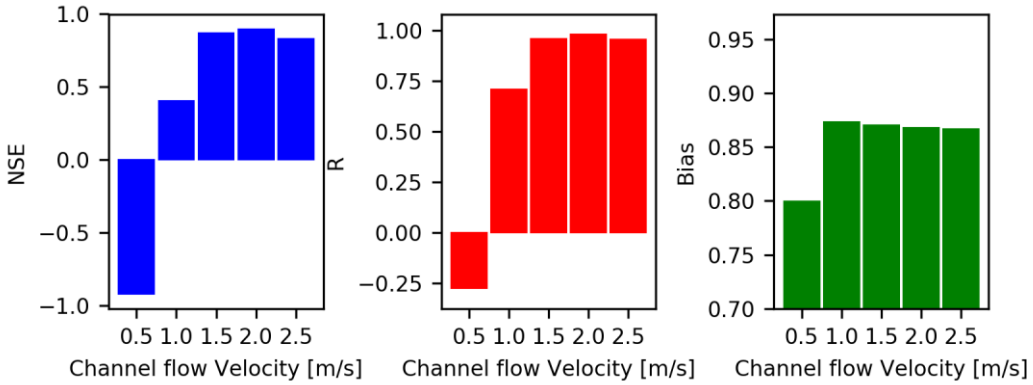

Figure 20. Performance indexes for the Naja river basin varying the channel velocities. Event: November 2012

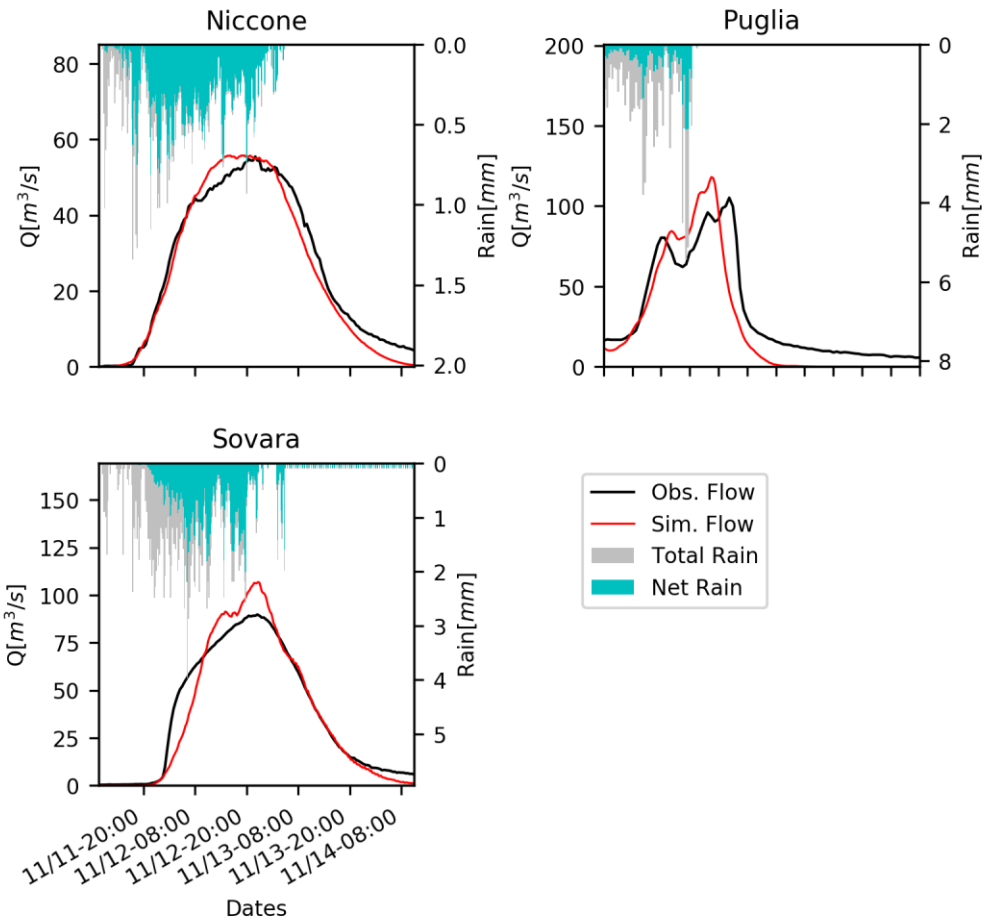

Figure 21. Comparison between the observed and the simulated flows using the calibrated channel velocities for Niccone, Puglia and Sovara basins (validation). Event: November 2012

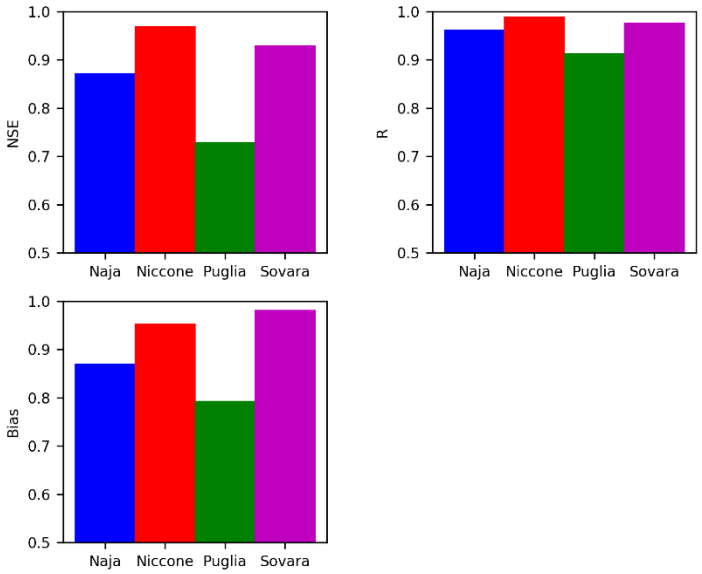

Figure 22. Values of the performance indexes for Niccone, Puglia and Naja river basins using the calibrated channel velocities. Event: November 2012

3.2.4. Application

The hydrologic model has been applied to the ungauged basins of the case study for different extreme events. In the following figures the resulting net hyetographs and hydrographs are showed for each basin. These hydrographs are used as a stochastic input for the hydraulic model creating an ensemble of inputs through a perturbation of the input hydrograph as explained in Section 4.2.

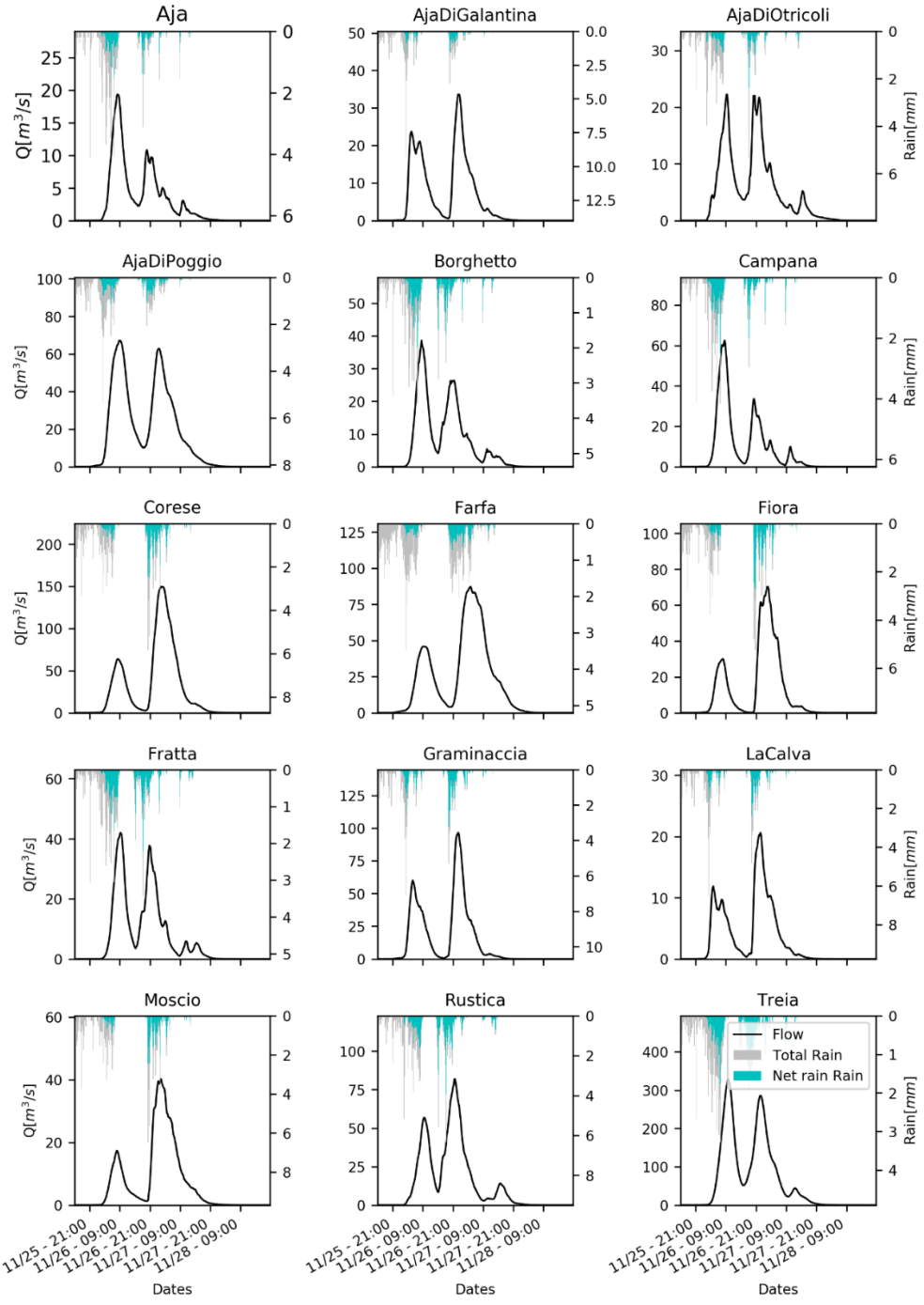

Figure 23. Results of the hydrologic model for the ungauged basins of the case study. Event: November 2005.

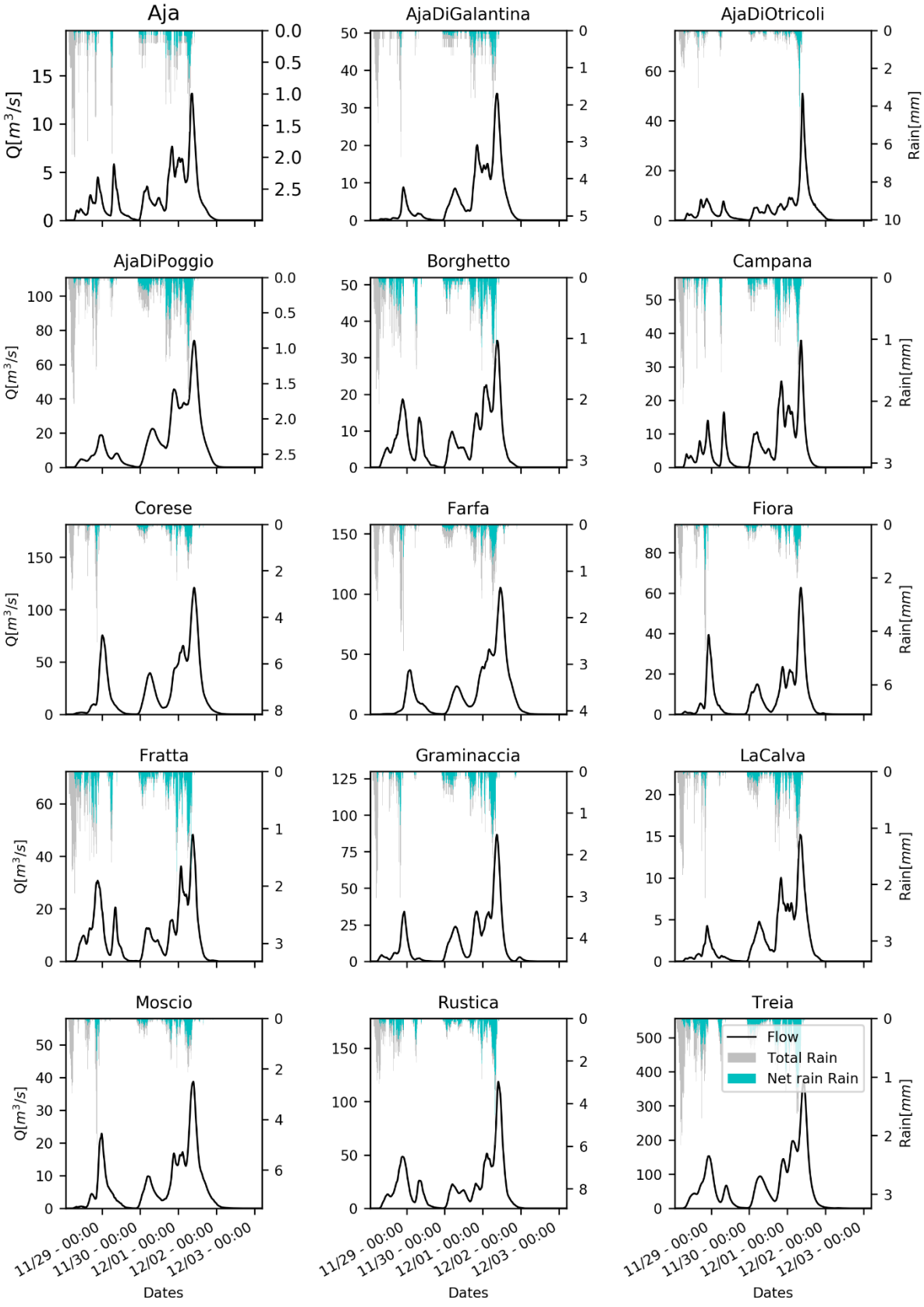

Figure 24. Results of the hydrologic model for the ungauged basins of the case study. Event: November 2010

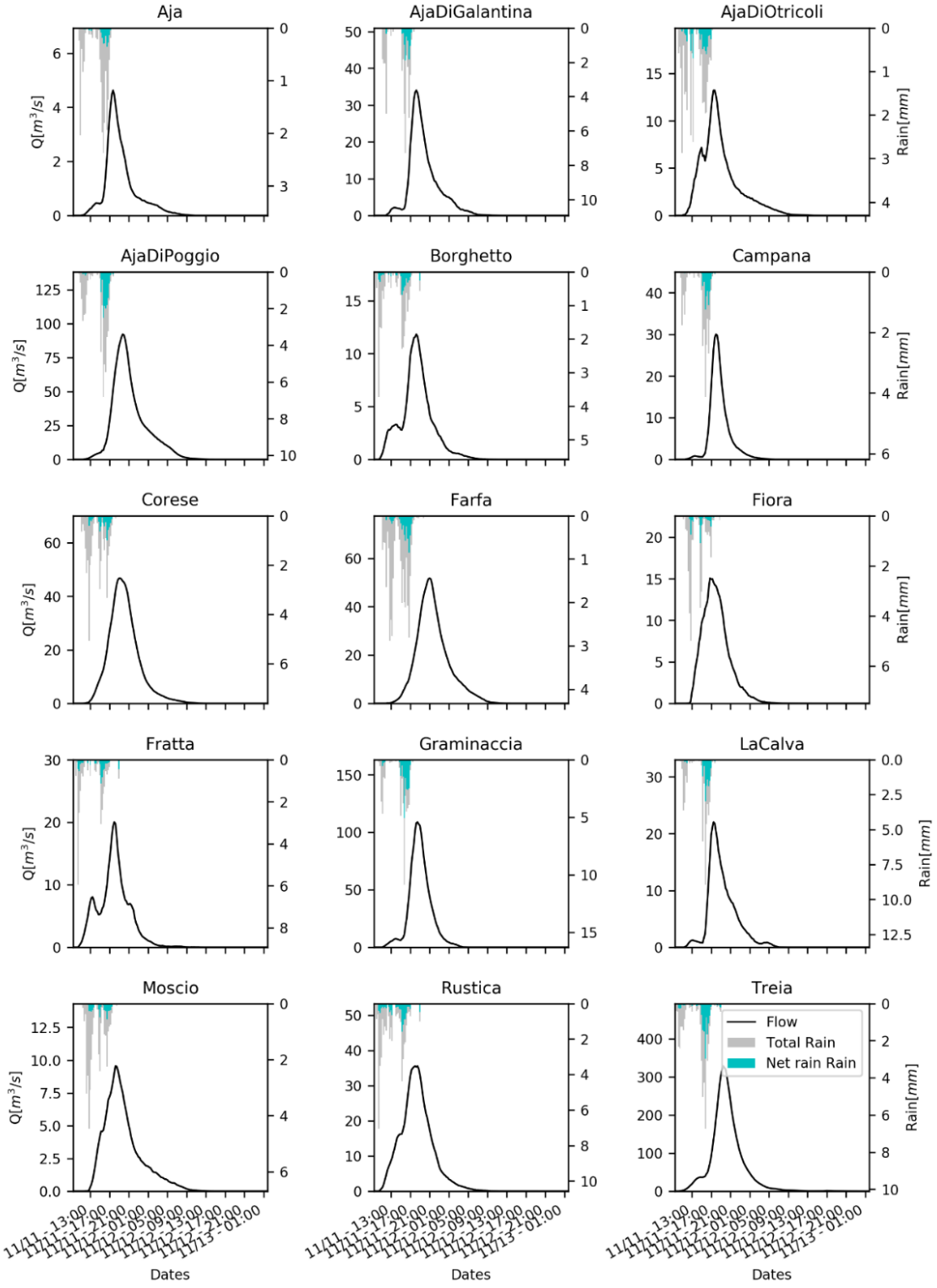

Figure 25. Results of the hydrologic model for the ungauged basins of the case study. Event: November 2012.

3.3. Geomorphic model for delineating the computational domain

The Quasi-2D hydraulic model requires a considerable computational effort, compared to the traditional 1-D hydraulic models. For this reason, a careful selection of computational domain is crucial for the application of a Data Assimilation method, in order to consider all the flood prone areas of the domain excluding the ones that could burden the calculation without contributing to the flood propagation.

Usually, the delineation of the computational domain is carried out considering the experience of the analyst, observing the extension of historical floods or synthetic flooded areas produced for territorial plans studies. However, the aforementioned flooded areas can be limited by levees, beyond them some areas can be potentially flooded in case of levee breaches, overtopping or culvert malfunctioning.

Considering also the hypothesis that a domain might be not subject of previous studies, or if existing, could not be available to the modeller, an a-priori methodology for delineating the computational domain has been proposed starting from a DEM based flood prone area algorithm. The analysis has been deepened also for investigating the application of this modelling for large scale flood-prone area mapping as further aim of this work, besides the DA application.

3.3.1. Introduction on the geomorphic floodplain delineation models

The identification of flood-prone areas has become a very topical issue in the last decades, since population in developing counties is dramatically growing (Di Baldassarre et al., 2010), enhancing the human pressure in riverine areas, thus increasing the flood risk and the consequent flood-related damages and fatalities (Emergency Events Database EM-DAT, 2013).

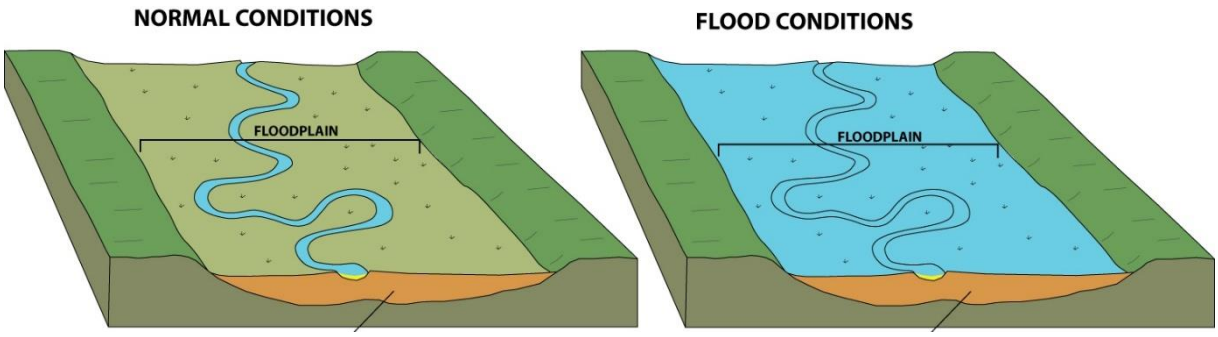

Figure 26. Sketch of a floodplain behaviour in normal and flood condition. Source: Public Works Department (https://www.villageofglencoe.org/government/departments/public_works/flood_plains.php)

Global flood hazard and mapping models are now technically feasible, also in remote ungauged areas, thanks to the availability of earth observation dataset and computationally efficient computer models (Alfieri et al. 2014; Sampson et al., 2015; Alfieri et al. 2016; Dottori et al. 2016). Although the efficiency and performance of global flood hazard models are increasing with the continuous development and availability of always more detailed and accurate topographic, hydrologic and hydraulic data and models, there are still major challenges and issues to solve, such as uncertainty of boundary conditions for inundation models, limitations in knowledge of river profile and roughness, proper consideration of the presence of anthropogenic features in hydraulic systems, such as dykes and levees (Ward et al., 2015).

Alongside global flood hazard models, there is another category of models for floodplain mapping that aim to identify fluvial buffers using the topography as main input information. Those geomorphic approaches enforce the theoretical principle that riparian areas are well distinguished flat areas along river corridors. A brief look at any aerial image of a river corridor shows the evident break line that separates hillslopes from the floodplain, a boundary condition that evidences the diverse morphology and colouring of fluvial ecotones as respect to surrounding slopes. Floodplain unique morphology, biogeochemical and ecologic features and processes represent, in fact, the effect of the water-driven erosion and deposition processes and of the different frequency of saturation that govern the riparian life as respect to surrounding non-aquatic habitats (Figure 26). The floodplain geomorphic footprint is evident, even in significantly dense urban ecosystems, where anthropic features (e.g. buildings, streets, levees, weirs and dams) have greatly altered the floodplain morphology and connectivity (Tockner and Stanford, 2002).

Geomorphic approaches are also increasingly developed and applied at large scale and their use and performance is consistently increasing with the growing availability and accuracy of Digital Terrain Models (DTMs). Several methods have been presented and tested proving DTM-based geomorphic delineation algorithms to be effective tools for floodplain mapping (Williams et al., 2000; Noman et al., 2001; Gallant and Dowling, 2003; McGlynn & Seibert, 2003; Mehlhorn et al., 2005; Dodov and Foufoula- Georgiou, 2006; Nardi et al., 2006; Manfreda et al., 2011; Nobre et al., 2011; Degiorgis et al., 2012; Jalayer et al., 2014; Manfreda et al., 2015; Jafarzadegan & Merwade, 2017).

The hydro-geomorphic floodplain approach proposed by Nardi et al. 2006 based on the application of a geomorphic law and other approaches based on the same principle, as the

Geomorphic Flood Index GFI (Samela et al., 2017), has proved to be very effective for delineating the floodplain areas comparing their extension and the ones obtained with other simplified approaches with the Standard hazard flood maps (FEMA maps) in USA (Samela et al., 2017).

However, several issues and limitations affect geomorphic models that must be properly accounted. The accuracy and resolution of input DTMs, the impact of terrain analysis hydrologic algorithms (Jenson & Domingue, 1988; Tarboton & Ames, 2001) with specific regard to the pit filling and flat areas issues (e.g. Jenson & Domingue, 1988; Garbrecht & Martz, 1997a; Garbrecht & Martz, 1997b; Jana et al., 2007, Nardi et al., 2008) and the geomorphic floodplain model parameter calibration and validation characterize the main challenges for large scale geomorphic floodplain mapping. The impacts of the DEM resolution and stream hortonian orders (thus the ranges of contributing areas) on the performance of these floodplain delineation methods is still not exhaustively investigated, and need to be deepened to provide reasonable parametrizations of the scaling laws related to contributing areas for a large scale application of these algorithms, especially in ungauged basins lacking of information on flood maps.

3.3.2. The Hydro-geomorphic Floodplain Delineation Method

In this work, the hydro-geomorphic floodplain model by Nardi et al., (2006) has been revised and applied to delineate the computational domain of the hydraulic model for the DA application. Further testing, that can be considered as an independent branch of this research not related to the DA framework, have been performed to evaluate the optimal set of parameters using different DEMs and considering the role of the stream orders that affect the optimal parametrization of the model. As reference traces for evaluating the performance of the floodplain delineation method, the standard flood hazard maps obtained applying hydrologic and hydraulic modelling starting from synthetic rain events, have been considered numerically comparing their extension with the ones provided by the adopted model. However, the hydro-geomorphic floodplain method has a different purpose from that of the standard flood hazard maps, because it is aimed to delineate all the areas that can be considered as floodplain because of their morphology that has been influenced by floods even before the Anthropogenic era.

Geomorphic scaling laws are applied considering the existence of hydraulic scaling relations describing the behaviour of the floodplain morphologic parameters across different hydrologic scales (Bhowmik, 1984; Nardi et al., 2006). Power laws of valley bottom width w and mean

depth *d* with varying maximum peak flow (i.e. $w = a_1 Q^{b_1}$, $d = a_2 Q^{b_2}$ where a_1, b_1, a_2 and b_2 are numerical constant of the power laws), as observed by Leopold and Maddock (1953), are implemented with the contributing area as a scaling parameter (Dodov and Foufoula-Georgiou, 2004). Floodplain flow depths are estimating as follows:

$$FH = aA^b \qquad [18]$$

where *FH* is the floodplain water depth [m], *A* is the contributing area in a cross section of a river [m^2], and *a* [m^{1-2b}] and *b* [dimensionless] are the power law coefficients. The power law parameters *a* and *b* depend on the hydrology, geomorphology and climatic of the river basin. Calibration of the power law parameters was explored for river channels (Leopold and Maddock, 1953; Dodov and Foufoula-Georgiou, 2004). Equation [18] can be applied in GIS environment using a DEM-based approach, giving the distribution of the contributing areas for each cell of the domain through the terrain analysis algorithms: pit filling, flow direction, flow accumulation (Jenson and Domingue, 1988). The selected algorithm by Nardi et al. (2006) was originally based on a procedure for estimating the power law parameters *a* and *b* that involved: the definition of a maximum discharge at the outlet associated to a predefined frequency (i.e. return time); the scaling of the peak discharge along the river network for associating a peak discharge to every channel node; the estimation of the maximum floodplain flow depth *d* per every channel node by solving the uniform flow Chezy's equation (floodplain cross section geometry extracted from DTM). The presented approach overrides the cross sections analysis and the need of an input maximum outlet peak discharge, investigating the implementation of Equation [18] and a methodology for evaluating the performance of the floodplain model as respect to standard flood hazard maps while calibrating *a* and *b* parameters with varying DTM resolution and scaling conditions.

The river network is identified by filtering cells with a contributing area greater than a predefined threshold (see also Tarboton et al., 1991; Tarboton and Ames, 2001). The threshold area for stream network extraction is dependent on DEM resolution, but also on geomorphic, geologic and climatic factors (Tarboton et al., 1991); however, in this work, the choice of the threshold area is done considering a minimum number of cells for delineating the floodplain width extension.

The hydraulic scaling relation of Equation [18] has to be customized for the DEM-based approach, because the power law coefficients *a* and *b* are also dependent on the resolution of the adopted DEM.

3.3.3. Inspection on the threshold area and the DEM resolution

The threshold area of the stream network is considered strongly dependent on the DEM resolution (McMaster, 2002). Higher DTM resolution determine a lower contributing area for which the topographic information is consistent with floodplain width (Leopold & Maddock, 1953, Nardi et al., 2006). This means that the stream network adopted for the floodplain model can represent the portion of the river network in which the floodplain width can be delineated with a minimum number of cells.

The constraint is linked to a minimum threshold of number of DTM grid cells that are able to depict the floodplain morphology. Analysing the different available DTMs, a minimum percentage (70%) of occurrences with floodplain width larger than the size of 2 cells was considered. The floodplain extension is also dependent on the *a* and *b* parametrization that has been performed before the above mentioned procedure using different threshold areas.

The floodplain model is able to delineate a floodplain extension for natural landscapes that is generally different from the one of the flood maps generated by hydraulic models that are influenced by anthropic features, i.e. levees, bridges, weirs, dams, and channel reshaping in urban areas. Nevertheless, standard flood hazard maps have been used as reference to get a range of the power law values. Different combinations of *a* and *b* parameters have been chosen (see Table 4) starting from literature values (Nardi et al. 2006; Nardi et al., 2013) considering a wide interval.

Power law parameter	Range of values
a [m^{1-2b}]	0.0002-1
b [-]	0.20-0.60

Table 4. Values range of the power law parameters a and b for the consistency analysis

To numerically evaluate the differences between the delineated hydro-geomorphic floodplain and the Italian standard flood boundaries PAI (Piano di Assetto Idrogeologico) derived using hydraulic modelling (200-year flood hazard maps), the objective measure-to-fit function (F) illustrated by Equation [6] was selected and implemented (F=A/ (A+B+C)). The terms of this equation follow the contingency scheme represented in Table 5

The D term in Table 5, representing all the hillslopes of the basin according to both the PAI maps and the floodplain polygon is not included in the F-index, but it has been taken in to

account adopting the sum of False Positive and False negative rate (Equation [9]) in the benchmarking analysis with other geomorphic methods (see Section 3.3.4.).

	Within the PAI map	Outside the PAI map
Within the Floodplain Polygon	A	B
Outside the Floodplain Polygon	C	D

Table 5. Contingency table showing F index variables.

It is worth to specify that the optimum values of the F-index, don't provide necessarily the best parameters for the power law, since that the anthropic features could lead to an underestimation or overestimation of the parameters. The comparative analysis has been performed varying the DEM resolution and considering separately the hortonian stream orders.

3.3.4. Benchmarking analysis with other geomorphic methods

The hydro-geomorphic floodplain algorithm has been compared with other floodplain delineation methodologies using a similar approach of Samela et al., 2017. Some geomorphic classifiers have been taken in to account optimizing their threshold indexes maximizing Eq. [6]. Different performance ratios (Equations [7]-[10]) have been considered as supplement of the information provided by Eq. [6].

The following simplified methods have been considered for a benchmarking analysis with the floodplain method:

- Constant water depth assignment to the stream network *H[m]*: this method, considering a similar approach of Nobre et al. (2011), calculates the floodplain extension considering a constant value of the water depth to each cell of the stream network and thus flagging as floodplain all the cells hydrologically connected to it with an elevation lower than the sum of the stream cell elevation and the assigned water depth;
- Constant flow hydrologic distance to the stream network *D[m]*. This method considers constant value of the hydrologic distance of the basin's cells to the stream network;
- Local Slope *S[%]*: A threshold value of the local slope of the basin is considered to distinguish the floodplain part to the rest of the basin.
- Topographic wetness index $= \ln(A_c/\tan(S))$, where A_c is the local contributing area per unit contour length and *S* is the local slope.

3.3.5. Results

Figure 27 represents the percentages of occurrences where the floodplain width is larger than 2 cells with the contributing area for each DEM.

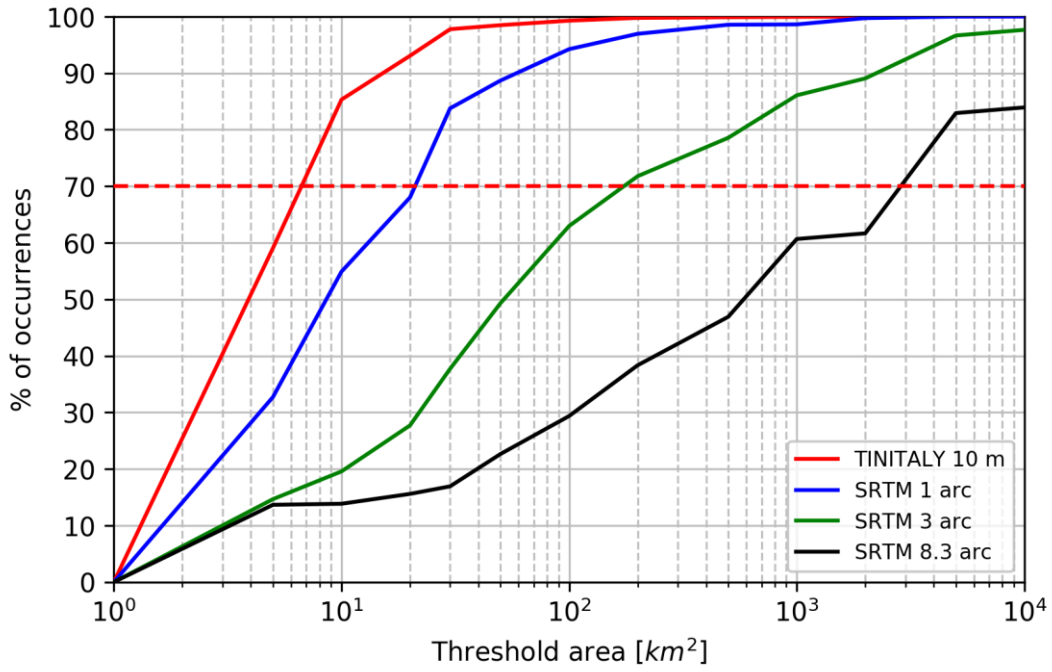

Figure 27. Plots of the percentages of occurrences where the floodplain width is larger than 2 cells for each DEM varying the threshold area

For 10 m and 30 m resolution (red and blue curves), the 100% of occurrences where the floodplain width is larger than 2 cells is reached with a relatively steep curve, so the 70% of occurrences is reached with a threshold area respectively of 6 and 20 km^2. For SRTM 3 arc and 8.3 arc resolution DEMs, the relative curves are less steep and the 70% of occurrences are obtained with a threshold area respectively of 200 and 3000 km^2. A threshold area larger than 10000 km^2 has not been considered because of the limited dimension of the study area (17500 km^2), even if this methodology can be generalized to basins of different size and climate.

A numerical measure to fit analysis of the floodplain polygon compared to the PAI floodmaps have been evaluated using Eq. [6] for different DEMs, as illustrated with the contour plots in Figure 28. In the semi-log plots, the optimal combination of the power law values *a* and *b* have a strong linear correlation regardless of the DTM resolution (greater than 0.97, see Table 6). Results demonstrate that the calibration of the model can be restricted to one parameter taking advantage of their linear interdependency. It is also shown that lower values of the *a* parameter

follow higher values of *b* value for reaching optimal performance and increasing the DTM resolution the optimal *b* value increases.

DEM	slope *s*	intercept *i*	correlation coefficient	standard error
TINITALY 10m	-0.0413	0.1457	-0.9781	0.0023
SRTM 1arc	-0.0375	0.1467	-0.9717	0.0024
SRTM 3arc	-0.0365	0.1489	-0.9728	0.0023
SRTM 8.3 arc	-0.0343	0.1519	-0.9731	0.0022

*Table 6. Results of linear correlation between the optimal log(a) and b values for each DEM [b(a)=i+s*log(a)]*

DEMs	Optimum b	F-index
TINITALY 10m	0.32	0.376
SRTM 1arc	0.30	0.413
SRTM 3arc	0.30	0.436
SRTM 8.3 arc	0.30	0.288

Table 7. Optimal values of the b parameter and the F-index for the selected DEMs in correspondence of an a parameter value equal to 0.01

This is expected considering the increasing water depths associated to same floodplain flow levels, an effect due to the higher accuracy of high resolution DTMs in catching the channel morphology (Figure 29). The differences among optimal combinations of the power law parameters varying the DEMs becomes less relevant for higher *a* values, that become more important than the *b* parameter, reducing their optimal values from 0.6 to 0.2 in the adopted range.

It is also evident that equivalent optimal values of the F-index can be obtained for a wide range of the *a* parameter, choosing the appropriate value of the *b* parameter. This behaviour confirmed that the exponent *b* of the power law can be considered as the only parameter governing the law, fixing the *a* parameter as constant. In Table 7 the maximum F-index values for each DEM are presented considering an *a* value equal to 0.01 [m^{1-2b}]. To be noted that the F-index analysis is affected by the heterogeneous spatial availability of PAI flood maps that don't cover the entire catchment, especially for upstream areas. This doesn't affect the validity of this comparative analysis that aims to provide a comparative impact of different DTMs and not the general validity of the hydrogeomorphic algorithm as surrogate of standard flood hazard models.

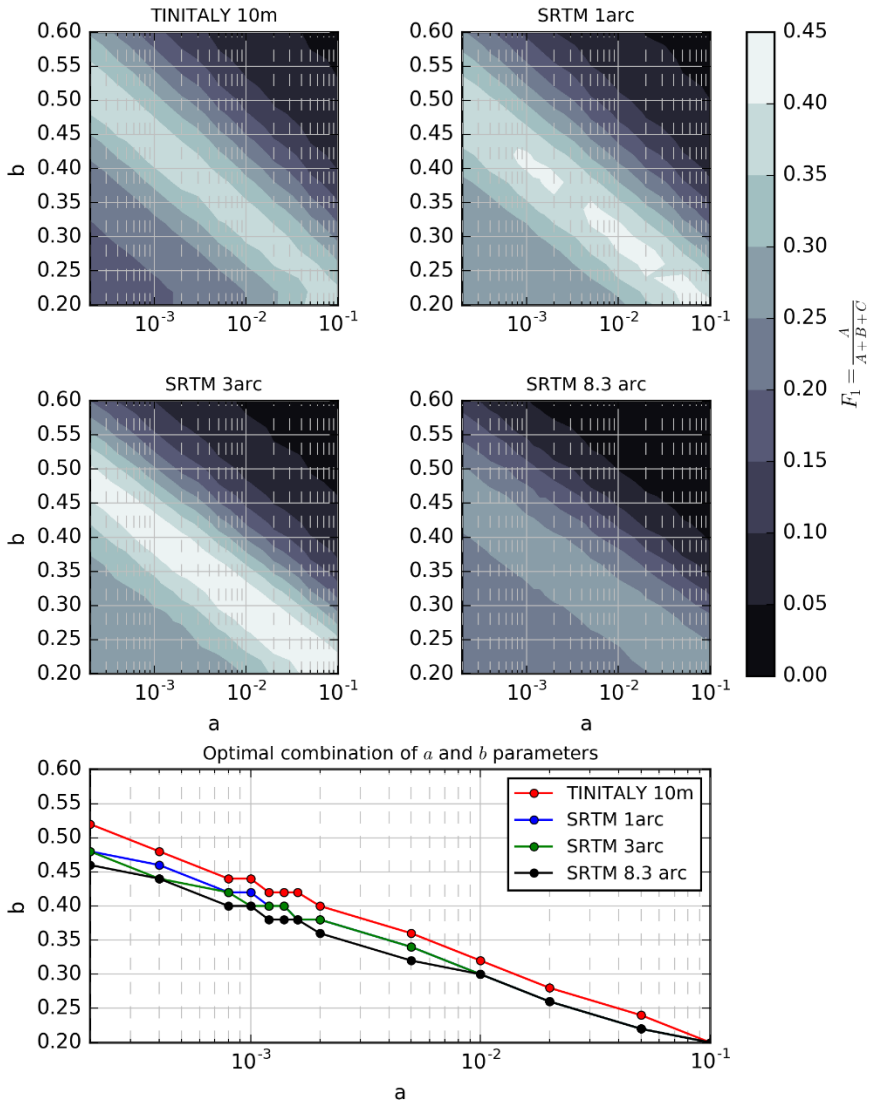

Figure 28. Contour plots of the F index for different DEMs and comparison among the optimal combinations

A further performance analysis is developed for evaluating the behaviour of the floodplain algorithm for different geomorphic conditions of the watershed associated to the hortonian orders of the drainage network. Figure 30 presents the floodplain performance using the SRTM 1arc DTM and a contributing area threshold of 10 km^2 (consistently with the floodplain initiation analysis of Figure 27).

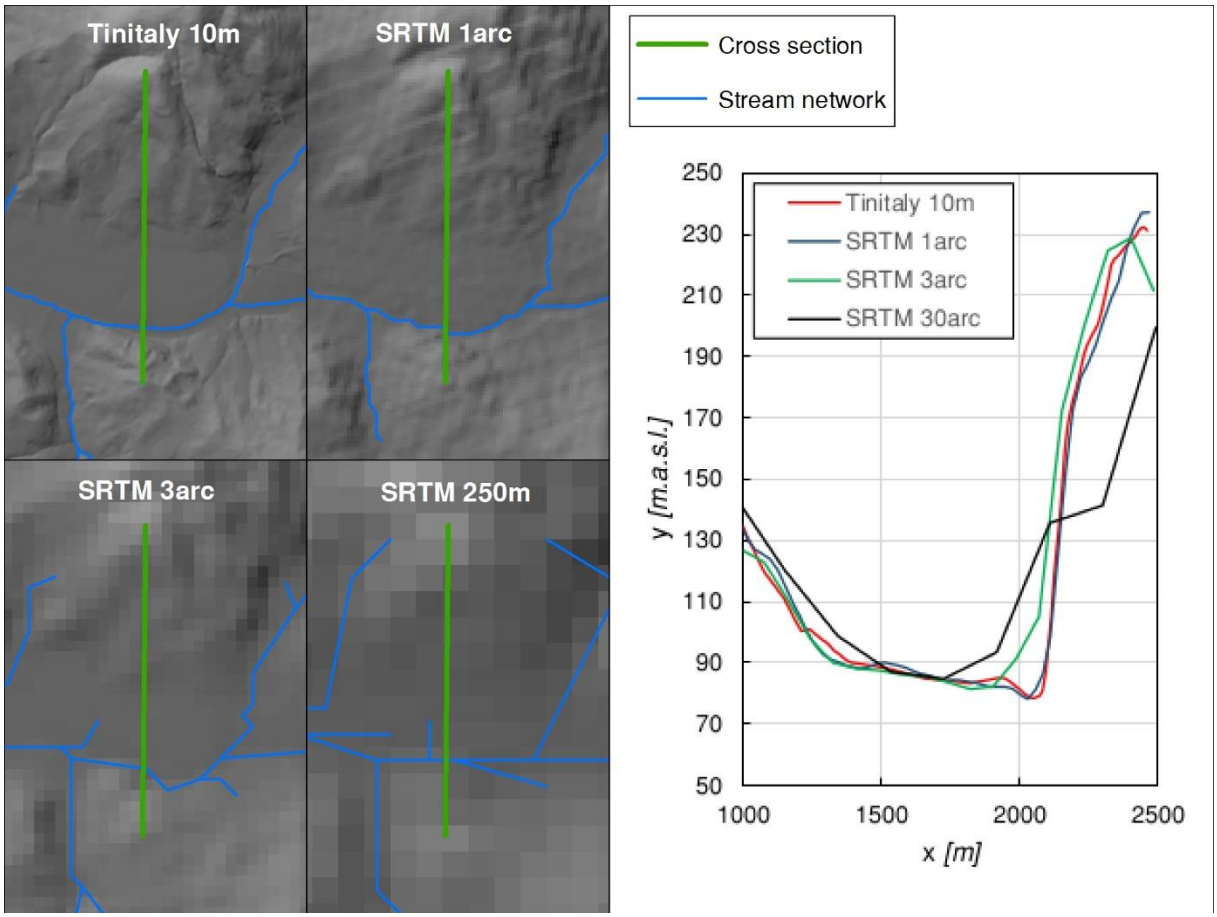

Figure 29. Example of representing a floodplain cross section using DEMs with different resolutions

It is clear that in order to have the optimal combination of the power law parameters, the higher is the stream order, the lower are the optimal values of *a* and *b* parameters. This is due principally to the fact that lower stream orders are the ones closer to the hillslopes were terrain are steeper, altitudes are higher, and the maximum extreme rainfall are higher. These factors generate higher unit peak flows than the ones in the downstream part of the basin, and this affects the optimal power law parameters of the floodplain polygon.

These results suggested that the power law relation with constant parameters' values can be improved considering different parameters for different ranges of contributing areas. For this reason, the floodplain algorithm has been improved imposing a changing of the power law values for each stream order. With this modification of the algorithm, the F index improved its values averagely of 6%.

Figure 31 shows the map of the floodplain polygon for the whole Tiber river basin generated from the SRTM 1 arc adopting an optimal combination of the Leopold power law. An

interesting aspect of the floodplain mapping is that for low contributing areas, the floodplain covers more areas than the standard flood hazard maps.

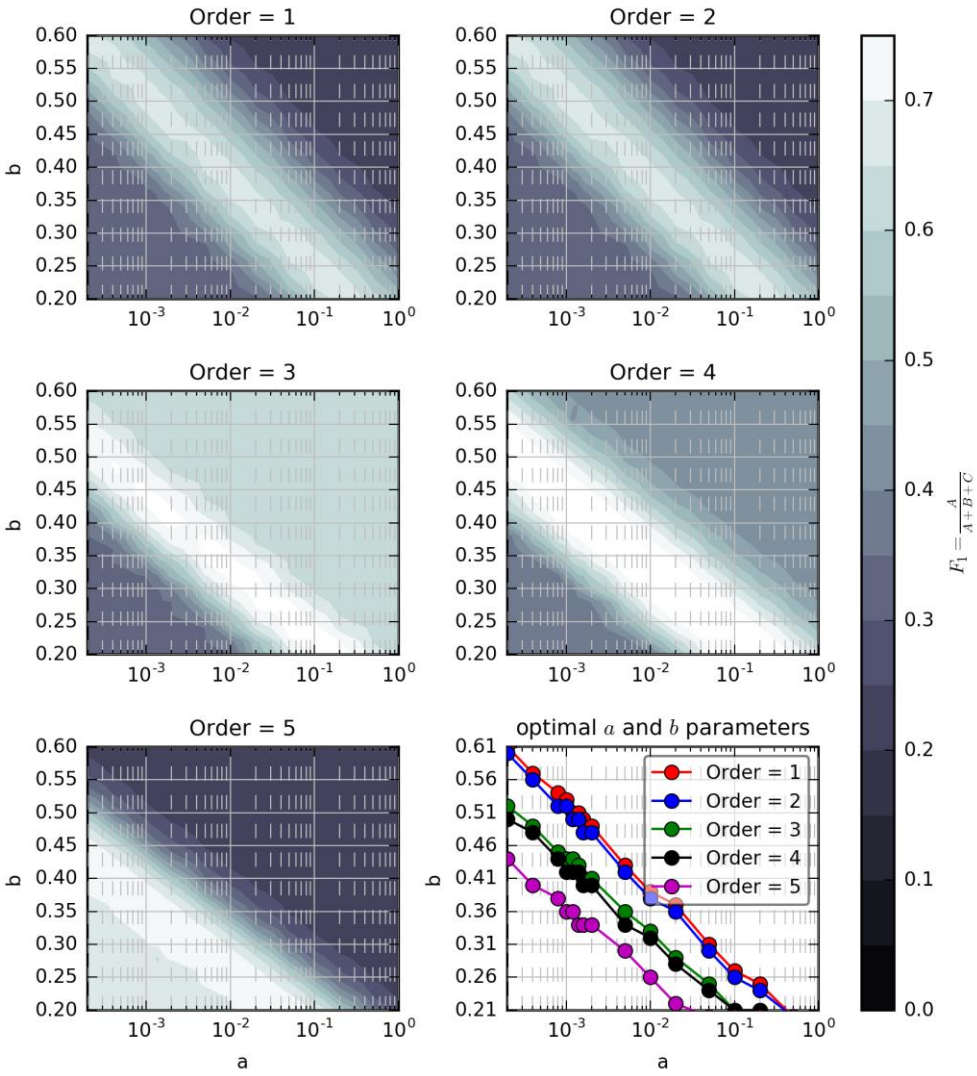

Figure 30. Contour plots of the F index for SRTM 1arc DEM for different stream orders and comparison among the optimal combinations

To perform the benchmarking analysis mentioned in section 3.3.4, the SRTM 1arc DEM has been taken in to account, considering that currently it is the higher resolution DEM available for 80% of the planet. Table 8 and Figure 32 show the better performance of the hydro-geomorphic floodplain method compared to the other ones mentioned in section 3.3.4.

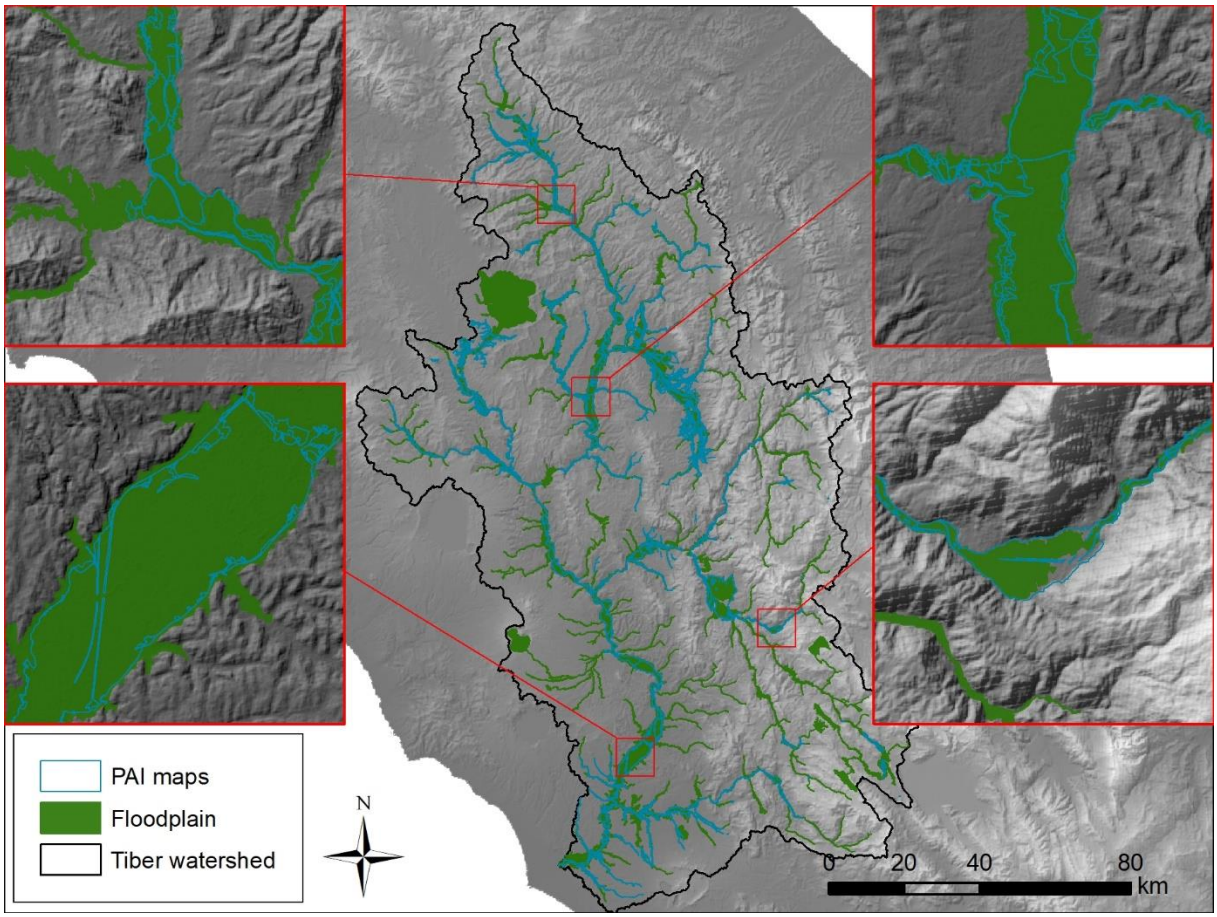

Figure 31. Map of the floodplain with the optimum values of the scaling law parameters for the SRTM 1arc DEM

Method	Threshold parameter	Threshold value	F-index	TP	FPN	Bias
FH	Exponent of the Leopold law *b*	0.30	0.408	0.76	0.283	1.621
H	Stream water depth [m]	0.50	0.065	0.998	0.715	15.471
D	Stream distance [m]	424.00	0.159	0.399	0.676	1.914
S	Slope value [%]	1.20	0.267	0.639	0.429	2.03
TWI	Index value [-]	8.00	0.076	0.322	0.839	3.586

Table 8. Summary of the performance indexes for the optimum threshold values of each floodplain delineation method

Specifically, the F-Index values are 60-80% higher than the other geomorphic indexes except for the slope index, whose F value is closer to the one obtained with the Floodplain method (30% lower). However, Samela et al. 2017 demonstrates that the slope index can have a much larger variability, in order to reach an optimum value and can be considered less reliable for delineating floodplains in areas without reference standard maps. The other performance indexes show as well a good behaviour of the floodplain algorithm compared to the other delineation methods.

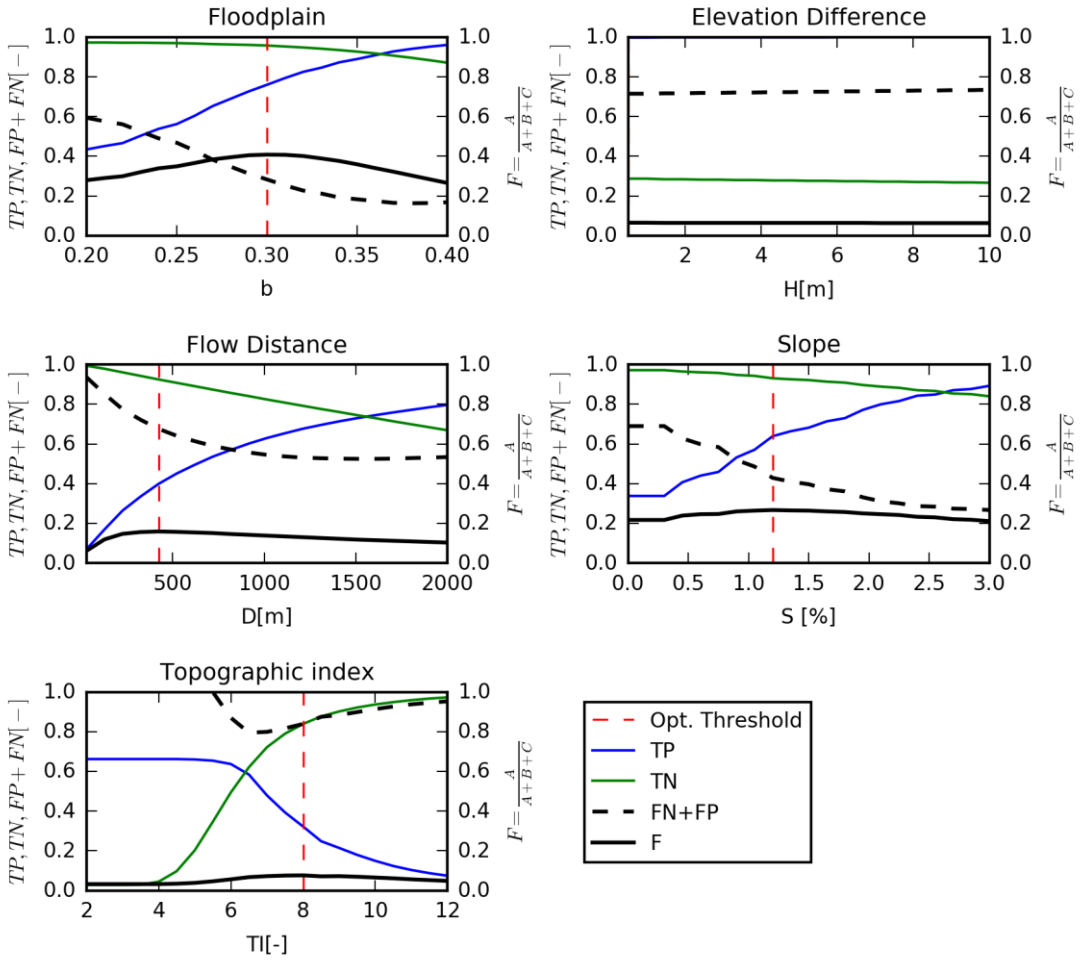

Figure 32 - Behaviour of some performance indexes (True positives rate TP, True negatives rate TN, sum of False Positives and False Negatives FN+FP, F-index) with the positioning of the optimum thresholds for each floodplain delineation method

The results obtained by the application of the optimal parametrization of the SRTM 1 arc DEM to the Tiber river have been used for delimiting the computational domain of the hydraulic model, thus excluding all the hillslope areas that cannot be interested by fluvial floods.

3.3.6. Conclusions and future insights

In this section, a testing of a DEM-based floodplain delineation algorithm has been performed considering the impact of the DEM resolution and the stream orders. Reference natural floodplain maps were not available, but only flood maps, whose extension is strongly influenced by anthropic features, i.e. levees, bridges, weirs and dams that change the natural flood profiles and thus their extension.

Nevertheless, the standard flood hazard maps have been used as reference for finding a range of power law parameters that can be considered as reliable for a zone, characterized by a specific

climate and geomorphic peculiarities. Four different DEMs with a cell resolution ranging between 10 and 250 meters have been adopted for this analysis. The choice of the threshold area for the stream network extraction on which delineating the floodplain algorithm, has been analysed evaluating the percentages of occurrence the floodplain width was larger than two cells, finding a relation between DEM resolution and reference values of threshold areas for stream network extraction. The optimal ranges of the power law parameters *a* and *b* for each DEM have been numerically evaluated with a measure-to-fit function, Eq.[6], using as reference maps the PAI standard flood hazard maps. The results showed, mostly for lower values of the *a* parameter, a dependency between the optimal power law parameters and the DEM resolution, denoting that the higher is the resolution, the higher are the values of the parameters needed to reach an optimal consistency of the floodplain polygon, compared to the PAI maps.

A dependence of the floodplain delineation performance on the stream order numbers has also been demonstrated, showing that the higher is the stream order, the lower are the values of the power law parameters in order to reach the optimal numerical fit with the PAI maps. This explains that the use of constant power law parameters is valid only for certain ranges of contributing areas (thus stream orders).

This analysis is proposed as potential guide for identify reasonable ranges of the parameter values at basin scale for the power law that is the core of the DEM-based floodplain delineation algorithm taking in to account the DEM resolution and the stream order influence. The methodology can be exploited for a floodplain zoning at larger scale.

For example, Figure 33 shows the parametrization of the *b* exponent adopted for the entire Italian territory using the SRTM 3arc DEM and imposing an "*a*" value equal to 0.01[m^{1-2b}]. The comparison has been performed for 1352 sub-basins where PAI maps were available (Figure 34). For the adopted value of the *a* parameter, the parametrization of the *b* exponent can be considered acceptable also for different DEM resolutions, as illustrated by Figure 28.

The variability of the optimal value of the *b* exponent has a relative low range, mostly for the highest stream orders. This low range of variability suggests that an application of a larger scale domain even in different climatic zones could provide a reasonable zoning of the flood prone areas.

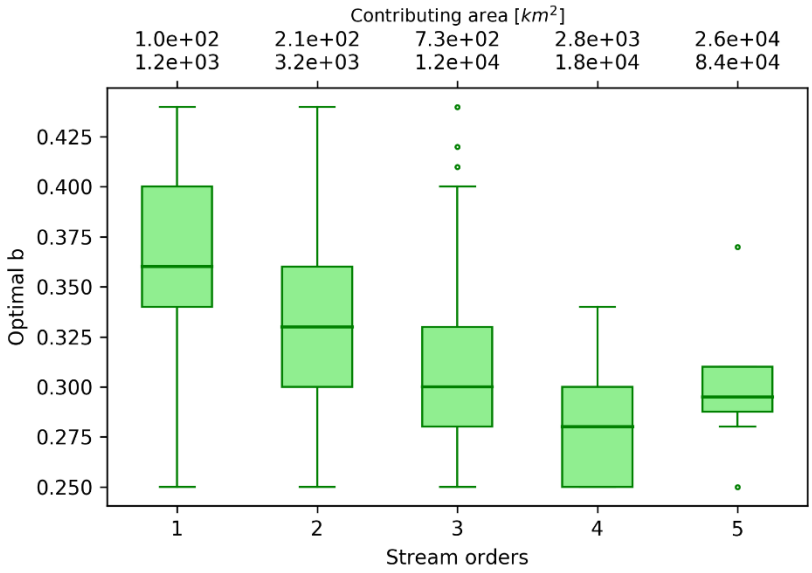

Figure 33. Boxplot of the optimal "b" parameter of the power law equation for the entire Italian territory. The b values have been varied between 0.25 and 0.45, while the a value has been fixed to 0.01[m^{1-2b}]. The SRTM 3arc DEM has been adopted, imposing a threshold area of 100 km^2

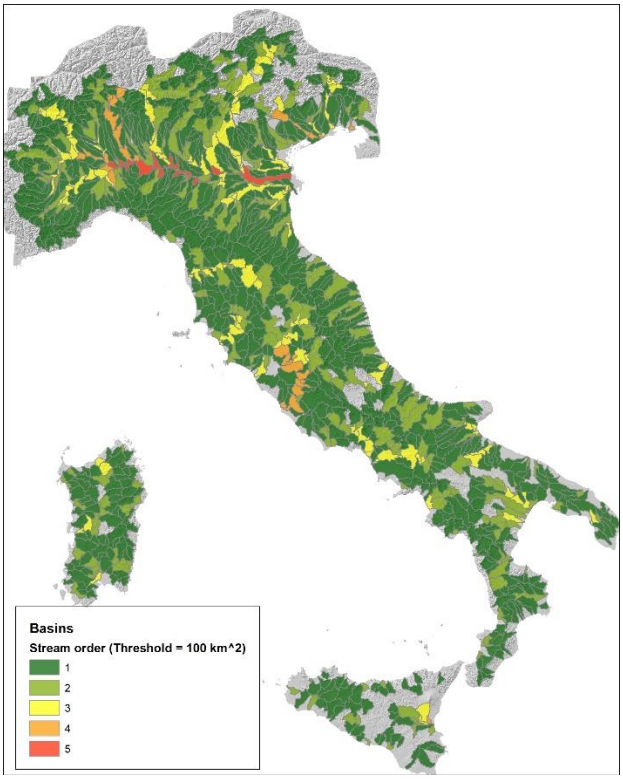

Figure 34. Map of the basins for which a standard flood hazard map were available.

Figure 35 shows a global floodplain delineation map applied to the SRTM 8.3 arc DEM, with a threshold area of 3000 km^2 and constant power law parameters (a=0.01 [m^{1-2b}], b=0.3). The value of the *b* parameter has been chosen considering the average optimal values obtained from the 3rd order of the Italian stream network, where contributing areas started to be greater than the threshold area imposed for the analysis (3000 km^2).

This first application needs to be validated for different climatic zones using local standard flood hazard maps or even lithological maps that provides the distribution of alluvial deposits.

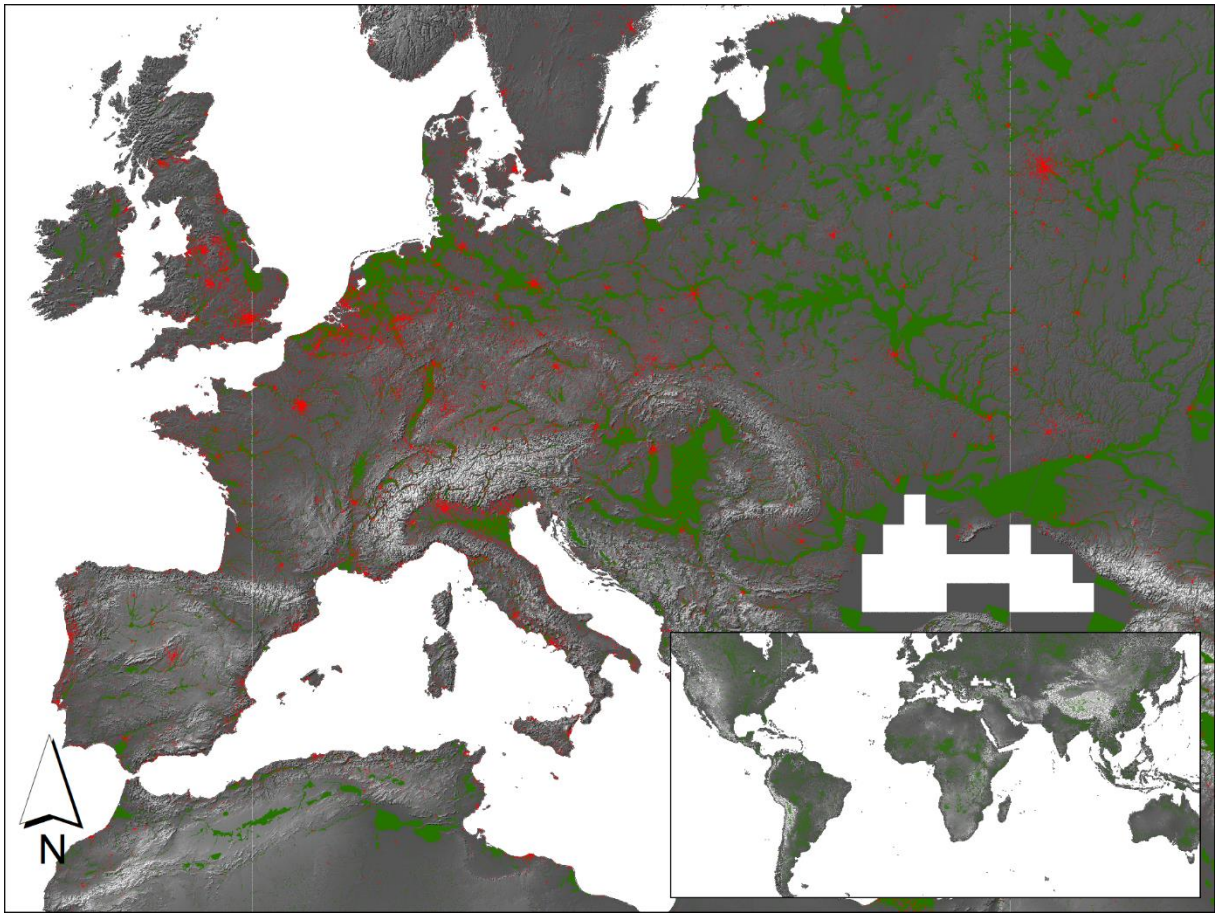

Figure 35. Flood prone areas mapping (green) applying the floodplain delineation algorithm to the SRTM 8.3 arc DEM for the whole available domain (80% of the Earth surface) using constant power law parameters (a=0.01 [m^{1-2b}], b=0.3) and a threshold area equal to 3000 km^2. Details are showed for the European continent, with the urbanized areas (red).

3.4. Bidimensional hydraulic model

3.4.1. Model theory and implementation

An existing hydraulic model, FLO-2D Pro (O'brien et al., 1993), has been adopted. This model has been considered very suitable for the research purposes for several reasons. Besides the ones related to its efficiency in representing the physical processes that will be illustrated below, another strong advantage of this model is the easy manipulation of the inputs files, the outputs files and the launching of the hydraulic engine, that makes it very suitable for being integrated in a superstructure such as a Data Assimilation framework that needs an automation in modifying the inputs and launching simultaneous simulations.

FLO-2D Pro is a physical process model that is able to route rainfall-runoff and flood hydrographs over unconfined flow surfaces (2D equations) or channels (1D equation) using the dynamic wave approximation to the momentum equation.

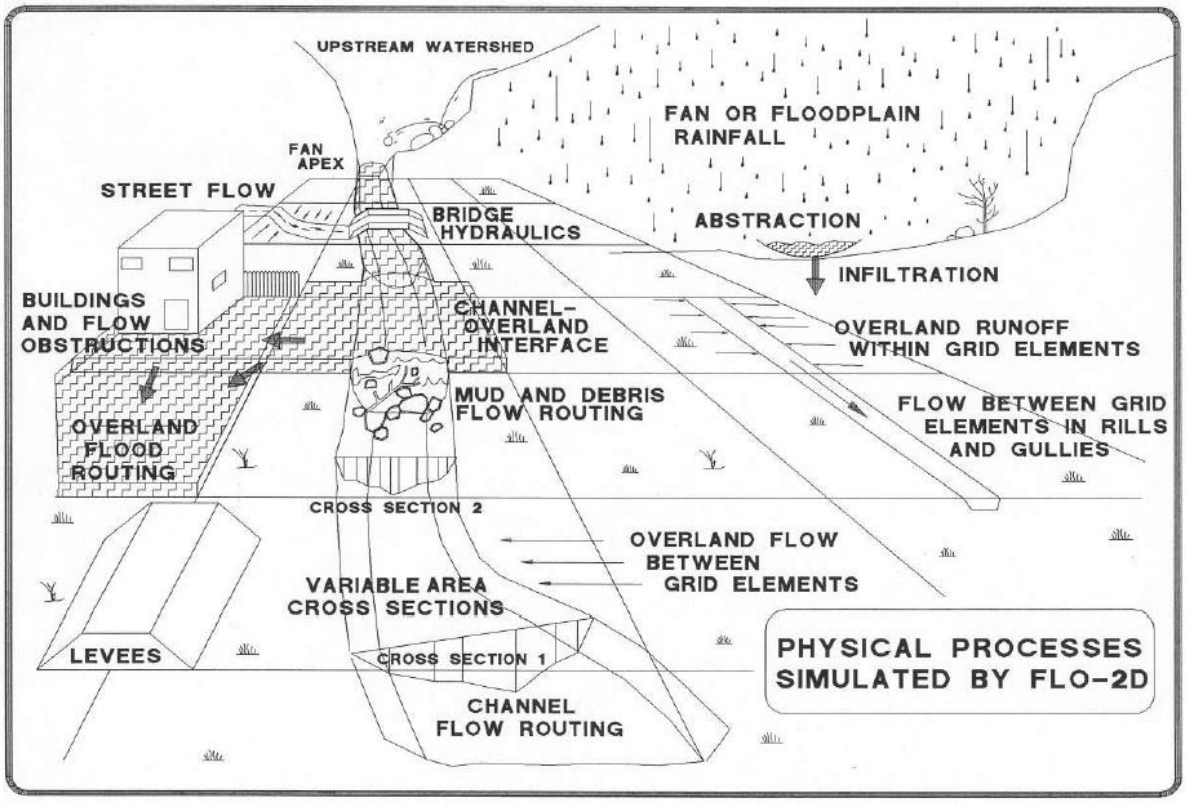

Figure 36. Physical Processes Simulated by FLO-2D. Source: FLO-2D Reference Manual

It has many components that simulate for example street flow, buildings, obstructions, sediment transport, mudflow, spatially variable rainfall and infiltration, floodways, storm drains, levees.

Simulated flow depths and velocities between the grid elements represent average hydraulic flow conditions computed for time steps that usually are on the order of seconds.

FLO-2D is a volume conservation model, whose floodwave progression over the flow domain is controlled by topography and resistance to flow. Specifically, flood routing in one (in the case of the channel element) and two (for overland flow) dimensions is accomplished through a numerical integration of the equation of motion and conservation of fluid volume for either a water flood or a hyperconcentrated sediment flow. FLO-2D numerically distributes the volume in finite fluid blocks to mimic the floodwave progression and timing over the discretized surface. Conceptually FLO-2D is a finite volume model that moves discrete parcels of fluid around on the grid system in eight directions with realistic flow velocities.

The governing equations of the model are the continuity equation:

$$\frac{\partial h}{\partial t} + \frac{\partial hV}{\partial x} = i \qquad [19]$$

and the momentum equation:

$$S_f = S_o - \frac{\partial h}{\partial x} - \frac{V}{g} \cdot \frac{\partial V}{\partial x} - \frac{1}{g} \cdot \frac{\partial V}{\partial t} \qquad [20]$$

where h is the flow depth, V is the depth-averaged velocity in one of the eight flow directions, spatially represented by the *x* variable, t is the time variable, i is the excess rainfall intensity (if the rainfall component is considered), S_f is the friction slope, based on Manning equation, S_o is the bed slope, g is the gravity acceleration. The second term to the right of Equation [20] is the pressure gradient (spatial variation of the flow depth). The third one is the convective term and the fourth is the local acceleration term. These equations represent the one dimensional depth averaged channel flow. For the floodplain, where a multi-directional flow approach is adopted, the equations of motion are applied computing the average flow velocity across a grid element boundary one direction at time. There are eight potential flow directions, the four compass directions (north, east, south and west) and the four diagonal directions (northeast, southeast, southwest and northwest). Each velocity computation is one-dimensional and is solved independently of the other seven directions. Since the flow is being shared with all of a given grid element neighbours, resolution of the velocity vectors is not required. The stability

of this explicit numerical scheme is based on strict criteria to control the magnitude of the variable computational time step.

The differential form of the continuity and momentum equations in the FLO-2D model is solved with a central, finite difference numerical scheme. This explicit algorithm solves the momentum equation for the flow velocity across the grid element boundary one element at a time. The solution to the differential form of the continuity and momentum equations results from a discrete representation of the equation when applied at a single point. Explicit schemes are simple to formulate but usually are limited to small timesteps by strict numerical stability criteria. Finite difference schemes can require lengthy computer runs to simulate steep rising or very slow rising floodwaves, channels with highly variable cross sections, abrupt changes in slope, split flow and ponded flow areas.

The FLO-2D computational domain is discretized into uniform, square grid elements. The computational procedure for overland flow involves calculating the discharge across each of the boundaries in the eight potential flow directions and begins with a linear estimate of the flow depth at the grid element boundary. The estimated boundary flow depth is an average of the flow depths in the two grid elements that will be sharing discharge in one of the eight directions. Other hydraulic parameters are also averaged between the two grid elements to compute the flow velocity including flow resistance (Manning's n-value), flow area, slope, water surface elevation and wetted perimeter. The flow velocity (dependent variable) across the boundary is computed from the solution of the momentum equation. Using the average flow area between two elements, the discharge for each time step is determined by multiplying the velocity times flow area.

The full dynamic wave equation is a second order, non-linear, partial differential equation. To solve the equation for the flow velocity at a grid element boundary, initially the flow velocity is calculated with the diffusive wave equation using the average water surface slope (bed slope plus pressure head gradient). This velocity is then used as a first estimate (or a seed) in the second order Newton-Raphson tangent method to determine the roots of the full dynamic wave equation. Manning's equation is applied to compute the friction slope. If the Newton-Raphson solution fails to converge after 3 iterations, the algorithm defaults to the diffusive wave solution.

In the full dynamic wave momentum equation, the local acceleration term is the difference in the velocity for the given flow direction over the previous timestep. The convective acceleration term is evaluated as the difference in the flow velocity across the grid element from the previous

timestep. For example, the local acceleration term ($1/g \cdot \partial V/\partial t$) for grid element *n* in the east direction converts to:

$$\Delta(V_t^e - V_{t-1}^e)_n/(g \cdot \Delta t) \qquad [21]$$

where V_t^e is the velocity in the east direction (*e*) for grid element *n* at time *t*, V_{t-1}^e is the velocity at the previous timestep (*t-1*) in the east direction, Δt is the timestep in seconds, and g is the acceleration due to gravity. A similar construct for the convective acceleration term ($V_x/g \cdot \partial V/\partial x$) is performed as follows:

$$V_t^e \cdot \Delta(V_t^e - V_t^w)_n/(g \cdot \Delta x) \qquad [22]$$

where V_t^w is the velocity in the west direction for grid element *n*.

The discharge across the grid element boundary is computed by multiplying the velocity times the cross sectional flow area. After the discharge is computed for all eight directions, the net change in discharge (sum of the discharge in the eight flow directions) in or out of the grid element is multiplied by the timestep to determine the net change in the grid element water volume. This net change in volume is then divided by the available surface area (*Asurf* = storage area) on the grid element to obtain the increase or decrease in flow depth *Δh* for the timestep:

$$\sum_{i=1}^{8} Q_n^i = A_{surf} \cdot \Delta h/\Delta t \qquad [23]$$

Where Q_n^i is the flow discharge for the element *n* across a boundary in the *i* direction, A_{surf} is the surface area of one grid element and $\Delta h/\Delta t$ change in flow depth in a grid element during one timestep.

The channel routing integration is performed in essentially the same manner except that the flow depth is a function of the channel cross section geometry and there are usually only one upstream and one downstream channel grid element for sharing discharge. The computational index is the flow direction (1 of 8 directions) not the grid element. This simplifies and reduces the number of steps in the solution algorithm. Each direction is visited only once during a sweep of the grid system domain and involves two grid elements whereas a grid element index requires each grid element to be visited.

The solution algorithm can be summarized in the following steps:

1. For a given flow direction in the grid system, the average flow geometry, roughness and slope between two grid elements are computed.
2. The flow depth h_x for computing the velocity across a grid boundary for the next timestep (*t+1*) is estimated from the previous timestep *t* using a linear estimate (the average depth between two elements).

$$h_x^{t+1} = (h_x^t + h_{x+1}^t)/2 \qquad [24]$$

3. The flow direction first velocity overland, 1-D channel or street estimate is computed using the diffusive wave equation. The only unknown diffusive wave equation variable is the velocity.
4. The predicted diffusive wave velocity for the current timestep is used as a seed in the Newton- Raphson method to solve the full dynamic wave equation for the velocity.
5. The discharge Q across the boundary is computed by multiplying the velocity by the cross sectional flow area. For overland flow, the flow width can be adjusted by the width reduction factors (WRFs), that can be inserted by the users in order to simulate a generic obstacle in the cells, like buildings. The incremental discharge for the timestep across the eight boundaries (or upstream and downstream channel elements) are summed as illustrated in Equation [23] and the change in volume (net discharge at the time step) is distributed over the available storage area within the grid or channel element to determine an incremental increase in the flow depth (Equation [23]).
6. The numerical stability criteria are then checked for the new flow depth. If the Courant Friedrich-Lewy (CFL) condition is exceeded (Jin & Frid, 1997), the timestep is reduced to the Courant number computed timestep, all the previous timestep computations are discarded and the velocity computations begin again with the first computational flow direction. The physical interpretation of the CFL condition is that a particle of fluid should not travel more than one spatial increment Δx (grid element side) in one timestep Δt (Fletcher, 1988). The time step is limited as follows:

$$\Delta t = C \cdot \Delta x/(\beta V + c) \qquad [25]$$

where C is the Courant number ($0.2 \leq C \leq 1.0$), Δx is the square grid element width or channel length, V is the computed average cross section velocity, β is a coefficient (5/3 for a wide channel), c is the computed wave celerity. When C is set to 1.0, artificial or

numerical diffusivity is theoretically zero for a linear convective equation (Fletcher, 1988)

7. The simulation progresses with increasing timesteps using a timestep algorithm until the stability criteria are exceeded again.

3.4.2. Application

The FLO-2D model has been applied in the case study area using the GDS Pro Interface, starting from a five meters resolution Digital Elevation Model provided by Regione Lazio. The extension of the computational domain has been determined applying the geomorphic methodology inspected and explained in Section 3.3. Given the fact that the DA application requires many simultaneous simulations of the hydraulic model characterized by an ensemble of perturbed inputs, to reduce the computational time, the DEM has been resampled at 200 meters resolution interpolating the DEM original topography on the grid domain. The channel is inserted hooking it to the grid elements using the geometry of the surveyed cross sections, integrated by Lidar and the 5 meter DEM, as reported in Section 2.2, and interpolating their geometry to the channel cells included between two contiguous surveyed cross sections. Flow input hydrographs have been inserted both in the upstream part of the Tiber river and also as the tributaries along the computational domain.

The distribution of the Manning values along the floodplain surface of the domain has been assigned considering literature values starting from the land use layer of the Corine Land Cover project at the fourth level provided by ISPRA for the whole Italian country. The values of Manning varies between 0.02 and 0.2 [$m^{-1/3}s$] and are showed in Table 9.

For the channel roughness, a testing of the model behaviour has been performed varying the channel Manning values between 0.03 and 0.05 [$m^{-1/3}s$]. In this case, the hydrologic input has been considered as deterministic. Then the uncertainties of both the hydrologic and the hydraulic models are taken in to account in the Data Assimilation framework.

The results show a general good behaviour of the model compared to the observed measurements, mostly for higher values of the water levels. For lower levels, the model tend to overstimate the water levels. This behaviour is typical for coarse resolution models, because the wetting and drying phenomena along preferential flow pathways are usually influenced by the micro-topography of the domain, that can be represented only in higher resolution models (Nicholas & Mitchell, 2003; Neal et al., 2011). On the other hand, larger floods tend to be valley

filling and the maximum extent can be easily predicted even by models with coarse resolution (Bates, 2012).

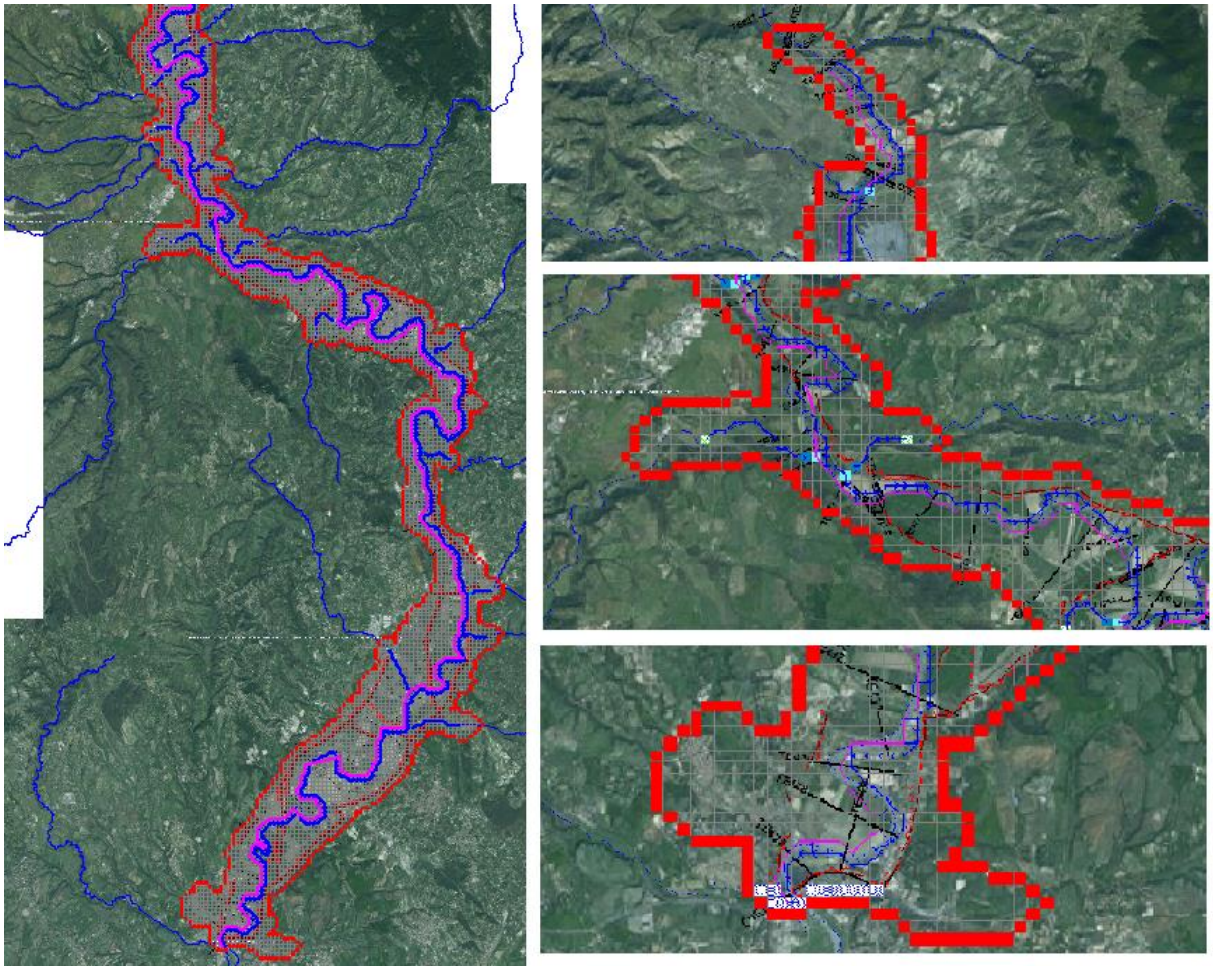

Figure 37. Illustration of some parts of the hydraulic model from the GDS interface. Model boundaries are represented with red cells, channel right and left bank are respectively blue and violet polylines, levees are red polylines, outflow elements are white cells with blue crosses, inflow element are white cells with green crosses.

Castel Giubileo gage station is located in correspondence of an important weir that controls the water level in the immediately upstream part (Figure 43). In fact, in the case of the 2005 and 2010 events, the peak flow does not cause a significant water level raise at that station (see Figure 40 and Figure 41). Furthermore, an accurate behaviour of this weir should require an higher resolution simulation, which is in contrast to the objective of having a large scale hydraulic model with reasonable calculation times. For this reason, this stage gage station has not been considered for calculating the performance of the forecasting model.

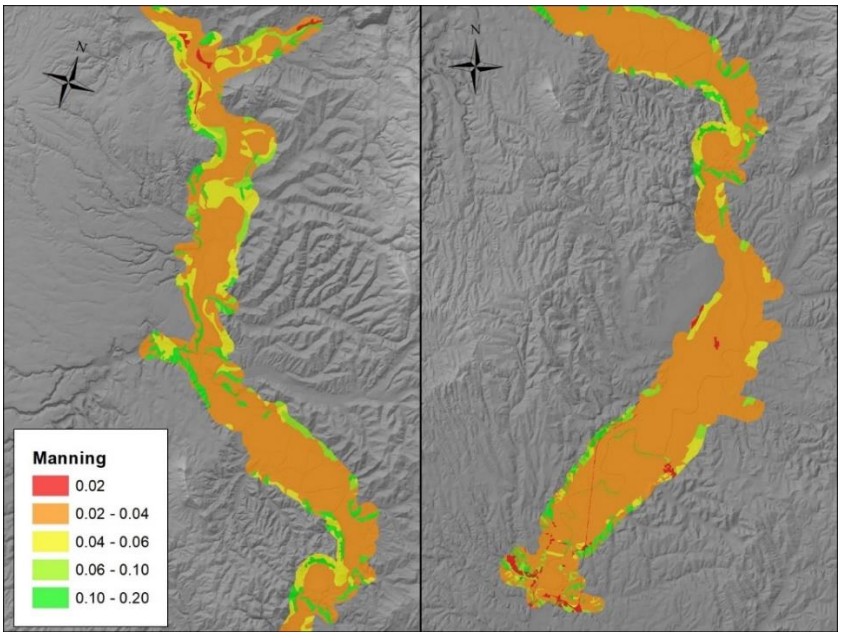

Figure 38. Distribution of the Manning values in the floodplain domain

CLC code	Description	Manning [$m^{-1/3}s$]	CLC code	Description	Manning [$m^{-1/3}s$]
131	Mineral extraction sites	0.04	1111	Continuous urban fabric	0.02
141	Green urban areas	0.035	1112	Discontinuous urban fabric	0.03
143	Green urban areas	0.035	1121	Discontinuous urban (50%-80%)	0.03
211	Non-irrigated arable land	0.06	1122	Residential Discontinuous urban (30%-50%)	0.035
221	Vineyards	0.06	1123	Port areas	0.02
222	Fruit trees and berry plantations	0.06	1211	Industrial or commercial units	0.03
223	Olive groves	0.06	1212	Areas for commercial activities	0.04
231	Pastures	0.1	1213	Industrial or commercial units	0.02
242	Complex cultivation	0.08	1221	Road and rail networks and associated land	0.02
243	Land principally occupied by agriculture, with significant areas of natural vegetation	0.06	1222	Secondary road and rail networks and associated land	0.02
311	Broad-leaved forest	0.2	1224	Road and rail networks and associated land	0.02
321	Natural grassland	0.04	1322	Dump sites	0.05
322	Moors and heathland	0.06	1331	Construction sites and in construction and excavation areas	0.03
324	Transitional woodland shrub	0.06	1332	Construction sites	0.03
333	Sparsely vegetated areas	0.04	1421	Sport and leisure facilities	0.04
334	Burnt areas	0.04	1422	Sport and leisure facilities	0.04
411	Inland marshes	0.05	2111	Non-irrigated arable land	0.04
421	Inland marshes	0.05	2113	Non-irrigated arable land	0.04
511	Water courses	0.03	2121	Permanently irrigated land	0.04
512	Water bodies	0.03	3241	Transitional woodland shrub	0.05

Table 9. Values of Manning assigned for each land use type in the hydraulic computational domain

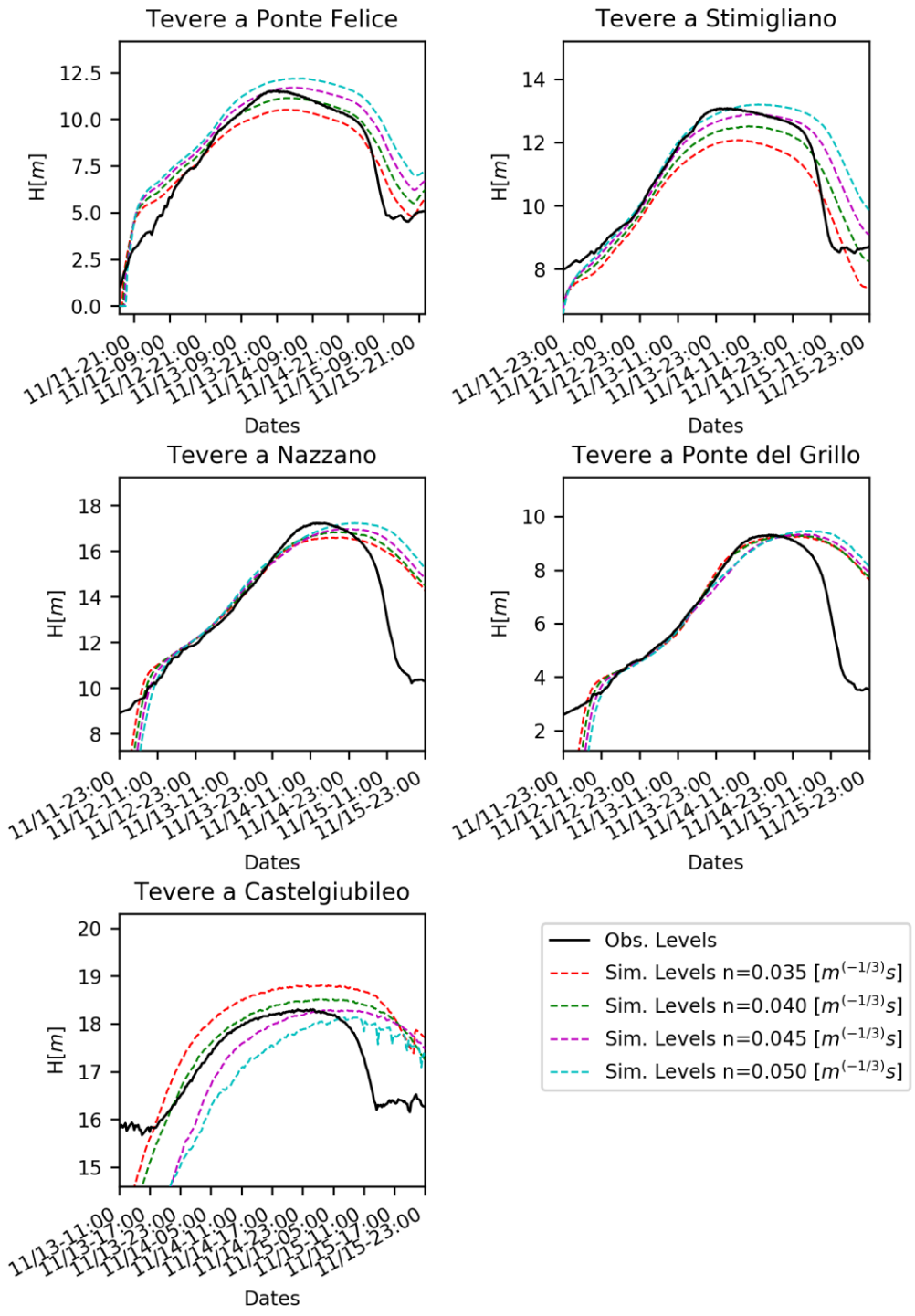

Figure 39. Comparison between the observed flow depths for each control station and the simulated ones for different channel Manning values. Event: November 2012

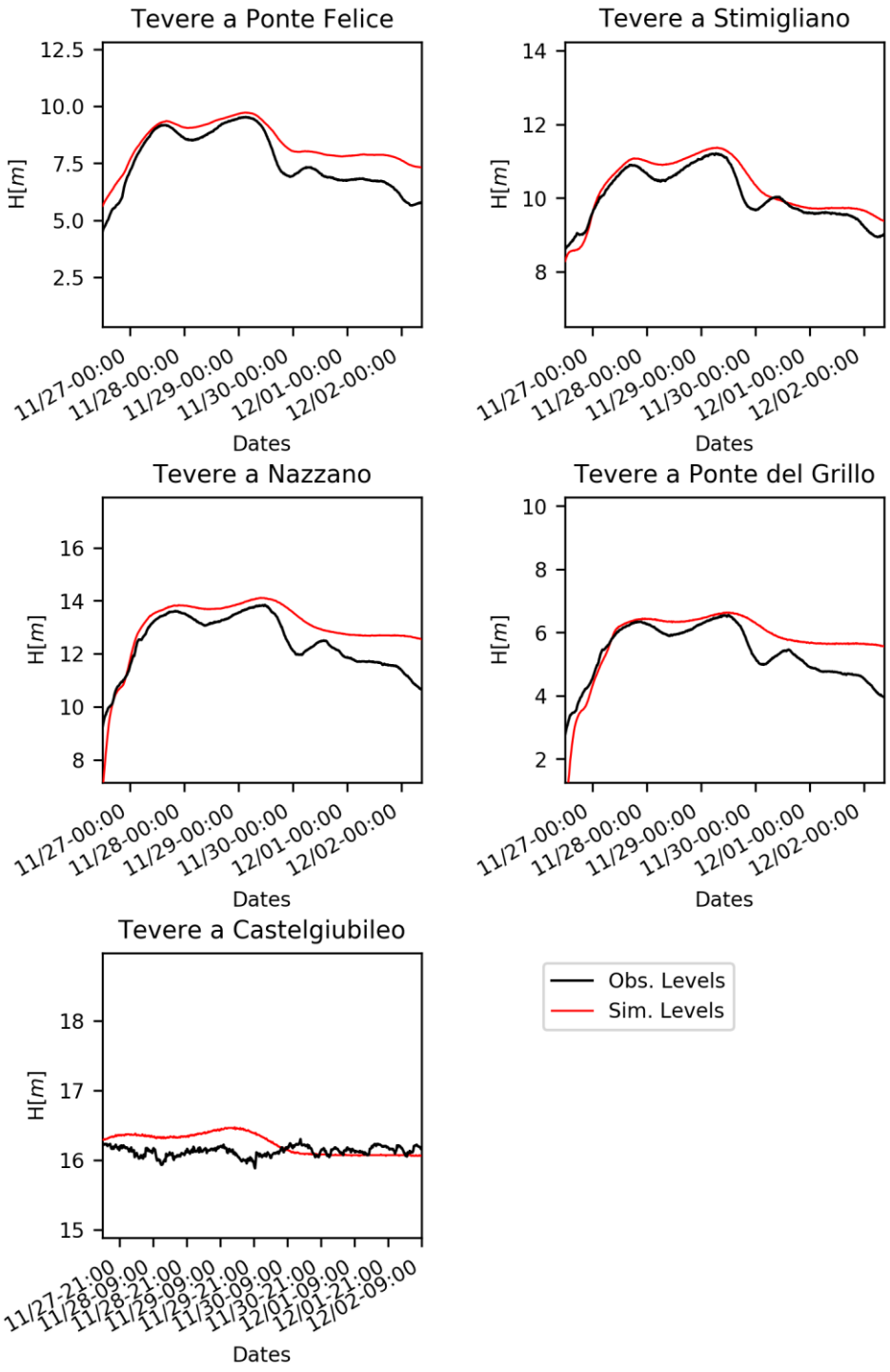

Figure 40. Comparison between the observed flow depths for each control station and the simulated ones.. Event: November 2005

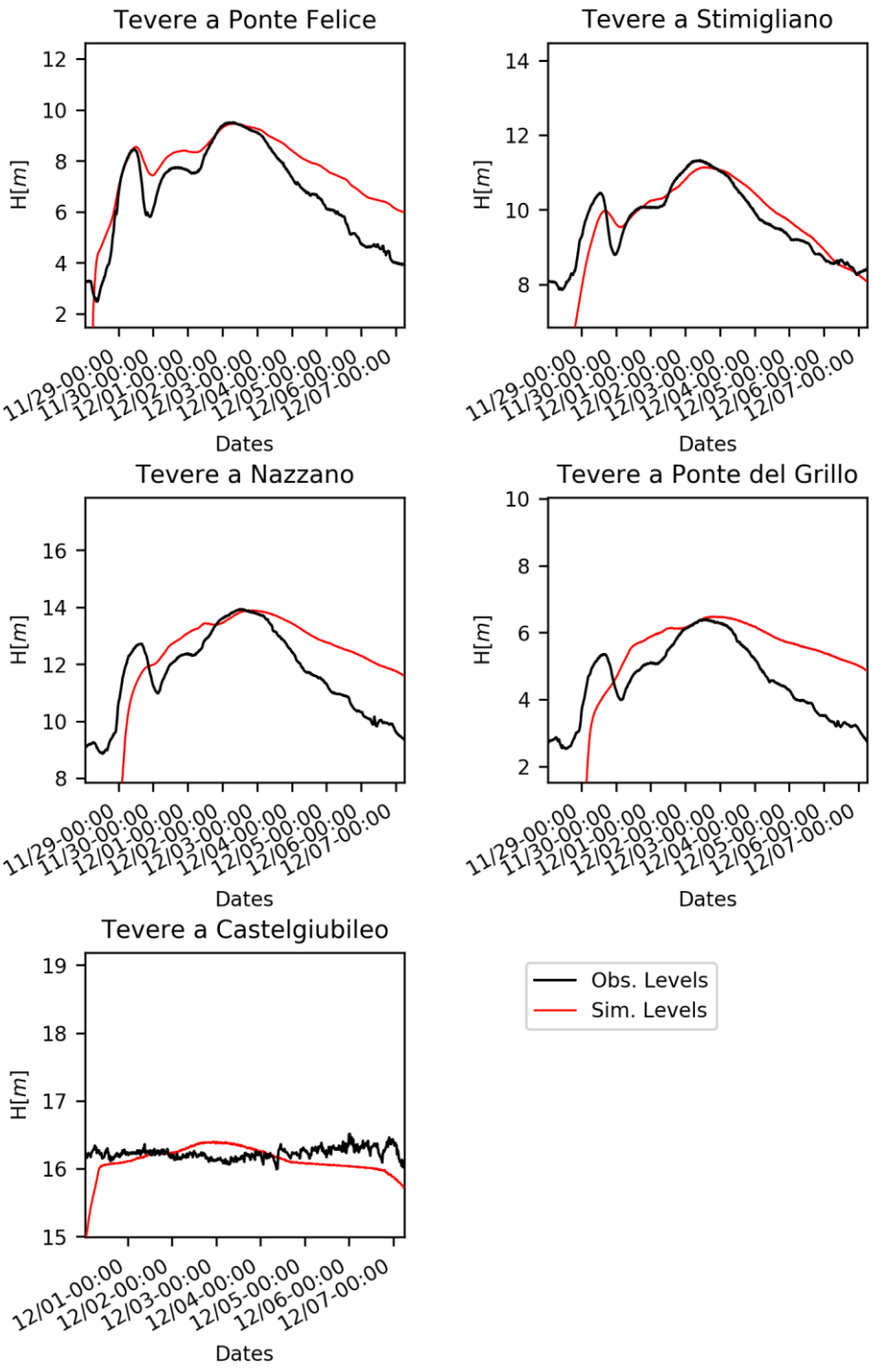

Figure 41. Comparison between the observed flow depths for each control station and the simulated ones. Event: November 2010

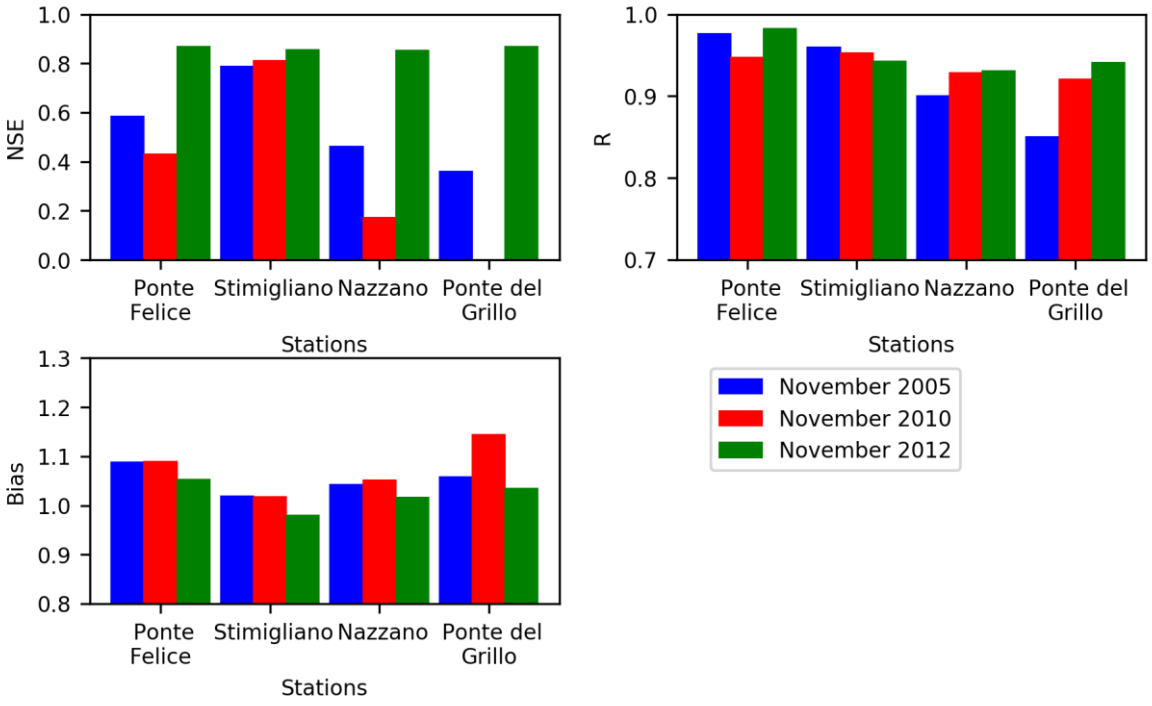

Figure 42. Performance indexes (NSE, R, Bias) for the hydraulic model for the three analysed flood events in each gage station

Figure 43. View of Castel Giubileo weir in a 3D reconstruction from satellite. Source: Google Earth

3.5.

3.6. The Data Assimilation method

3.6.1. Model theory

Hydrological and hydraulic models need input variables that can be estimated from other models, requiring variables and parameters, or directly measured. Typically, parameters are considered constant with time, while state variables may vary in time. The model outputs, i.e. discharge, water levels an flow velocities for hydrologic and hydraulic models, are measurable and these measurements can be used for updating the models when are available, applying Data Assimilation (DA, Refsgaard, 1997). As anticipated in Section 1.4, DA methods can be used for:

- Updating the input variables of the model, thus reducing the uncertainties related to their values, e.g. the rainfall for hydrologic models or the flow for hydraulic models.
- Updating a state variable forecasted by the model, e.g. the soil moisture for an hydraulic model.
- Updating the model parameters. This case is less common than the other ones because, especially in extreme events that have relatively short duration, model parameters remain reasonably constant and recalibrating the model at every time step has no real advantages (Kachroo, 1992).
- Updating the output variables, namely the flow or the water levels for hydrologic and hydraulic models.

In this work, the Ensemble Kalman Filter method (Evensen, 2003) is applied to a forecasting Quasi-2D hydraulic model. This methodology revealed to be very effective for strong non-linear dynamics and for this reason has been widely used in literature.

According to Jazwinski (2007), a generic non-linear stochastic-dynamic system can be expressed as:

$$x_{t+1} = M(x_t, I_t, \theta) + w_t \qquad w_t \sim N(0, S_t^m) \qquad [26]$$

where x_{t+1} and x_t are n-dimensional vectors representing the system state variables respectively at time $t+1$ and t. The non linear function $M(\dots)$ is the forecasting model that contains the state variable at the previous time step x_t, the deterministic forcing data I_t and the time-invariant model parameters θ. w_t is the model error, that usually is state dependent and it

has a random distribution with 0 mean and variance S_t^m representing all the model uncertainties. If a set of observations y_{t+1} is taken at time $t+1$, these can be assimilated into the model. The observations can be expressed as:

$$y_{t+1} = H(x_{t+1}, \theta) + v_{t+1} \qquad v_{t+1} \sim N(0, R_t^y) \qquad [27]$$

where $H(...)$ is a propagator that related the state variables to the measured variables and provides the expected value of the output given the model state and parameters. v_{t+1} is the sample of the observation errors, assumed having a random normal distribution with zero mean and variance R_t^y, usually considered time dependent.

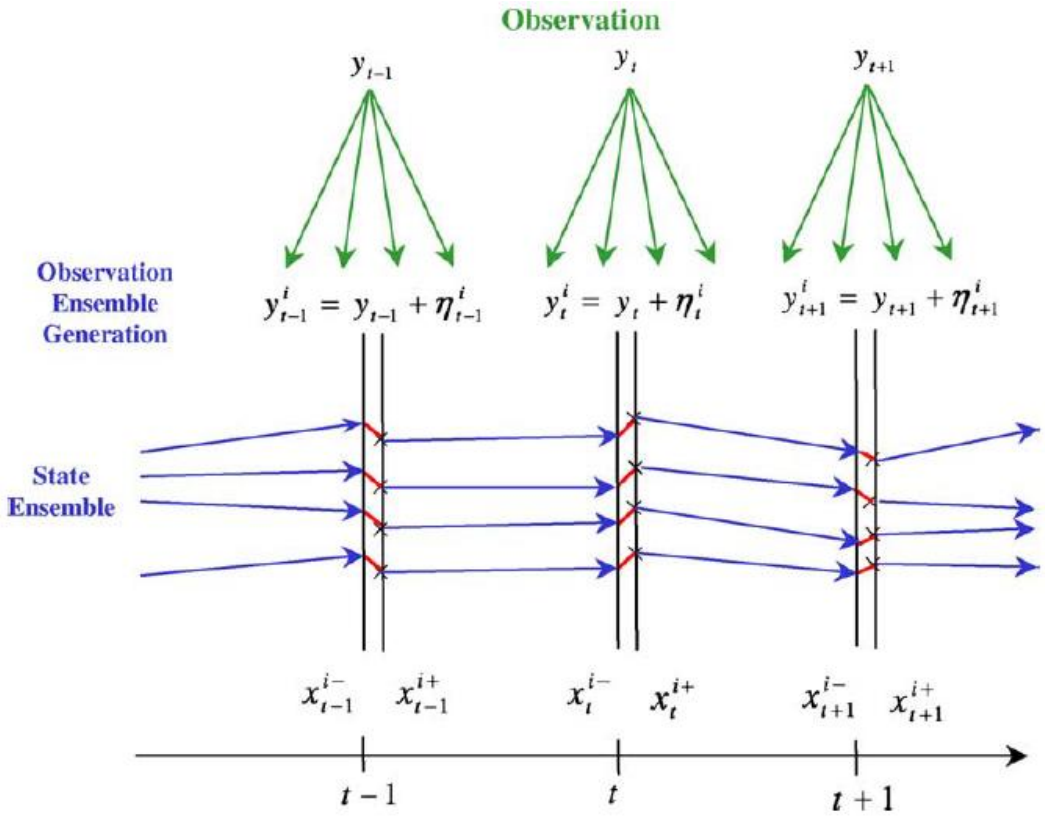

Figure 44. Scheme of the Ensemble Kalman Filter. Source: Moradkhani et al., 2005a

The EnKF model is a sequential DA method that estimates the model state based on the observations at each time step they are available. The method is based on ensemble generations: the forecast (a priori) state error covariance matrix is approximated propagating the ensemble of the model states, characterized by the aforementioned errors, from the previous time step; at the same time, an ensemble of observations at each update time is generated according to their error distribution introducing the noise term v_{t+1}. The DA process is characterized by two steps: the forecast step and the updated step, whose variables will be represented respectively

with the apex $-$ for forecasting and $+$ for updating (See Figure 44). The updated probability density function (*pdf*) of the model states is given by a combination between data likelihood and forecasted *pdf* of the model states by means of Bayesian update.

According to Equation [26], the state variable $x_{t+1}^{i-}$of forecast model in the EnKF, for the *i*-element of the ensemble at time $t+1$ can be expressed as:

$$x_{t+1}^{i-} = M\left(x_t^{i+}, I_t^i, \theta_i, t\right) + w_t^i \qquad i = 1, \dots, n \qquad [28]$$

where x_t^{i+} is the i^{th} updated ensemble member at time t, w_t^i is the model error of the i^{th} ensemble member, generated randomly as showed in Equation [26]; The forcing input I_t^i and the parameters θ_i of the i^{th} ensemble member are generated starting from the deterministic value and adding a random normal error with zero mean and a certain variance, namely $I_t^i = I_t + N(0, S_t^I)$ and $\theta_i = \theta + N\left(0, S^\theta\right)$.

Assuming that the true state variables are known, the error covariance matrix associated to the forecasted estimation would be:

$$P_{t+1}^- = E[(x_{t+1}^- - x_{t+1}^{true})\,(x_{t+1}^- - x_{t+1}^{true})^T] \qquad [29]$$

However, the true state is generally unknown, otherwise the DA method would not be needed. Therefore, the ensemble covariance matrix can be calculated (Evensen, 2003):

$$P_{t+1}^- = \frac{1}{n-1} X_{t+1} X_{t+1}^T \qquad [30]$$

Where:

$$X_{t+1} = [x_{t+1}^{1-} - \bar{x}_{t+1}^-, x_{t+1}^{2-} - \bar{x}_{t+1}^-, \dots, x_{t+1}^{n-} - \bar{x}_{t+1}^-] \qquad [31]$$

is the ensemble anomaly (Clark et al., 2008) for each ensemble member at time $t+1$ and

$$\bar{x}_{t+1}^- = \frac{1}{n} \sum_{i=1}^{n} x_{t+1}^{i-} \qquad [32]$$

is the ensemble mean of the forecasted matrix at time $t+1$.

From the *a priori* estimate of the state variable $\bar{x}_{t+1}^-$, the posterior estimate $\bar{x}_{t+1}^+$ is calculated using the observation y_{t+1} performing a linear correction with the Kalman filter to the forecasted state ensemble members:

$$x_{t+1}^{i+} = x_{t+1}^{i-} + K_{t+1}\left(y_{t+1}^{i} - \hat{y}_{t+1}^{i}\right) \quad [33]$$

where $y_{t+1}^{i}$is the perturbed observation for the i^{th} ensemble member adding to the observation y_{t+1} a noise η_{t+1}^{i}as follows:

$$y_{t+1}^{i} = y_{t+1} + \eta_{t+1}^{i} \qquad \eta_{t+1}^{i} \sim N\left(0, R_{t+1}^{y}\right) \quad [34]$$

The observation for the i^{th} ensemble member is generated as a random variable with a mean equal to the actual observation at time $t+1$ and a variance with a predefined value dependent on the degree of accuracy assigned to the actual observation at the same time step.

The term K_{t+1} is the Kalman gain matrix, expressed as :

$$K_{t+1} = \frac{P_{t+1}^{-} H^{T}}{H P_{t+1}^{-} H^{T} + R_{t+1}^{y}} \quad [35]$$

Where P_{t+1}^{-} is the ensemble covariance matrix expressed in Equation [30], H is the observation transition operation introduced in Equation [27] and R_{t+1}^{y} is the variance of the observation error.

The updated covariance matrix can be expressed as:

$$P_{t+1}^{+} = P_{t+1}^{-} - K_{t+1} H P_{t+1}^{-} \quad [36]$$

3.6.2. Choice of the ensemble size

The performance of the ensemble forecast is influenced by the spread of the ensemble (Murphy, 1988; Anderson, 2001) but also by the ensemble size, that has to be enough big to represent a statistically significant sample, but at the same time it has to impact the computational efficiency of the model in an acceptable way considering the purpose of the application (e.g. real time or near-real time forecasting).

In this work, the approach proposed by Anderson (2001) for determining the ensemble size has been chosen. This approach has been adopted by several researchers, such as Moradkhani et al. (2005a) and Brocca et al. (2012) among others. The author indicated that, in order to have an ideal spread of the ensemble, the ensemble size has to be so as to bring closer to 1 the Normalized RMSE Ratio (NRR):

$$NRR = \frac{R_a}{E[R_a]} \quad [37]$$

where R_a is given by:

$$R_a = \frac{R_1}{R_2} \quad [38]$$

namely the ratio between the time-averaged root mean square error (RMSE) of the ensemble mean R_1 and the time-averaged mean RMSE of the ensemble members R_2:

$$R_1 = \frac{1}{T}\sum_{t=1}^{T}\sqrt{\left[\left(\frac{1}{n}\sum_{i=1}^{n}\hat{y}_t^i\right) - y_t^i\right]^2} \quad [39]$$

$$R_2 = \frac{1}{n}\sum_{i=1}^{n}\sqrt{\frac{1}{T}\sum_{t=1}^{T}\left(\hat{y}_t^i - y_t^i\right)^2} \quad [40]$$

Where n and T are the ensemble size and the period of the analysis respectively. If the actual observation is statistically indistinguishable from n ensemble members, the expected value of the RMSE ratio, as illustrated by Murphy (1988) and Anderson (2001) can be expressed as:

$$E[R_a] = \sqrt{\frac{(n+1)}{2n}} \quad [41]$$

If $NRR > 1$, the ensemble has too little spread, while if $NRR < 1$ the ensemble has too much spread.

3.6.3. Application

In the present work, the EnKF model is applied to a Quasi-2D hydraulic model, forced by flow hydrographs given by both stage gages measurements and simulations of an hydrological model for small ungauged basins. In this case, the state variable x_t is considered as the water depth in a specific point of the computational domain. In case the observation is a stage gage measurement, the spatial position of the state variable is located in the closest channel cell of the domain to the position of the stage gage. In case of an observation coming from a flood extension gathered from a satellite image, the EnKF method have to be applied to both the channel and the floodplain cells interested by the observation. In case of a crowdsourced

information, namely a photo from which gathering the water depth or a description of the depth from a user, the state variable can be located in the channel, but more likely in the floodplain, where people usually could come across a flood event. The non-linear function $M(...)$ introduced in Equation [26] is the hydraulic model engine, whose forcing term I_t is the ensemble of the flow hydrographs and the parameters θ are mainly the channel and floodplain roughness. The model error w_t is estimated considering the uncertainties related by the input forcing I_t and the model parameters. The uncertainties related to the input forcing are different if the input is given using a rating table for converting the stage gage measurement to flow or from the output of an hydrologic model. Specifically, an analysis of the model errors is performed in Section 4.2. The observation y_t is a water depth value gathered directly (i.e. the stage gage) or indirectly (i.e. the satellite image and VGI) by the sensor. For this reason, the observation transition operation H introduced in Equation [27] is an identity matrix, being a direct relation between state variable and observation. The perturbation v_t to be assigned to the observation ensemble is strongly dependent on the nature of the observation, and will be extensively described in Sections 4.3.2, 4.4.3, 4.5.3, dedicated to each type of observation.

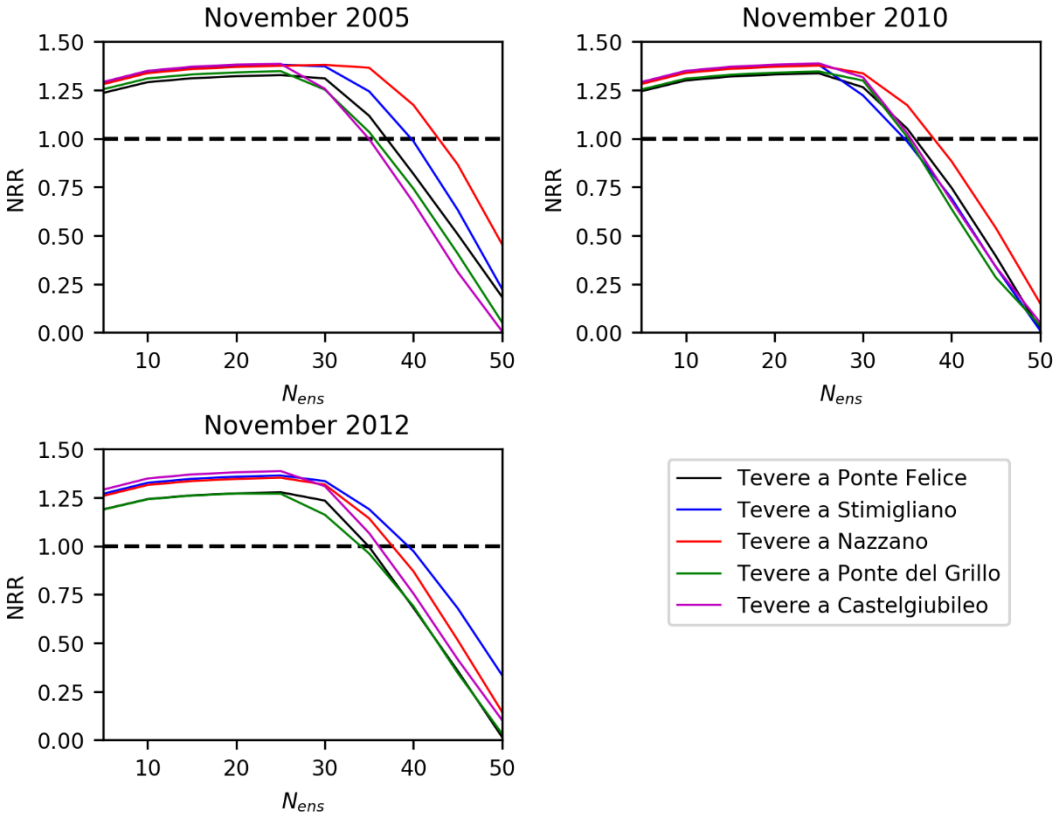

Figure 45. Results of the Normalized RMSE Ratio (NRR) for the three events and different gage stations to calculate the optimal value of the ensemble size (N_{ens})

As illustrated in Section 3.6.2, the ensemble size for the EnKF application has been chosen applying the Anderson (2001) approach for evaluating the similarity of truth versus randomly selected members of the ensemble (See Eq.[37]-[41]). The results illustrated in Figure 45, show the optimal ensemble sizes for the different stage gages, reached where the Normalized RMSE Ratio is equal to one, stay between 35 and 40. In this work, an ensemble size of 40 has been chosen for each simulation.

3.7. Flood detection from satellite imagery

As introduced in Section 1.2, the water detection procedure from satellite imagery can be performed starting from SAR or multispectral data. Usually SAR imagery are more suitable for flood model validation, because of their ability to penetrate the clouds and their no sensitivity to light. Furthermore, their potential resolution, can be much higher (e.g. 1-5 m) than the one of the Multispectral images (30 m). Several methodologies for flood detection from SAR and multispectral images have been proposed in literature and have been already listed in Section 1.2. In this section, a standard procedure for detecting flood from SAR images is illustrated. Moreover, some different techniques for detecting water from multispectral images, are tested considering three floods already detected in different parts of the world. One the illustrated techniques is adopted for detecting the water extension in the case study of this work.

3.7.1. SAR images

For SAR images, besides the commercial platforms for manipulating the products (e.g. the ENVI software), many scripts and GIS tools are available online. One of the most comprehensive and reliable free platform is the ESA's *Sentinel Application Platform* (*SNAP*). Starting from the raw satellite image, the platform allow to detect the water extension through the following steps:

- Radiometric calibration;
- Speckle filtering;
- Binarization, in which a threshold value for backscatter coefficient is required for discriminating water from non-water pixels;
- Geometric correction to re-project the image from the geometry of the sensor to the geographic correction

3.7.2. Multispectral images

3.7.2.1. Preliminary testing of the water indexes

All the water detection techniques from multispectral images are usually validated for water bodies not during flood periods, where clouds does not compromise the bands of the image. In this work, a further inspection of the most common and also recent water detection algorithms where tested in few flood case studies where image were not totally compromised by clouds and at the same time the correspondent delineated water extent were available. A consistent analysis for testing these indexes would require a statistically significant sample of different

images, but the simultaneous occurrence of having both a multispectral image not compromised by clouds during a flood event and the availability of a delineated water extension from another source is still quite rare. For this reason, this analysis can be considered a preliminary test without pretending to determine the best indexes with adequate statistical confidence. Table 10 shows the indexes considered for detecting the water extension.

Index	*Name*	*Source*	*Equation*	
AWEISH	Automated Water Extraction Index shadow	Feyisa et al., 2014	$\rho_{b1} + 2.5 \cdot \rho_{b2} - 1.5(\rho_{b4} + \rho_{b5}) - 0.25\ \rho_{b7}$	[42]
AWEINSH	Automated Water Extraction Index non shadow	Feyisa et al., 2014	$4 \cdot (\rho_{b2} - \rho_{b5}) - 0.25(\rho_{b4} + 2.75 \cdot \rho_{b7})$	[43]
MDWI	Modified Normalized Difference Water Index	Xu, 2006	$(\rho_{b2} - \rho_{b5})/(\rho_{b2} + \rho_{b5})$	[44]
NDMI	Normalized Difference Moisture Index	Wilson & Sader, 2002	$(\rho_{b4} - \rho_{b5})/(\rho_{b4} + \rho_{b5})$	[45]
NDVI	Normalized Difference Vegetation Index	Rouse et al. 1973	$(\rho_{b4} - \rho_{b3})/(\rho_{b4} + \rho_{b3})$	[46]
NDWI	Normalized Difference Water Index	McFeeters, 1996	$(\rho_{b2} - \rho_{b4})/(\rho_{b2} + \rho_{b4})$	[47]
TCW	Tasselled Cap Wetness	Crist, 1985	$0.0315 \cdot \rho_{b1} + 0.2021 \cdot \rho_{b2} + 0.3102 \cdot \rho_{b3} + 0.1594 \cdot \rho_{b4} - 0.6806 \cdot \rho_{b5} - 0.6109\ \rho_{b7}$	[48]
WI1	Water Index	Fisher et al., 2016	$1.7204 + 171 \cdot \rho_{b2} + 3 \cdot \rho_{b3} - 70 \cdot \rho_{b4} - 45 \cdot \rho_{b5} - 71\ \rho_{b7}$	[49]
WRI	Water Ratio Index	Shen & Li, 2010	$(\rho_{b2} + \rho_{b3})/(\rho_{b4} + \rho_{b5})$	[50]

Table 10. List of indexes adopted for the water detection testing from multispectral images. Inputs are surface reflectance (ρ) for each band (b1–b7)

All the indexes are designed for water extraction, with the exception of NDVI and NDMI whose purpose is respectively vegetation and soil moisture classification, but are taken in to account because they are also commonly used for water classification.

Landsat Mission	*Country*	*Time*	*Reference map*	*Delay between SAR image and Landsat Image*
L5	Angola	26/03/2008	DMC (25/03/2008)	1 day
L5	Namibia	19/03/2009	ASAR (17/03/2009)	2 days
L8	Pakistan	17/09/2014	TerraSar-X (15/09/2014)	2 days

Table 11. Landast images analysed for testing the water indexes

As reference map for the indexes comparison, a database of flood maps from the UNOSAT Website has been considered (http://floods.unosat.org/).

These maps are delineated detecting the water extension from SAR imagery generated by different missions (e.g. TerraSAR-X, Radarsat-1, ALOS-1, Worldview, Komsat, Pleiades, ASAR, RISAT, DMC). Figure 46 shows the Landsat look of the three images taken into account for flood mapping. It is evident that the clouds partially compromise the images. These cloudy areas have been masked from the computational domain.

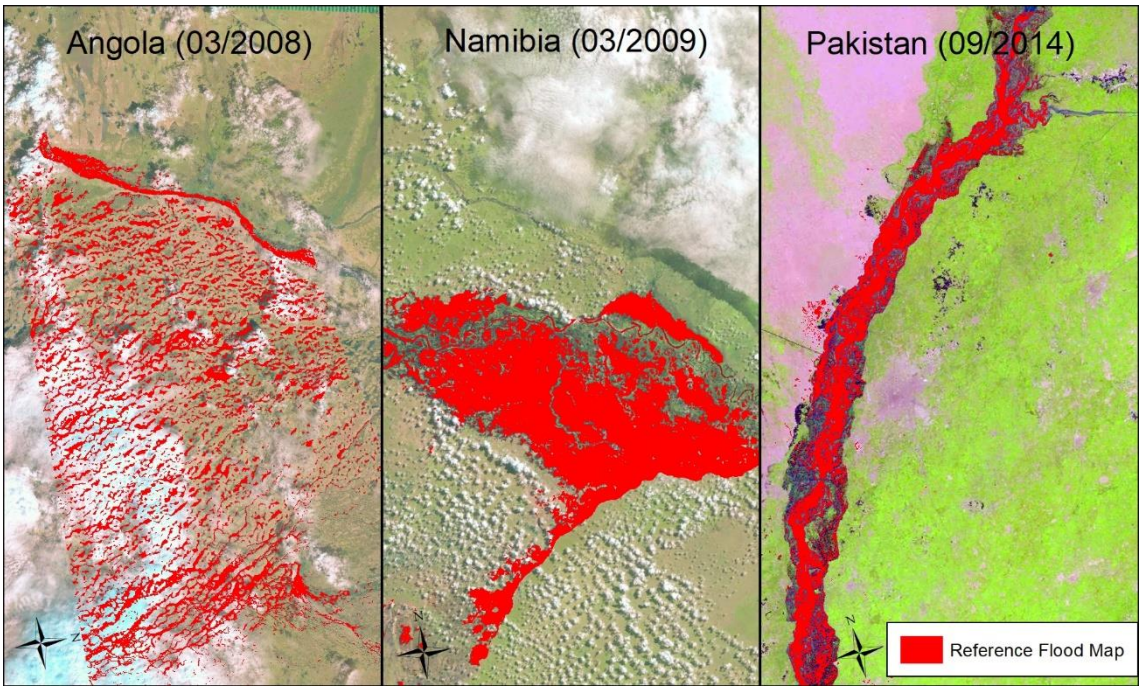

Figure 46- Representation of the three reference maps and the relative Landsat Look

The three images have been pre-processed for atmospheric and radiometric correction. Each index has been reclassified into different intervals. Considering the upper value of each interval as a threshold value for water classification, the number of true positives (TP) (cells considered flooded in the reference map and in the index), false positive FP (cells overpredicted by the index) and false negatives FN (cells underpedicted by the index) have been calculated. As spatial comparison index, Equation [6] (Horrit & Bates, 2001) has been adopted, and here shown (A=TB, B=FN, C=FN):

$$F = \frac{TP}{TP + FP + FN} \qquad [51]$$

Figure 47 shows the optimum threshold value obtained according to the measurement function *F* for the Angola case study. All the threshold values have to be considered as the minimum value of each index for water classification with the exception of NDVI for which all their values below the threshold have to be considered as water.

Figure 48 compares the 9 indexes using the measurement function *F*, the True positives, the false positives and the false negatives rates. The results are also illustrated in Table 12. Overall, the best performance indexes are the most recent ones, namely AWEISH, MNDWI, WI and WRI.

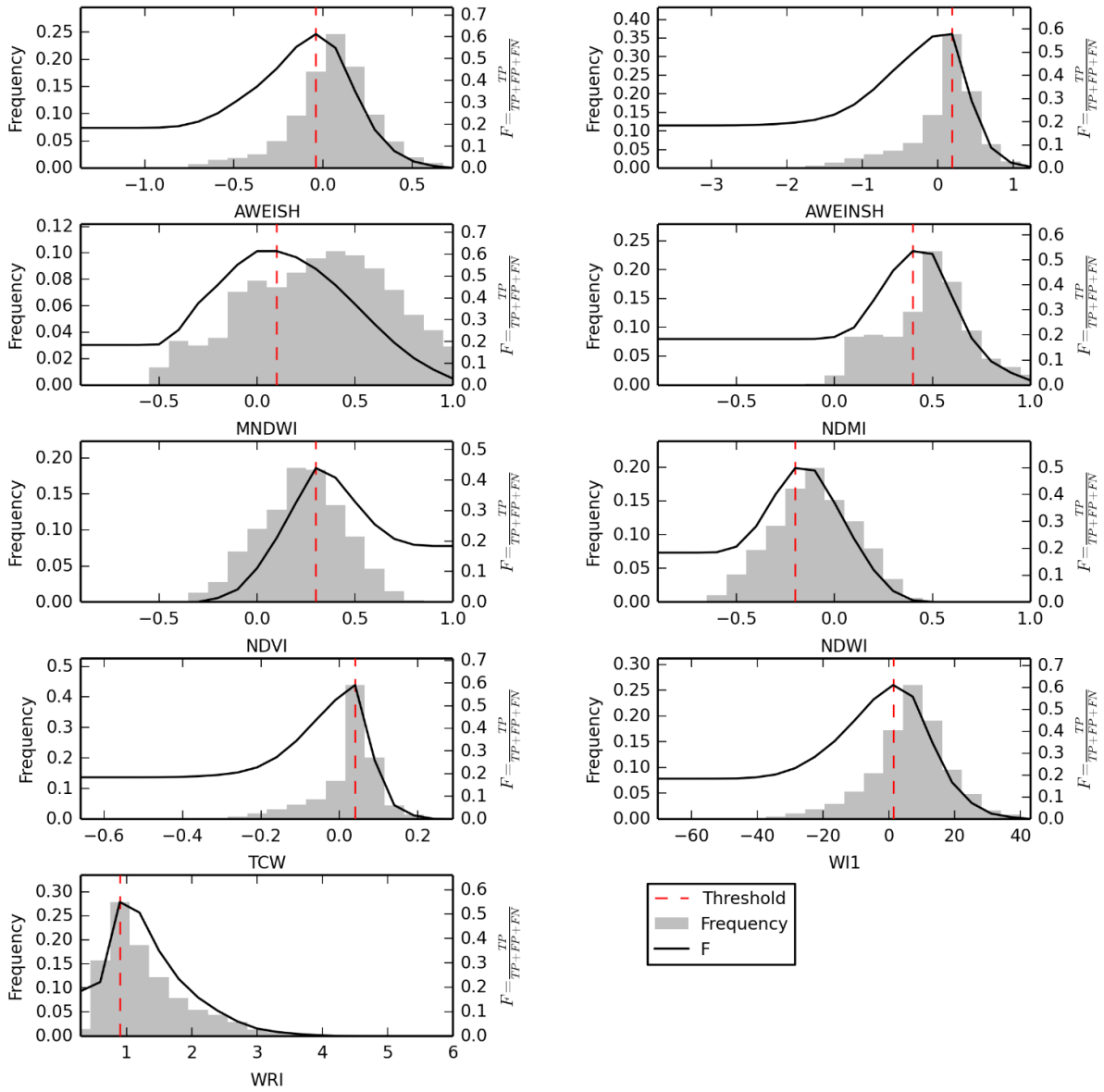

Figure 47. Automatic selection of the threshold value for water classification for each index. Plots of the frequencies of true positives values [%] and the measurement function F (Angola case study)

In Figure 49, False Positives (FP) and False Negatives (FN) of the Angola case study are highlighted in a detail of the domain. Some of the FP ad FN are in the borders of the flooded areas. These errors can partially due to the shadows of the ponds and also to a small change in extension of these ponds during the time between the Landsat and the reference map acquisitions.

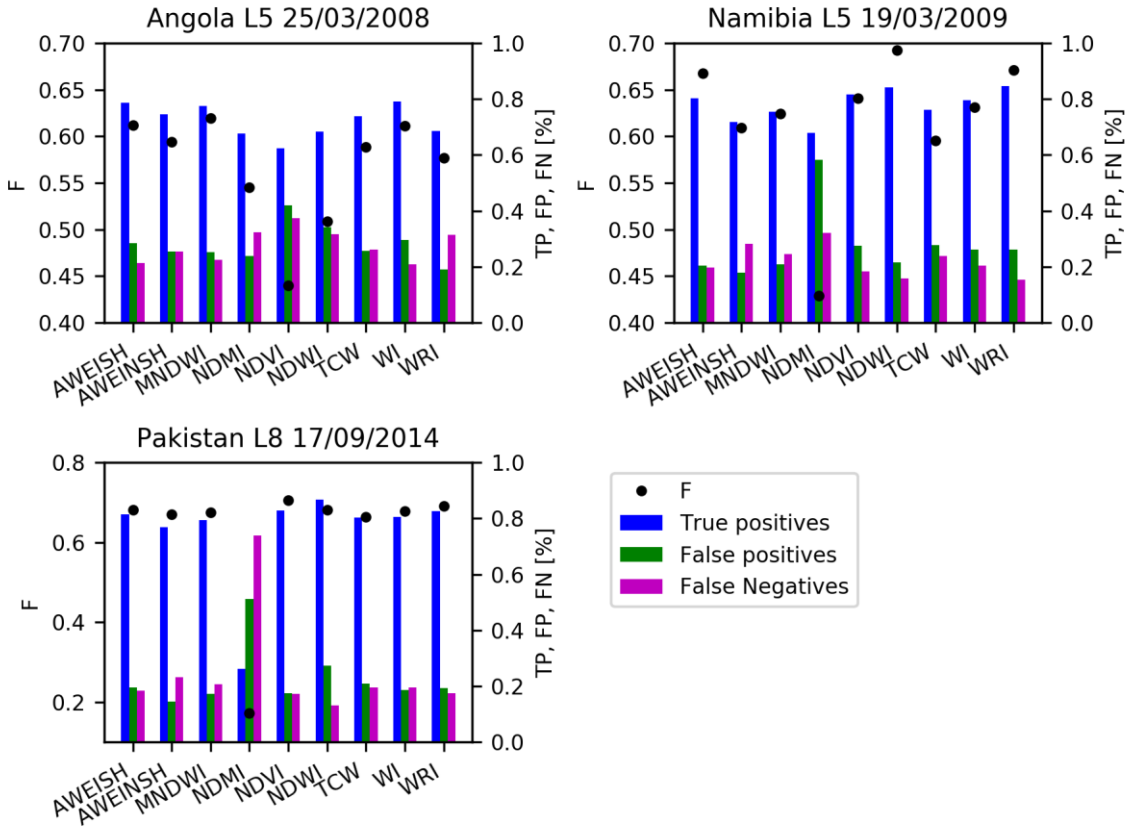

Figure 48. Comparison of the performance for each index for Angola, Namibia and Pakistan Landsat.

Index	*F value*			
	Angola	*Namibia*	*Pakistan*	*Mean*
AWEISH	0.612	0.667	0.682	**0.654**
AWEINSH	0.594	0.609	0.67	0.624
MNDWI	0.62	0.624	0.676	**0.64**
NDMI	0.545	0.429	0.173	0.382
NDVI	0.44	0.641	0.705	0.595
NDWI	0.509	0.693	0.681	0.628
TCW	0.588	0.596	0.664	0.616
WI	0.611	0.631	0.678	**0.64**
WRI	0.577	0.671	0.692	**0.647**

Table 12. Values of F for the three case studies

The most recent indexes designed for water detection in literature (Feyisa et al. 2014, Fisher et al., 2016) consider the reflectance of NIR (ρ_{b4}), SWIR 1 (ρ_{b5}) and SWIR 2(ρ_{b7}) but they do not

consider the thermal band that is affected by the colder temperature of the water bodies. In order to see the sensitivity of each band of the satellite image for different land uses, an analysis of the distribution of the Digital number of the bands have been performed.

The 2012 land use layer of the whole Europe with a 100 m resolution has been downloaded from the Copernicus Land Monitoring Service website (http://land.copernicus.eu/pan-european/corine-land-cover/clc-2012).

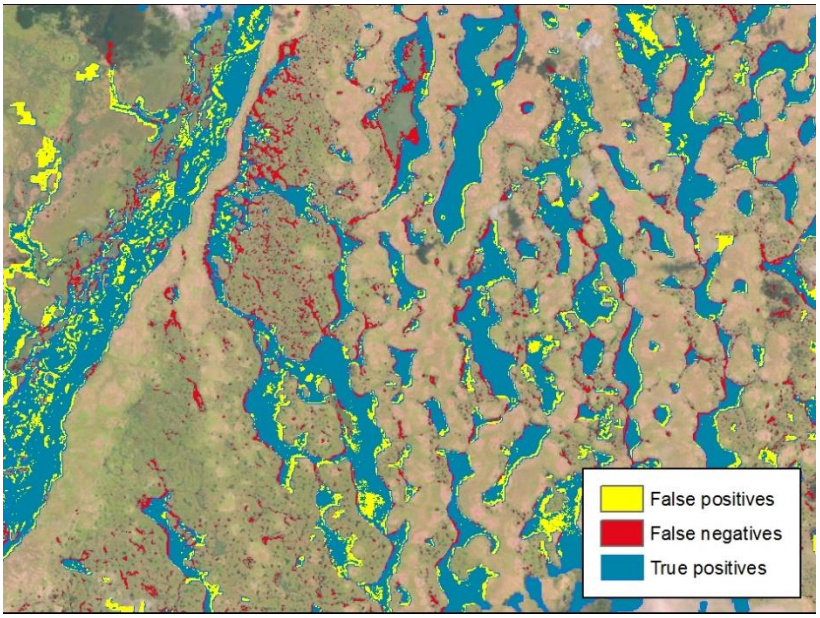

Figure 49. A detail of the flooded map from MNDWI with the True Positives (Blue), False Positives (Yellow), False Negatives (red) (Angola case study)

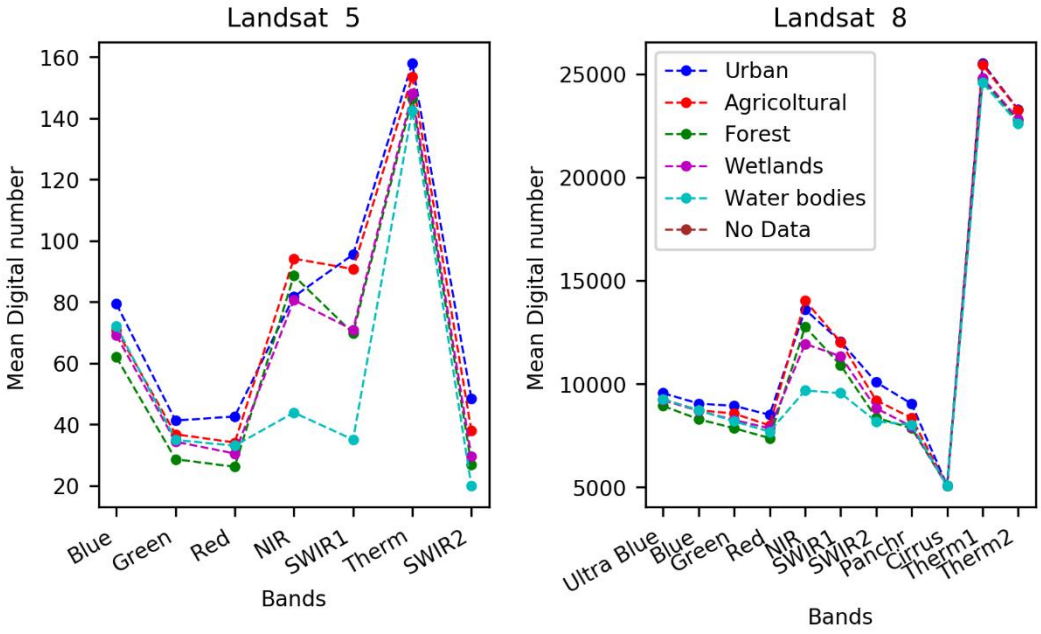

Figure 50. Values of mean digital number for each band in Landsat 5 and 8

This land cover is divided in 45 different land uses that have been resampled in 5 different macro categories, specifically: Urban areas, Agricultural areas, Forests, Wetlands and Water bodies. As first analysis, the Bosnia Erzegovina (affected by several floods in the past) has been taken in to account for evaluating the digital number values of the Landsat 5 and 8 Bands for the macro categories.

Both Landsat 5 and Landsat 8 (Figure 50) confirm that water surface absorbs Near Infrared (NIR), Short Wave Infrared 1 (SWIR1), Short Wave Infrared 2 (SWIR2) and the Thermal band(s) (THERM1 and THERM2 for L8) more than the other land uses. The major differences are given by the NIR and SWIR1 bands.

As future insight for improving the water index, the inclusion of the thermal band can be tested. In this work a methodology for a testing a new index is proposed. The most recent index, the Water Index (Feysa et al., 2016), has been considered as starting point for a formulation of a new index considering also the Thermal band. Specifically the new index can be considered as:

$$NEW_{WI} = WI - K \cdot DN_{therm} = 1.7204 + 171 \cdot \rho_{b2} + 3 \cdot \rho_{b3} - 70 \cdot \rho_{b4} - 45 \cdot \rho_{b5} - 71\,\rho_{b7} - K \cdot DN_{therm} \quad [52]$$

Where:

- **K** is a coefficient that have to be calibrated;
- $\boldsymbol{DN_{therm}}$ is the normalized digital number of the Thermal band (band 6 for the Landsat 5 or 7). In case of using the Landsat 8 imagery, both bands 10 and 11 can be considered.

The new index has been compared with the original WI (Feysa et al., 2016) varying the K coefficient in order to see potential improvements in its performance.

Specifically K has been varied between 10 and 80. The thermal band seems to have a slightly positive effect on the performance of the water detection (Figure 51): the optimum values are obtained for values of K between 30 and 40. Further inspections with a wider sample of images accompanied by their relative reference flood maps need to be performed.

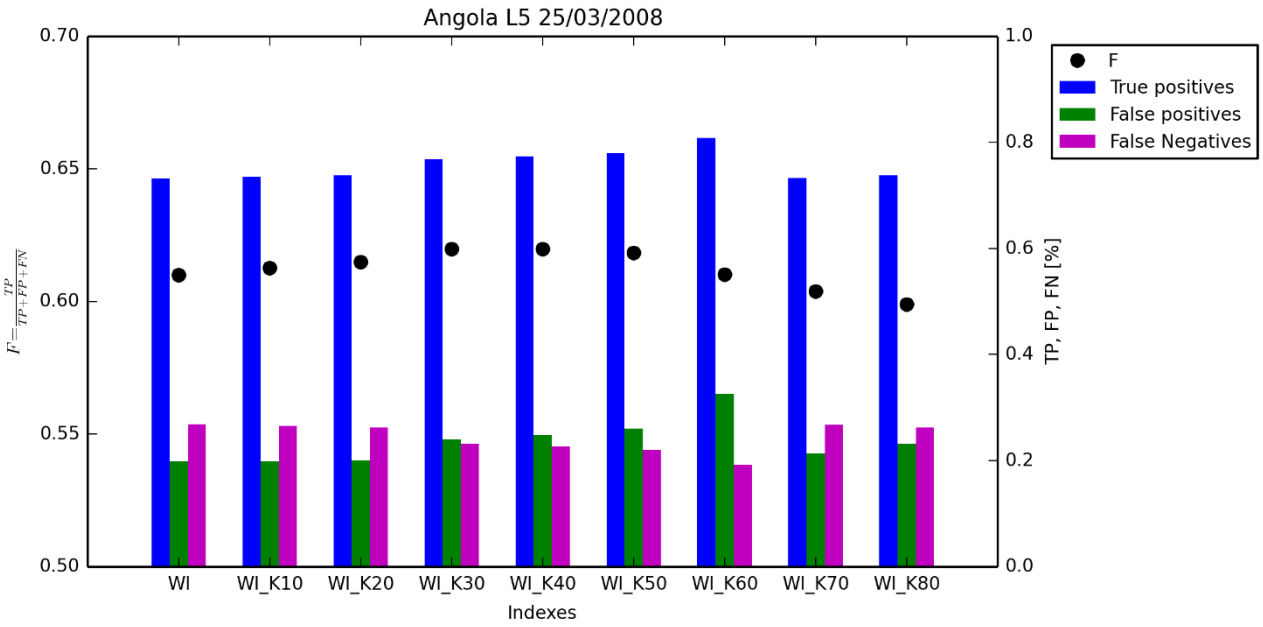

Figure 51 - Results for the F measurement function varying the value of the constant K for the thermal band

3.7.2.2. Application to the case study

For the case study of the Tiber river, the Landsat 7 image (acquisition date: 14/11/2012 - 09.43) has been used for extracting the flood extension using Equation [64] . Unfortunately, Landsat 7 products are affected by evident corruptions due to a failure of the Scan Line Corrector (SLC) in the satellite of that mission. For this reason, the water trace detected from the image is characterized by some empty stripes.

However, these stripes do not compromise the correct transversal extension of the flood, but only its continuity along the longitudinal direction of the flow. This can lead to lower values of the F measure to fit index when it is compared to the flood extensions given by other different models, but the relative difference of *F* among the maps of the models will be not affected. Figure 52 shows the extension of the detected flood. The extension of the detected flood raster has been clipped using the floodplain polygon described in Section 3.3. The water extension gathered from the SI will be compared with the ensemble of the flood extensions given by the hydraulic simulations in order to indirectly define the observed water levels used in the DA methodology. This procedure is illustrated in Section 4.4.

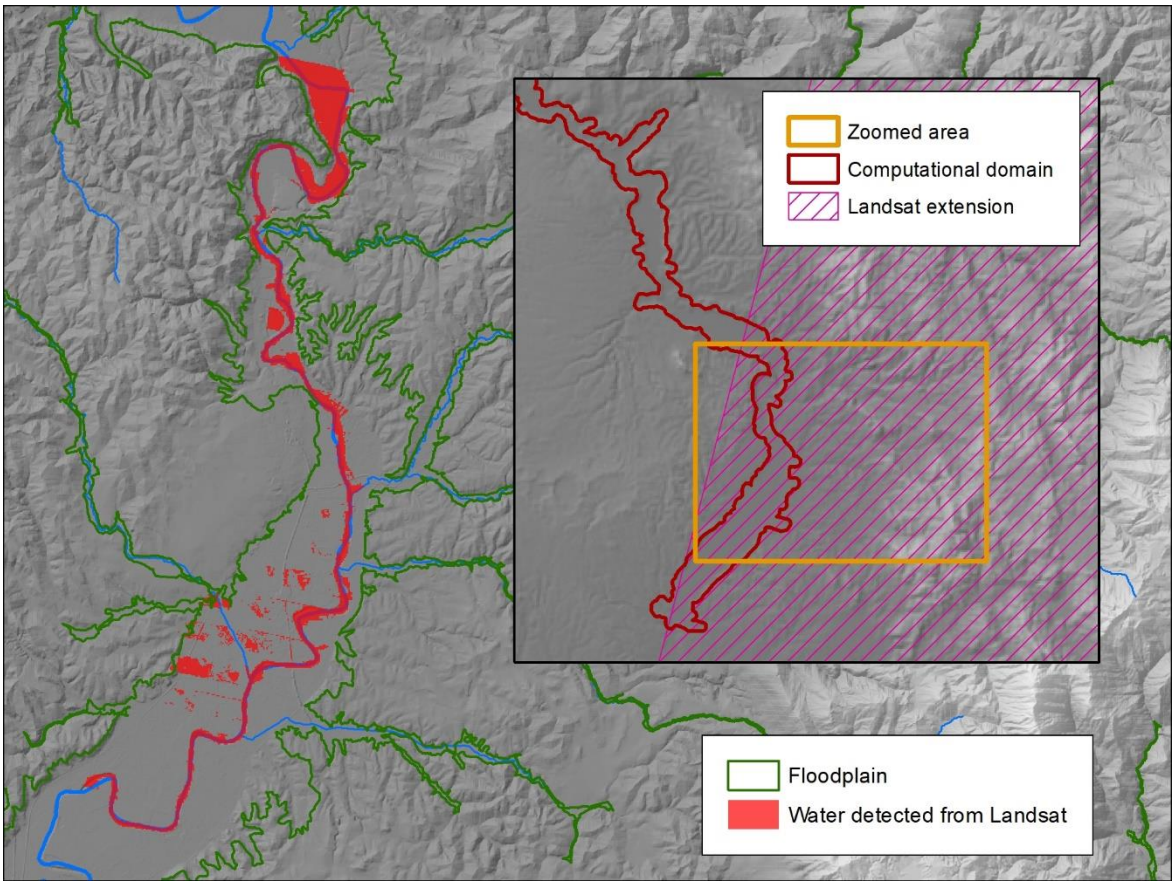

Figure 52. Extension of the water detected from the Landsat 7 image (acquisition date: 14/11/2012 - 09.43) in the computational hydraulic domain

4. Assimilation of different type of observed measurements in a Quasi-2D hydraulic model

This Chapter describes the application of the Data Assimilation methodology to the case study and illustrates the main results. Section 4.1 introduces the main issues and some literature related to the application of DA methodologies in case of 2D hydraulic models and also to the different types of observations used in the past for updating the hydrologic and hydraulic models.

Section 4.2 describes the model errors, due principally to its parametrization and its forcing inputs, given by the stage measurements and the hydrologic modelling.

Sections 4.3, 4.4 and 4.5 illustrate the adopted methodology for implementing the DA model respectively in case of Static sensors, Satellite images and VGI data, presenting the results obtained for each type of observations.

These observations are then integrated together and the related results are showed in Section 4.6.

4.1. Foreword

In the last years, DA has been increasingly implemented in hydraulic models for reducing the uncertainty in flood forecasting using both observed levels from in-situ sensors and also from remote sensed sensors (Schumann et al., 2009, Yan et al., 2015b).

There are few cases in literature of implementing the Data Assimilation methodology in a 2D hydraulic model (Kim et al., 2012, Kim et al., 2013). The reason is mainly due to the fact that 2D models are usually time consuming compared to 1D models, and DA procedures for non-linear systems require often simultaneous simulations (e.g. the Ensemble Kalman Filter) or operational research methods (e.g. the Variational methodology) for each time step the observation have to be assimilated. Furthermore, almost only the water depths from static sensors have been considered in the past as observation measurement to be assimilated for 2D hydraulic model, with the exception of Hostache et al. (2010) who adopted a satellite image in a DA framework for calibrating the floodplain roughness.

Mazzoleni et al., 2015, Mazzoleni et al., 2017 and Mazzoleni, 2017 investigated the assimilation of synthetic crowdsourced data in simplified hydrologic and hydraulic models.

The final aim of this chapter is investigating the use of static sensor measurements, satellite images and VGI data in large scale flood modelling in order to improve the results of the forecast model in potential data scarce regions. In fact, the limitations or the absence of observations coming from a specific sensor can be compensated by the contributions of the other types of observation. The proposed methodology deals with assimilating observations from punctual measurements from channel (Stage gages) and floodplain (VGI) locations and also from distributed measurements coming from satellite images. Therefore, the methodology can be also applied using other types of punctual or distributed measurements if their related error is known.

4.2. Model errors

The EnKF takes in to account the uncertainty related to the model errors through a realization of the model results, that in this case is generated perturbing:

1. the forcing input given by the static sensors and the hydrologic model;
2. the model parameters, namely the channel roughness expressed by the Manning values.

4.2.1. Error of the static sensor input

The uncertainty related to discharge observation is the sum of two different components (Clark et al., 2008): the estimation of the water level from the static sensor (EWL) and the transformation of the water level into discharge with the rating curve (ERC). Di Baldassarre and Montanari (2009) pointed that the uncertainty induced by the measurement of the river stage with a static physical sensor can be negligible, and for this reason, usually DA frameworks in hydrology consider only the uncertainty given by the errors related to the rating curve. Weerts and El Serafy (2006) proposed to represent the ensemble of the streamflow observations for representing their uncertainty as showed in the following equation:

$$Q^{o}{}_{StS,t,i} = Q^{true}{}_{StS,t} \cdot \gamma + \eta_{StS,t,i} \qquad [53]$$

Where $Q^{o}{}_{StS,t,i}$is the streamflow measure by the static sensor (StS) for the *i*-element of the ensemble at time *t*, γ is a parameter that accounts for the uncertain estimation of the synthetic discharge, $Q^{true}{}_{StS,t}$ is the streamflow observation from StS at time *t*, $\eta_{StS,t,i}$ is a noise term $N(0, R_{StS})$ normally distributed with zero mean and a given variance (R_{StS}) at time *t*, expressed as:

$$R_{StS} = \left(\alpha_{StS,t} \cdot Q^{true}{}_{StS,t}\right)^2 \qquad [54]$$

Where $\alpha_{StS,t}$ is the coefficient of variation related to the uncertainty in the discharge measurement. Equation [54] expresses the intuitive concept that high values of discharge should be more uncertain than the small values.

Weerts and El Serafy (2006), Clark et al. (2008) and Rakovec et al. (2012) considering the only component of the error given by the rating curve, assumed the variance $\alpha_{StS,t}$ equal to 0.1. However Mazzoleni et al. (2015) consider also a component due to the water level estimation by the static sensor adding a 0.02 value to the error given by the rating curve. If $Q^{true}{}_{StS}$ is assumed to be affected by bias, the γ parameter is considered a random uniform number

between -1.3 and +1.3 (Mazzoleni et al., 2015) for generating the ensemble of the observed streamflow. In the present work the value of $\alpha_{StS,t}$ as been chosen equal to 0.12 and the γ value equal to 1. Figure 53 shows the ensemble spread related to the Orte Scalo input in the upstream boundary of the hydraulic computational domain, applying the abovementioned perturbation for the three analysed flood events.

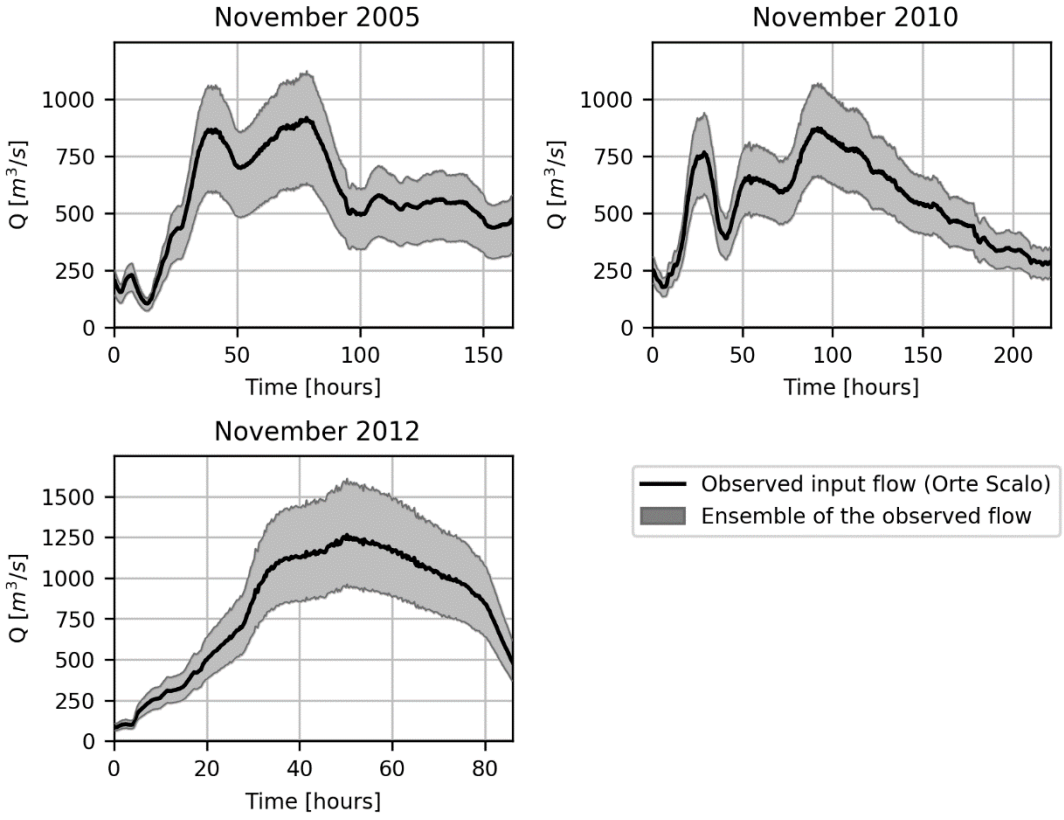

Figure 53. Representation of the ensemble of the flow observations from the upstream Static sensor (Orte Scalo)

4.2.2. Error of the input forcing from hydrologic model

The hydrologic model adopted to force the hydraulic model, is characterized by strong assumptions, given the small amount of available physic data and thus of the input variables. Several uncertainties affect the model results, as the measured rain and its distribution on the basin, the simplified modelling of the flow routing, the neglected physical process as the groundwater flow, the mud and debris flow, the antecedent soil moisture conditions. In particular, the latter affects dramatically the flow entity (Berthet et al., 2009), and, in case of the SCS-method application, it influences both the coefficient of initial abstraction and the CN values. From the validation of the hydrologic model (Section 3.1.3) an analysis of the simulated flow errors, considering the observed flows as the true ones, has been performed and showed in Figure 54. The left plot shows that the errors tend to spread more the more is the relative

observed flow. This confirms that usually, for a DA application in hydrologic and hydraulic models, the input flow errors are considered proportional to the relative value of the flow. The right plot of Figure 54 shows the frequency distribution of the relative flow errors, characterized by an almost zero mean and a standard deviation equal to 0.28.

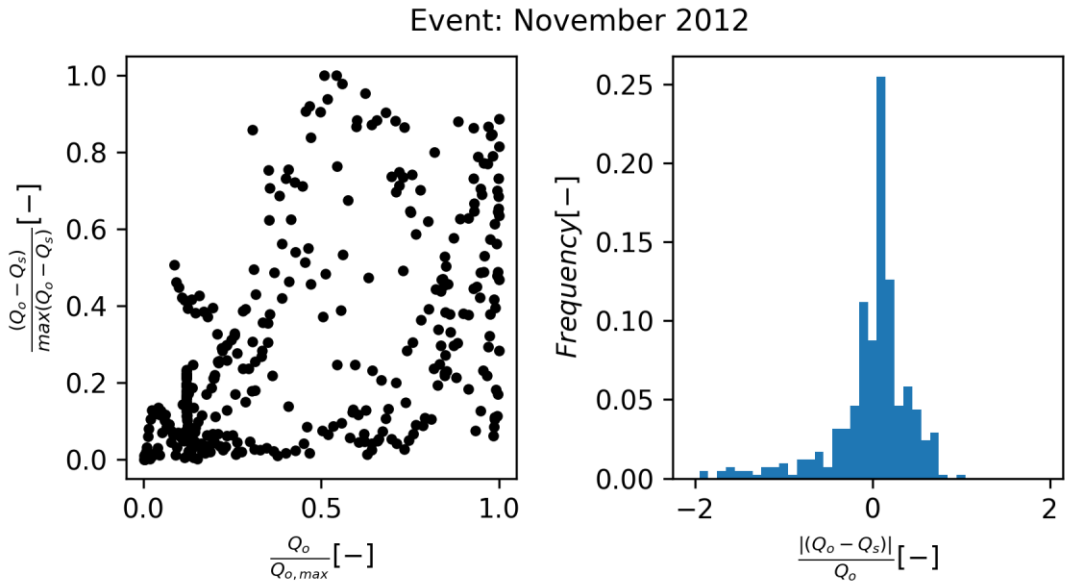

Figure 54. Relation among flow and estimation error between observed and simulated flow (left); Frequency distribution of the relative flow errors (right). Both graphs are referred to the validation of the hydrologic model (See Section 3.2.3)

The input forcing of an hydrologic or hydraulic model is sometimes perturbed adopting an uniform distribution (Clark et al., 2008; McMillan et al., 2013; Mazzoleni et al., 2015) as showed below:

$$Q^S{}_{I,t,i} = Q^S{}_{I,t} + U\left(-\varepsilon_I \cdot Q^S{}_{I,t}, +\varepsilon_I \cdot Q^S{}_{I,t}\right) \quad [55]$$

$Q^S{}_{I,t,i}$ is the perturbed simulated flow at time *t* for the i-element of the ensemble, $Q^S{}_{I,t}$ is the simulated flow at time *t*, U is the uniform distribution, is ε_I the fractional input error.

However, considering the distribution of the flow errors showed in Figure 54, the following perturbation has been adopted

$$Q^S{}_{I,t,i} = Q^S{}_{I,t} + N\left(0, R_{I,t}\right) \quad [56]$$

Where $N\left(0, R_{I,t}\right)$ is a noise term normally distributed with zero mean and the variance $(R_{I,t})$ at time *t*, expressed as:

$$R_{I,t} = \left(\alpha_I \cdot Q^S{}_{I,t}\right) \quad [57]$$

and α_I is the coefficient of variation related to the uncertainty in the simulated flow, in this case assumed equal to 0.3. Figure 55 shows the results of the perturbed simulated flow values for the November 2012 event.

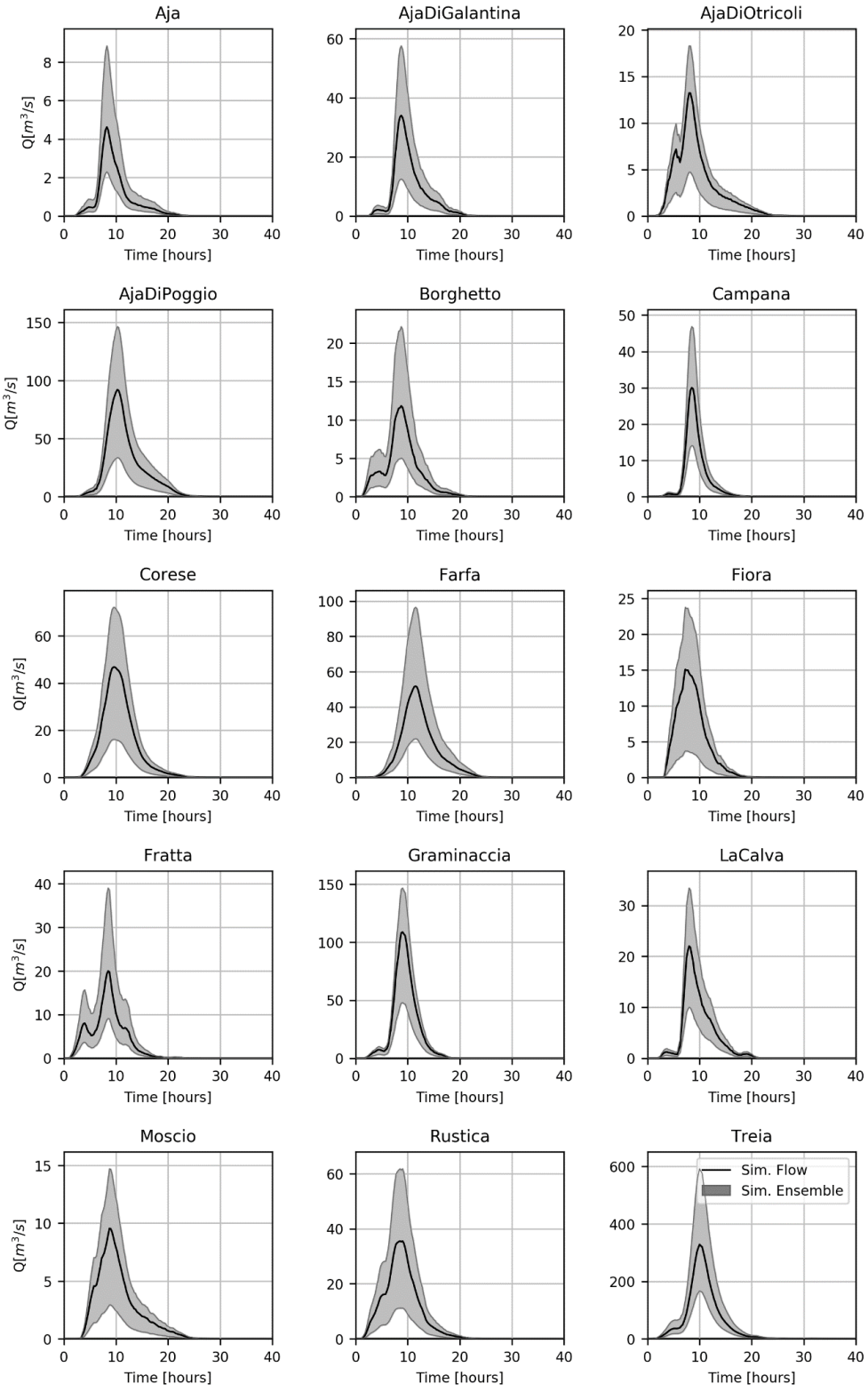

Figure 55. Perturbed simulated hydrograph considering the hydrologic model errors. Event: November 2012

4.2.3. Error of the model's parameter

The uncertainty related to the model parameters is considered as follows (Clark et al., 2008; McMillan et al., 2013):

$$p^s{}_i = p^s + U(-\varepsilon_P \cdot p^s, +\varepsilon_P \cdot p^s) \quad [58]$$

Where $p^s{}_i$ is the perturbed model parameter for the *i*-element of the ensemble, p^s is the model parameter and ε_P is the fractional parameter error. In this case, the channel roughness has been chosen as the perturbed parameter, and ε_P is assumed equal to 0.25. This limits the value Manning of the channel between 0.030 and 0.050 $m^{-1/3}s$.

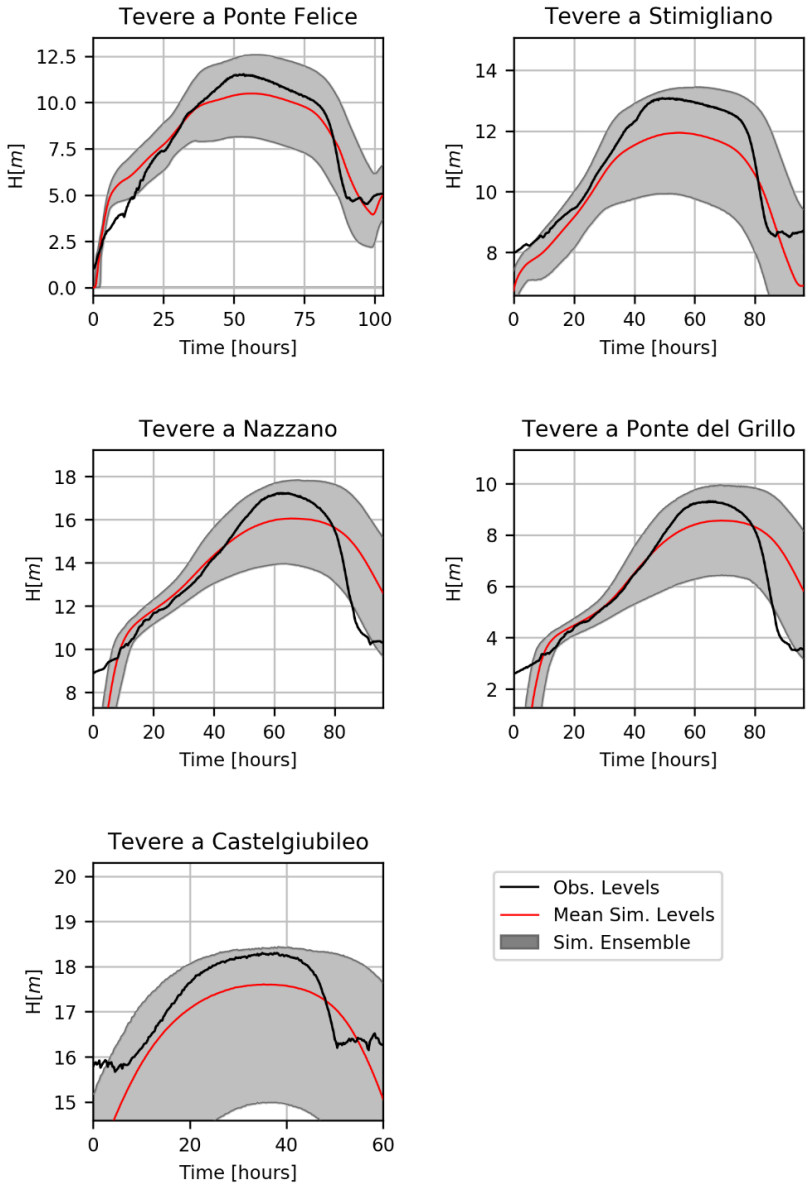

Figure 56. Observed water levels and the ensemble of the simulated ones by the hydraulic model considering the model and the input errors. Event: November 2012

The floodplain roughness has been considered a lower source of uncertainty because for most of the simulation time, the flow stays inside the channel and, during the peak flow, the flooding along the floodplain affects not the whole computational domain.

The ε_P value has been chosen considering that Manning values smaller than the correspondent lower limit (0.3 $m^{-1/3}s$), could lead to instability in the hydraulic model. Figure 56 shows the result of the hydraulic simulation ensemble given by the perturbations of the model parameter and inputs. A detail of the variability of the flood extension among the simulations of the ensemble is illustrated in Figure 57.

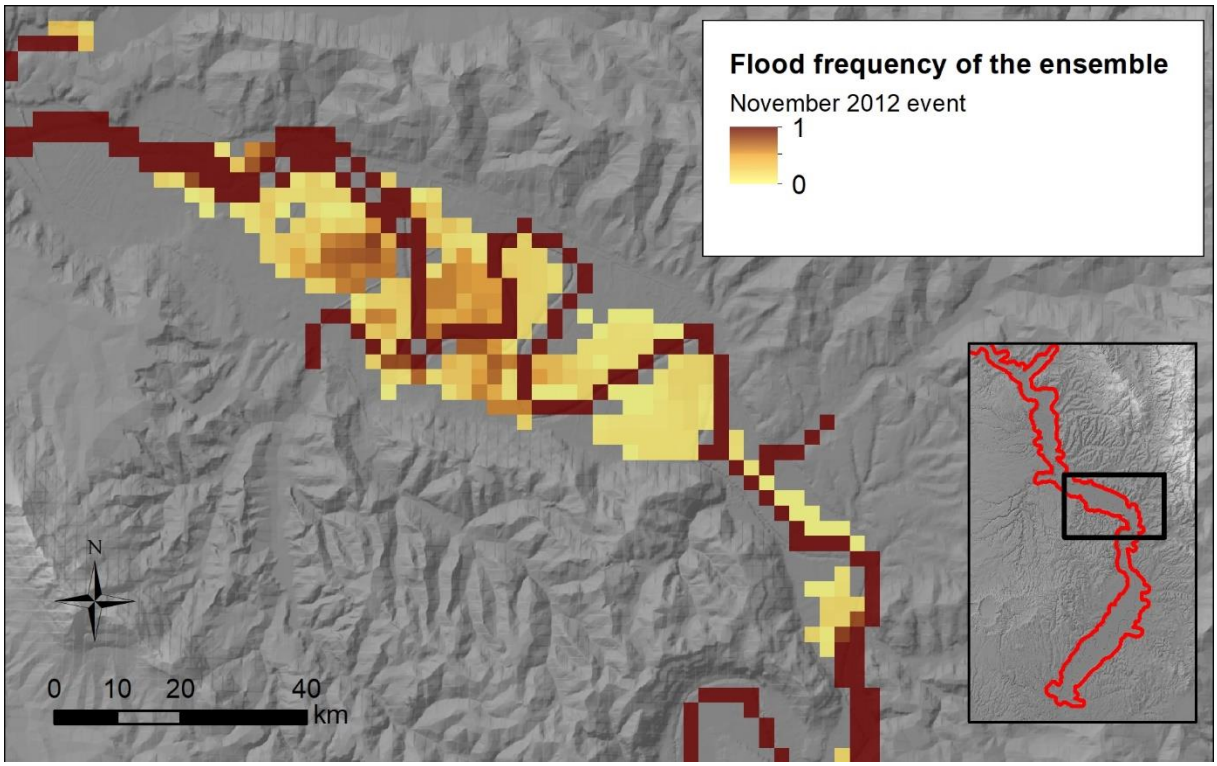

Figure 57. Detail of the flood frequency map normalized by the ensemble size

4.3. Assimilation of Static Sensors observations

4.3.1. Methodology

The adopted Quasi-2D hydraulic model is characterized by a 1D simulation inside the channel of the domain. When the water surface elevation in the channel reaches and overcomes the riverbank elevation, a 2D simulation is triggered along the floodplain domain. For this reason, the updating of the water levels during a Data Assimilation application has to take in to account both the channel and the floodplain domain whose dynamics affect each other. In case of water level correction from static sensors (stage gages), the observation comes from a channel element, where usually the static measurement system is placed taking advantage of the presence of an hydraulic structure, like a bridge or a weir. In the DA model not only each cell of the channel domain placed in a static stage gage, but also all the floodplain cells whose position is the closest to the mentioned channel cells are considered for updating the water level corrections derived from the EnKF application (Figure 58).

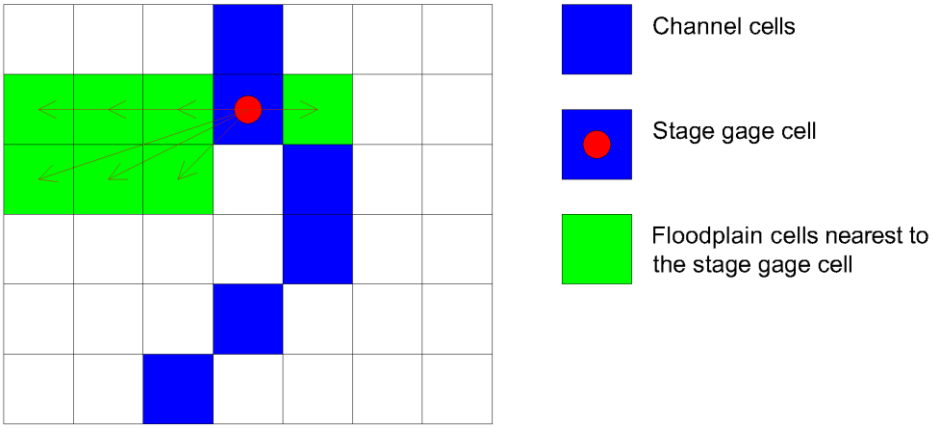

Figure 58. Scheme of the cells updating in the floodplain domain assimilating the stage gages measurements

If the correction of the water depth in a channel cell is relatively important, e.g. order of meters, some surging phenomena could occur because of an excessive steepness among the contiguous channel cells. For this reason, adopting a similar approach of Madsen & Skotner (2005), the water depth update given by the DA procedure is propagated using the following gain function:

$$g(i) = A \cdot \exp\left(-\frac{1}{2}\left(\frac{g(i)'}{1/3}\right)^2\right) \qquad [59]$$

Where $g(i)$ is the gain assigned to the i-cell, A is the gain amplitude (assumed equal to 1), $g(i)'$ is a term given by the following expression:

$$g(i)' = \begin{cases} \dfrac{x_{obs} - x_i}{x_{obs} - x_{uc}}, & x_{uc} \le x_i \le x_{obs} \\ \dfrac{x_i - x_{obs}}{x_{dc} - x_{obs}}, & x_{obs} \le x_i \le x_{dc} \end{cases} \quad [60]$$

x_{obs}, x_i , x_{uc}, x_{dc} are the linear coordinates along the channel of respectively the cell with the observation measurement, the *i*-cell to be updated, the upstream and downstream bounds for the gain function. The two latest terms depend on how far the updating due to the assimilation has to influence the channel profile. If there are many stage observations at the same time step, the bounds of the gain for a i-cell has to be limited by the position of the closest stage gage cells. Figure 59 shows the scheme of how the gain function is propagated upstream and downstream the observation point.

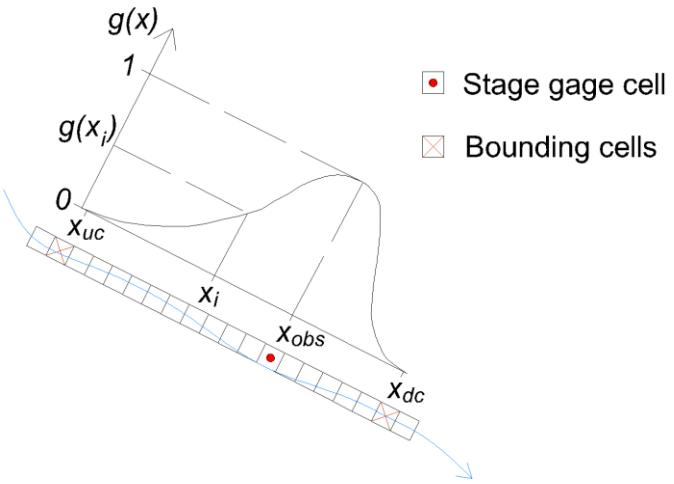

Figure 59. Scheme of the exponential gain for propagating the observation measurement along the channel

Furthermore, in order to simultaneously assimilate more than one stage gage observation, the portions of the channel (and its hydraulically connected floodplain) that is between two different stage observations, is updated considering both these observations using as weight the inverse of the distance of its connected channel cell from each stage gage cell (Figure 60). The water level correction for the *i*-cell ($\Delta H(x_i)$) is given by the following expression:

$$\Delta H(x_i) = \frac{\Delta H(x_{obs,u}) \cdot g(x_{i,u}) \cdot \dfrac{1}{x_i - x_{obs,u}} + \Delta H(x_{obs,d}) \cdot g(x_{i,d}) \cdot \dfrac{1}{x_{obs,d} - x_i}}{\dfrac{1}{x_{obs,d} - x_{obs,u}}} \quad [61]$$

Where $\Delta H(x_{obs,u})$ and $\Delta H(x_{obs,d})$ are the water level updates respectively in the upstream and downstream stage gages, $g(x_{i,u})$ and $g(x_{i,d})$ are the gains relative respectively to the upstream and downstream observation, $x_{obs,u}$ and $x_{obs,d}$ are the linear coordinates along the channel of respectively the upstream and downstream cell with observation measurements.

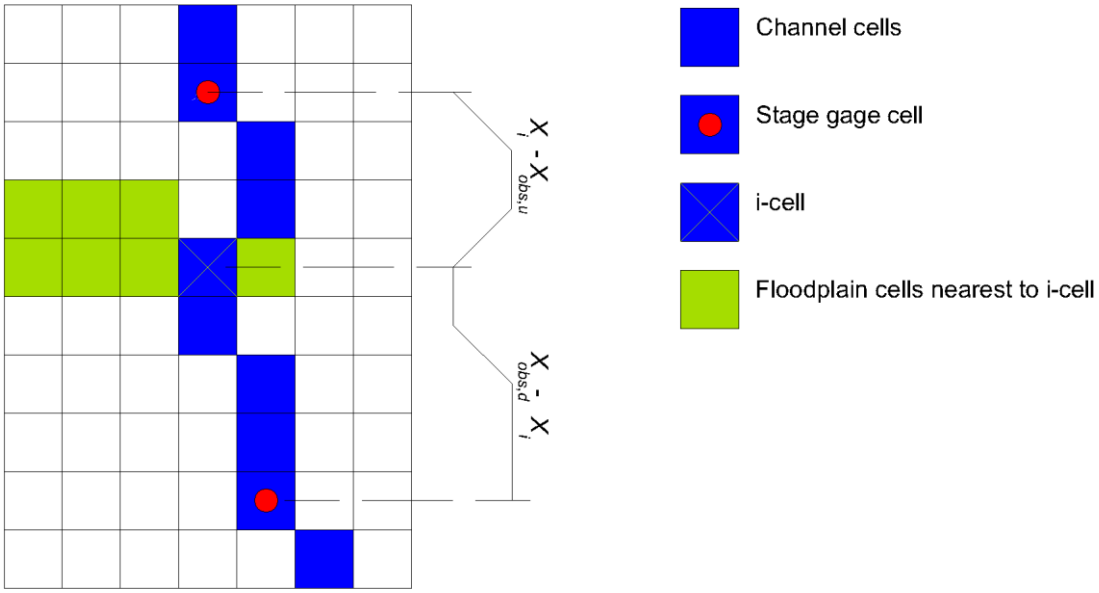

Figure 60. Scheme of the cell and floodplain water depth updating between two stage gage cells

When the gain function is propagated upstream and the water level correction is positive, a counterslope of the water levels could occur, bringing the model to numerical instability. This unwanted possibility is illustrated in Figure 61. The stage gage measurements (black dots) are assimilated, correcting the no updated levels (blue) to the updated water levels (red). However, the application of the gain function illustrated by Equation [61] mitigates the positive correction going upstream, with the consequence of having the mentioned counterslopes, undelined by the green circles. In order to avoid this possibility, a further condition has been imposed: the absolute water level in the cell of the channel $H^+(x_i)$, cannot be lower than the following downstream channel $H^+(x_i)$ cell, but, at least, should be the same:

$$H^+(x_i) = \begin{cases} H^-(x_i) + \Delta H(x_i)\,, & H^+(x_i) \geq H^+(x_{i+1}) \\ H^+(x_{i+1}), & H^+(x_i) < H^+(x_{i+1}) \end{cases} \qquad [62]$$

The eventuality of having a counterslope in water profile is accepted only if also the no-updated simulation is characterized by this behaviour for the presence of hydraulic structures.

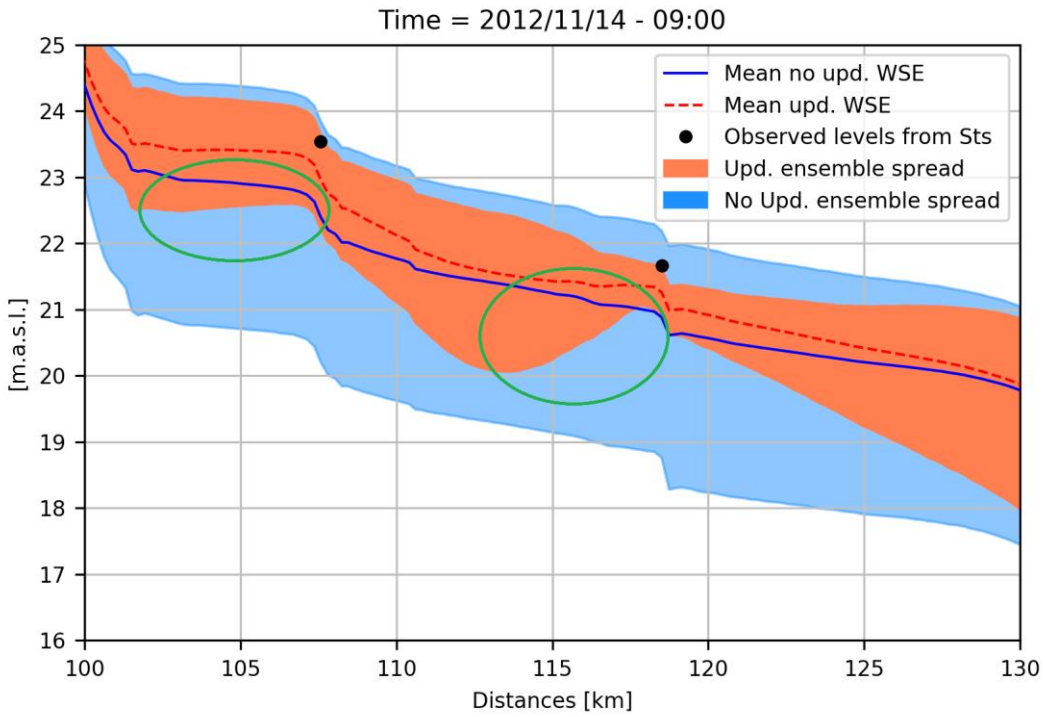

Figure 61. An example of how the gain function can create counterslopes of water levels when positive correction are applied in the Data Assimilation methodology

Each time step when observation measurements are available, the hydraulic simulation is stopped and the water levels and volume conservation outputs are saved in binary files. Then the EnKF is applied and the water depth corrections are inserted in the binary files. Flow velocities in each of the 8 direction are automatically corrected in order to satisfy the local volume balance that is changed depending on the water level variation.

4.3.2. Observation errors

To represent the observation errors, the stages gages measurements are perturbed using a similar approach adopted for perturbing the input flow from stage gages (Section 4.2.1), with the exception that, in this case, there is no error due to the rating curve transformation, because the observed water level are directly compared to the simulated ones.

The water depth for the *i*-element of the ensemble at time *t* is given by:

$$WD^{o}{}_{StS,t,i} = WD^{true}_{StS,t} + N\left(0, R_{StS,i}\right) \qquad [63]$$

Where $WD^{true}_{StS,t}$ is the observed water level by the static sensor (StS) at time *t*, $N\left(0, R_{StS,i,t}\right)$ is a noise term normally distributed with zero mean and a given variance ($R_{StS,i,t}$) at time *t* expressed as:

$$R_{StS,i,t} = \left(\alpha_{StS,i} \cdot WD_{StS,t}^{true}\right) \quad [64]$$

$\alpha_{StS,i}$ is the coefficient of variation related to the uncertainty in the water level measurement, assumed equal to 0.02.

4.3.3. Results and discussion

Figure 62-Figure 67 show the comparison among the observed and the simulated hydrographs for each gauge station. For every flood event, the updating of the state variable improves the prediction of the water levels. For the events characterized by multiple peaks, e.g. *November 2005*, the updating allows to better follow the level variations, overcoming the lower variability of the no-updated simulation, probably due to the coarse resolution of the model. For the *November 2012* event, the updating improves significantly the prediction of the levels at the peak flow. This is numerically confirmed by the performance indexes. Specifically, the NSE index is significantly increased for the updated hydrographs compared to the one given by the no-updated simulations. Bias in the updated simulation tend to remain constantly equal to 1, while in the no-updating, they tends to increase above 1 going downstream because of its overestimation of the water levels, especially after the peak flow, in the recession curve . For all the simulations, the more the flow is far from to the upstream inflow, the more the R coefficient tends to decay, but in case of updating simulation, this decay is mitigated.

The Quasi-2D model allowed to make a comparison also in terms of potential maximum flood extension between the updated and the no-updated simulations, averaged among the ensembles (Figure 68).

Before this comparison, the resolution of the flood maps given by the hydraulic model is refined at the same resolution of the LiDAR DEM through the following procedure:

- The absolute water surface elevation of each node of the domain is interpolated applying the Kriging methodology and using the floodplain polygon as buffer for the interpolation creating a raster with the same resolution of the LiDAR;
- The interpolated Water Surface Elevation (WSE) grid is intersected with a high resolution DEM and the positive values of the difference between the WSE and the DEM elevation are considered as flooded.

This methodology provides the extension of the potential flooded cells with an higher resolution representation than the one of the hydraulic model. In this case the potential flooded areas are actually the ones where the water levels underlie the terrain elevation.

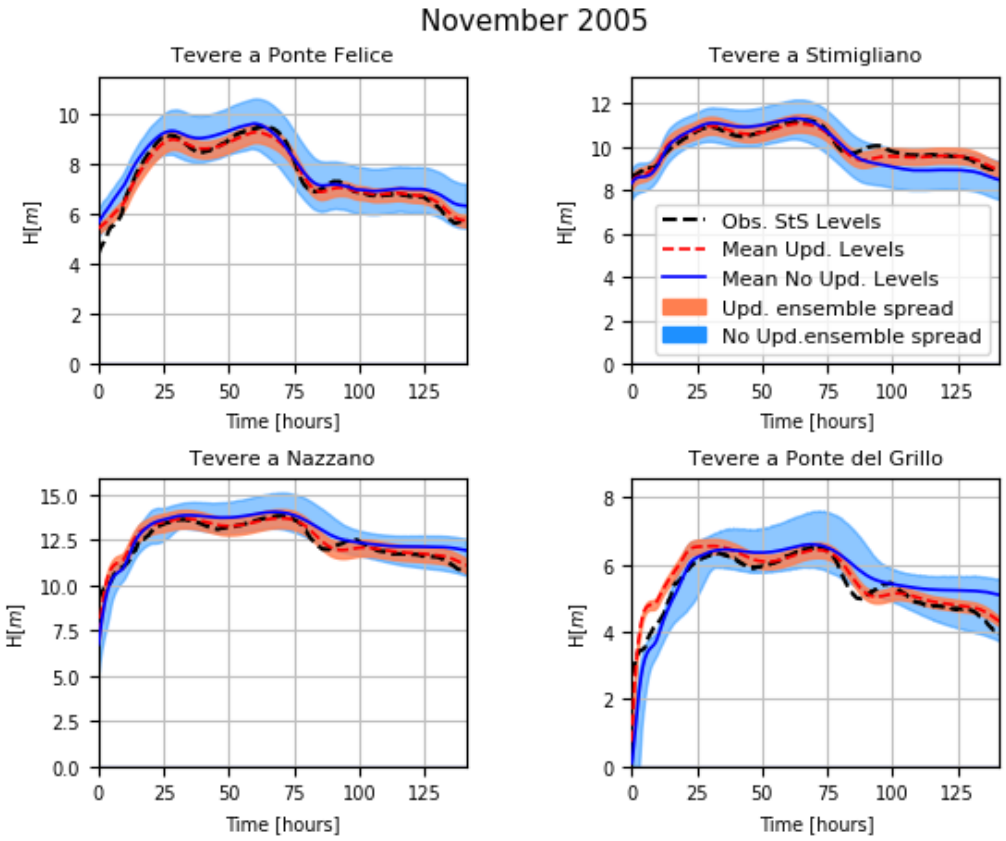

Figure 62. Observed and simulated hydrographs in case of no-updating and updating applying the DA method. Event: November 2005

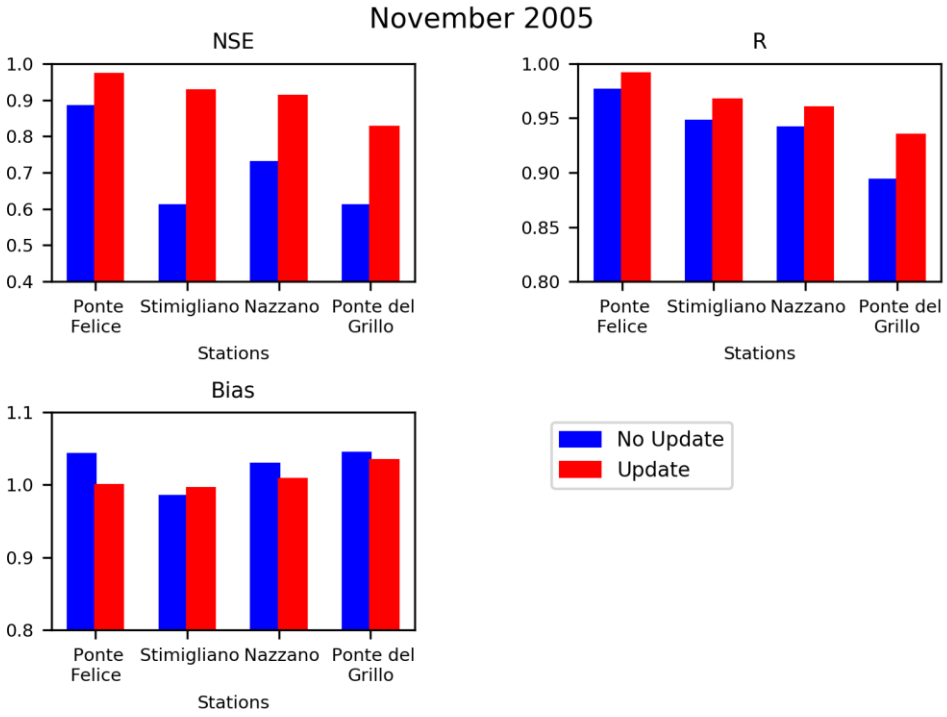

Figure 63. Performance indexes of the no-update and updated hydrographs. Event: November 2005

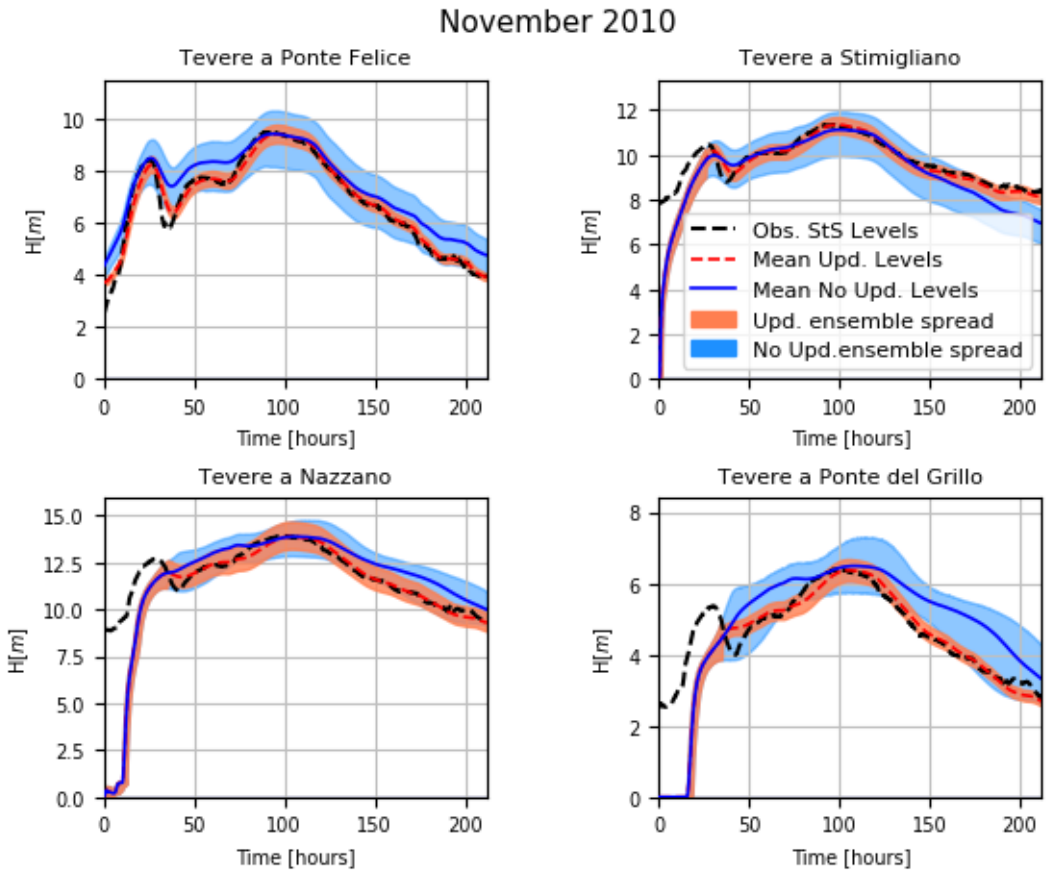

Figure 64. Observed and simulated hydrographs in case of no-updating and updating applying the DA method. Event: November 2010

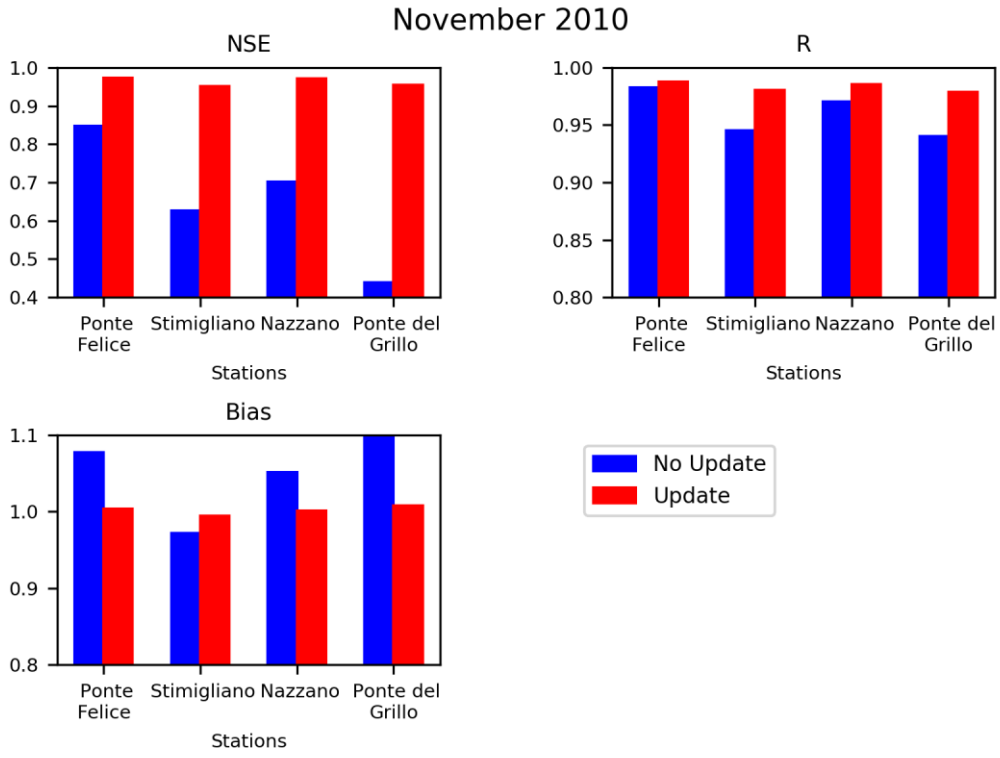

Figure 65. Performance indexes of the no-update and updated hydrographs.Event: November 2010

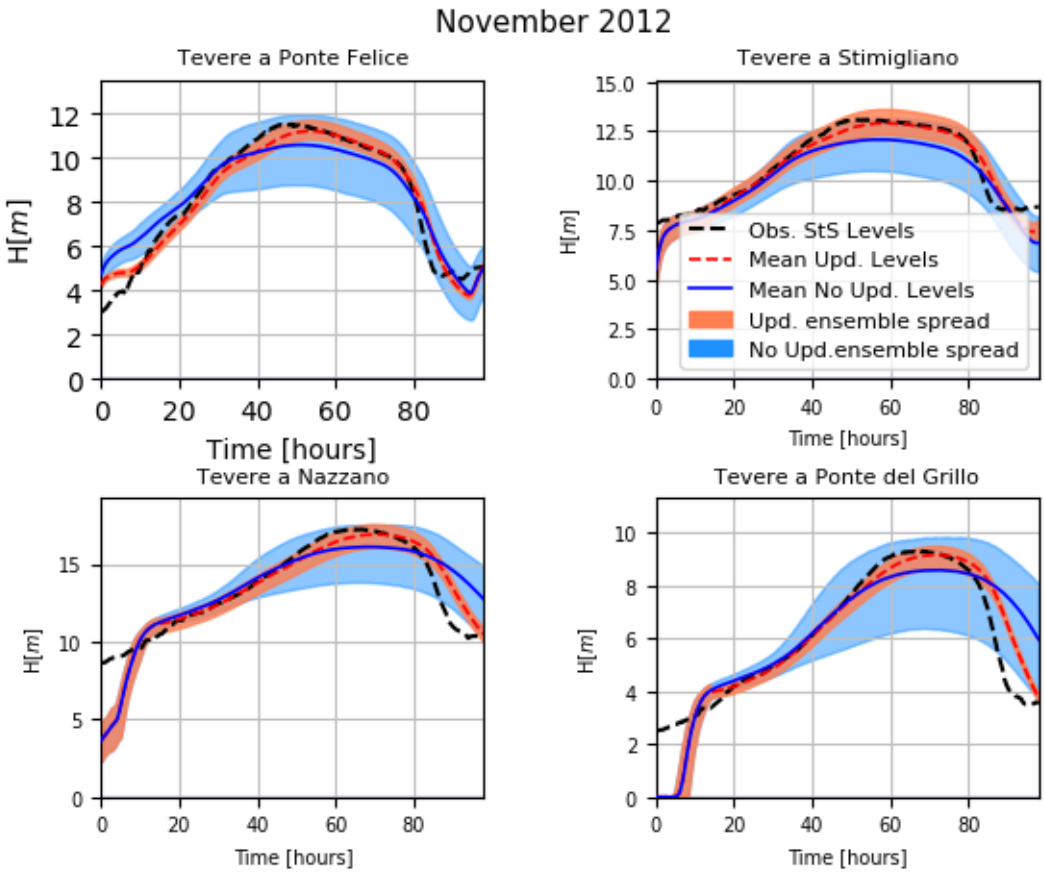

Figure 66. Observed and simulated hydrographs in case of no-updating and updating applying the DA method. Event: November 2012

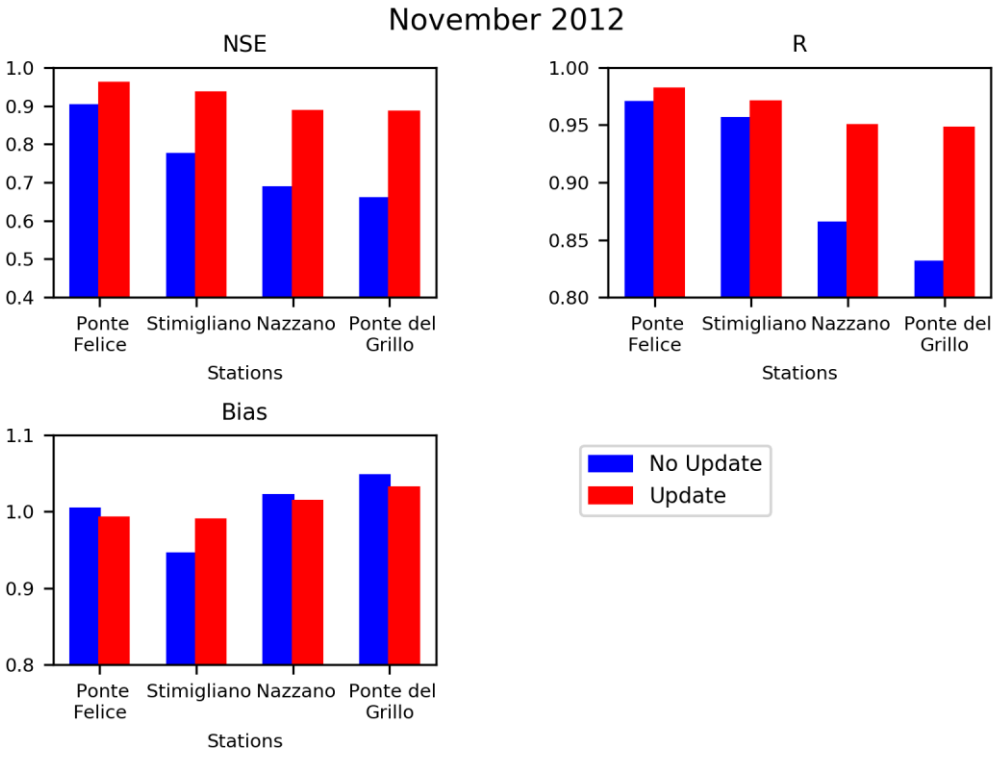

Figure 67 Performance indexes of the no-update and updated hydrographs.Event: November 2012

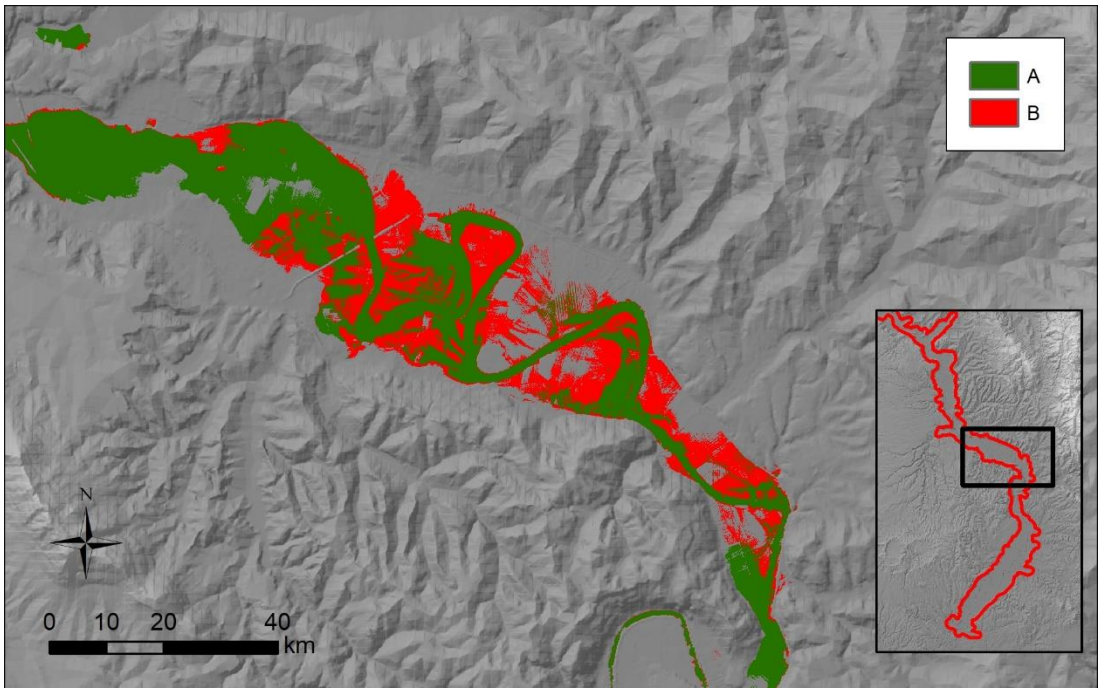

Figure 68. Comparison between the flooded areas related to the mean water levels simulated with and without updating. Event: November 2012. A= matching areas; B= Flooded areas of updated models and not in the no-updated model;

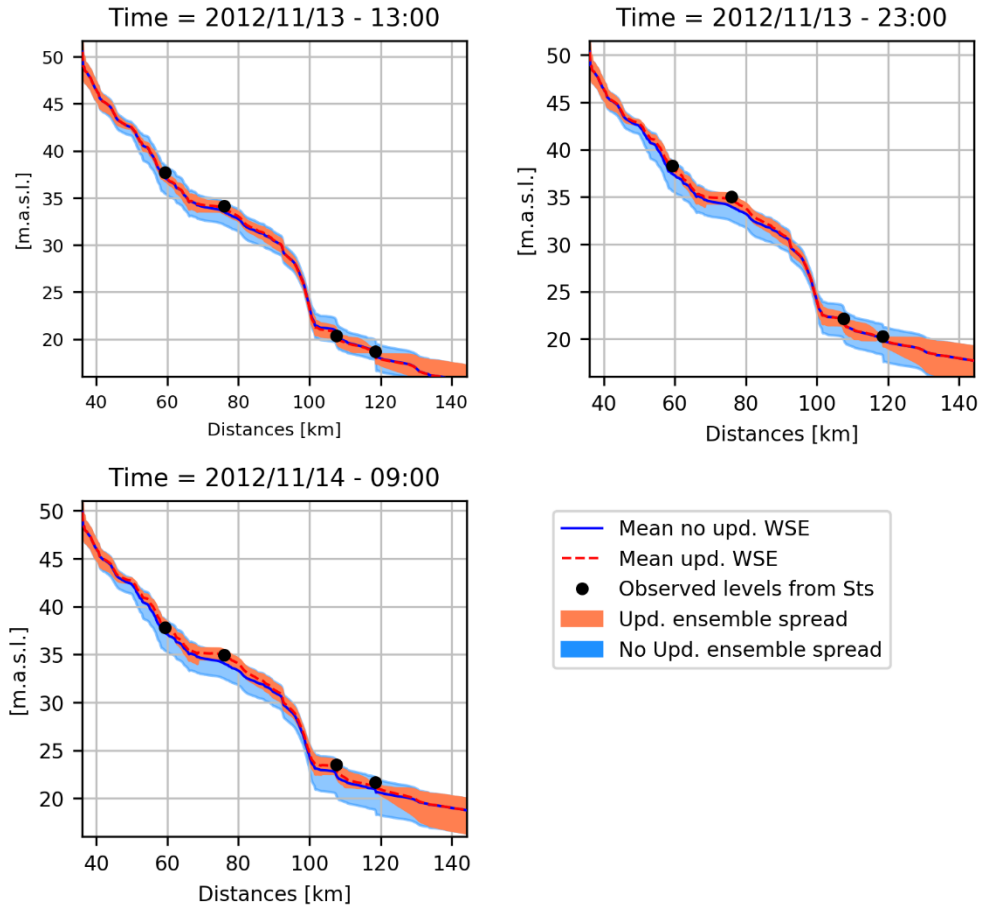

Figure 69. Plot of the hydraulic profiles for the updated and no updated simulations for three different time steps. Event: November 2012

Figure 68 shows that the updating of the water levels can modify significantly the maximum extension of the flood (about 17 km^2 of difference in the whole domain in case of the November 2012 event), since the planar configuration of the floodplain, in the some areas, makes the flooding very susceptible to water levels changes.

Figure 69 shows the behaviour of the hydraulic profiles for three different time steps for the updated and no updated simulations of the November 2012 flood event. The effect of the gain function is evident looking at the decay of the reduction of the ensemble spread and the correction of the mean water levels.

Figure 70 shows the values of Bias, RMSE and standard deviation of the ensemble over time for the updated and no updated simulations at each stage gage station. For most of the plots, all the performance of the updated simulations tends to increase the detachment from the performance of the no updated simulations, that tend to decrease during and after the peak flow.

Despite the promising results obtained from the three analysed flood events for this case study, the application of this methodology has some limitations. The simultaneous launching of tens of Quasi-2D hydraulic simulations is quite time consuming, since the overall simulations for each flood event requires averagely 4 hours for 100 simulated hours, because every 15 minutes of simulation, observations where available to be assimilated. However, part of the computational burden is due to the fact that each time step an observation is available, the simulation needs to be stopped, saving all the binary and text files that contains information of all the cells of the domain and reporting the summaries of the simulation. The performance in terms of computational time can be considerably improved with a further modification of the hydraulic code that makes more agile the assimilation of new observations without producing the whole text files that are not necessary before the final interruption for the simulation. Moreover, this computational burden required to adopt an hydraulic model with a coarse resolution, whose performance can be considered acceptable for valley filling flood events, but it could have some limitations in representing the flow along the floodplain in shallow water, where micro topography can have an important role (Bates, 2012). A further test considering a smaller domain with a higher resolution 2D hydraulic model needs to be done also to verify the stability of the model when water levels corrections (ΔH) are applied in smaller cells dimensions (ΔX).

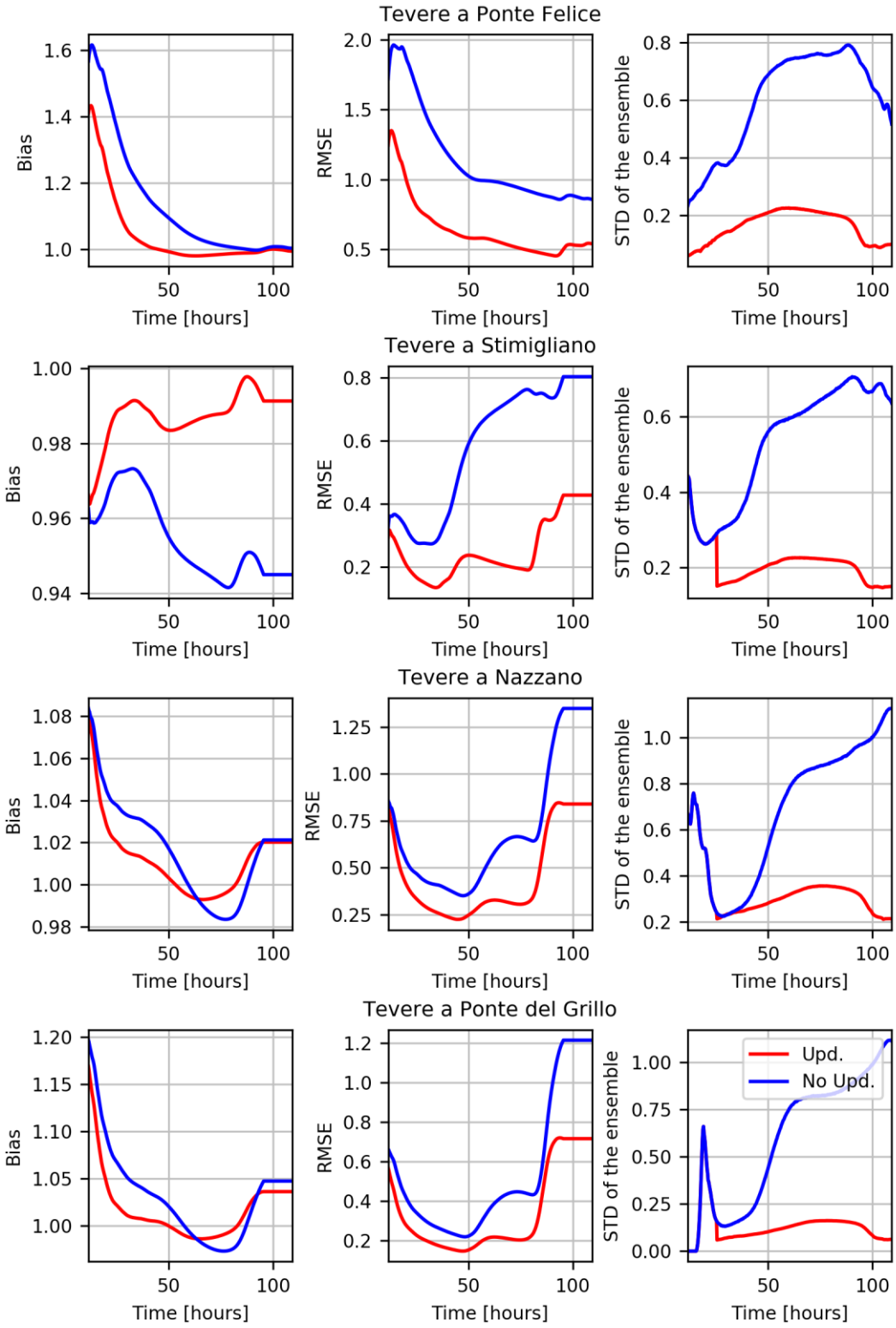

Figure 70. Values of Bias, RMSE and the standard deviation of the ensemble during time. Bias and RMSE are calculated using the StS observations as reference. STD of the ensemble is calculated from its mean.

4.4. Assimilation of Satellite images observations

4.4.1. Introduction

The availability of satellite images is not immediate after the acquisition time (Mason et al., 2012b), since they need to be pre-processed and uploaded by the supplier agency. For this reason, these images have not be widely adopted yet in a flood forecasting model, but only for hindcasting, reproducing a past flood event. However, Matgen et al. (2010) proposed a SAR-based flood monitoring system that can be a good starting point for a flood forecasting application. Furthermore, the temporal frequency of satellite image acquisition, in the same place and with the same inclination, is limited by the number of satellites currently active (Schumann et al., 2009). These aspects are strong limitations for the application of the satellite images for validating flood models in short time, especially in basins characterized by concentration times lower than the frequency of the satellite images acquisition. Nevertheless, both the temporal frequency and their availability is quickly improving and these products are expected to be more and more used in flood validation. (Bates, 2012).

In the following section, an expeditious methodology for assimilating water levels from a satellite image is presented. The procedure involves a series of different steps that add errors to the observation measurement. However, in data scarce regions with high uncertainties on the hydrologic model (poor rain and soil moisture data), and the hydraulic model (channel geometry, Manning values), this procedure could both improve the simulation and suggest potential model correction.

4.4.2. Methodology

The assimilation of flow depths derived from a satellite image can be summarised by the following steps:

- Flood detection from satellite image. The Water index (Equation [49]) mentioned in Section 3.7 has been adopted for detecting the water extension of the November 2012 flood.
- Comparison of the flood extent detected from the satellite image with the ensemble of flood extents given by the hydraulic model (Section 4.4.2.2). This procedure requires refining the resolution of the water surface elevation layer provided by the hydraulic model using a geostatistical technique and intersecting this surface with a DEM.

- Derivation of the water elevation profile along the channel from the satellite image starting from the ensemble of the water elevation profiles of the hydraulic model (Section 4.4.2.3).

Each of the abovementioned steps brings an uncertainty that has to be taken into account by the DA model perturbing adequately the water depths indirectly observed from the satellite image (Section 4.4.3).

All the procedure has been implemented in GIS environment in order to be automated for any reference image acquired in any part of the domain at any time step.

4.4.2.1. Flood detection

The flood detection application for the satellite image of the case study has been illustrated in Section 3.7.2.2 (see Figure 52).

The extension of the Landsat 7 image covers Nazzano and Ponte del Grillo gages stations and its acquisition time is closer to the one the peak flow passes over the two stations (Figure 71).

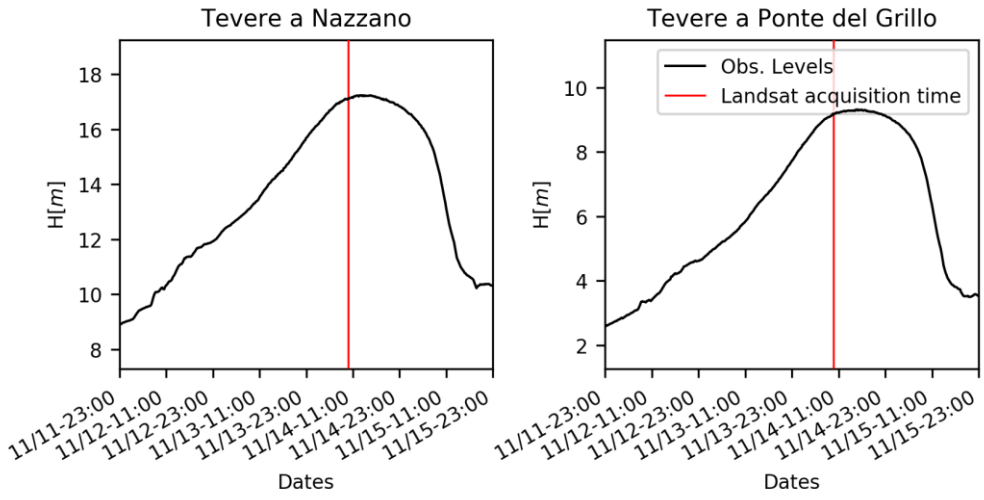

Figure 71. Position of the Landsat acquisition time compared to the time series of the water depths in Nazzano and Ponte del Grillo gage stations

4.4.2.2. Flood maps comparison

The satellite detected water extension is compared with the ensemble of the hydraulic model maps at the time step of the Landsat image's acquisition date. Before this comparison, the resolution of the flood maps given by the hydraulic model is refined at the same resolution of the satellite image through the same procedure illustrated in Section 4.3.3 for representing the results of the model at the same resolution of the source DEM:

- The absolute water surface elevation of each node of the domain is interpolated applying the Kriging methodology and using the floodplain polygon as buffer for the interpolation creating a raster with the same resolution of the Landsat image;
- The interpolated Water Surface Elevation (WSE) is intersected with a high resolution DEM and the positive values of the difference between the WSE and the DEM elevation are considered as potentially flooded.

Once the ensemble of the water extensions from the hydraulic model have the same resolution of the water extension derived from the satellite image, the two categories of maps can be compared numerically using the measurement index given by Equation [6] ($F = (A_{ref} \cap A_{mod})/(A_{ref} \cup A_{mod})$) and also the Bias given by Equation [10] $Bias = (A + B)/(A + C)$.

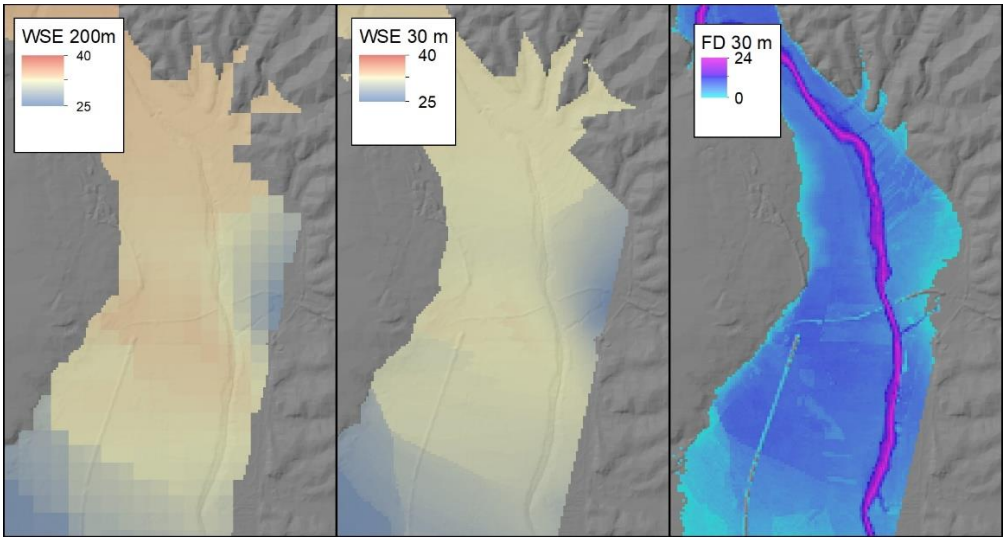

Figure 72. Example of the procedure for refining the hydraulic model Flow Depths (FD): from the starting WSE with the resolution of the hydraulic model (left), application of the Kriging method using a finer resolution (centre) and intersection with a high resolution DEM (right)

4.4.2.3. Hydraulic profile derivation

The extension from the ensemble with the higher value of the F index is supposed to have an hydraulic profile closer to the real one associated with the extension of the satellite image. If the maximum value of F index correspond to a Bias value > 1, its relative hydraulic profile can be considered as overpredicting the water extension and vice versa for Bias <1.

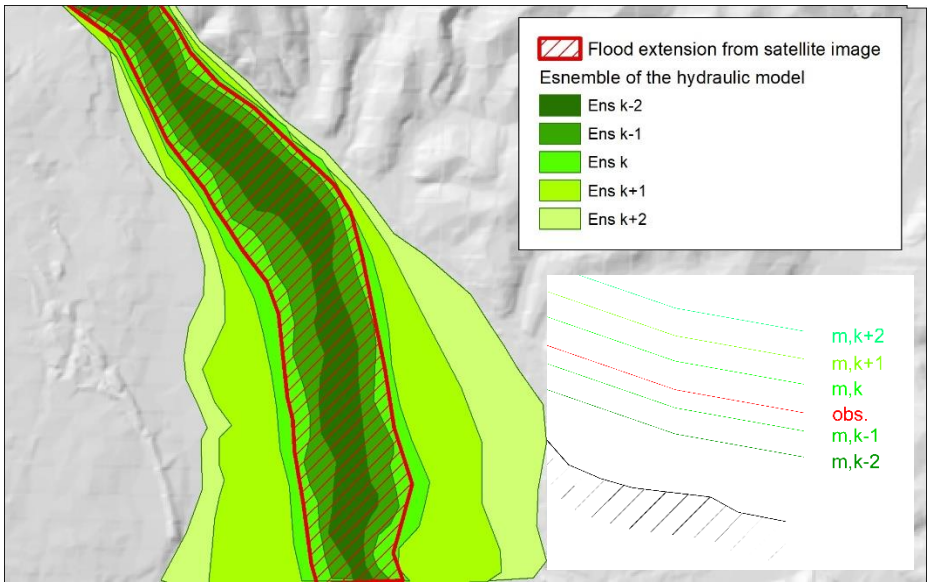

Figure 73. Planimetric scheme of the comparison between the flood extension derived from satellite imagery and the ensemble of the hydraulic model

For the generic *i*-cell belonging to the hydraulic model, the observed WSE $H^{i}_{o,t*}$ at the time (t*) of the satellite imagery acquisition, is expressed as:

$$H^{i}_{o,t*} = H^{i-}_{m,k-1,t*} \cdot \frac{F^{-}_{k-1}}{F^{-}_{k-1} + F^{+}_{k}} + H^{i+}_{mk,t*} \cdot \frac{F^{+}_{k}}{F^{-}_{k-1} + F^{+}_{k}} \quad [65]$$

Where $H^{i-}_{mk-1,t*}$ $H^{i+}_{mk,t*}$ are the WSE at time t* of the *i*-cell for the two ensembles of the model with the maximum F indexes (F^{-}_{k-1} and F^{+}_{k}) with Bias respectively <1 and >1. If both the two elements of the ensemble with maximum values of the F index are related to Bias < 1 or >1, all the ensemble tend to underpredict or overpredict the water levels. This means that the amplitude of the model's perturbation (or the amplitude of the observation error) is not sufficiently adequate and the value of the $H^{i}_{o,t*}$ takes the maximum (if all the Bias are < 1) or the minimum (if all the Bias are > 1) of the WSE generated by the ensemble of the hydraulic model.

4.4.3. Observation errors

The procedure for extracting the hydraulic profile from the satellite image is affected by a series of errors that have to be taken in to account when applied in a DA framework and here listed:

Error in the water detection from satellite imagery (err_{wd}): this error is due to 1) the water detection technique $err_{wd,SI}$ that could overestimate and underestimate the water extension; 2) the resolution $err_{res,SI}$ of the satellite image. The error due to the water detection technique $err_{wd,SI}$ is dependent on weather condition in case of multispectral images. The most recent indexes demonstrated to have very good performance in good weather condition, and the

overprediction and underprediction errors can stay below 0.4 % (Fisher et al. 2016), but during storm condition this error can be greater. SAR imagery are not affected by the presence of clouds and resolution can be much higher than the multispectral images, so the correspondent $err_{wd,SI}$ is potentially lower. In this work the error in water detection technique is taken into account perturbing the threshold of the Water Index for discriminating between water and non-water cells. Specifically, considering that the optimum value of the WI is around 0, a range between -1 and +1 has been chosen. The resolution ΔL_{res} [m] is dependent on the type of adopted image. For a Landsat image, the resolution is currently 30 meters (but is going to decrease to 15 m for Landsat 9, whose mission will be launched in 2020), while, for a SAR image it can vary from 100 meters (e.g. SCANSAR) to 3-5 m (STRIPMAP) or even to 1 m (SPOTLIGHT). The planimetric error due to the water detection has to be related to the correspondent vertical error of the flow depth, thus to the slope of the computational domain: the higher is the terrain slope, the higher is the vertical variation of flow depth in correspondence of a unitary planimetric transversal variation. Figure 74 shows the distribution of the local slopes along the computational domain, namely the floodplain of the Tiber river. The perturbation of the observation $err_{wd,t*,i}$ of the Satellite Imagery (SI) of the *i*-element of the ensemble at the time of the image acquisition *t** given by the water detection is expressed as:

$$err_{wd,t*,i} = N(0, {R^{SI}}_{wd}) \quad [66]$$

Where $N(0, {R^{SI}}_{wd})$ is a noise term normally distributed with zero mean and a given variance $({R^{SI}}_{wd})$ expressed as:

$${R^{SI}}_{wd} = (\Delta L_{res}) \cdot \left(\left|N\left(0, R_{slope}\right)\right|\right) \quad [67]$$

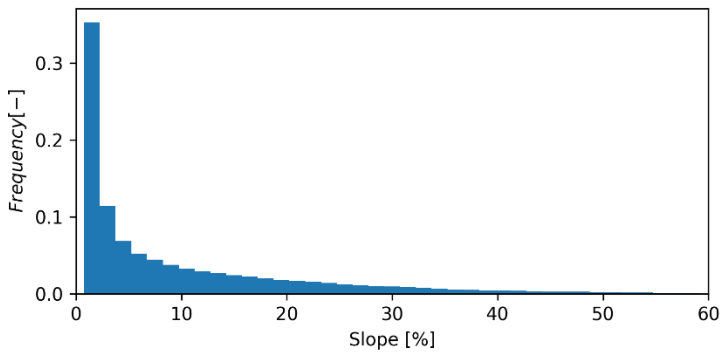

Figure 74. Distribution of the local slopes [%] in the computational domain.(Standard deviation: 8.9%)

Where $\left|N\left(0, R_{slope}\right)\right|$ is a positive noise term normally distributed with zero mean and variance equal to the one resulting from the distribution of the slopes inside the water detected area (e.g. Figure 74)

Figure 75 shows the relation between the planar error due to water detection and the correspondent vertical error. The expression of this error can be applied for a local analysis, but in a spatially distributed water detection, the overprediction of a specific zone can be compensated an underprediction of another one. This suggests that an improvement of the effectiveness of this methodology can be the partition of the computational domain in different sub-zones where performing the water detection analysis.

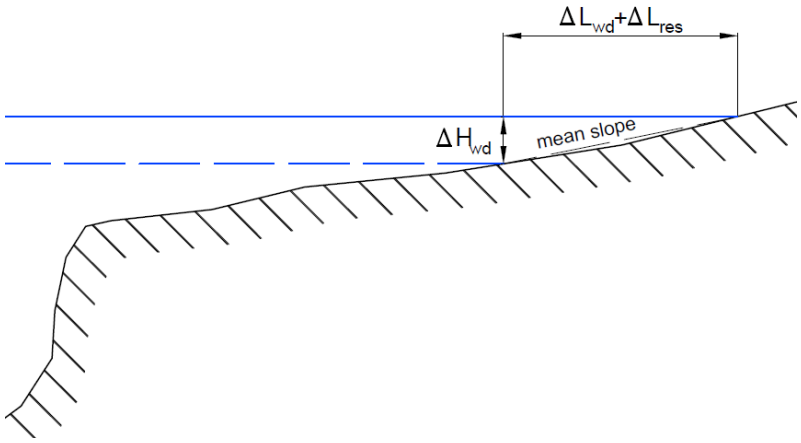

Figure 75. Scheme of the relation between the planar error due to water detection and the correspondent vertical error

Error of the water surface extraction from the WSE of the hydraulic model (err_{DI}): This is due to the vertical error of the DEM with which the interpolated water surface elevation is intersected.

There are no information regarding the accuracy of the adopted DEM, so its error has been chosen considering literature values for similar DEMs. Leon et al.(2014) used a standard deviation of 0.18 m for simulating the uncertainties of a 1m Lidar; Hodgson & Bresnahan (2004), determined RMSE values between 0.2 and 0.3 m over different types of land, specifying that for scale mapping operations they can increase to 1.5 m. In this work, a standard deviation of 0.3 m has been chosen.

The use of independent normally distributed errors in the spatial domain does not accurately represent errors in the elevation data (Raaflaub & Collins, 2006; Heuvelink et al., 2007; Brouwer at al., 2017) that usually are characterized by spatially autocorrelated errors. Since there are also no information regarding the Correlation Distance Error (CDE) for the adopted

DEM, literature values have been considered (CDE =173-253 m from Li et al. 2011; CDE =143-178 m for a 2 m resolution DEM from Livne & Svoray, 2011; CDE= 4 m for a 0.5 m resolution DEM and CDE =50 m for a 10 m resolution DEM from Mudron et al., 2013; CDE = 102 m for a 1 m resolution DEM from Leon et al., 2014). A CDE equal to 100 m (as Brouwer et al., 2017) has been imposed for perturbing the original 5 m resolution DEM (Figure 76)

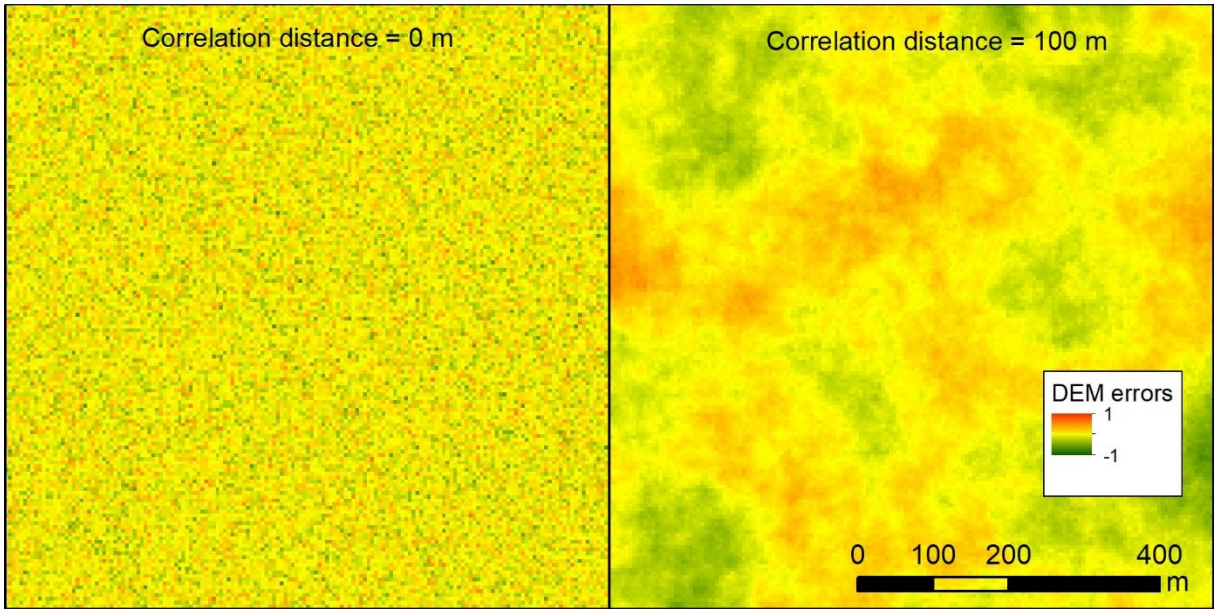

Figure 76. Example of simulating DEM errors using a spatially normal distribution (mean=0 m, Std. deviation = 0.3 m) with correlation distances equal to 0 (left) and 100 meters (right).

For each element of the ensemble, the DEM has been perturbed using a spatially distributed normal error with zero mean and a variance variable between 0 and 0.3 m following an uniform distribution $U(0,0.3)$. The original DEM with the added errors has been then resampled to the satellite image resolution. For assigning a spatially normally distributed error with zero mean, variance 0-0.3m and CDE equal to 100 m, the following procedure has been adopted for each ensemble:

- A raster (NR) of random values with a normal Gaussian distribution (μ=0, σ=1) is created for the entire extension of the DEM;
- A raster with the statistic (SR) of the NR values within a neighbourhood equal to CDE around it is created;
- The error distribution raster (Err) is created dividing the SR raster by its spatially averaged standard deviation and multiplying the result for the adopted variance ($U(0,0.3)$);
- The Err raster is added to the original DEM

Error of the profile derivation from the ensemble of the hydraulic models (err_{PD}): equation [65] assumes a linear relation between the value of the water elevation of two hydraulic profiles and the weight of their relative F indexes compared to the observed water extension from SI. However, if there are changes in floodplain slope in the areas between the boundaries of the two WSE derived from the hydraulic model, the weighted mean of the simulated WSE using the F index as a linear weight could lead to an inaccuracy on the vertical estimation of the WSE (Figure 77). This error is as lower as higher in the number of the ensemble, because the WSE simulated by the hydraulic model tend to be closer among themselves and the linear approximation using equation [65] becomes more acceptable.

The perturbation error due to the profile derivation err_{PD} for the *i*-element of the ensemble is expressed as a random uniform noise:

$$err_{PD,i} = U(-0.25 \cdot \Delta H_k, +0.25 \cdot \Delta H_k) \qquad [68]$$

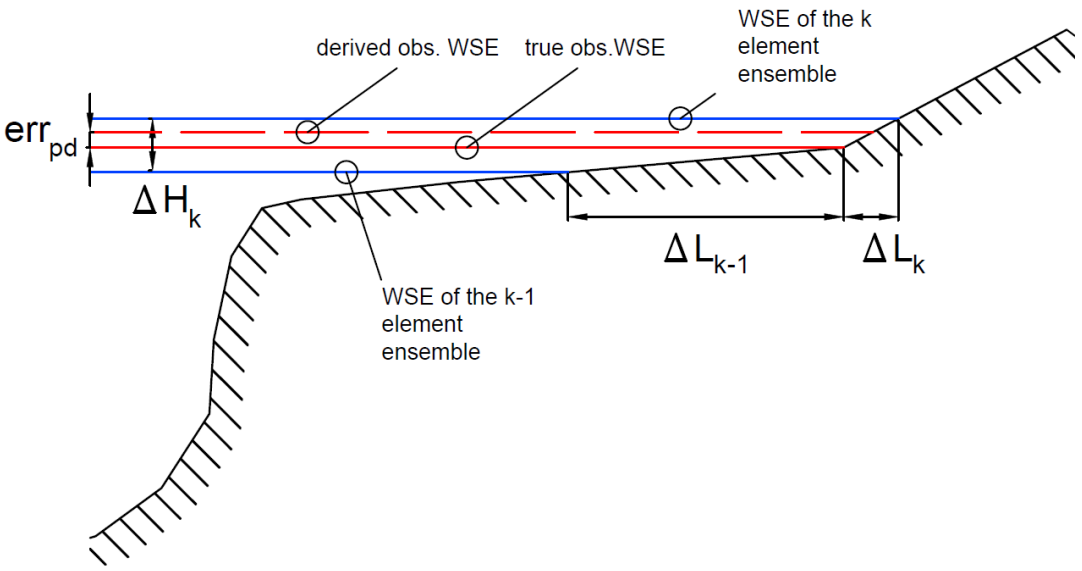

Figure 77. Scheme of the error due to the profile derivation starting from the ensemble of the hydraulic model

Where ΔH_k is the water level difference between the two hydraulic simulations with the highest values of the F index and the 0.25 coefficient limits the oscillation considering the gentle elevation changes of the floodplain in the computational domain.

4.4.4. Results and discussion

The Data Assimilation methodology using the Landsat image has been applied for the *November 2012* event. Figure 78 shows that the updated mean water levels at the SI acquisition time are slightly raised, and remain higher than the ones of the no-updated simulation for few hours. The spread of the ensemble of the updated simulation is significantly reduced in

correspondence of the SI observation and this reduction is gradually damped until is nullified in about 8 hours Positive effects of the assimilation are evident also from the Bias and RMSE over time (see Figure 83). The improvement of the performance of the overall simulation in case of SI assimilation are almost negligible (Figure 79), since the correction maintains its effect for only few hours, as showed in Figure 83.

The flood extent is not considerably changed with the correction of the water levels, as showed in Figure 80. Specifically, for the entire domain a mean increase of 0.635 km^2 of flood extension has been observed for the updated simulations compared to the no-updated simulations. The reduction of the uncertainty in the extension of the flood at the time of the satellite image acquisition after the updating of the model is showed in Figure 81.

Since the derivation of the observed hydraulic profile has been performed as a combination of the simulated hydraulic profiles applying Equation [65], the correction of the water levels has been performed for the entire domain, reducing the uncertainties of the water levels for the whole hydraulic profile (Figure 82).

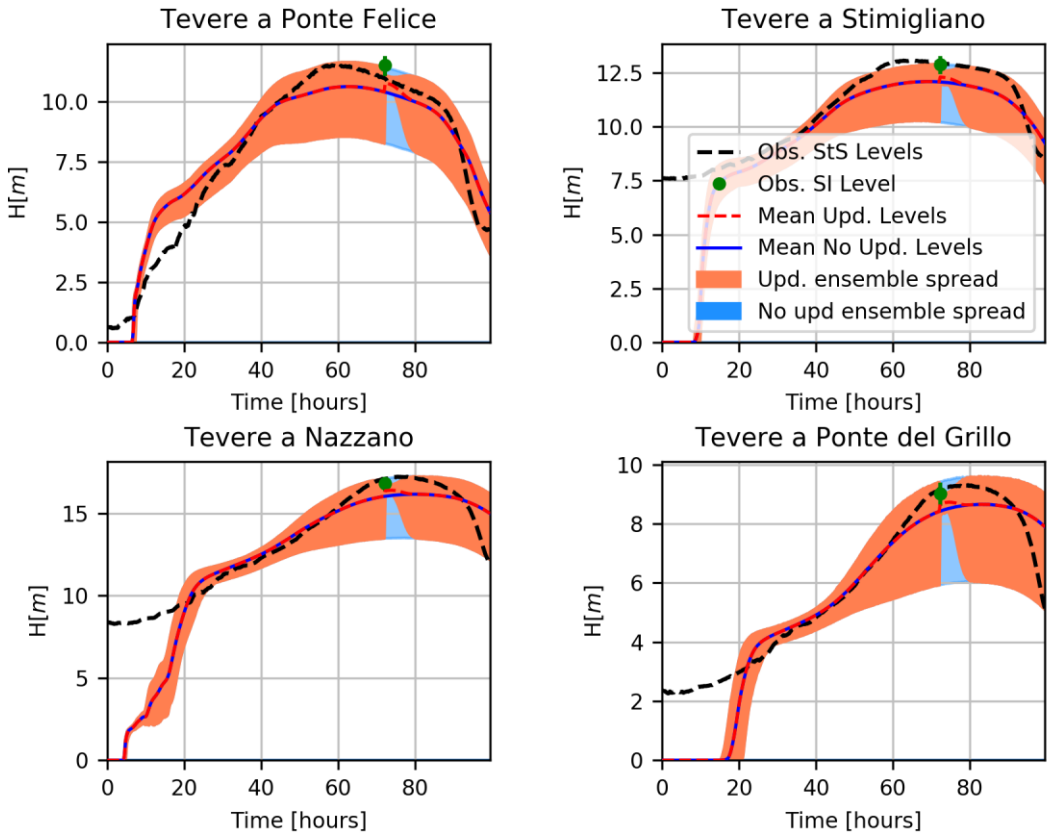

Figure 78. Hydrographs of the updated and no-updated simulations assimilating the Satellite Image observation (SI) at two stage gages locations. Event: November 2012

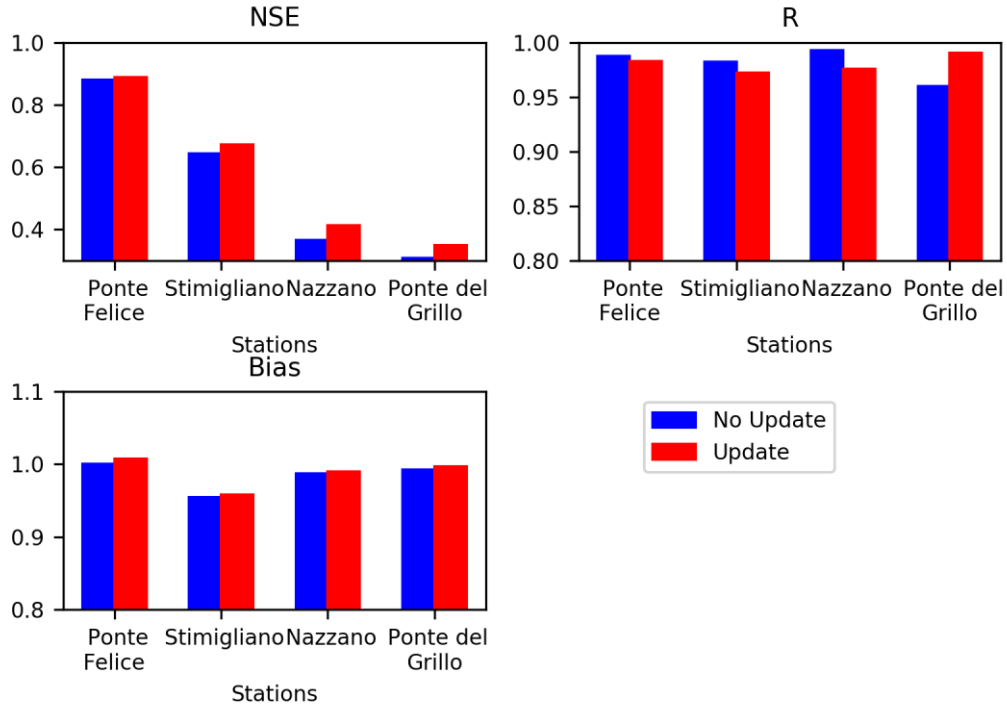

Figure 79. Performance indexes after the SI observation for the updated and non-updated simulations. Event: November 2012

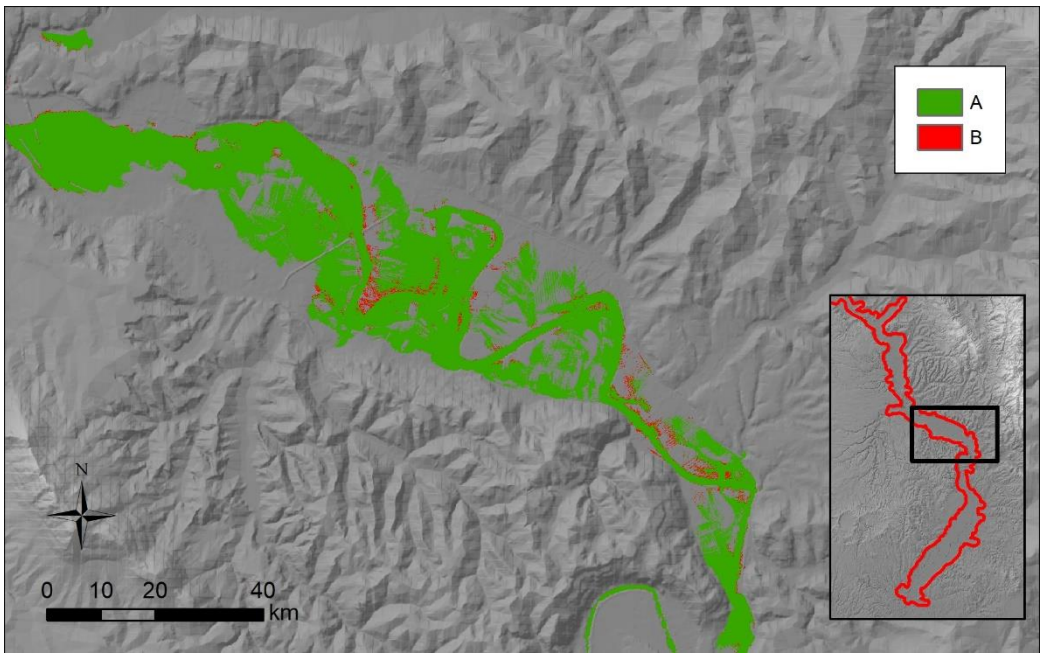

Figure 80. Comparison between the extension of the areas where the mean water levels underlie the terrain elevation at the time of the Satellite Image acquisition for the no-updated and updated simulations. Event: November 2012. A= matching areas; B= Flooded areas of updated model and not in the no-updated model.

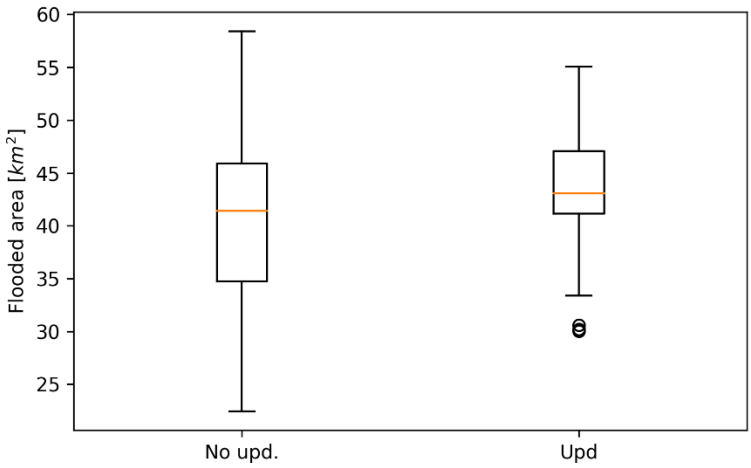

Figure 81. Boxplot of the areas where water levels underlie the terrain elevation at the time of the Satellite Image acquisition for the no-updated and updated simulations

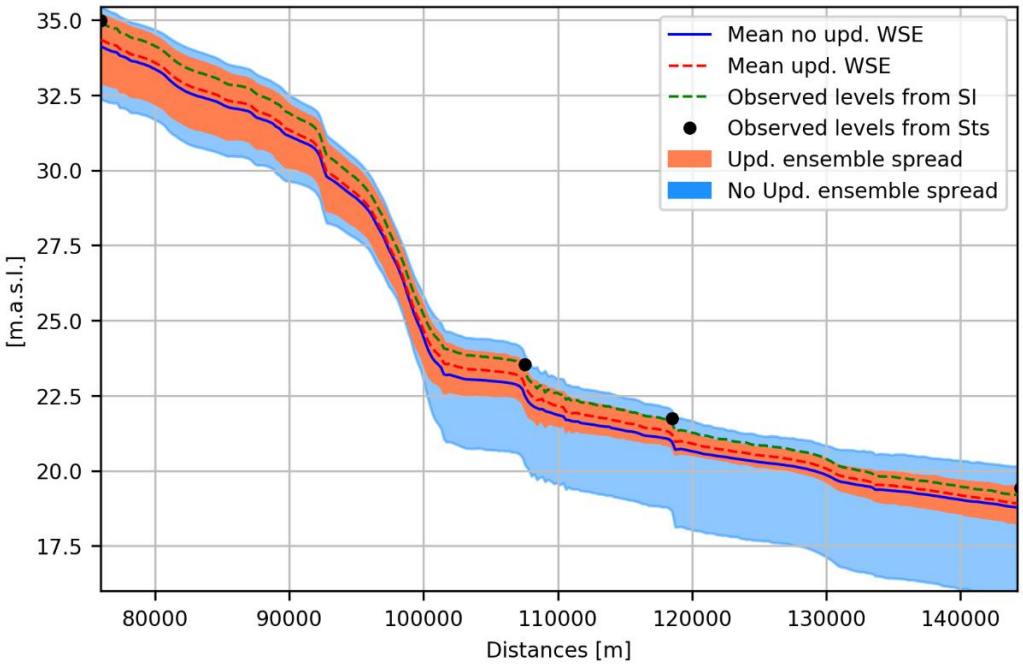

Figure 82. Hydraulic profiles of the mean updated and no-updated simulations at the time of the satellite image observation. Event: November 2012

The use of a multispectral image to assimilate water levels during a flood event is one of the most important limitations of the adopted methodology. Multispectral images are in fact affected by the presence of clouds, that most of the times cover the sky upon the rivers when the flow peak is propagating over them. However, SAR images can easily overcome this limitation, being able to penetrate clouds, and, in case of Stripmap and Spotlight products, they can have a considerably higher resolution (1-5 m), thus reducing the uncertainty related to the water extension. The adopted methodology for assimilating the detected water extension is, in

fact, applicable regardless the type of image, with the exception for the water detection technique. Another important limitation, as anticipated in Section 1.2, is the satellite revisit time of the current satellite missions that, in case of small basins, can be much higher than the time that the peak flow takes to travel from upstream to downstream. For example, for the three analysed flood events in the Tiber river basin, only one useful satellite image has been found in the November 2012 event and the correction of the water levels with the DA method improved the performance of the model for only few hours. Furthermore, usually multispectral SAR images require time for being processed, so a real time application of the methodology can be strongly affected by this aspect. However, as explained in Section 1.2, the progress of the technology will overcome these limitations. In fact, new satellite missions and also the combination of more constellations will considerably reduce the revisit time, allowing to have different images for the same area every few hours. Moreover, recent automatic satellite image techniques for extracting the flood extension has been inserted in real time services for flood mapping (Martinis et al., 2014).

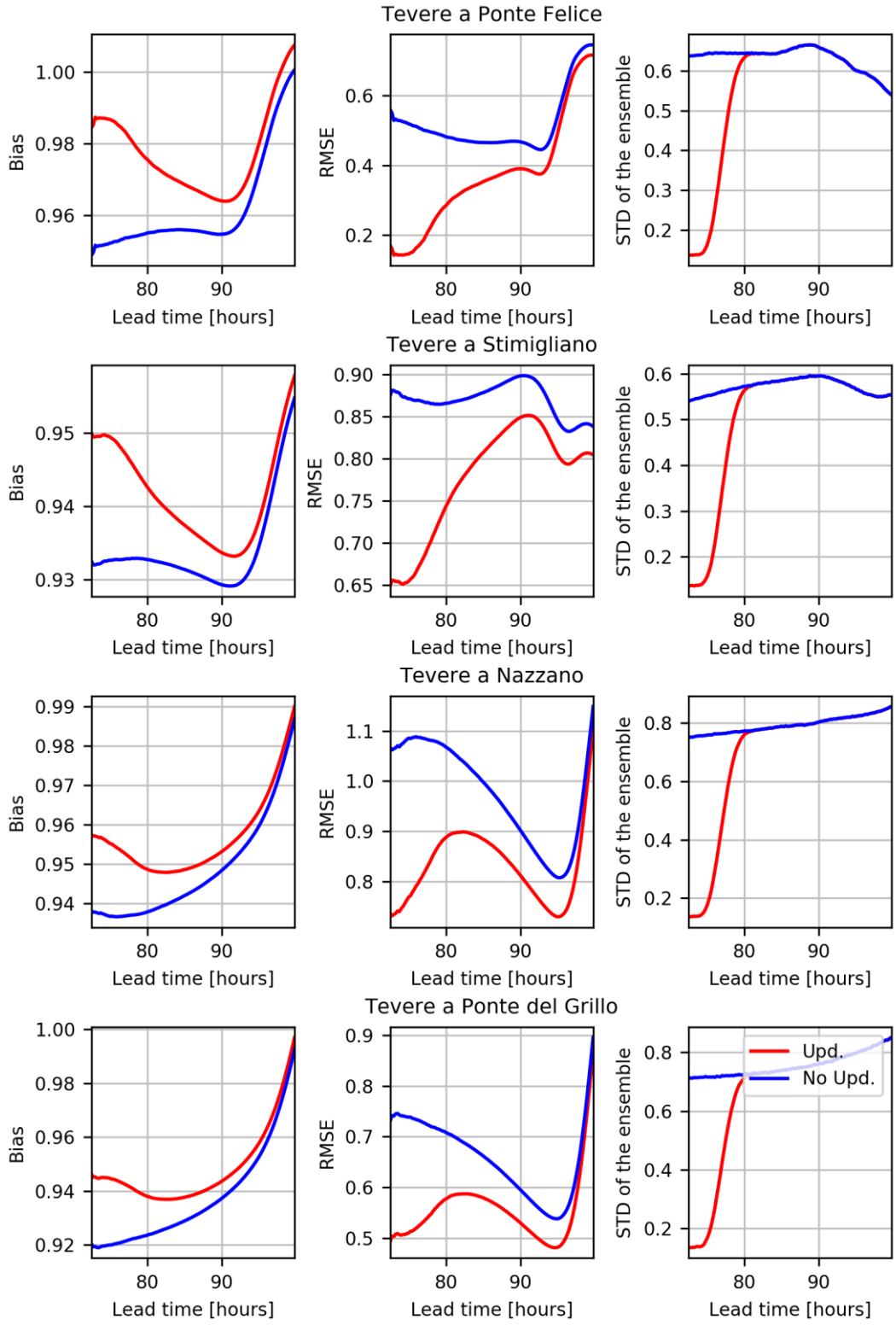

Figure 83. Performance indexes (Bias, RMSE and variance of the ensemble spread) along the lead time after the acquisition time of the SI observation. Event: November 2012

4.5. Assimilation of VGI data

4.5.1. Introduction

In the last 5 years, several studies, already mentioned in Section 1.3, have been done for validating hydrologic-hydraulic models or reproducing the flood extension starting from VGI data. Currently there are few examples in literature of DA application in hydrologic and hydraulic modelling using VGI data. Specifically, Mazzoleni et al., 2015, Mazzoleni et al., 2017 and Mazzoleni, 2017 demonstrated the potential of crowdsourced information for improving the real-time flood forecasting using simplified hydrologic and hydraulic models. These analyses have been performed generating synthetic intermittent observations adopting a specific error behaviour considering the uncertainty of the Crowdsourced data, underlying the influence of the quantity and the position of these observations to the model performance. Further analysis and inspections need to be done using both more complex models, such as Quasi-2D hydraulic models and real VGI data, whose availability is becoming more and more abundant because of the tremendous spreading of smart devices and social media accounts.

4.5.2. Methodology

VGI observation in terms of water depths could be related to the channel, but most likely to the floodplain domain, where people can be directly affected by flood. In case the VGI observation is related to a channel cell of the domain, the technical procedure of the data assimilation is implemented as explained in Section 4.3.1 for assimilating the observation from static sensors, except for the observation errors that will be explained in Section 4.5.3.

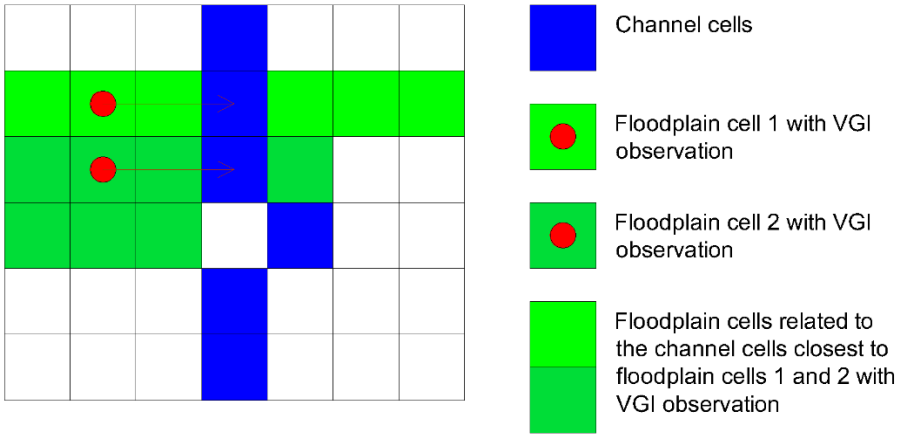

Figure 84. Scheme of the floodplain and channel cells corrected by a VGI observation in a floodplain cell

In case of VGI observation in a floodplain cell or group of cells, the procedure identifies all closest channel cells related to the floodplain cells affected by observations. Than the correction

is done to all the floodplain cells whose closest channel cells are the ones previously identified (Figure 84).

The water depth updating given by the DA procedure is propagated downstream and upstream using the gain function showed in Equation [57]. In case of simultaneous assimilation of different VGI data, the gain function can be applied with the same principle proposed in Section 4.3.1 and illustrated by Equation [61], assigning a weight to the water level correction in a cell proportional to the inverse of the distance between the cell and each observation.

4.5.3. Observation errors

The observation errors related to VGI are given by the composition of three different factors: *location error*, *timing error* and the *water depth estimation error*.

- **Location error (err_{loc}^{VGI})**

Usually Data Assimilation models consider the location of an observation as certain. This is reasonable for typical oceanographic or hydrologic measurement methods, so the issue related to a potential location error is still not much deepened in literature. However, Sengupta et al. (2012) implement successfully an adjusted linear Kalman Filter methodology in order to take in to account the location error, since their case study involved the assimilation of animal-borne sensor data with uncertain location. For their case study, the observation y_t is not characterized by the classical random noise equal to $N(0, v_t)$, but it includes also a location error, so that the overall error is given by $N\big(0, V(y_t|\xi_t, y_{\leq t-1})\big)$ where ξ_t is the estimate of the true location X_t, expressed as the random variable $X_t \sim N\big(\xi_t, V(X_t|\xi_t)\big)$ and $V(y_t|\xi_t, y_{\leq t-1})$ is expressed with a first-order Taylor approximation as:

$$V(y_t|\xi_t, y_{\leq t-1}) \approx V(y_t|X_t, y_{\leq t-1}) + \left\{\left[\frac{\partial}{\partial X_t}\big(E(y_t|X_t, y_{\leq t-1})\big)\right]_{X_t=\xi_t}^{T} V(y_t|\xi_t)\left[\frac{\partial}{\partial X_t}\big(E(y_t|X_t, y_{\leq t-1})\big)\right]_{X_t=\xi_t}\right\} \quad [69]$$

Where $E(y_t|X_t, y_{\leq t-1})$ is the expectation of the observation y_t at the true position X_t. With this adjustment, the covariance and the Kalman gain are modified considering the new expression of the observation error. In the final discussion the authors suggest to adopt their methodology also for non linear filtering, such the EnKF.

Locational information of VGI, for example tweets, can be uncertain because geotags are available for only a very small number of tweets and may deviate from the actual location of the observation (Hahmann et al., 2014).

If the VGI element is a picture, even if the geotagged position is in a wrong place, the image could provide landmarks to place the correct position of the observation, whose location error can be lower than the resolution of the large-scale hydraulic model, thus negligible. If the VGI is a text message from a social platform or it is an image without any recognizable landmark, the geotagged position of the VGI can vary considerably depending on its typology. McClanahan and Gokhale (2015), found an average error of 1720 m from derived locations from the text in tweets, in New York City.

Brouwer et al. (2017) stated that if the geotagged VGI is pinpointed, the error location, for a case study in York (UK), has a standard deviation σ around 50 meters, with outliers even of 200 meters. If the geotagged location is referred to streets or neighbourhoods, the location error has 290 m of standard deviation with outliers that go to 2000 meters. For another case study in Jakarta, Brouwer (2016) found that the location error for tweets can be very different if the geotagging mentions Point of Interest (POI) (σ=236 m, max≈2000m), streets (σ=659 m, max≈4000m), or neighbourhoods (σ=642 m, max≈2000m). Eilander et al. (2016) estimated the likelihood of flooded areas by harvesting tweets considering the number of tweets found for individual administrative areas rather than knowledge about the actual errors in the data used. The perturbation of the VGI observation given by locational error for the i-element of the ensemble can be expressed as a noise error normally distributed with zero mean and variance R_{loc}^{VGI}:

$$err_{loc,i}^{VGI} = N(0, R_{loc}^{VGI}) \quad [70]$$

In the adopted hydraulic model, this error can be implemented moving the position of the cells to which a VGI observation is assigned considering how much times the location error of the i-element of the ensemble is greater than resolution of the model both for x and y coordinates (Figure 85):

$$(X_i^{VGI}, Y_i^{VGI}) = \left(X^{VGI} + N(0, R_{loc}^{VGI}), Y^{VGI} + N(0, R_{loc}^{VGI})\right) \quad [71]$$

Where X^{VGI} and Y^{VGI} are the North and East coordinates of the geotagged VGI.

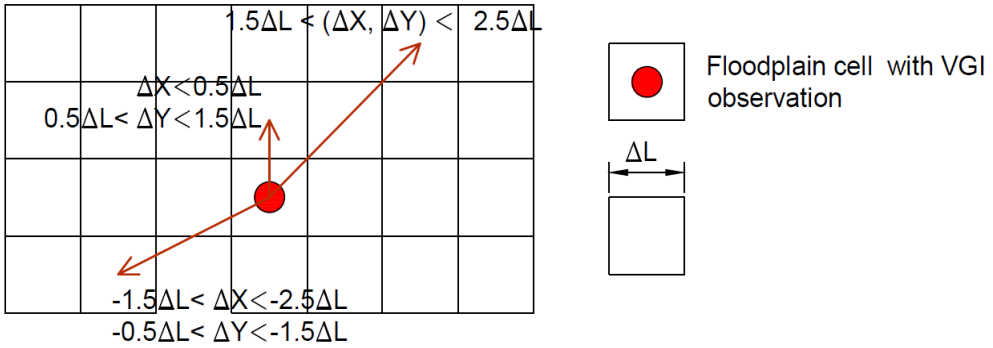

Figure 85. Example of perturbation error due to location for VGI observation

The variance R_{loc}^{VGI} varies depending on the type of geotagging. Considering a similar approach to Sengupta et al. (2012), for the time step in which an observation is assimilated, if the location of the observation related to *i*-element of the ensemble (X_i^{VGI}, Y_i^{VGI}) is different to (X^{VGI}, Y^{VGI}) , the observation at this location is derived considering how it could be if an observation at (X_i^{VGI}, Y_i^{VGI}) is assimilated. Hence, the water depth at location (X^{VGI}, Y^{VGI}) is given by:

$$WD^{+}_{(X^{VGI},Y^{VGI}),t+1} = WD^{+}_{(X_i^{VGI},Y_i^{VGI}),t+1} + \left(WD^{-}_{(X^{VGI},Y^{VGI}),t+1} - WD^{-}_{(X_i^{VGI},Y_i^{VGI}),t+1}\right) \quad [72]$$

In other words, the observation at the original location (X^{VGI}, Y^{VGI}) is measured starting from the observation at the perturbed location (X_i^{VGI}, Y_i^{VGI}) and considering the reciprocal water level differences before the updating step of the Data Assimilation.

- **Timing error (err_{time}^{VGI})**

The timing error, namely the error of assigning a specific time to a VGI information is composed of two components.

The error related to the wrong time set in the device: this error is not more than few seconds or few minutes and can be negligible considering that for large scale analysis, the change of water levels in rivers drained by thousands of square kilometres is almost the same in a time lag of seconds compared to the model error and to the water level derivation error.

The lag time between the information acquisition and the posting time: if the VGI data has not text reporting the exact time of the information to be used, or this information is imprecise, the time between the information acquisition and its sharing by the user can be considerably high, i.e. several hours. In order to take in to account of this error, the model can perturb the timing of the VGI information.

The time step related to the VGI observation of the i-element of the ensemble can be perturbed using the following expression:

$$t_i^{VGI} = t^{VGI} + N\left(0, R_{time}^{VGI}\right) \quad [73]$$

Being $N\left(0, R_{time}^{VGI}\right)$ a noise error normally distributed with zero mean and variance R_{time}^{VGI}[hours].

If at time step t_k the i-element of the ensemble is affected by a VGI observation, its correspondent perturbed observation is directly given by Equation [34]. If the i-element of the ensemble is not affected by an observation at time t_k but it has been already affected by the observation at time t_{k-1}, its water depth observation at time t_k should be the value assumed in case of a correction given by Equation [34] at time t_{k-1}. Lastly, if the i-element of the ensemble is not affected by an observation at time $t_k$but it will be affected by the observation at time t_{k+1}, its water depth observation at time t_k should be the value assumed by its variable if no updating has been performed to that simulation at time t_k.

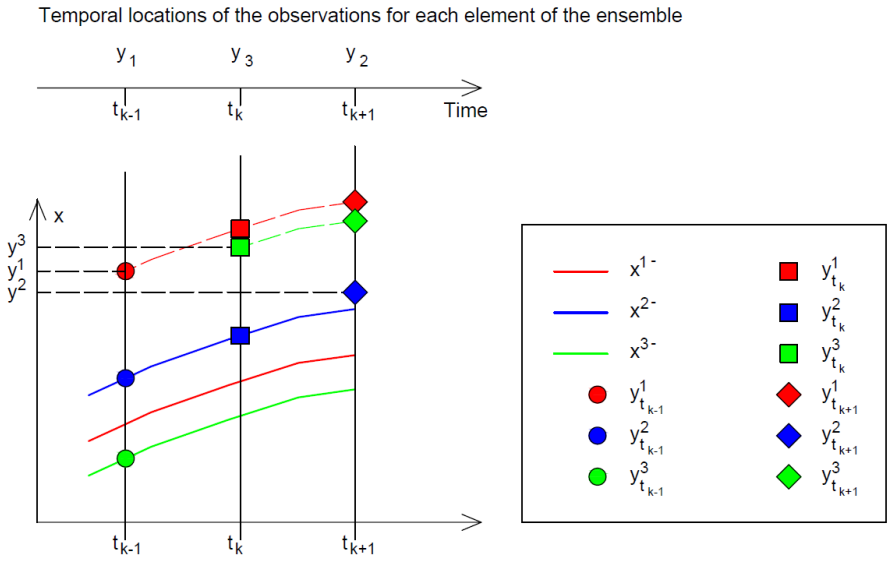

Figure 86. Scheme of the perturbation of the ensemble considering the timing error. The continuous lines are the forecasting variables; the dashed lines are the auxiliary simulations to set each time step the value of the observation for every ensemble.

- **Water depth derivation (err_{wd}^{VGI})**

Water surface elevation have been derived by adding the water depth observed from VGI data to the local ground elevation (Fohringer et al., 2015; Brouwer at al., 2017). Water depths can be derived both from image interpretation or from text messages describing the flood. Brouwer (2016) observed that water depths mentioned by tweet messages are generally higher than the water depths derived from the visual interpretation of the photographs, with errors lower than

55 cm. However, a statistical test could not confirm the mean error in water depth was any different from zero, so the water depth estimation errors have been simulated using a normal distribution with zero mean and a standard deviation of 20 cm. Mazzoleni et al. (2017) reproduced the uncertain nature of water depth observations from synthetic dynamic sensors (i.e. citizen with smartphones) expressing their perturbation as: $WD_t = WD_{true} + WD_{true} \cdot U(\gamma_{min}, \gamma_{max})$ where γ is a random stochastic variable function of the time, having minimum and maximum values ranging from -0.3 and +0.3. The water depth are then inserted in an hydrologic model where, in order to take into account the uncertainty of the observed flow hydrograph, a further noise with zero mean and standard deviation equal to $R_t = \left(\alpha_{t,s} \cdot Q_t^{true}\right)^2$ is assigned to the measured flow. α_t is a random stochastic variable uniformly distributed in time t and space s as $U(\alpha_{min}, \alpha_{max})$ where α_{min} and α_{max}were set to 0.2 and 0.5, thus considering the unpredictable accuracy of the crowdsourced observations.

4.5.4. Crowdsourced data sample

For the *November 2012* event, three images have been selected for being used in the Data Assimilation model. These images are related to three different places located along the computational domain in correspondence of the urbanized areas: Orte Scalo, Torrita Tiberina and Monterotondo (Figure 87). The selected VGI data, being images in which landmarks are clearly visible, are affected by a low location error that can be neglected (R_{loc}^{VGI}=0) if compared with the resolution of the hydraulic model. On the other hand, the timing of the images is much uncertain, thus the time has been perturbed between -30 min and + 30 min for each image. The water surface elevation has been derived as a sum of the terrain elevation given by the LiDAR DTM and the depth deduced by the visual interpretation of the image. The perturbation of the water surface elevation for the i-element of the ensemble is assigned as follows:

$$err_{wse,i} = N(0, R_{DEM}) + N\left(0, R_{Depth}\right) \quad [74]$$

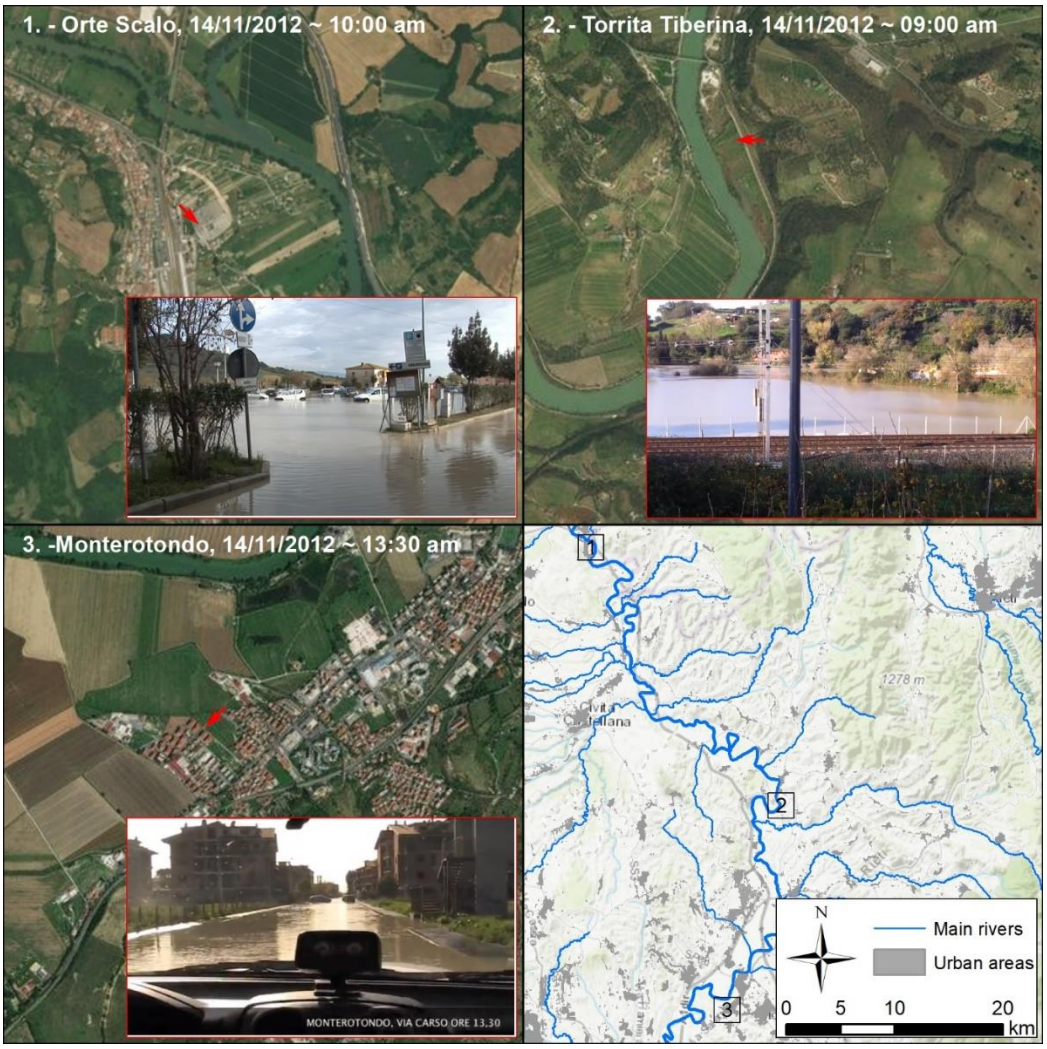

Figure 87. Position of the VGI images for the November 2012 event

Where R_{DEM} is the variance related to the DEM error, assigned equal to 0.3 m (See section 4.4.2.3) and R_{Depth} is the variance of the water depth derivation from visual interpretation, assigned equal to 0.2 m, as in Brouwer (2016). However, a lower limit of 0.05 m has been assigned for the water depth derivation in order to not have negative or zero values of water depths. The water depth has been deduced comparing the images during the flood with the same images get in dry conditions from Google Street View.

4.5.5. Results and discussion

Figure 88 and Figure 89 show the hydrographs respectively at the closest channel cells to the floodplain cells were VGI observation has been captured and at the stage gages locations. In the first graphs, the corrections produce an evident decreasing of the simulation spread, but a slight modification of the average levels. The correction begins before the time location of the

observed VGI data (points in magenta colour) because of the timing error applied to the DA model. On the other hand, at the stage gage locations, the corrections are less evident because of the gradually decreasing effect of the gain function and because of the damping effect of the correction propagation. This aspect suggests that a more significant effect of VGI data for improving the model performance can be obtained with a largest number of observation data, whose influence on the model is limited by their relatively low reliability that has been assigned. The possibility af having an increased availability of VGI data can be considered very likely in future, given the high increasing of smart phone and social media users (Figure 3). As in the case of assimilating the SI, the overall improving of the performance indexes in case of updated simulations can be considered negligible (Figure 90) because of the spatially and temporally local effect of the correction.

Figure 91 shows the profile correction at the time steps when VGI are assimilated in case of no-updated and updated simulations. The plots illustrate the effect of the gain function (Equation [59]) for propagating the correction upstream and downstream in order to avoid a shock in the water profile at the location of the correction.

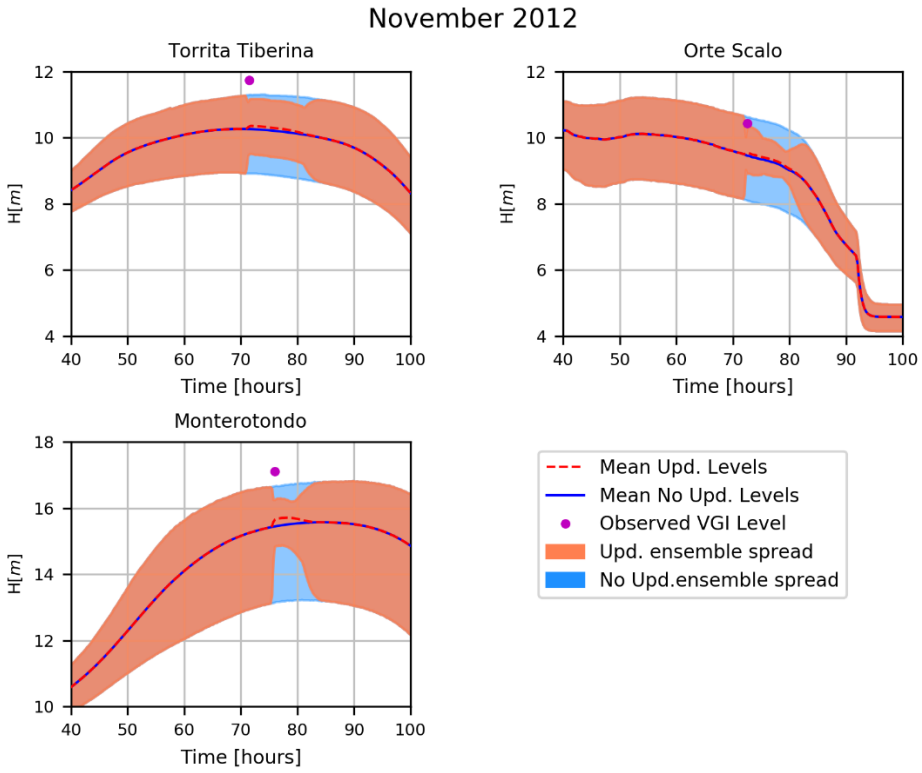

Figure 88. Hydrographs of the updated and no-updated simulations assimilating the 3 VGI data at the correction locations. Event: November 2012

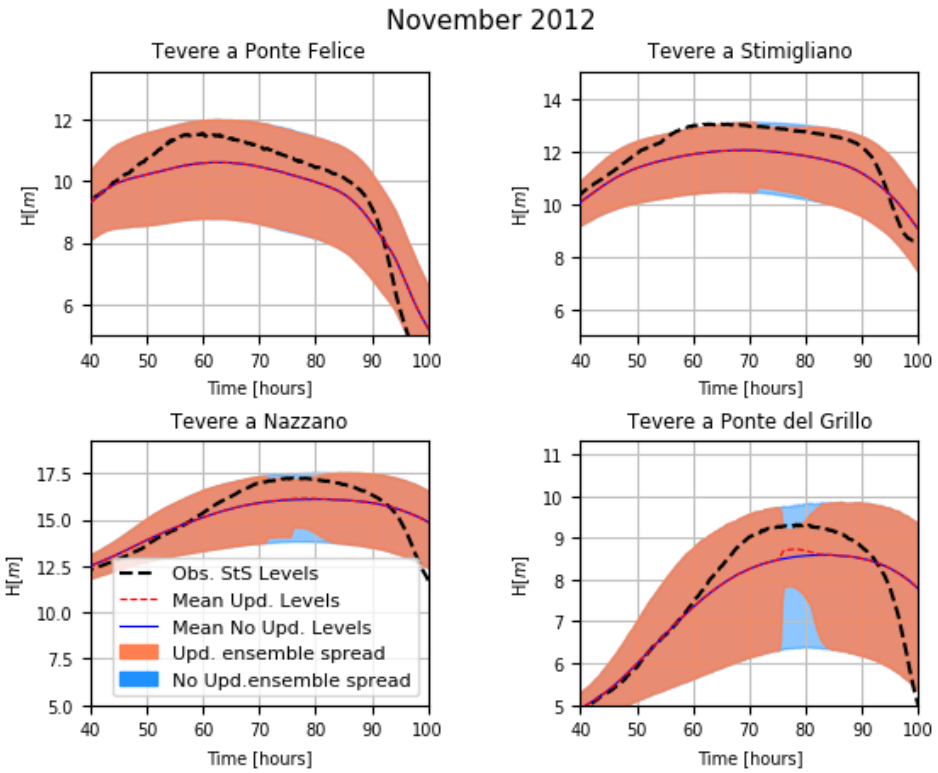

Figure 89. Hydrographs of the updated and no-updated simulations assimilating the 3 VGI data at the stage gages locations. Event: November 2012

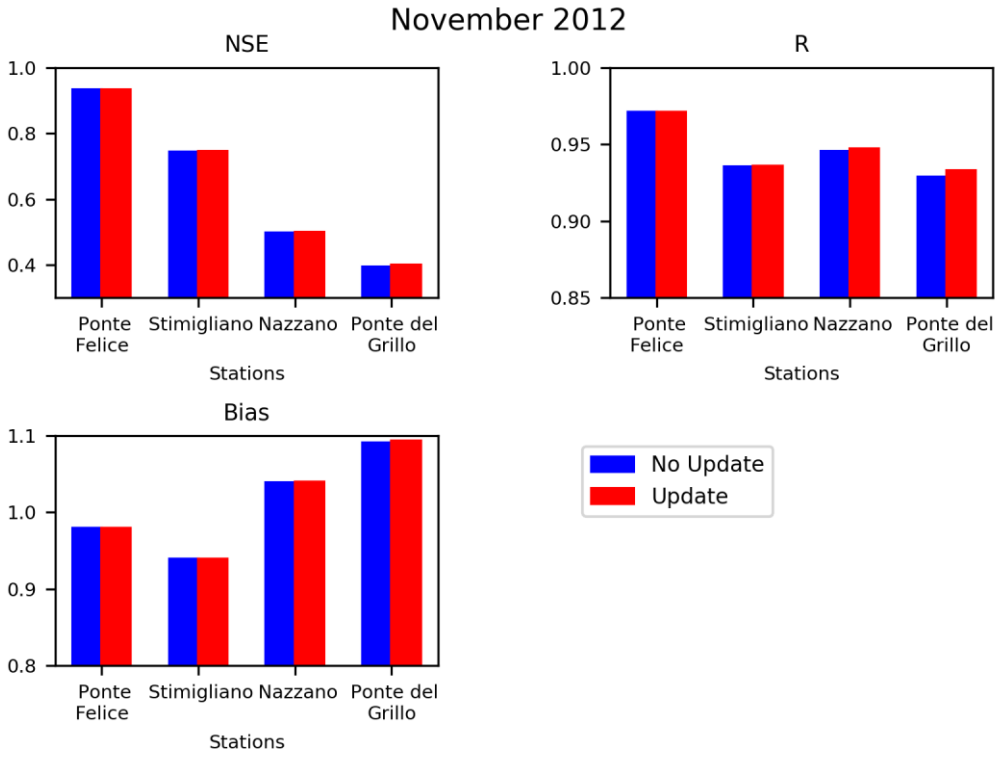

Figure 90. Performance indexes for no-updating simulations assimilating the 3 VGI data. Event: November 2012

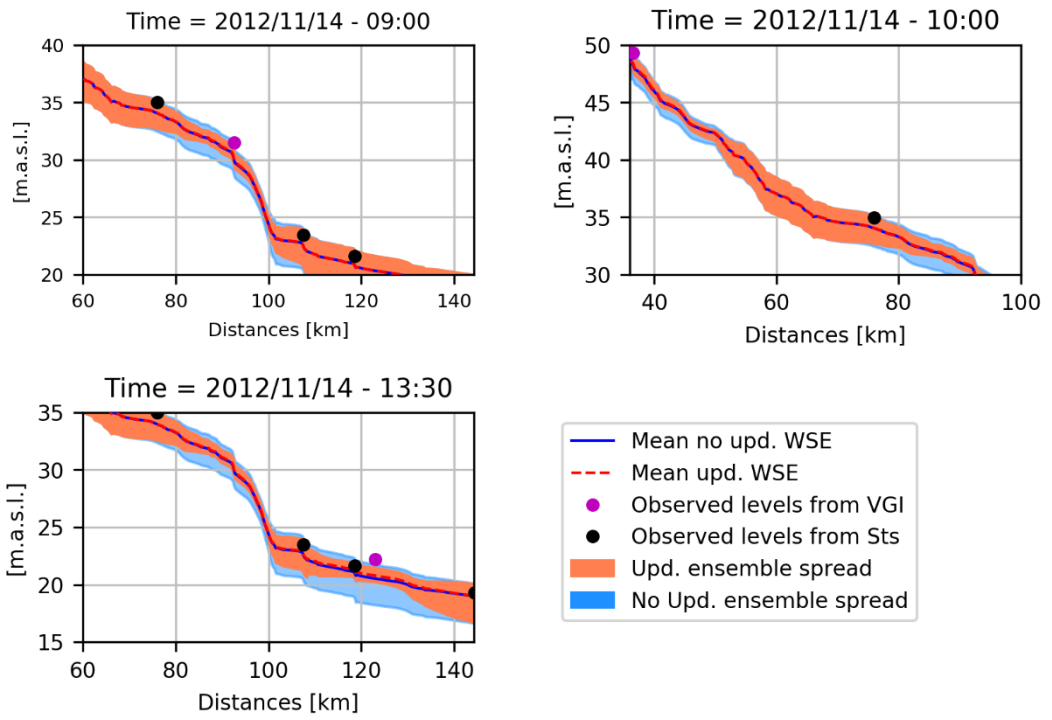

Figure 91. Hydraulic profiles at the time of the VGI observations for the no-updated and updated simulations assimilating the VGI observations.

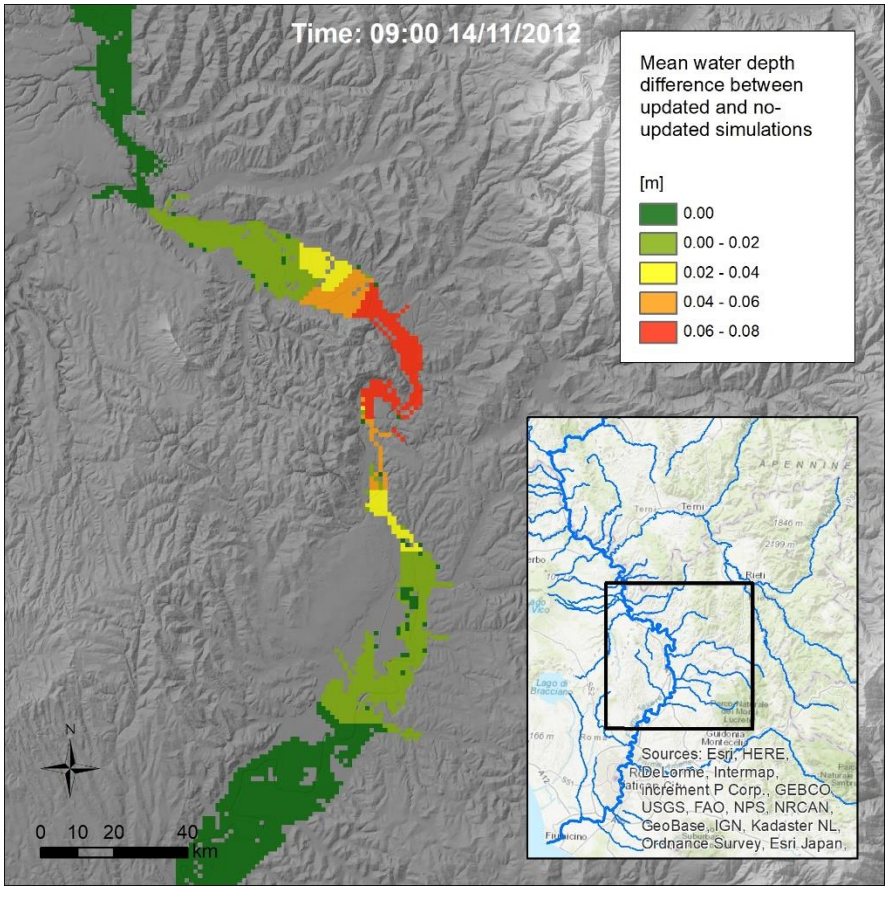

Figure 92. Map of the water level correction at the time of the Torrita Tiberina VGI acquisition (09:00 14/11/2012)

The correction of the water levels does not considerably affect the flood extension considering the mean values of the water surface elevation. For example, at 9:00 on 14/11/2012, namely at the time of the correction of the VGI data from Torrita Tiberina, the increasing of the flooded areas after the correction is only equal to 0.079 km^2. Figure 92 show the spatial distribution of the mean water level corrections at the time of the Torrita Tiberina VGI acquisition. The correction stays under 8 cm and it is evident how the gain function influences the propagation of the correction.

4.6. Simultaneous assimilation of all observations

4.6.1. Methodology

As final analysis of the DA application, the three different types of observations have been implemented in the same simulation (November 2012), assigning to each of them their relative reliability through the determination of the observation error.

A failure of the static sensors operation has been simulated, assuming an interruption of the gage measurements at the time 11/11/2012, 09:30. This failure is assumed shortly before the peak flow, so that the other less accurate observations (SI and VGI) could cover the lack of the StS observations. In case of simultaneous observations from different measurement types for the same area, the priority is given to the most reliable measurement, thus the measurement with the smaller error spread. In this specific case, the Satellite observation occurs in a time step that overlaps the VGI observation in Orte Scalo, whose temporal location is distributed over time considering the timing error. At the time of the overlapping, the priority is given to the SI observation, that is considered more reliable and also spatially distributed.

4.6.2. Results and discussion

Figure 93 shows the hydrographs at the stage locations comparing the simulations in case of no-updating and updating the three different types of measurements. After the simulated failure of the StS, the spread of the ensemble related to the updated simulation gradually widens until it reaches the spread of the no-updated one; shortly after the peak flow, the combination of the SI and VGI assimilation generate another narrowing of the spread, with small increasing of the mean water levels. The correction using the VGI observation has a lower influence than the one due to the SI observation, because of the dampening of the correction given by the gain function (Equation [59]) proportional to the distances between the stage gages and the VGI locations.

At the VGI correction locations (Figure 94), the effect of the correction related to the StS is dampened by the gain function. On the other hand, the correction of the VGI is more heightened at the VGI correction. In particular, in Monterotondo the different spreads due to the SI and the VGI correction are quite evident.

The improvement of the correction is confirmed numerically by the NSE and Bias coefficients (Figure 95). The combined assimilation of the three types of observation brought to a better overall improvement than the ones obtained in case of assimilation of only SI (Figure 79) and

VGI (Figure 90) data. This demonstrates the potential benefit of assimilating simultaneously different observations together.

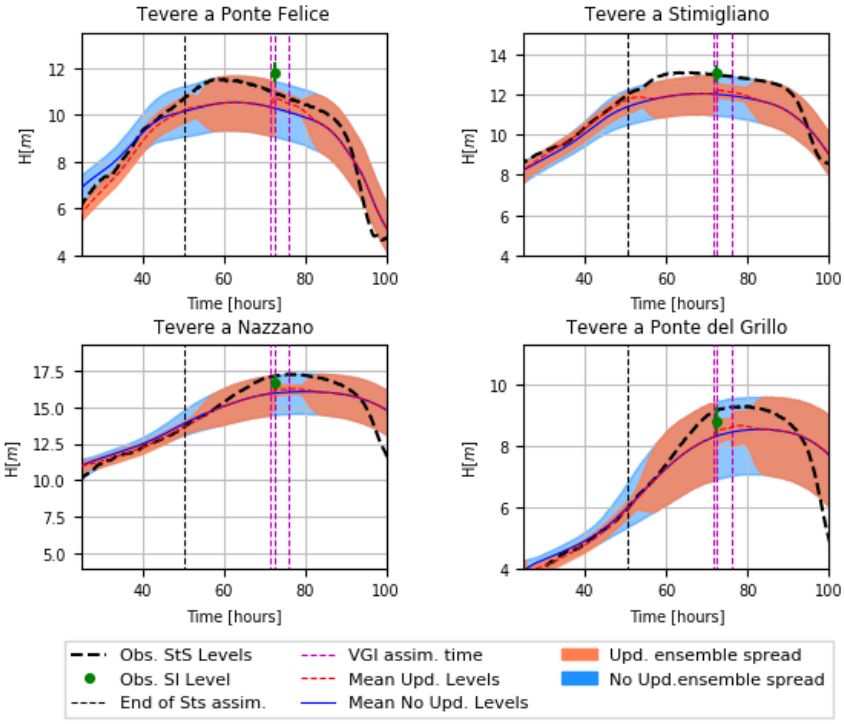

Figure 93. Hydrographs of the updated and no-updated simulations assimilating all types of observation at the stage gages locations. Event: November 2012

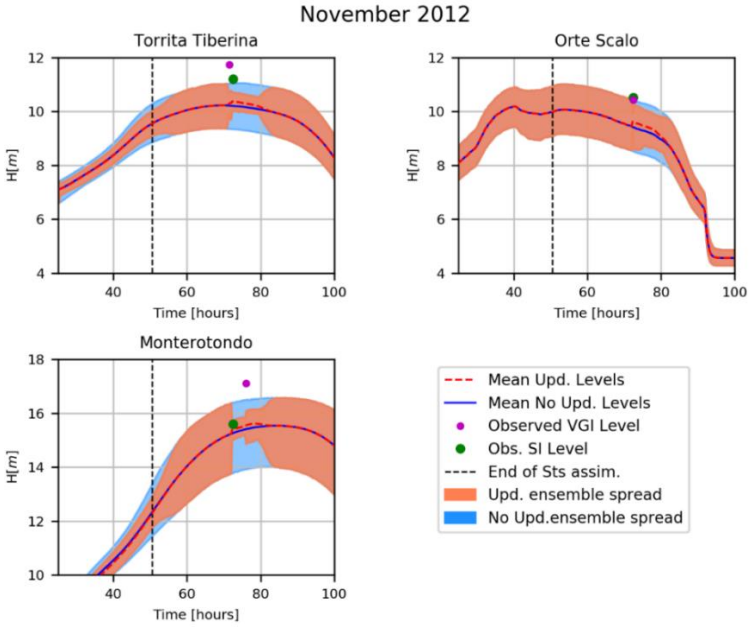

Figure 94.Hydrographs of the updated and no-updated simulations assimilating all types of observation at the VGI correction locations. Event: November 2012

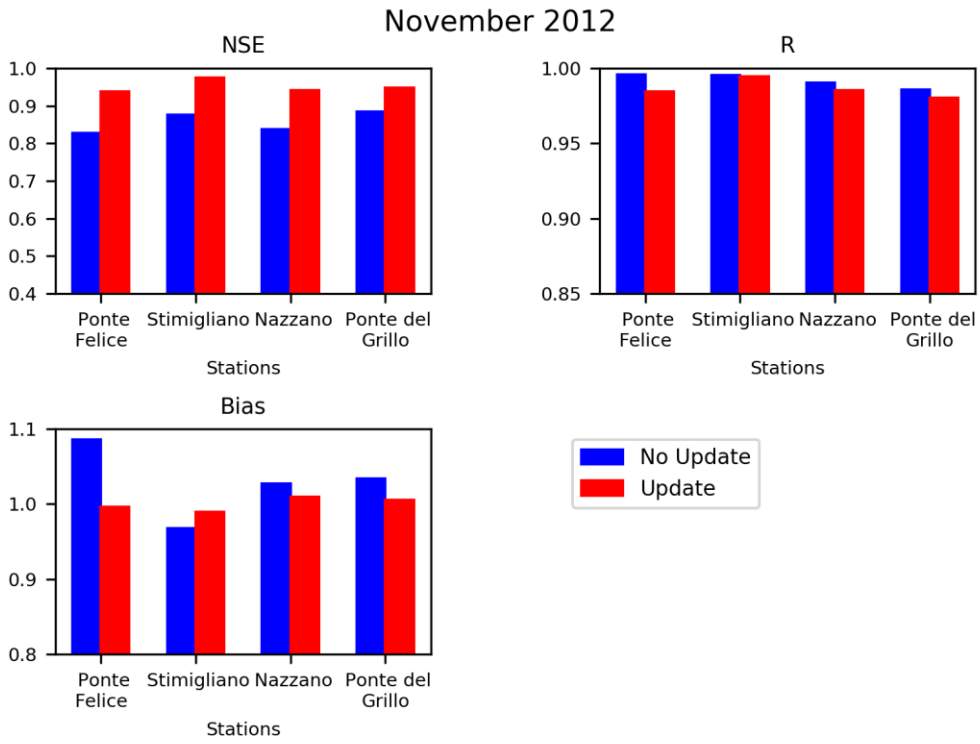

Figure 95. Performance indexes of the non-updated and updated simulations with all types of observations

5.Conclusions

In this section, the principal outcomes, limitations and future insights of this research are summarized. Specifically, in Section 5.1 the outcomes related to every insight addressed in the work are illustrated, from the hydrologic and the floodplain delineation models, to the Quasi-2D hydraulic model and the application of the Data Assimilation methodology for each type of observation and for their simultaneous integration. Section 5.2 is focused on underlining the novelties and the limitation of the work, giving also some recommendations for improving the analysis and making future developments.

5.1. Research outcomes

In this work, an investigation on the integration of hydro-geomorphic models, Quasi-2D hydraulic models, traditional, new and non conventional observation data has been performed.

The main case study of this work is the Tiber River basin, that is the second largest basin in Italy, and in particular the Middle Valley of the basin plays a strategic role for the protection of the city of Rome and also of small urbanized areas that sometimes are affected by flood related damages and fatalities.

As forcing input for the Quasi-2D hydraulic model in case of small ungauged basins, an hydrologic model has been developed and implemented in python environment. This WFIUH model, takes the basic inspiration from the one developed by Grimaldi et al. (2012) The IUH of the model is calculated considering the distribution of the flow velocities cell by cell as function of the slope, land use and soil type. However, the way in which the parameters related to the flow velocities are calculated is different from Grimaldi et al. (2012), since the time concentration calculated with empirical formulas has not been taken in to account, but these parameters are chosen through a calibration and validation considering four small gaged basins that are part of the Tiber River basin. The errors derived by the validation in terms of NSE, R and Bias are taken in to account for evaluating the model error in the DA implementation.

The computational domain of the hydraulic model has been delineated using a hydro-geomorphic model in order to remove the sloping areas of the basin that cannot be affected by fluvial floods. This procedure can help the modeller to optimize the extension of the computational domain that usually is delineated by the analyst from its experience or using standard flood hazard maps. These boundaries of these maps could be limited by levees, excluding the some parts of the domain that can be interested by potential flood in case of overtopping or levee breach. Besides the delineation of the computational domain for the DA application, a further analysis of the floodplain delineation algorithm for large scale flood-prone area mapping has been performed as a secondary independent aim of the proposed research. The DEM-based model is an application of a geomorphic law that relates the contributing area to the flow height as proposed by Nardi et al. (2006). This original formulation involved the input of the peak discharge at the outlet, the scaling of the peak discharge along the river network and the derivation of the flow height by extracting floodplain cross sections and using the Chezy's law. In this work, the peak discharge of the basin at the outlet has not been involved, but the parametrization of the scaling law have been performed through an automatic and

recursive numerical comparison of the floodplain polygon extension with the one of the Italian standard flood hazard maps. A methodology for choosing the threshold area considering a minimum width of the floodplain equal to two cells has been proposed. Moreover, a sensitivity of the floodplain model to the DEM resolution and the hortonian stream orders has been quantified. This sensitivity suggested to modify the floodplain delineation algorithm in order to take in to account the variability of the b parameter with the stream orders, thus improving the F index of 6%. The aim of this analysis is to provide a reasonable parametrization for a large scale flood-prone area mapping not only for defining the computational domain of an hydraulic model, but also for delineating the floodplain extension in the river network on which advanced hydraulic modelling studies are absent. For this reason, the optimal parametrization of the *b* parameter has been also extended for the entire Italian territory, imposing a constant *a* parameter and adopting the SRTM 3 arc DEM for all the sub-basins where the standard hazard flood maps are available. This parametrization confirmed the average low variability of the *b* parameter, especially for high stream orders, suggesting to perform a larger scale floodplain delineation mapping, as illustrated in Figure 35.

The adopted hydraulic model is FLO-2D PRO, a Quasi-2D model that applies the continuity and the momentum equations in 1D in the channel and in 2D when the flow surmounts the river banks and goes in the floodplain. The model has been calibrated varying the channel roughness.

As Data Assimilation method, the Ensemble Kalman Filter has been applied. The method requires to generate and ensemble of the state variable considering the model errors, given by the input flows from the stage gages and the hydrologic model, and by the model parameters. The ensemble size has been chosen applying the criterion proposed by Anderson (2001).

The observation measurements from stage gages has been assimilated applying the water level correction to the channel cell relative to the stage gage and to all the floodplain cells closest to the stage gage. The correction is then propagated upstream and downstream with a gain function adopting a similar approach to Madsen & Skotner (2005), with the utmost cares of considering the contiguous effect of more gages at the same position and of avoiding counterslopes of the water levels from upstream to downstream. The assimilation of the stage gage measurements led to an improvement of the model performance in terms of bias, Person correlation and NSE. Moreover, the spread of the ensemble has been significantly reduced with the updating of the state variable. The correction of the state variable caused also an evident variation of the flood extent in some flat areas of the floodplain domain.

A procedure for extracting the water levels from a satellite image for being assimilated in the hydraulic model has been developed. This procedure requires a series of steps. Firstly, a technique for extracting the water extension from the satellite image has to be applied. This procedure changes depending on the type of remote sensed product adopted. As auxiliary analysis for the DA application, the most important water indexes for multispectral images gathered from literature have been tested in few case studies in which Landsat images and reference maps related to past floods were available. The analysis confirmed that the most recent water indexes seem to be the most effective even in case of flood events. The testing of the water indexes suggested to carry out, a preliminary analysis using of the thermal bands for improving the water indexes performance. That testing has been strongly limited by the small sample of observed floods and can be considered as a suggestion for a future study.

The second step for extracting the water levels from satellite images is the numerical comparison, using Equation [6], of the water extension derived from the satellite image with the extension of the flood simulated by each element of the hydraulic model ensemble at the same time of the SI acquisition. To compare the flood maps derived by the hydraulic models at the same resolution of the satellite image, a GIS based geostatistical methodology based on the use of an high resolution DEM is adopted. The water levels derived from the SI are obtained as a combination of the water levels obtained by the hydraulic model. The assimilation of this indirect observation of the water levels took into account the errors of each of the mentioned steps, from the water detection technique, to the DEM related errors, to the errors related to the combination of the hydraulic profiles of the ensemble of the simulations.

The results of assimilating the satellite image show a substantial improvement of the model at the peak flow, at the time of the SI acquisition. The applied methodology allowed to perform the water level correction to the whole domain, since Equation [65] is applied to all the channel cells (and their related floodplain cells) that are part of the domain. This improvement is gradually decreased with the lead time until it is nullified after about 8 hours. The performance indexes relative to the simulation during the whole flood event have a relatively small improvement in case of updated simulation, because of the limited amount of hours when the effect of the correction can be observed.

The third application of the DA methodology is with the VGI data as observations. The observation error related to these data is due not only to the estimation of the water depth deduced by the data, but also to the their location and the timing. The implementation of these

two error components in DA application are not well documented in literature. In this work, a way of taking in to account these components has been proposed. The application of the VGI assimilation has been carried out using three images gathered from social media related to three different zones of the domain. These three observations belong to almost the same time window that is the morning after the flow peak, when people woke up and observed the ongoing effects of the flood expansion. Results show local improvements in the simulated water levels, mostly in terms of reduction of uncertainty, but not significant in term of mean average water levels. Moreover, as in the case of assimilating the SI, the performance indexes relative to the simulation during the whole flood event have a negligible improvement, partly because of the same reasons explained in the case of assimilating the SI image, and partially because of the local correction of the water levels that is not in the same position of the stage gages, where performance is measured.

Finally, an integration of all the three types of observations in the Data Assimilation model has been simultaneously performed. Since the Static sensors observations are the most reliable but also the most expensive ones, their functioning has been assumed interrupted before the time of the peak flow in order to partially overcome the lack of StS measurements with the available SI and VGI observations. The performance indexes of the updated simulation combining all the three observations are better than the ones obtained assimilating only SI or VGI data, as expected.

5.2. Limitations and future developments

The proposed research has different limitations that have to be mentioned for defining the appropriate context of its application and also for providing insights of future development.

The implemented parsimonious hydrologic model is suited for determining the flow hydrograph of small basins characterized by an impulsive response. The represented physics of the hydrological process does not directly take in to account of the groundwater flow and the presence hydraulic control structures such as dams and weirs. For this reason, the application of this model is not recommended for basins whose groundwater component during the peak flow is strongly relevant or with one or more control structures that are able to greatly modify the flow regulation. However, the uncertainties related both to the input and to the schematization of physical processes are taken in to account in the formulation of the Data Assimilation model, perturbing the input inflow that has been determined from the hydrologic model. Furthermore, the SCS-CN method for determining the infiltration rate can be used only for a single rain event, because it does not consider the increase of the infiltration soil capacity after the rain event due to evapotranspiration and percolation. This enforces to re-set the soil parameters every time an extreme event has to be simulated. More advanced hydrologic models, if supported by adequate inputs data, could reduce the uncertainties related to the whole hydraulic model error and thus better predicting the flood dynamics. In this context, the simplified model is adopted assuming to work in a data poor environment with ungauged basins whose contribution need to be taken in to account.

The floodplain delineation algorithm adopted for defining the hydraulic computational domain proved to be a quick tool for an expeditious delineation of the flood prone areas, that can be consider as a secondary aim of the proposed research. However, this tool can be affected by the terrain analysis issues related to flat areas or spurious elements in the DEMs that could compromise the flow direction grid, for example excluding zones that should be connected to the computational domain. These issues are well known and have been already addressed in literature (Jenson & Domingue, 1988, Garbrecht & Martz, 1997a; Garbrecht & Martz, 1997b; Jana et al., 2007, Nardi et al., 2008). A careful check of the obtained results has to be done by the modeller especially if flat areas or large size hydraulic structures are part of the computational domain. However, the performed parametrization can be extended to larger domains to have flood prone area mapping even at global scale, since the freely available DEMs cover most of emerged land.

The application of a DA methodology to a Quasi-2D hydraulic model able to acquire different types of measurements is one of the novelties of this research, since the very few cases of a 2D model application in a DA framework are related to only static stage gages (Kim et al., 2012, Kim et al., 2013) or to only satellite image (Hostache et al., 2010) and there are also few cases of using Crowdsourced data in simplified hydrologic and 1D hydraulic models (Mazzoleni et al., 2015, Mazzoleni et al., 2017 and Mazzoleni, 2017).

Because of the scarcity of new data in the case study, the DA methodology integrating all the three types of observation data has been performed for only one historic flood event. This means that further testing and analysis need to be carried out for evaluating the robustness of the methodology.

Moreover, the use of a multispectral image as reference map for assimilating the derived distribution of the water levels can be considered as a rare occurrence, since in most of the cases, during the flood events the Landsat images are corrupted by clouds. This is confirmed also by the difficulty of finding an enough number of Landsat images not corrupted by clouds and their relative reference maps for testing the current water indexes in literature and new potential indexes. In this regard, the analysis carried out in Section 3.7.2.1 can be considered as preliminary but not statistically solid; nevertheless the preliminary results of the water indexes testing confirm the better behaviour of the most recent ones compared to the previous ones even during food events. The limitations related to the multispectral images can be easily overcome adopting SAR images, that can penetrate the clouds and can be characterized also by higher resolution.

The assimilation of only three VGI data brought to a slight local correction of the mean water levels simulated by the model. In case of updating, the spread of the ensemble is reduced at the time of the correction with the VGI observation, but at the stage gages the correction is considerably reduced and the performance are not appreciably improved. This behaviour suggest that a richer VGI data environment could lead to more significant improvements. The possibility of having a richer VGI data environment is very plausible considering the incredible increasing of smartphone users and social media accounts (Figure 3). A way of gathering in real time or near-real time VGI data is an important scientific challenge (Gao et al., 2011). Automatic methods for extracting social media information (e.g. Twitter API) are available, but additional time is needed to interpret the information and deduce water levels if users are not

trained. Innovative techniques for image interpretation such as distance metric learning (Yu et al., 2017) could prove to be of great support for this purpose.

Finally, the promising results of integrating all the three observations together in the Data Assimilation framework confirm the potential of new and non-conventional data for improving the performance of flood dynamics even in terms of uncertainties of the model prediction. This contribution can be particularly crucial in data scarce environment, where distributed measurements of physical variables (rain gages, soil moisture, topography etc.) can affect the reliability of the model.

References

Abbott, M. B., Bathurst, J. C., Cunge, J. A., O'Connell, P. E., & Rasmussen, J. (1986). An introduction to the European Hydrological System—Systeme Hydrologique Europeen,"SHE", 1: History and philosophy of a physically-based, distributed modelling system. *Journal of hydrology*, 87(1-2), 45-59.

Abdelkader, M., Shaqura, M., Claudel, C. G., & Gueaieb, W. (2013). A UAV based system for real time flash flood monitoring in desert environments using Lagrangian microsensors. *In Unmanned Aircraft Systems (ICUAS), 2013 International Conference. IEEE,* 25-34.

Aerts, J. C., Botzen, W. W., Emanuel, K., Lin, N., de Moel, H., & Michel-Kerjan, E. O. (2014). Evaluating flood resilience strategies for coastal megacities. *Science*, 344(6183), 473-475.

Alfieri, L., Bisselink, B., Dottori, F., Naumann, G., Roo, A., Salamon, P., . . . Feyen, L. (2016). Global projections of river flood risk in a warmer world. *Earth's Future, 5(2)*, 171-182.

Alfieri, L., Salamon, P., Bianchi, A., Neal, J., Bates, P., & Feyen, L. (2014). Advances in pan-European flood hazard mapping. *Hydrological Processes, 28(13)*, 4067-4077.

Alsdorf, D. E., Rodriguez, E., & Lettenmaier, D. P. (2007b). Measuring surface water from space. *Reviews of Geophysics*, 45(2).

Alsdorf, D., Bates, P., Melack, J., Wilson, M., & Dunne, T. (2007a). Spatial and temporal complexity of the Amazon flood measured from space. *Geophysical research letters*, 34(8).

Alsdorf, D., Han, S. C., Bates, P., & Melack, J. (2010). Seasonal water storage on the Amazon floodplain measured from satellites. *Remote Sensing of Environment*, 114(11), 2448-2456.

Anderson, J. L. (2001). An ensemble adjustment Kalman filter for data assimilation. *Monthly weather review, 129(12)*, 2884-2903.

Andreadis, K. M., & Schumann, G. J. (2014). Estimating the impact of satellite observations on the predictability of large-scale hydraulic models. *Advances in Water Resources*, 73, 44-54.

Andreadis, K. M., Clark, E. A., Lettenmaier, D. P., & Alsdorf, D. E. (2007). Prospects for river discharge and depth estimation through assimilation of swath-altimetry into a raster-based hydrodynamics model. *Geophysical Research Letters*, 34(10).

Andreadis, K. M., Schumann, G. J., & Pavelsky, T. (2013). A simple global river bankfull width and depth database. *Water Resources Research*, 49(10), 7164-7168.

Aronica, G., Bates, P. D., & Horritt, M. S. (2002). Assessing the uncertainty in distributed model predictions using observed binary pattern information within GLUE. *Hydrological Processes, 16(10),* , 2001-2016.

Aronica, G., Hankin, B., & Beven, K. (1998). Uncertainty and equifinality in calibrating distributed roughness coefficients in a flood propagation model with limited data. *Advances in water resources,* , 22(4), 349-365.

Arulampalam, M. S., Maskell, S., Gordon, N., & Clapp, T. (2002). A tutorial on particle filters for online nonlinear/non-Gaussian Bayesian tracking. *IEEE Transactions on signal processing*, 50(2), 174-188.

Babovic, V., & Keijzer, M. (2002). Rainfall runoff modelling based on genetic programming. *Hydrology Research*, 33(5), 331-346.

Bardossy, A., Bogardi, I., & Duckstein, L. (1990). Fuzzy regression in hydrology. *Water Resources Research*, 26(7), 1497-1508.

Bates, P. (2012). Integrating remote sensing data with flood inundation models:how far have we got? *Hydrological processes*.

Bates, P. D., & De Roo, A. P. (2000). A simple raster-based model for flood inundation simulation. *Journal of hydrology*, 236(1), 54-77.

Bates, P. D., G., A. M., Baird, L., Walling, D. E., & Simm, D. (1992). Modelling floodplain flows using a two-dimensional finite element model. *Earth surface processes and landforms*, 17(6), 575-588.

Bates, P. D., Horritt, M. S., & Fewtrell, T. J. (2010). A simple inertial formulation of the shallow water equations for efficient two-dimensional flood inundation modelling. *Journal of Hydrology,* 387(1), 33-45.

Bates, P. D., Horritt, M. S., Aronica, G., & Beven, K. (2004). Bayesian updating of flood inundation likelihoods conditioned on flood extent data. *Hydrological Processes*, 18(17), 3347-3370.

Bates, P. D., Neal, J. C., Alsdorf, D., & Schumann, G. J. (2014). Observing global surface water flood dynamics. *Surveys in Geophysics*, 35(3), 839-852.

Bates, P., Anderson, M., & Hervouet, J. (1995). Initial comparison of 2-dimensional finite-element codes for river flood simulation. *Proceedings of the institution of civil engineers-water maritime and energy*, 112(3):238–48.

Berthet, L., Andréassian, V., Perrin, C., & Javelle, P. (2009). How crucial is it to account for the antecedent moisture conditions in flood forecasting? Comparison of event-based and continuous approaches on 178 catchments. *Hydrology and Earth System Sciences Discussions, (13)*, p-819.

Beven, K. (2001). How far can we go in distributed hydrological modelling? *Hydrology and Earth System Sciences Discussions*, 5(1), 1-12.

Beven, K. (2016). Facets of uncertainty: epistemic uncertainty, non-stationarity, likelihood, hypothesis testing, and communication. *Hydrological Sciences Journal*, 61(9), 1652-1665.

Beven, K. J. (1990). A discussion of distributed hydrological modelling. *In Distributed hydrological modelling (pp. 255-278). Springer Netherlands.*

Beven, K., & Binley, A. (1992). The future of distributed models: model calibration and uncertainty prediction. *Hydrological processes*, 6(3), 279-298.

Beven, K., & Freer, J. (2001). Equifinality, data assimilation, and uncertainty estimation in mechanistic modelling of complex environmental systems using the GLUE methodology. *Journal of hydrology*, 249(1), 11-29.

Bhowmik, N. G. (1984). Hydraulic geometry of floodplains. *Journal of hydrology*, 68(1-4), 369-401.

Biancamaria, S., Bates, P. D., Boone, A., & Mognard, N. M. (2009). Large-scale coupled hydrologic and hydraulic modelling of the Ob river in Siberia. *Journal of Hydrology*, 379(1), 136-150.

Bird, T. J., Stuart-Smith, R., Wotherspoon, S., Krkosek, M., Stuart-Smith, J. F., Pecl, G., . . . Frusher, S. (2014). Statistical solutions for error and bias in global citizen science datasets. *Biological Conservation*, 173, 144-154.

Birkett, C. M., Mertes, L. A., Dunne, T., Costa, M. H., & Jasinski, M. J. (2002). Surface water dynamics in the Amazon Basin: Application of satellite radar altimetry. *Journal of Geophysical Research: Atmospheres*, 107(D20).

Birkinshaw, S. J., O'donnell, G. M., M. P., G., K. C., Fowler, H. J., & Berry, P. A. (2010). Using satellite altimetry data to augment flow estimation techniques on the Mekong River. *Hydrological Processes*, 24(26), 3811-3825.

Blöschl, G., & Montanari, A. (2010). Climate change impacts—throwing the dice? *Hydrological processes*, 24(3), 374-381.

Blöschl, G., Hall, J., Parajka, J., Perdigão, R. A., Merz, B., Arheimer, B., & Čanjevac, I. (2017). Changing climate shifts timing of European floods. *Science*, 357(6351), 588-590.

Bonney, R., Shirk, J. L., Phillips, T. B., Wiggins, A., Ballard, H. L., Miller-Rushing, A. J., & Parrish, J. K. (2014). Next steps for citizen science. *Science*, 343(6178), 1436-1437.

Bordogna, G., Carrara, P., Criscuolo, L., Pepe, M., & Rampini, A. (2014). A linguistic decision making approach to assess the quality of volunteer geographic information for citizen science. *Information Sciences*, 258, 312-327.

Brivio, P. A., Colombo, R., Maggi, M., & Tomasoni, R. (2002). Integration of remote sensing data and GIS for accurate mapping of flooded areas. *International Journal of Remote Sensing*, 23(3), 429-441.

Brocca, L., Melone, F., Moramarco, T., Wagner, W., Naeimi, V., Bartalis, Z., & Hasenauer, S. (2010). Improving runoff prediction through the assimilation of the ASCAT soil moisture product. *Hydrology and Earth System Sciences*, 14(10), 1881.

Brocca, L., Moramarco, T., Melone, F., Wagner, W., Hasenauer, S., & Hahn, S. (2012). Assimilation of surface-and root-zone ASCAT soil moisture products into rainfall–runoff modeling. *IEEE Transactions on Geoscience and Remote Sensing*, 50(7), 2542-2555.

Brouwer, T. (2016). Potential of Twitter derived flood maps: comparing interpolation methods and assessing uncertainties. *University of Twente, Deltares*, Report.

Brouwer, T., Eilander, D., van Loenen, A., Booij, M. J., Wijnberg, K. M., Verkade, J. S., & Wagemaker, J. (2017). Probabilistic flood extent estimates from social media flood observations. *Natural Hazards and Earth System Sciences, 17(5)*, 735.

Brunner, G. W. (1995). HEC-RAS River Analysis System. Hydraulic Reference Manual. Version 1.0. *HYDROLOGIC ENGINEERING CENTER DAVIS CA*.

Burnash, R. J. (1995). The NWS river forecast system-catchment modeling. *Computer models of watershed hydrology*, 188, 311-366.

Buytaert, W., Zulkafli, Z., Grainger, S., Acosta, L., Alemie, T. C., Bastiaensen, J., . . . Paudel, D. S. (2014). Citizen science in hydrology and water resources: opportunities for knowledge generation, ecosystem service management, and sustainable development. *Frontiers in Earth Science*, 2, 26.

Cervone, G., Sava, E., Huang, Q., Schnebele, E., Harrison, J., & Waters, N. (2016). Using Twitter for tasking remote-sensing data collection and damage assessment: 2013 Boulder flood case study. *International Journal of Remote Sensing*, 37(1), 100-124.

Chen, J., Zhang, W., Gao, J., & Cao, K. (2012). Assimilating multi-site measurements for semi-distributed hydrological model updating. *Quaternary international*, 282, 122-129.

Chesworth, W., Fairbridge, R., & Herschy, R. (1998). Encyclopedia of earth sciences series. *Springer Netherlands*(DOI: 10.1007/1-4020-4497-6_220).

Chow, V. T., Maidment, D. R., & Larry, W. (1988). Applied Hydrology. *International edition, MacGraw-Hill, Inc, 149*.

Cifelli, R., Doesken, N., Kennedy, P., Carey, L. D., Rutledge, S. A., Gimmestad, C., & Depue, T. (2005). The community collaborative rain, hail, and snow network: Informal education for scientists and citizens. *Bulletin of the American Meteorological Society*, 86(8), 1069-1077.

Ciravegna, F., Huwald, H., Lanfranchi, V., & Wehn de Montalvo, U. (2013). Citizen observatories: the WeSenseIt vision. *Proceedings of the INSPIRE*.

Clark, M. P., Rupp, D. E., Woods, R. A., Zheng, X., Ibbitt, R. P., Slater, A. G., . . . Uddstrom, M. J. (2008). Hydrological data assimilation with the ensemble Kalman filter: Use of streamflow observations to update states in a distributed hydrological model. *Advances in water resources, 31(10)*, 1309-1324.

Cobby, D. M., Mason, D. C., Horritt, M. S., & Bates, P. D. (2003). Two-dimensional hydraulic flood modelling using a finite-element mesh decomposed according to vegetation and topographic features derived from airborne scanning laser altimetry. *Hydrological processes*, 17(10), 1979-2000.

Crawford, N. H., & Linsley, R. K. (1966). Digital Simulation in Hydrology'Stanford Watershed Model 4. *Technical Report No. 39, Department*, 120.

Crist, E. (1985). A TM tasseled cap equivalent transformation for reflectance factor data. *Remote Sensing of Environment*, 17, 301–306.

Cronshey, R. (1986). Urban hydrology for small watersheds. US Dept. of Agriculture, Soil Conservation Service, Engineering Division.

Crutzen, P. J. (2002). Geology of mankind. *Nature*, 415(6867), 23-23.

Dankers, R., Arnell, N. W., Clark, D. B., Falloon, P. D., Fekete, B. M., Gosling, S. N., . . . Wisser, D. (2014). First look at changes in flood hazard in the Inter-Sectoral Impact Model Intercomparison Project ensemble. *Proceedings of the National Academy of Sciences*, 111(9), 3257-3261.

Dawson, C. W., & Wilby, R. L. (2001). Hydrological modelling using artificial neural networks. *Progress in physical Geography*, 25(1), 80-108.

Degiorgis, M., Gnecco, G., Gorni, S., Roth, G., Sanguineti, M., & Taramasso, A. (2012). Classifiers for the detection of flood-prone areas using remote sensed elevation data. *Journal of Hydrology*, 470, 302-315. DOI: http://dx.doi.org/10.1016/j.jhydrol.2012.09.006.

Devia, G. K., Ganasri, B. P., & Dwarakish, G. S. (2015). A review on hydrological models. *Aquatic Procedia*, 4, 1001-1007.

Di Baldassarre, G., & Montanari, A. (2009). Uncertainty in river discharge observations: a quantitative analysis. *Hydrology and Earth System Sciences, 13(6)*, 913.

Di Baldassarre, G., Laio, F., & Montanari, A. (2012). Effect of observation errors on the uncertainty of design floods. *Physics and Chemistry of the Earth, Parts A/B/C*, 42, pp 85-90.

Di Baldassarre, G., Montanari, A., Lins, H., Koutsoyiannis, D., Brandimarte, L., & Blöschl, G. (2010). Flood fatalities in Africa: from diagnosis to mitigation. *Geophysical Research Letters*, 37(22).

Di Baldassarre, G., Schumann, G., & Bates, P. (2009b). Near real time satellite imagery to support and verify timely flood modelling. *Hydrological Processes*, 23(5), 799-803.

Di Baldassarre, G., Schumann, G., & Bates, P. D. (2009a). A technique for the calibration of hydraulic models using uncertain satellite observations of flood extent. *Journal of Hydrology*, 367(3), 276-282.

Di Baldassarre, G., Schumann, G., Bates, P. D., Freer, J. E., & Beven, K. J. (2010). Flood-plain mapping: a critical discussion of deterministic and probabilistic approaches. *Hydrological Sciences Journal*, 55(3), 364-376.

Di Baldassarre, G., Schumann, G., Brandimarte, L., & Bates, P. (2011). Timely low resolution SAR imagery to support floodplain modelling: a case study review. *Surveys in Geophysics*, 32(3), 255-269.

Di Baldassarre, G., Viglione, A., Carr, G., Kuil, L., Yan, K., Brandimarte, L., & Blöschl, G. (2015). Debates—Perspectives on socio-hydrology: Capturing feedbacks between physical and social processes. *Water Resources Research*, 51(6), 4770-4781.

Dibike, Y. B., & Solomatine, D. P. (2001). River flow forecasting using artificial neural networks. *Physics and Chemistry of the Earth, Part B: Hydrology, Oceans and Atmosphere*, 26(1), 1-7.

Dodov, B. A., & Foufoula-Georgiou, E. (2004). Generalized hydraulic geometry: Derivation based on a multiscaling formalism. *Water resources research*, 40, no. 6.

Domeneghetti, A., Tarpanelli, A., Brocca, L., Barbetta, S., Moramarco, T., Castellarin, A., & Brath, A. (2014). The use of remote sensing-derived water surface data for hydraulic model calibration. *Remote sensing of environment*, 149, 130-141.

Dooge, J. (1973). Linear theory of hydrologic systems. *Agricultural Research Service, US Department of Agriculture.*, (No. 1468).

Dottori, F., Salamon, P., Bianchi, A., Alfieri, L., Hirpa, A., F., & Feyen, L. (2016). Development and evaluation of a framework for global flood hazard mapping. *Advances in Water Resources, 94*, 87-102.

Duan, Q., Ajami, N. K., Gao, X., & Sorooshian, S. (2007). Multi-model ensemble hydrologic prediction using Bayesian model averaging. *Advances in Water Resources*, 30(5), 1371-1386.

Eilander, D., Trambauer, P., Wagemaker, J., & van Loenen, A. (2016). Harvesting social media for generation of near real-time flood maps. *Procedia Engineering*, 154, 176-183.

Emergency Events Database (EM-DAT). (2013). : The OFDA/CRED International Disaster Database, Université catholique de Louvain.

Ercolani, G., & Castelli, F. (2017). Variational assimilation of streamflow data in distributed flood forecasting. *Water Resources Research*, 53(1), 158-183.

Evensen, G. (2003). The ensemble Kalman filter: Theoretical formulation and practical implementation. *Ocean dynamics*, 3(4), 343-367.

Falorni, G., Teles, V., Vivoni, E. R., Bras, R. L., & Amaratunga, K. S. (2005). Analysis and characterization of the vertical accuracy of digital elevation models from the Shuttle Radar Topography Mission. *Journal of Geophysical Research: Earth Surface*, 110(F2).

Farr, T., Rosen, P., Caro, E., Crippen, R., Duren, R., Hensley, S., . . . Alsdorf, D. (2007). The shuttle radar topography mission. *Reviews of geophysics*, 45(2).

Feldhaus, R., Hottges, R., Brockhaus, T., & Rouve´, G. (1992). Finite element simulation of flow and pollution transport applied to. *In: Falconer, R.A., Shiono, K., Matthews, R.G.S. (Eds.). Hydraulic and Environmental Modelling: Estuarine and River Waters, Ashgate, Aldershot,*, 323-334.

Feng, Q., Liu, J., & Gong, J. (2015). Urban flood mapping based on unmanned aerial vehicle remote sensing and random forest classifier—A case of Yuyao, China. *Water*, 7(4), 1437-1455.

Fewtrell, T. J., Duncan, A., Sampson, C. C., Neal, J. C., & Bates, P. D. (2011). Benchmarking urban flood models of varying complexity and scale using high resolution terrestrial LiDAR data. *Physics and Chemistry of the Earth, Parts A/B/C*, 36(7), 281-291.

Feyisa, G., Meilby, H., Fensholt, R., & Proud, S. (2014). Automated Water ExtractionIndex: A new technique for surface water mapping using Landsat imagery. *Remote Sensing of Environment*, 140, 23–35. http://dx.doi.org/10.1016.

Fisher, A., Flood, N., & Danaher, T. (2016). Comparing Landsat water index methods for automated water classification in eastern Australia. *Remote Sensing of Environment*, 175, 167-182.

Fletcher, C. A. (1988). Computational techniques for fluid dynamics. Volume 1-Fundamental and general techniques. Volume 2-Specific techniques for different flow categories. *Berlin and New York, Springer-Verlag, p. Vol. 1, 418 p.; vol. 2, 493 p.*

Fohringer, J., Dransch, D., Kreibich, H., & Schröter, K. (2015). Social media as an information source for rapid flood inundation mapping. *Natural Hazards and Earth System Sciences*, 15(12), 2725-2738.

Frappart, F., Calmant, S., Cauhopé, M., Seyler, F., & Cazenave, A. (2006). Preliminary results of ENVISAT RA-2-derived water levels validation over the Amazon basin. *Remote sensing of Environment*, 100(2), 252-264.

French, J. R. (2003). Airborne LiDAR in support of geomorphological and hydraulic modelling. *Earth surface processes and landforms*, 28(3), 321-335.

Gallant, J. C., & Dowling, T. I. (2003). A multiresolution index of valley bottom flatness for mapping depositional areas. *Water Resources Research*, 39(12), 1347, doi:10.1029/2002WR001426.

Gao, H., Barbier, G., & Goolsby, R. (2011). Harnessing the crowdsourcing power of social media for disaster relief. *IEEE Intelligent Systems*, 26(3), 10-14.

Garbrecht, J., & Martz, L. W. (1997a). The assignment of drainage direction over flat surfaces in raster digital elevation models. *Journal of Hydrology*, 193, 204–213.

Garbrecht, J., & Martz, L. W. (1997b). TOPAZ: An automated digital landscape analysis tool for topographic evaluation, drainage identification, watershed segmentation and subcatchment parameterization. *TOPAZ User Manual. ARS Publ. GRL 97-4, US Dept Agric., Agric. Res. Service, Grazinglands Research Laboratory, El Reno, Oklahoma, USA.*

García-Martinez, R., Espinoza, R., Valera, E., & González, M. (2006). An explicit two-dimensional finite element model to simulate short-and long-term bed evolution in alluvial rivers. *Journal of Hydraulic Research*, 44(6), 755-766.

García-Pintado, J., Neal, J. C., Mason, D. C., Dance, S. L., & Bates, P. D. (2013). Scheduling satellite-based SAR acquisition for sequential assimilation of water level observations into flood modelling. *Journal of Hydrology*, 495, 252-266.

Giannoni, F., Roth, G., & Rudari, R. (2005). A procedure for drainage network identification from geomorphology and its application to the prediction of the hydrologic response. *Advances in Water Resources*, 28(6), 567-581.

Gilles, D., Young, N., Schroeder, H., Piotrowski, J., & Chang, Y. J. (2012). Inundation mapping initiatives of the Iowa Flood Center: Statewide coverage and detailed urban flooding analysis. *Water*, 4(1), 85-106.

Giustarini, L., Hostache, R., Matgen, P., Schumann, G. J., Bates, P. D., & Mason, D. C. (2013). A change detection approach to flood mapping in urban areas using TerraSAR-X. *IEEE transactions on Geoscience and Remote Sensing*, 51(4), 2417-2430.

Giustarini, L., Matgen, P., Hostache, R., Montanari, M., Plaza, D., Pauwels, V. R., . . . Savenije, H. H. (2011). Assimilating SAR-derived water level data into a hydraulic model: a case study. *Hydrology and Earth System Sciences*, 15(7), 2349-2365.

Goodchild, M. F. (2007). Citizens as sensors: the world of volunteered geography. *GeoJournal*, 69(4), 211-221.

Govindaraju, R. S., & Rao, A. R. (2013). Artificial neural networks in hydrology. *(Vol. 36). Springer Science & Business Media.*

Grimaldi, S., Petroselli, A., & Nardi, F. (2012). A parsimonious geomorphological unit hydrograph for rainfall–runoff modelling in small ungauged basins. *Hydrological Sciences Journal, 57(1),* , 73-83.

Grimaldi, S., Petroselli, A., Alonso, G., & Nardi, F. (2010). Flow time estimation with spatially variable hillslope velocity in ungauged basins. *Advances in Water Resources, 33(10)*, 1216-1223.

Gupta, V. K., Waymire, E., & Wang, C. T. (1980). A representation of an instantaneous unit hydrograph from geomorphology. *Water resources research*, 16(5), 855-862.

Gura, T. (2013). Amateur experts. *Nature*, 496(11), 259-261.

Haan, C. T., Barfield, B. J., & Hayes, J. C. (1994). Design hydrology and sedimentology for small catchments. *Elsevier*.

Hahmann, S., Purves, R. S., & Burghardt, D. (2014). Twitter location (sometimes) matters: Exploring the relationship between georeferenced tweet content and nearby feature classes. *Journal of Spatial Information Science*, (9), 1-36.

Hall, A. C., Schumann, G. J., Bamber, J. L., & Bates, P. D. (2011). Tracking water level changes of the Amazon Basin with space-borne remote sensing and integration with large scale hydrodynamic modelling: A review. *Physics and Chemistry of the Earth, Parts A/B/C*, 36(7), 223-231.

Hall, J., & Solomatine, D. (2008). A framework for uncertainty analysis in flood risk management decisions. *International Journal of River Basin Management*, 6(2), 85-98.

Havnø, K., Madsen, M. N., & Dørge, J. (1995). MIKE 11–a generalized river modelling package. *Computer models of watershed hydrology*, 733-782.

Hess, L. L., Melack, J. M., Filoso, S., & Wang, Y. (1995). Delineation of inundated area and vegetation along the Amazon floodplain with the SIR-C synthetic aperture radar. *IEEE Transactions on Geoscience and Remote Sensing*, 33(4), 896-904.

Heuvelink, G. B., Brown, J. D., & van Loon, E. E. (2007). A probabilistic framework for representing and simulating uncertain environmental variables. *International Journal of Geographical Information Science*, 21(5), 497-513.

Hinkel, J., Lincke, D., Vafeidis, A. T., Perrette, M., Nicholls, R. J., Tol, R. S., . . . Levermann, A. (2014). Coastal flood damage and adaptation costs under 21st century sea-level rise. *Proceedings of the National Academy of Sciences*, 111(9), 3292-3297.

Hodgson, M. E., & Bresnahan, P. (2004). Accuracy of airborne lidar-derived elevation. *Photogrammetric Engineering & Remote Sensing*, 70(3), 331-339.

Hoeppe, P. (2016). Trends in weather related disasters–Consequences for insurers and society. *Weather and Climate Extremes*, 11, 70-79.

Holderness, T., & Turpin, E. (2015). From Social Media to GeoSocial Intelligence: Crowdsourcing Civic Co-management for Flood Response in Jakarta, Indonesia. *Social media for government services, Springer International Publishing*, 115-133.

Horritt, M. (1999). A statistical active contour model for SAR image segmentation. *Image and Vision Computing*, 17(3), 213-224.

Horritt, M. S. (2000). A methodology for the validation of uncertain flood inundation models. *Journal of Hydrology*, 326(1), 153-165.

Horritt, M. S., & Bates. (2001). Effects of spatial resolution on a raster based model of flood flow. *Journal of Hydrology, 253(1)*, 239-249.

Horritt, M. S., Bates, P. D., & Mattinson, M. J. (2006). ffects of mesh resolution and topographic representation in 2D finite volume models of shallow water fluvial flow. *Journal of Hydrology*, 329(1), 306-314.

Horritt, M. S., Di Baldassarre, G., Bates, P. D., & Brath, A. (2007). Comparing the performance of a 2-D finite element and a 2-D finite volume model of floodplain inundation using airborne SAR imagery. *Hydrological Processes*, 21(20), 2745-2759.

Horritt, M. S., Mason, D. C., & Luckman, A. J. (2001). Flood boundary delineation from synthetic aperture radar imagery using a statistical active contour model. *International Journal of Remote Sensing*, 22(13), 2489-2507.

Hostache, R., Lai, X., Monnier, J., & Puech, C. (2010). ssimilation of spatially distributed water levels into a shallow-water flood model. Part II: Use of a remote sensing image of Mosel River. *Journal of hydrology*, 390(3), 257-268.

Hunter, N. M. (2005). *Development and assessment of dynamic storage cell codes for flood inundation modelling.* Bristol, U. K.: Ph.D. thesis, Univ. of Bristol.

Hunter, N. M., Bates, P. D., Horritt, M. S., De Roo, A. P., & Werner, M. G. (2005b). Utility of different data types for calibrating flood inundation models within a GLUE framework. *Hydrology and Earth System Sciences Discussions*, 9(4), 412-430.

Hunter, N. M., Horritt, M. S., Bates, P. D., Wilson, M. D., & Werner, M. G. (2005a). An adaptive time step solution for raster-based storage cell modelling of floodplain inundation. *Advances in Water Resources*, 28(9), 975-991.

Irwin, A. (1995). Citizen science: A study of people, expertise and sustainable development. *Psychology Press.*

Jafarzadegan, K., & Merwade, V. (2017). A DEM-based approach for large-scale floodplain mapping in ungauged watersheds. *Journal of Hydrology*, 550, 650-662.

Jalayer, F., De Risi, R., De Paola, F., Giugni, M., Manfredi, G., Gasparini, P., . . . Renner, F. (2014). Probabilistic GIS-based method for delineation of urban flooding risk hotspots. *Natural hazards*, 73(2), 975-1001. doi: http://dx.doi.org/10.1007/s11069-014-1119-2.

Jana, R., Reshmidevi, T. V., Arun, S. P., & Eldho, T. I. (2007). An enhanced technique in construction of the discrete drainage network from low-resolution spatial database. *Computers & Geosciences, 33(6),* , 717–727.

Jazwinski, A. H. (2007). Stochastic processes and filtering theory. *Courier Corporation*.

Jenson, S., & Domingue, J. (1988). Extracting Topographic Structure from Digital Elevation Data for Geographic Information System Analysis. *Photogrammetric Engineering And Remote Sensing*, 1593-1600.

Jin, M., & Fread, D. L. (1997). Dynamic flood routing with explicit and implicit numerical solution schemes. *Journal of Hydraulic Engineering, 123(3)*, 166-173.

Jongman, B., Hochrainer-Stigler, S., Feyen, L., Aerts, J. C., Mechler, R., Botzen, W. J., . . . Ward, P. J. (2014). Increasing stress on disaster-risk finance due to large floods. *Nature Climate Change*, 4(4), 264.

Jung, H. C., Jasinski, M., Kim, J. W., Shum, C. K., Bates, P., Neal, J., . . . Alsdorf, D. (2012). Calibration of two-dimensional floodplain modeling in the central Atchafalaya Basin Floodway System using SAR interferometry. *Water Resources Research*, 48(7).

Jung, Y., & Merwade, V. (2012). Uncertainty quantification in flood inundation mapping using generalized likelihood uncertainty estimate and sensitivity analysis. *Journal of Hydrologic Engineering*, 17(4), 507-520.

Kachroo, R. K. (1992). River flow forecasting. Part 1. A discussion of the principles. *Journal of Hydrology*, 133(1-2), 1-15.

Kalman, R. E. (1960). A new approach to linear filtering and prediction problems. *Journal of basic Engineering*, 82(1), 35-45.

Kalyanapu, A. J., Shankar, S., Pardyjak, E. R., Judi, D. R., & Burian, S. J. (2011). Assessment of GPU computational enhancement to a 2D flood model. *Environmental Modelling & Software*, 26(8), 1009-1016.

Kapelan, Z. S., Savic, D. A., & Walters, G. A. (2007). Calibration of water distribution hydraulic models using a Bayesian-type procedure. *Journal of Hydraulic Engineering*, 133(8), 927-936.

Kim, K. J., Moskowitz, H., & Koksalan, M. (1996). Fuzzy versus statistical linear regression. *European Journal of Operational Research*, 92(2), 417-434.

Kim, Y., Tachikawa, Y., Kim, S., Shiiba, M., Yorozu, K., & Noh, S. J. (2012). Short term prediction of water level and discharge using a 2D dynamic wave model with particle filters. *Journal of Japan Society of Civil Engineers, Ser. B1 (Hydraulic Engineering)*, 68(4), I_25-I_30.

Kim, Y., Y., T., Shiiba, M., Kim, S., Yorozu, K., & Noh, S. J. (2013). Simultaneous estimation of inflow and channel roughness using 2D hydraulic model and particle filters. *Journal of flood risk management, 6(2)*, 112-123.

Koutsoyiannis, D. (2010). HESS Opinions" A random walk on water". *Hydrology and Earth System Sciences*, 14(3), 585-601.

Krzhizhanovskaya, V. V., Shirshov, G. S., Melnikova, N. B., Belleman, R. G., Rusadi, F. I., Broekhuijsen, B. J., . . . Meijer, R. (2011). Flood early warning system: design, implementation and computational modules. *Procedia Computer Science*, 4, 106-115.

Krzysztofowicz, R. (1999). Bayesian theory of probabilistic forecasting via deterministic hydrologic model. *Water Resources Research*, 35(9), 2739-2750.

Krzysztofowicz, R. (2001). The case for probabilistic forecasting in hydrology. *Journal of hydrology*, 249(1), 2-9.

Kuczera, G., Kavetski, D., Franks, S., & Thyer, M. (2006). Towards a Bayesian total error analysis of conceptual rainfall-runoff models: Characterising model error using storm-dependent parameters. *Journal of Hydrology*, 331(1), 161-177.

Lacasta, A., Morales-Hernández, M., Murillo, J., & García-Navarro, P. (2014). An optimized GPU implementation of a 2D free surface simulation model on unstructured meshes. *Advances in engineering software*, 78, 1-15.

Lahoz, W. A., & Schneider, P. (2014). Data assimilation: making sense of Earth Observation. *Frontiers in Environmental Science*, 2, 16.

Lamb, R., Crossley, M., & Waller, S. (2009). A fast two-dimensional floodplain inundation model. *In Proceedings of the Institution of Civil Engineers-Water Management. Thomas Telford Ltd.*, 162(6), 363-370.

Lane, S. N. (2005). Roughness–time for a re-evaluation? *Earth Surface Processes and Landforms*, 30(2), 251-253.

Le Dimet, F. X., & Talagrand, O. (1986). Variational algorithms for analysis and assimilation of meteorological observations: theoretical aspects. *Tellus A: Dynamic Meteorology and Oceanography*, 38(2), 97-110.

Lee, H., Seo, D. J., & Koren, V. (2011). Assimilation of streamflow and in situ soil moisture data into operational distributed hydrologic models: Effects of uncertainties in the data and initial model soil moisture states. *Advances in water resources*, 34(12), 1597-1615.

Leedal, D., Neal, J., Beven, K., Young, P., & Bates, P. (2010). Visualization approaches for communicating real-time flood forecasting level and inundation information. *Journal of Flood Risk Management*, 3(2), 140-150.

LeFavour, G., & Alsdorf, D. (2005). Water slope and discharge in the Amazon River estimated using the shuttle radar topography mission digital elevation model. *Geophysical Research Letters*, 32(17).

Leon, J. X., Heuvelink, G. B., & Phinn, S. R. (2014). Incorporating DEM uncertainty in coastal inundation mapping. *PLoS one*, 9(9), e108727.

Leopold, L. B., & Maddock, J. T. (1953). The hydraulic geometry of stream channels and some physiographic implications. *252*.

Leopold, L. B., & Maddock, T. (1953). The hydraulic geometry of stream channels and some physiographic implications. *US Government Printing Office*.

Lhomme, J., Sayers, P. B., Gouldby, B. P., Samuels, P. G., Wills, M., & Mulet-Marti, J. (2009). Recent development and application of a rapid flood spreading method. *In Flood Risk Management: Research and Practice, Samuels P, Huntington S, Allsop W, Harrop J (eds). CRC Press: London;* , 15–24.

Li, S., MacMillan, R. A., Lobb, D. A., McConkey, B. G., Moulin, A., & Fraser, W. R. (2011). Lidar DEM error analyses and topographic depression identification in a hummocky landscape in the prairie region of Canada. *Geomorphology*, 129(3), 263-275.

Lindström, G., Johansson, B., Persson, M., Gardelin, M., & Bergström, S. (1997). Development and test of the distributed HBV-96 hydrological model. *Journal of hydrology*, 201(1-4), 272-288.

Liu, Y., & Gupta, H. V. (2007). Uncertainty in hydrologic modeling: Toward an integrated data assimilation framework. *Water Resources Research*, 43(7).

Liu, Y., Weerts, A. H., Clark, M., Hendricks Franssen, H. J., Kumar, S., Moradkhani, H., . . . Restrepo, P. (2012). Advancing data assimilation in operational hydrologic forecasting: Progresses, challenges, and emerging opportunities. *Hydrology and Earth System Sciences*, 16(10), 3863–3887, doi:10.5194/hess-16-3863-2012.

Livne, E., & Svoray, T. (2011). Components of uncertainty in primary production model: the study of DEM, classification and location error. *International Journal of Geographical Information Science*, 25(3), 473-488.

Ljung, L. (1979). Asymptotic behavior of the extended Kalman filter as a parameter estimator for linear systems. *IEEE Transactions on Automatic Control*, 24(1), 36-50.

Lowry, C. S., & Fienen, M. N. (2013). CrowdHydrology: crowdsourcing hydrologic data and engaging citizen scientists. *GroundWater*, 51(1), 151-156.

Lü, H., Yu, Z., Zhu, Y., Drake, S., Hao, Z., & Sudicky, E. A. (2011). Dual state-parameter estimation of root zone soil moisture by optimal parameter estimation and extended Kalman filter data assimilation. *Advances in water resources*, 34(3), 395-406.

MacIntosh, H., & Profeti, G. (1995). The use of ERS SAR data to manage flood emergencies at the smaller scale. *In 2nd ERS Applications Workshop, European Space Agency, London*, 243-246.

Madsen, H., & Canizares, R. (1999). Comparison of extended and ensemble Kalman filters for data assimilation in coastal area modelling. *International Journal for Numerical Methods in Fluids*, 31(6), 961-981.

Madsen, H., & Skotner, C. (2005). Adaptive state updating in real-time river flow forecasting—A combined filtering and error forecasting procedure. *Journal of Hydrology, 308(1)*, 302-312.

Manfreda, S., Di Leo, M., & Sole, A. (2011). Detection of Flood Prone Areas using Digital Elevation Models. *Journal of Hydrologic Engineering*, 16(10), 781-790. doi: http://dx.doi.org/10.1061/(ASCE)HE.1943-5584.0000367.

Manfreda, S., Nardi, F., Samela, C., Grimaldi, S., Taramasso, A. C., Roth, G., & Sole, A. (2014). Investigation on the use of geomorphic approaches for the delineation of flood prone. *Journal of Hydrology*, 517, 863-876.

Manfreda, S., Samela, C., Gioia, A., Consoli, G., Iacobellis, V., Giuzio, L., & Sole, A. (2015). Flood-prone areas assessment using linear binary classifiers based on flood maps obtained from 1D and 2D hydraulic models. *Natural Hazards*, Vol. 79 (2), pp 735-754. doi: http://dx.doi.org/10.1007/s11069-015-1869-5.

Mantovan, P., & Todini, E. (2006). Hydrological forecasting uncertainty assessment: Incoherence of the GLUE methodology. *Journal of hydrology*, 330(1), 368-381.

Marks, K., & Bates, P. (2000). Integration of high-resolution topographic data with floodplain flow models. *Hydrological Processes*, 14(11-12), 2109-2122.

Martinis, S., Kersten, J., & Twele, A. (2014). A fully automated TerraSAR-X based flood service. *ISPRS Journal of Photogrammetry and Remote Sensing*, 104, 203-212.

Martinis, S., Twele, A., & Voigt, S. (2009). Towards operational near real-time flood detection using a split-based automatic thresholding procedure on high resolution TerraSAR-X data. *Natural Hazards and Earth System Sciences*, 9(2), 303-314.

Mason, D. C., Bates, P. D., & Dall'Amico, J. T. (2009). Calibration of uncertain flood inundation models using remotely sensed water levels. *Journal of Hydrology*, 368(1), 224-236.

Mason, D. C., Cobby, D. M., Horritt, M. S., & Bates, P. D. (2003). Floodplain friction parameterization in two-dimensional river flood models using vegetation heights derived from airborne scanning laser altimetry. *Hydrological processes*, 17(9), 1711-1732.

Mason, D. C., Davenport, I. J., Neal, J. C., Schumann, G. J., & Bates, P. D. (2012a). Near real-time flood detection in urban and rural areas using high-resolution synthetic aperture radar images. *IEEE transactions on Geoscience and Remote Sensing*, 50(8), 3041-3052.

Mason, D. C., Giustarini, L., Garcia-Pintado, J., & Cloke, H. L. (2014). Detection of flooded urban areas in high resolution Synthetic Aperture Radar images using double scattering. *International Journal of Applied Earth Observation and Geoinformation*, 28, 150-159.

Mason, D. C., Schumann, G. P., Neal, J. C., Garcia-Pintado, J., & Bates, P. D. (2012b). Automatic near real-time selection of flood water levels from high resolution Synthetic Aperture Radar images for assimilation into hydraulic models: a case study. *Remote Sensing of Environment*, 124, 705-716.

Matgen, P., Hostache, R., Schumann, G., Pfister, L., Hoffmann, L., & Savenije, H. H. (2011). Towards an automated SAR-based flood monitoring system: Lessons learned from two case studies. *Physics and Chemistry of the Earth, Parts A/B/C*, 36(7), 241-252.

Matgen, P., Montanari, M., Hostache, R., Pfister, L., Hoffmann, L., Plaza, D., . . . Savenije, H. H. (2010). Towards the sequential assimilation of SAR-derived water stages into hydraulic models using the Particle Filter: proof of concept. *Hydrology and Earth System Sciences*, 14(9), 1773-1785.

Matgen, P., Schumann, G., Pappenberger, F., & Pfisterz, L. (2007). Sequential assimilation of remotely sensed water stages in flood inundation models. *IAHS Publication*, 316, 78.

Mazzoleni, M. (2017). Improving flood prediction assimilating uncertain crowdsourced data into hydrologic and hydraulic models. *CRC Press.*

Mazzoleni, M., Alfonso, L., Chacon-Hurtado, J., & Solomatine, D. (2015). Assimilating uncertain, dynamic and intermittent streamflow observations in hydrological models. *Advances in Water Resources, 83,* 323-339.

Mazzoleni, M., Cortes Arevalo, V. J., Wehn, U., Alfonso, L., Norbiato, D., Monego, M., . . . Solomatine, D. P. (2017). Towards assimilation of crowdsourced observations for different levels of citizen engagement: the flood event of 2013 in the Bacchiglione catchment. *Hydrology and Earth System Sciences*, https://doi.org/10.5194/hess-2017-59, in review.

McClanahan, B., & Gokhale, S. S. (2015). Location inference of social media posts at hyper-local scale. *In Future Internet of Things and Cloud (FiCloud), 3rd International Conference on IEEE*, 465-472.

McCuen, R. H. (1989). Hydrologic analysis and design. *Englewood Cliffs, NJ: Prentice-Hall.*, 143-147.

McDougall, K. (2011). Using volunteered information to map the Queensland floods. *In Proceedings of the 2011 Surveying and Spatial Sciences Conference: Innovation in Action: Working Smarter (SSSC 2011). Surveying and Spatial Sciences Institute.*, 13-23.

McFeeters, S. (1996). The use of the Normalized Difference Water Index (NDWI) in the delineation of open water features. *International Journal of Remote Sensing*, 17, 1425–1432. http://dx.doi.org/10.1080/01431169608948714.

McGlynn, B. L., & Seibert, J. (2003). Distributed assessment of contributing area and riparian buffering along stream networks. *Water Resources research*, 39(4), 1082, doi:10.1029/2002WR001521.

McLaughlin, D. (2002). An integrated approach to hydrologic data assimilation: interpolation, smoothing, and filtering. *Advances in Water Resources*, 25(8), 1275-1286.

McMaster, K. J. (2002). Effects of digital elevation model resolution on derived stream network positions. *Water Resources Research*, 38(4).

McMillan, H. K., Hreinsson, E. Ö., Clark, M. P., Singh, S. K., Zammit, C., & Uddstrom, M. J. (2013). Operational hydrological data assimilation with the recursive ensemble Kalman filter. *Hydrology and Earth System Sciences, 7(1), 21*.

Mehlhorn, J., Feyen, L., Banovsky, I., & Menzinger, I. (2005). FRAT1.0-an example of applying the Geomorphologic Regression approach for detailed single location flood risk assessment. *Geophysical Research Abstracts*, Vol. 7, p. 07419.

Mendoza, P. A., McPhee, J., & Vargas, X. (2012). Uncertainty in flood forecasting: A distributed modeling approach in a sparse data catchment. *Water Resources Research*, 48(9).

Merz, B., & Thieken, A. H. (2005). Separating natural and epistemic uncertainty in flood frequency analysis. *Journal of Hydrology*, 309(1), 114-132.

Mesa, O. J., & Mifflin, E. R. (1986). On the relative role of hillslope and network geometry in hydrologic response. *In: V.K. Gupta, I. Rodriguez-Iturbe and E. F. Wood, Scale problems in hydrology,*, 1–17. Dordrecht: D.Reidel.

Min, S. K., Zhang, X., Zwiers, F. W., & Hegerl, G. C. (2011). Human contribution to more-intense precipitation extremes. *Nature*, 470(7334), 378-381.

Moore, R. J. (1985). The probability-distributed principle and runoff production at point and basin scales. *Hydrological Sciences Journal*, 273-297.

Moradkhani, H., Hsu, K. L., Gupta, H., & Sorooshian, S. (2005a). Uncertainty assessment of hydrologic model states and parameters: Sequential data assimilation using the particle filter. *Water resources research*, 41(5).

Moradkhani, H., Sorooshian, S., Gupta, H. V., & Houser, P. R. (2005b). Dual state–parameter estimation of hydrological models using ensemble Kalman filter. *Advances in water resources*, 28(2), 135-147.

Mudron, I., Podhoranyi, M., Cirbus, J., Devečka, B., & Bakay, L. (2013). Modelling the Uncertainty of Slope Estimation from a Lidar-Derived Dem: a Case Study from a Large-Scale Area in the Czech Republic. *GeoScience Engineering*, 59(2) 25-39. doi:10.2478/gse-2014-0051.

Murphy, J. M. (1988). The impact of ensemble forecasts on predictability. *Quarterly Journal of the Royal Meteorological Society*, 114(480), 463-493.

Naden, P. S. (1992). Spatial variability in flood estimation for large catchments: the exploitation of channel network structure. *Hydrological Sciences Journal*, 37(1), 53-71.

Nardi, F., Biscarini, C., Di Francesco, S., Manciola, P., & Ubertini, L. (2013). Comparing A Large-Scale Dem-Based Floodplain Delineation Algorithm With Standard Flood Maps: The Tiber River Basin Case Study. *Irrigation and Drainage, 62(S2),*, 11-19.

Nardi, F., Grimaldi, S., Santini, M., Petroselli, A., & Ubertini, L. (2008). Hydrogeomorphic properties of simulated drainage patterns using digital elevation models: the flat area issue. *Hydrological Sciences Journal*, 53(6), 1176-1193.

Nardi, F., Morrison, R., Annis, A., & Grantham, T. (2017). The hydrologic and ecologic impact of human-made interventions in fluvial corridors: a methodology for large scale hydrogeomorphic floodplain mapping. *Hydrology and Earth System Sciences*.

Nardi, F., Vivoni, E., & Grimaldi, S. (2006). Investigating a floodplain scaling relation using a hydrogeomorphic delineation method. *Water Resources Research, ,* 42 (9), 15 pp.

Nash, J. E., & Sutcliffe, J. V. (1970). River flow forecasting through conceptual models part I—A discussion of principles. *Journal of hydrology*, 10(3), 282-290.

Neal, J. C., Fewtrell, T. J., Bates, P. D., & Wright, N. G. (2010). A comparison of three parallelisation methods for 2D flood inundation models. *Environmental Modelling & Software*, 25(4), 398-411.

Neal, J., Schumann, G., & Bates, P. (2012). A subgrid channel model for simulating river hydraulics and floodplain inundation over large and data sparse areas. *Water Resources Research*, 48(11).

Neal, J., Schumann, G., Bates, P., Buytaert, W., Matgen, P., & Pappenberger, F. (2009). A data assimilation approach to discharge estimation from space. *Hydrological Processes*, 23(25), 3641-3649.

Neal, J., Schumann, G., Fewtrell, T., Budimir, M., Bates, P., & Mason, D. (2011). Evaluating a new LISFLOOD-FP formulation with data from the summer 2007 floods in Tewkesbury, UK. *Journal of Flood Risk Management*, 4(2), 88-95.

Neitsch, S. L., Arnold, J. G., Kiniry, J. R., & Williams, J. R. (2011). Soil and water assessment tool theoretical documentation version 2009. *Texas Water Resources Institute*.

Nicholas, A. P., & Mitchell, C. A. (2003). Numerical simulation of overbank processes in topographically complex floodplain environments. *Hydrological Processes*, 17(4), 727-746.

Nobre, A. D., Cuartas, L. A., Hodnett, M., Rennó, C. D., Rodrigues, G., Silveira, A., . . . Saleska, S. (2011). Height Above the Nearest Drainage–a hydrologically relevant new terrain model. *Journal of Hydrology*, 404(1), 13-29.

Noman, N. S., Nelson, E. J., & Zundel, A. K. (2001). Review of automated floodplain delineation from digital terrain models. *Journal of Water Resources Planning and Management*, 127(6), 394-402. doi: http://dx.doi.org/10.1061/(ASCE)0733-9496(2001)127:6(394).

Noto, L. V., & La Loggia, G. (2007). Derivation of a distributed unit hydrograph integrating GIS and remote sensing. *Journal of Hydrologic Engineering*, 12(6), 639-650.

NRCS (Natural Resources Conservation Service). (1997). Ponds-Planning, design, construction. *Washington, DC: US Natural Resources Conservation Service, Agriculture Handbook no. 590*.

O'brien, J. S., Julien, P. Y., & Fullerton, W. T. (1993). Two-dimensional water flood and mudflow simulation. *Journal of hydraulic engineering*, 119(2), 244-261.

Özelkan, E. C., & Duckstein, L. (2000). Multi-objective fuzzy regression: a general framework. *Computers & Operations Research*, 27(7), 635-652.

Pachauri, R. K., Allen, M. R., Barros, V. R., Broome, J., Cramer, W., Christ, R., . . . Gomez-Echeverri, L. (2014). Climate change 2014: synthesis report. Contribution of Working Groups I, II and III to the fifth assessment report of the Intergovernmental Panel on Climate Change. *IPCC*, 151.

Pappenberger, F. K., Frodsham, K., Beven, R., Romanowicz, & Matgen, P. (2007). Fuzzy set approach to calibrating distributed flood inundation models using remote sensing observations. *Hydrol. Earth Syst. Sci., 11*, 739–752.

Pappenberger, F., & Beven, K. J. (2006). Ignorance is bliss: Or seven reasons not to use uncertainty analysis. *Water resources research*, 42(5).

Pappenberger, F., Matgen, P., Beven, K. J., Henry, J. B., Pfister, L., & Fraipont, P. (2006). Influence of uncertain boundary conditions and model structure on flood inundation predictions. *Advances in Water Resources*, 29(10), 1430-1449.

Patro, S., Chatterjee, C., Singh, R., & Raghuwanshi, N. S. (2009). Hydrodynamic modelling of a large flood-prone river system in India with limited data. *Hydrological Processes*, 23(19), 2774-2791.

Pearson, K. (1985). Note on regression and inheritance in the case of two parents. *Proceedings of the Royal Society of London*, 58, 240-242.

Pereira, L. G., & Wicherson, R. J. (1999). Suitability of laser data for deriving geographical information: A case study in the context of management of fluvial zones. *ISPRS Journal of Photogrammetry and Remote Sensing*, 54(2), 105-114.

Perrin, C., Michel, C., & Andréassian, V. (2003). Improvement of a parsimonious model for streamflow simulation. *Journal of hydrology*, 279(1), 275-289.

Poff, N. L., Allan, J. D., Bain, M. B., Karr, J. R., Prestegaard, K. L., Richter, B. D., . . . Stromberg, J. C. (1997). The natural flow regime. *BioScience*, 47(11), 769-784.

Poser, K., & Dransch. (2010). Volunteered geographic information for disaster management with application to rapid flood damage estimation. *Geomatica*, 64(1), 89-98.

Pulvirenti, L., Pierdicca, N., Chini, M., & Guerriero, L. (2011). An algorithm for operational flood mapping from Synthetic Aperture Radar (SAR) data using fuzzy logic. *Natural Hazards and Earth System Sciences*, 11(2), 529.

Raaflaub, L. D., & Collins, M. J. (2006). The effect of error in gridded digital elevation models on the estimation of topographic parameters. *Environmental Modelling & Software*, 21(5), 710-732.

Rabuñal, ,. J., Puertas, J., Suarez, J., & Rivero, D. (2007). Determination of the unit hydrograph of a typical urban basin using genetic programming and artificial neural networks. *Hydrological processes*, 21(4), 476-485.

Rakovec, O., Weerts, A. H., Hazenberg, P., Torfs, P. J., & Uijlenhoet, R. (2012a). State updating of a distributed hydrological model with Ensemble Kalman Filtering: effects of updating frequency and observation network density on forecast accuracy. *Hydrology and Earth System Sciences, 16(9)*, 3435-3449.

Rakovec, O., Weerts, A. H., Sumihar, J., & Uijlenhoet, R. (2012b). Operational aspects of asynchronous filtering for flood forecasting. *Hydrology and Earth System Sciences*, 19(6), 2911-2924.

Refsgaard, J. C. (1997). Validation and intercomparison of different updating procedures for real-time forecasting. *Hydrology Research*, 28(2), 65-84.

Reggiani, P., Sivapalan, M., & Hassanizadeh, S. M. (1998). A unifying framework for watershed thermodynamics: balance equations for mass, momentum, energy and entropy, and the second law of thermodynamics. *Advances in Water Resources*, 22(4), 367-398.

Reichle, R. H. (2008). Data assimilation methods in the Earth sciences. *Advances in water resources*, 31(11), 1411-1418.

Rinaldo, A., Marani, A., & Rigon, R. (1991). Geomorphological dispersion. *Water Resources Research*, 27(4), 513-525.

Rodriguez, E., Morris, C. S., & Belz, J. E. (2006). A global assessment of the SRTM performance. *Photogrammetric Engineering & Remote Sensing*, 72(3), 249-260.

Rodríguez-Iturbe, I., & Rinaldo, A. (1997). Fractal river basins: chance and self-organization. *Cambridge University Press*.

Rodríguez-Iturbe, I., & Valdes, J. B. (1979). The geomorphologic structure of hydrologic response. *Water resources research*, 15(6), 1409-1420.

Rodríguez-Iturbe, I., González-Sanabria, M., & Bras, R. L. (1982). A geomorphoclimatic theory of the instantaneous unit hydrograph. *Water Resources Research*, 18(4), 877-886.

Romanowicz, R., Beven, K. J., & Tawn, J. (1996). Bayesian Calibration of Flood Inundation Models. *Floodplain Processes*, 333-360.

Rosser, J. F., Leibovici, D. G., & Jackson, M. J. (2017). Rapid flood inundation mapping using social media, remote sensing and topographic data. *Natural Hazards*, 87(1), 103-120.

Rouse, J., Haas, R., Schell, J., & Deering, D. (1973). Monitoring Vegetation Systems in the Great Plains with ERTS (Earth Resources Technology Satellite). *In Proceedings of Third Earth Resources Technology Satellite Symposium, Greenbelt, ON, Canada, 10–14 December*, Volume SP-351, pp. 309–317.

Samela, C., Troy, T., & Manfreda, S. (2017). Geomorphic classifiers for food-prone areas delineation for data-scarce environments. *Advances in Water Resources*, doi: 10.1016/j.advwatres.2017.01.007.

Sampson, C. C., Smith, A. M., Bates, P. D., Neal, J. C., Alfieri, L., & Freer, J. E. (2015). A high-resolution global flood hazard model. *Water Resources Research*, 51(9), 7358-7381.

Sanders, B. F. (2007). Evaluation of on-line DEMs for flood inundation modeling. *Advances in Water Resources*, 30(8), 1831-1843.

Savic, D. A., Walters, G. A., & Davidson, J. W. (1999). A genetic programming approach to rainfall-runoff modelling. *Water Resources Management*, 13(3), 219-231.

Schnebele, E., & Cervone, G. (2013). Improving remote sensing flood assessment using volunteered geographical data. *Natural Hazards and Earth System Sciences*, 13(3), 669.

Schnebele, E., & Waters, N. (2014). Road assessment after flood events using non-authoritative data. *Natural Hazards and Earth System Science*, 14(4), 1007.

Schubert, J. E., Monsen, W. W., & Sanders, B. F. (2015). Metric-resolution 2D river modeling at the macroscale: Computational methods and applications in a Braided River. *Frontiers in Earth Science*, 3, 74.

Schumann, G. P., Neal, J. C., Voisin, N., Andreadis, K. M., Pappenberger, F., Phanthuwongpakdee, N., & Hall, A. B. (2013). A first large-scale flood inundation forecasting model. *Water Resources Research*, 49(10), 6248-6257.

Schumann, G., Bates, P. D., Horritt, M. S., Matgen, P., & Pappenberger, F. (2009). Progress in integration of remote sensing–derived flood extent and stage data and hydraulic models. *Reviews of Geophysics*, *47(4)*.

Schumann, G., Di Baldassarre, G., Alsdorf, D., & Bates, P. D. (2010). Near real-time flood wave approximation on large rivers from space: Application to the River Po, Italy. *Water Resources Research*, 46(5).

Schumann, G., Henry, J. B., Hoffmann, L., Pfister, L., Pappenberger, F., & Matgen, P. (2005). Demonstrating the high potential of remote sensing in hydraulic modelling and flood risk management. Portsmouth, U. K.: Annual Conference of the Remote Sensing and Photogrammetry Society With the NERC Earth Observation Conference, Remote Sens. and Photogramm. Soc.

Schumann, G., Matgen, P., Cutler, M. E., Black, A., Hoffmann, L., & Pfister, L. (2008). Comparison of remotely sensed water stages from LiDAR, topographic contours and SRTM. *ISPRS Journal of Photogrammetry and Remote Sensing*, 63(3), 283-296.

Sengupta, A., Foster, S. D., Patterson, T. A., & Bravington, M. (2012). Accounting for location error in kalman filters: Integrating animal borne sensor data into assimilation schemes. *PloS one*, 7(8), e42093.

Seo, D. J., Kerkez, B., Zink, M., Fang, N., Gao, J., & Yu, X. (2015). iSPUW: A Vision for Integrated Sensing and Prediction of Urban Water for Sustainable Cities. *In Dynamic Data-Driven Environmental Systems Science. Springer, Cham.*, 68-78.

Seo, D. J., Koren, V., & Cajina, N. (2003). Real-time variational assimilation of hydrologic and hydrometeorological data into operational hydrologic forecasting. *Journal of Hydrometeorology*, 4(3), 627-641.

Shen, L., & Li, C. (2010). Water Body Extraction from Landsat ETM+ Imagery Using Adaboost Algorithm. *In Proceedings of 18th International Conference on Geoinformatics*, 18–20 June 2010, Beijing, China; pp. 1–4.

Sivapalan, M., Takeuchi, K., Franks, S. W., Gupta, V. K., Karambiri, H., Lakshmi, V., . . . Zehe, E. (2003). AHS Decade on Predictions in Ungauged Basins (PUB), 2003–2012: Shaping an exciting future for the hydrological sciences. *Hydrological sciences journal*, 48(6), 857-880.

Smith, L. C. (1997). Satellite remote sensing of river inundation area, stage, and discharge: A review. *Hydrological processes*, 11(10), 1427-1439.

Smith, L., Liang, Q., James, P., & Lin, W. (2015). Assessing the utility of social media as a data source for flood risk management using a real-time modelling framework. *Journal of Flood Risk Management*, doi:10.1111/jfr3.12154.

Stanski, H. R., Wilson, L., & Burrows, W. R. (1989). Survey of common verification methods in meteorology. Geneva, Switzerland.: World Weather Watch Tech. Rep. 8 World Meteorol. Organ.

Statista. (2017a). Number of smartphone users worldwide from 2014 to 2020 (in billions). Source: https://www.statista.com/statistics/330695/number-of-smartphone-users-worldwide/.

Statista. (2017b). Number of monthly active Twitter users worldwide from 1st quarter 2010 to 2nd quarter 2017 (in millions). Source: https://www.statista.com/statistics/282087/number-of-monthly-active-twitter-users/.

Stephens, E. M., Bates, P. D., Freer, J. E., & Mason, D. C. (2012). The impact of uncertainty in satellite data on the assessment of flood inundation models. *Journal of Hydrology*, 414, 162-173.

Stokstad, E. (1999). Scarcity of rain, stream gages threatens forecasts. *Science*, 285: 1199–1200.

Straatsma, M. W., & Baptist, M. J. (2008). Floodplain roughness parameterization using airborne laser scanning and spectral remote sensing. *Remote Sensing of Environment*, 112(3), 1062-1080.

Sun, D., Li, S., Zheng, W., Croitoru, A., Stefanidis, A., & Goldberg, M. (2016). Mapping floods due to Hurricane Sandy using NPP VIIRS and ATMS data and geotagged Flickr imagery. *International Journal of Digital Earth*, 9(5), 427-441.

Syme, W. J. (1992). Dynamically linked two-dimensional/one-dimensional hydrodynamic modelling program for rivers, estuaries & coastal waters. *The University of Queensland*.

Tachikawa, T., Kaku, M., Iwasaki, A., Gesch, D. B., Oimoen, M. J., Zhang, Z., . . . Crippen, R. (2011). ASTER global digital elevation model version 2-summary of validation results. *NASA*.

Tarboton, D. G., & Ames, D. P. (2001). Advances in the mapping of flow networks from digital elevation data. *Bridging the Gap: Meeting the World's Water and Environmental Resources Challenges*, 1-10.

Tarboton, D. G., Bras, R. L., & Rodriguez-Iturbe, I. (1991). On the extraction of channel networks from digital elevation data. *Hydrological processes*, 81-100.

Tarpanelli, A., Brocca, L., Melone, F., & Moramarco, T. (2013). Hydraulic modelling calibration in small rivers by using coarse resolution synthetic aperture radar imagery. *Hydrological Processes*, 27(9), 1321-1330.

Thiemann, M., Trosset, M., Gupta, H., & Sorooshian, S. (2001). Bayesian recursive parameter estimation for hydrologic models. *Water Resources Research*, 37(10), 2521-2535.

Thiessen, A. (1911). Precipitation for large areas. *Monthly Weather Review, 39*, 1082–1084.

Tkachenko, N., Jarvis, S., & Procter, R. (2017). Predicting floods with Flickr tags. *PloS one*, 12(2), e0172870.

Tockner, K., & Stanford, J. A. (2002). Riverine flood plains: present state and future trends. *Environmental conservation*, 29(3), 308-330.

Tokar, A. S., & Johnson, P. A. (1999). Rainfall-runoff modeling using artificial neural networks. *Journal of Hydrologic Engineering*, 4(3), 232-239.

Triglav-Čekada, M., & Radovan, D. (2013). Using volunteered geographical information to map the November 2012 floods in Slovenia. *Natural Hazards and Earth System Sciences*, 3(11), 2753-2762.

Tulloch, A. I., & Szabo, J. K. (2012). A behavioural ecology approach to understand volunteer surveying for citizen science datasets. *Emu-Austral Ornithology*, 112(4), 313-325.

UDFCD (Urban Drainage and Flood Control District). (1992). Urban Drainage Criteria Manual. 3.

United Nations Office for Disaster Risk Reduction (UNISDR). (2015). Making Development Sustainable: The Future of Disaster Risk Management. Global Assessment Report on Disaster Risk Reduction. www.unisdr.org/we/inform/publications/42809.

USACE-HEC, United States Army Corps of Engineers,Hydrologic Engineering Center. (2006). Hydrologic modeling systemHEC-HMS technical user's manual. *Davis,California*.

Van Beek, L. P., Wada, Y., & Bierkens, M. F. (2011). Global monthly water stress: 1. Water balance and water availability. *Water Resources Research*, 47(7).

Vandecasteele, A., & Devillers, R. (2013). Improving volunteered geographic data quality using semantic similarity measurements. *ISPRS-International Archives of the Photogrammetry, Remote Sensing and Spatial Information Sciences*, 1(1), 143-148.

Viero, D. P. (2017). Comment on "Can assimilation of crowdsourced data in hydrological modelling improve flood prediction?" by Mazzoleni et al.(2017). *Hydrology and Earth System Sciences Discussion*, doi:10.5194/hess-2017-102.

Villanueva, I., & Wright, N. G. (2006). Linking Riemann and storage cell models for flood prediction. *In Proceedings of the Institution of Civil Engineers-Water Management (Vol. 159, No. 1, pp. 27-33). Thomas Telford Ltd.*

Walker, J. P., & Houser, P. R. (2005). Hydrologic data assimilation. *Advances in water science methodologies. Londres: Taylor & Francis*, 25-48.

Wan, E. A., & Van Der Merwe, R. (2000). The unscented Kalman filter for nonlinear estimation. *In Adaptive Systems for Signal Processing, Communications, and Control Symposium 2000. AS-SPCC. The IEEE 2000*, 153-158.

Wang, W., Yang, X., & Yao, T. (2012). Evaluation of ASTER GDEM and SRTM and their suitability in hydraulic modelling of a glacial lake outburst flood in southeast Tibet. *Hydrological Processes*, 26(2), 213-225.

Ward, P. J., Jongman, B., Salamon, P., Simpson, A., Bates, P., De Groeve, T., . . . Winsemius, H. C. (2015). Usefulness and limitations of global flood risk models. *Nature Climate Change*, 5(8), 712.

Warren, I. R., & Bach, H. (1992). MIKE 21: a modelling system for estuaries, coastal waters and seas. *Environmental Software*, 7(4), 229-240.

Weerts, A. H., & El Serafy, G. Y. (2006). Particle filtering and ensemble Kalman filtering for state updating with hydrological conceptual rainfall-runoff models. *Water Resources Research, 42(9).*

Wheater, H. S., Jakeman, A. J., & Beven, K. J. (1993). Progress and directions in rainfall-runoff modelling. *Model. Change Environ. Syst.*

Whigham, P. A., & Crapper, P. F. (2001). Modelling rainfall-runoff using genetic programming. *Mathematical and Computer Modelling*, 33(6-7), 707-721.

Wilby, R. L., Beven, K. J., & Reynard, N. S. (2008). Climate change and fluvial flood risk in the UK: More of the same? *Hydrological processes*, 22(14), 2511-2523.

Williams, W. A., Jensen, M. E., Winne, J. C., & Redmond, R. L. (2000). An automated technique for delineating and characterizing valley-bottom settings. *Environmental monitoring*, 64(1), 105-114. doi: http://dx.doi.org/10.1023/A:1006471427421.

Wilson, E., & Sader, S. (2002). Detection of forest harvest type using multiple dates of Landsat TM imagery. *Remote Sensing of Environment*, 80, 385–396.

Wilson, M., Bates, P., Alsdorf, D., Forsberg, B., Horritt, M., Melack, J., . . . Famiglietti, J. (2007). Modeling large-scale inundation of Amazonian seasonally flooded wetlands. *Geophysical Research Letters*, 34(15).

Wing, O. E., Bates, P. D., Sampson, C. C., Smith, A. M., Johnson, K. A., & Erickson, T. A. (2017). Validation of a 30 m resolution flood hazard model of the conterminous United States. *Water Resources Research*, 53(9), 7968-7986.

Woolhouse, G. (2008). Infoworks 2D–a new dimension to flood modelling. *WaPUG Spring Meeting, 3 June 2008, Coventry*.

World Meteorological Organization. (1992). Simulated Real-Time Intercomparison of Hydrological Models by WMO. *WMO*.

Xie, X., & Zhang, D. (2010). Data assimilation for distributed hydrological catchment modeling via ensemble Kalman filter. *Advances in Water Resources*, 33(6), 678-690.

Xu, C. Y. (2002). Hydrologic models. *Textbooks of Uppsala University. Department of Earth Sciences Hydrology.*

Xu, H. (2006). Modification of normalised difference water index (NDWI) to enhance open water features in remotely sensed imagery. *International Journal of Remote Sensing*, 27, 3025–3033.

Yamazaki, D., O'Loughlin, F., Trigg, M. A., Miller, Z. F., Pavelsky, T. M., & Bates, P. D. (2014). Development of the global width database for large rivers. *Water Resources Research*, 50(4), 3467-3480.

Yan, K., Di Baldassarre, G., & Solomatine, D. P. (2013). Exploring the potential of SRTM topographic data for flood inundation modelling under uncertainty. *Journal of hydroinformatics*, 15(3), 849-861.

Yan, K., Di Baldassarre, G., Solomatine, D. P., & Schumann, G. J. (2015a). A review of low-cost space-borne data for flood modelling: topography, flood extent and water level. *Hydrological Processes, 29(15)*, 3368-3387.

Yan, K., Tarpanelli, A., Balint, G., Moramarco, T., & Di Baldassarre, G. D. (2015b). Exploring the potential of SRTM topography and radar altimetry to support flood propagation modeling: Danube case study. *Journal of Hydrologic Engineering*, 20(2), 04014048.

Yu, D., & Lane, S. N. (2006). Urban fluvial flood modelling using a two-dimensional diffusion-wave treatment, part 1: mesh resolution effects. *Hydrological Processes*, 20(7), 1541-1565.

Yu, J., Yang, X., Gao, F., & Tao, D. (2017). Deep multimodal distance metric learning using click constraints for image ranking. *IEEE transactions on cybernetics*, 47(12), 4014-4024.

Aknowledgments

After these three past years of hard work and great experiences, I am pleased to thank all the people, companies and authorities that contributed to, or inspired, my work.

To my supervisors: prof. Fernando Nardi, who introduced me to the world of science in flood risk and hydrology and involved me in several activities that made me grown professionally and personally; prof. Fabio Castelli who has been always available to provide precious advices and food for thought.

To my German tutor Prof. Wolfgang Niemeier and Dr. Björn Riedel, who welcomed me for three months at the Technical University of Braunschweig and involved me in exciting discussions finding contact points between our different backgrounds.

This work is part of a research project on the flood risk mitigation of the Tiber River's Middle Valley (Research grant 'Media Valle del fiume Tevere') founded by Regione Lazio that I'm glad to thank for the technical and financial support. A sincere gratitude to the Civil Protection CFD of Regione Lazio and in particular to Cristina Pompi, for her continuous support in providing me the necessary data for my work. Likewise, I express my thanks to the Civil Protection CFD of Regione Umbria for providing additional rainfall and flow observations for the Umbria region.

To all the staff the Florida International University at which I spent 5 intense months. A special thanks for Prof. Assefa Melesse for his kindness and availability and my hydro-lab mates Anteneh, Ike, Manzar and Sam.

I extend a special gratitude also to the FLO-2D Software INC, especially to Dr. Noemi González for her constant support in adapting the software code to the purpose of my modelling.

A really thank the external reviewers of the thesis, Prof. Assefa Melesse and Prof. Giuliano Di Baldassarre for their fruitful comments for improving the thesis.

Many joyful thanks to all my PhD colleagues with which I spent side by side every moment of my days in Germany, forming a united group of dear friends: Davide, Giovanna, Giulia, Laura & Laura, Lorenzo, Luca, Sara, Silvia and Tommaso.